Characterization of Intermolecular Interactions in Nanostructured Materials

Amanda Gayle Hudson

Dissertation submitted to the faculty of the Virginia Polytechnic Institute and State University in partial fulfillment of the requirements for the degree of

Doctor of Philosophy
in
Chemistry

Robert B. Moore, Committee Chair
Alan R. Esker
Tijana Z. Grove
Harold M. McNair

September 23, 2015
Blacksburg, VA

Keywords: isothermal titration calorimetry, variable temperature FTIR, surfactant, polymeric gene delivery, hydrogen bonding

Abstract

Advanced analytical techniques were utilized to investigate the intermolecular forces in several nanostructured materials. Techniques including, but not limited to, isothermal titration calorimetry (ITC), variable temperature Fourier transform infrared (FTIR) spectroscopy, and ultraviolet-visible (UV-Vis) thermal curves were used to study the fundamental interactions present in various nanomaterials, and to further probe the influence of these interactions on the overall behavior of the material. The areas of focus included self-assembly of surfactant micelles, polycation complexation of DNA, and temperature-dependent hydrogen bonding in polymeric systems.

ITC was successfully used to determine the low critical micelle concentration (CMC) for a novel gemini surfactant with limited water solubility. CMCs were measured at decreasing methanol molar fractions (x_{MeOH}) in water and the resulting linear relationship between CMC and methanol concentration was used to mathematically extrapolate to a predicted CMC at $x_{MeOH} = 0$. Using this technique, the CMC value for the novel gemini surfactant was predicted to be 0.037 ± 0.004 mM. This extrapolation technique was also validated with surfactant standards.

ITC was also used to investigate the binding thermodynamics of polyplex formation with polycations and DNA. The imidazolium-containing and trehalose-based polycations were both found to have endothermic, entropically driven binding with DNA, while the adenine-containing polycation exhibited exothermic DNA binding. In addition, ITC was also used to confirm the stoichiometric binding ratio of linear polyethylenimine and DNA polyplexes as determined by a novel NMR method. Dynamic light scattering (DLS) and zeta potential measurements were also performed to determine the size and surface charge of polyplexes. Circular dichroism (CD) and

FTIR spectroscopies provided information regarding the structural changes that may occur in the DNA upon complexation with polymers. UV-Vis thermal curves indicated that polyplexes exhibit a greater thermal stability than DNA by itself.

Variable temperature FTIR spectroscopy was used to quantitatively compare the hydrogen bonding behavior of multi-walled carbon nanotube (MWCNT)-polyurethane composites. Spectra were collected from 35 to 185 ºC for samples containing various weight percent loadings of MWCNTs with different hydrogen bonding surface functionalities. Peak fitting analysis was performed in the carbonyl-stretching region for each sample, and the hydrogen-bonding index (R_{index}) was reported. R_{index} values were used to quantitatively compare all of the composite samples in regards to temperature effects, weight percent loadings of MWCNTs, and the different functionalizations. In general, higher weight percent loadings of the MWCNTs resulted in greater R_{index} values and increased hydrogen bond dissociation temperatures. In addition, at 5 and 10 wt% loadings the initial R_{index} values displayed a trend that tracked well with the increasing hydrogen bonding capacity of the various surface functionalities.

Acknowledgements

There are an incredible number of people that I need to thank for getting me to this point in life, but I first and foremost want to thank my Heavenly Father. God has taught me an enormous lesson about hope and faith throughout this process, and it is only through Him that I have made it this far. Next, I want to thank my amazingly patient and wonderful husband, Tim. I knew he was a keeper when we met while I was taking undergraduate physical chemistry and he still wanted to stick around. He has seen me at my best and my worst for the past eight years, but he has been my constant rock, shoulder to cry on, and unyielding source of love and support. I also want to thank my incredible parents, Tim and Melinda Neighbors. Their love, guidance, and constant encouragement have shaped me into the person that I am today. They've believed in me from my very first day of kindergarten all the way through today and have given me the courage to follow my dreams.

I come from a wonderfully loving and tight-knit family, that I have had the fortune of never being far away from, even during graduate school. It is an incredible gift to know that when everything else goes wrong you can always go home to a circle of people that love you and welcome you with open arms, and I thank all of them for their love. I also have an amazing group of friends that have made surviving graduate school possible. Kacey and Alice, thank you for being my co-conspirators in every adventure that grad school brought our way, and for always being a constant source of advice, support, pep talks, and friendship. Candace and Stella, thank you for the endless supply of encouragement, smiles, and hugs. And Dr. Burkhardt, thank

you for not only showing me what I could do with chemistry at RU, but for also remaining a close friend. I would also like to give a special thanks for the many friendships formed in the Moore group. The camaraderie in our lab made doing chemistry fun on a daily basis.

Finally, I would like to send my sincerest gratitude to my advisory committee for seeing me through this process. Dr. McNair, thank you for first sparking my interest in pursuing analytical chemistry, and for always believing in me and my graduate career before I even knew I wanted one. Dr. Esker and Dr. Grove, thank you for going above and beyond in your guidance with several of my projects. Your support and advice will forever be appreciated. And last, but certainly not least, I would like to give a special thanks to my advisor, Dr. Robert Moore. You have seen me through many obstacles in my graduate experience, and your continuous encouragement, patience, and guidance will never be forgotten.

Table of Contents

List of Tables

List of Figures

Chapter 1 : Introduction

Currently, one of the biggest buzzwords in the field of science is "nano." From nanotubes to nanomedicine, there is a huge array of studies being conducted on this very small nanoscale. As scientists, we require special tools to probe these nanoenvironments so that we can learn more about the fundamental interactions that are taking place on the molecular level. Fortunately, there are a vast number of advanced analytical techniques available to explore the structure-property relationships present in nanomaterials of every variety. In this work, we sought to employ some of these analysis methods to answer fundamental questions about several novel, nanostructured materials.

1.1 Scope of Dissertation

Chapter 2 describes the search for a method using isothermal titration calorimetry (ITC) to determine the critical micelle concentration (CMC) for a new gemini surfactant with very low water solubility. By exploring the Henry's Law regime for water-methanol mixtures, we were able to overcome solubility limitations and use the correlation between CMC and methanol concentration to mathematically predict a CMC for the gemini surfactant in water only. The analysis method was also verified with two other well-known surfactant standards.

Chapter 3 discusses the use of a low volume ITC for determining the thermodynamic parameters associated with polycations binding to DNA to form nanoparticles called polyplexes. Experimental conditions were optimized for these binding systems, and reproducible results were obtained for various polymeric systems. Furthermore, conclusions were made regarding the

enthalpic and entropic contributions to binding for each system. This discussion is continued in Chapter 4 for an additional polycation vector. However, in addition to ITC results, several other techniques are used to explore the structure-property relationship of the polyplexes. Circular dichroism (CD) and Fourier transform infrared (FTIR) spectroscopies are employed to probe the structural effects observed in pDNA upon binding to polymers. The size, charge, and aggregation of these nanoparticles are investigated with dynamic light scattering (DLS) and zeta potential measurements. And finally, the thermal stability of the polyplexes is determined from thermal curves collected with temperature controlled ultraviolet-visible (UV-Vis) spectroscopy.

Chapters 5, 7, and 8 all deal with exploring the hydrogen bonding interactions present in copolymer systems using variable temperature FTIR. Specifically, Chapter 5 addressed the need for a quantitative means to compare the hydrogen bonding content within carbon nanotube (CNT) and polyurethane composites. Variable temperature FTIR and peak fitting analysis (continued in Chapter 8) were used to compare the hydrogen bonding interactions across four different series of CNT functionalization and at various concentrations of CNT loadings. Chapter 7 outlines several other collaborations involving variable temperature FTIR hydrogen-bonding studies for samples including polyurethanes with triptycene in the hard segments, oxamide-containing copolymers, and nucleobase-containing ABA triblock copolymers.

1.2 Review of Techniques

1.2.1 Critical Micelle Concentration (CMC) Determination by Isothermal Titration Calorimetry (ITC)

Surfactants are used in variety of applications, including detergents, petroleum production, cosmetics and hygiene, and even pharmaceuticals.[1-3] The critical micelle concentration (CMC) is a principal parameter for any new surfactant in these applications. The CMC is defined as the concentration, or very narrow concentration range, of surfactant at which micelles begin to form.[4] It is also associated with the concentration at which there is a significant change in a physical property of the solution, such as surface tension, density, or conductivity. The CMC is a vital piece of information when investigating the self-assembly behavior of surfactant and amphiphiles solutions.[5] There are numerous analytical techniques currently used in the literature to determine CMCs, including, but not limited to, UV-Vis spectroscopy, electronic conductivity, fluorescence spectroscopy, and surface tension measurements.[1, 6-9] However, due to its high sensitivity and the vast amount of information that can be gleaned from a single experiment, isothermal titration calorimetry (ITC) is quickly gaining popularity as a means to measure critical micelle concentrations.[6] One particularly common area of use for CMC determination by ITC is in the pharmaceutical field. Some examples include the analysis of bile salt aggregation,[10] amino acid-containing surfactant micelle formation,[11] and the interaction of sodium dodecyl sulfate (SDS) and casein.[12]

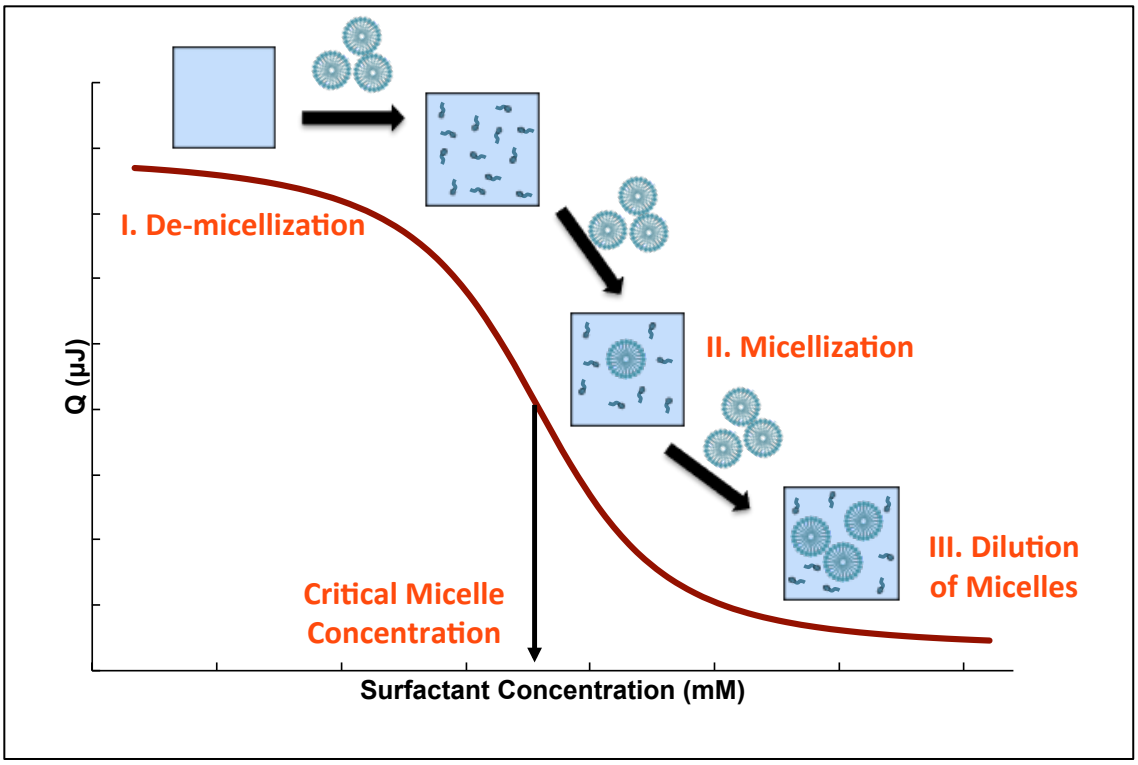

Figure 1.1 Illustration of a typical CMC titration by ITC (adapted from Hamberger, *et al*., 2011)

In an ITC experiment to determine the CMC, small amounts of a concentrated micellar solution are titrated into the solvent of interest, and the resultant heats accompanying demicellization, micellization, and dilution are measured. A typical sigmoidal CMC titration can be broken up into three regions, as shown in Figure 1.1. An initial plateau at the beginning of the titration corresponds to the dissociation of micelles, from the concentrated solution in the buret, into surfactant unimers as they are injected into the solvent. As the titration progresses and the CMC of the surfactant is reached within the cell, an abrupt change in the measured heat is observed and reflected as a sharp drop in the enthalpogram. This is due to the fact that the equilibrium between dissociation and association of micelles has shifted to the latter now that the

CMC has been reached and the micelles are no longer dissociating upon injection. Finally, the plateau at the end of the titration corresponds to the much lower heats that are associated with dilution of micelles. The CMC can be determined as the concentration of surfactant that corresponds to the inflection point in the observed sigmoidal curve.[6, 13] In addition to determining the CMC of a surfactant, a single titration can also yield the thermodynamic parameters associated with that micellization, such as the enthalpy, entropy, and Gibb's free energy of micellization.[6]

The sample of interest in Chapter 2 is an ionic gemini surfactant. Where typical ionic surfactants include a hydrophobic tail attached to a single ionic head-group, gemini surfactants contain multiple (usually two) ionic head-groups, connected by a linker, and, consequently, two hydrophobic tails.[14-15] One notable characteristic of gemini surfactants is that they tend to have very low critical micelle concentrations.[15] Consequently, a sensitive technique, such as ITC, is required to measure these low (usually micromolar) CMC values.

1.2.2 Analytical Techniques for the Investigation of Structure-Property Relationships in Polycation-DNA Polyplexes

In recent years, nucleic acid therapeutics have been gaining considerable notice as possible treatments for various genetic and acquired diseases.[16] The idea behind these being that a specific gene or set of genes within the body is already coding for a protein(s) that is(are) responsible for the targeted disease. If the correct nucleic acid therapeutic could be delivered effectively, it would be able to take the place of or fix the responsible, defective gene, and in doing so hopefully cure the disease by up-regulating or down-regulating in a therapeutic

manner.[17] Some of the more common therapeutics being investigated are plasmid DNAs (pDNA), siRNA, and short oligonucleotide decoy DNAs. However the obstacles preventing successful delivery of therapeutics into the body are many-fold.[16] In an effort to solve this problem without the use of viral vectors, which pose the potential for immunogenic responses and/or mutations, researchers have moved toward the study of biocompatible and nontoxic cationic polymers as alternative nucleic acid delivery vehicles.[17]

Many of the polymers developed for gene delivery vehicles are characterized only through biological assays, such as cytotoxicity and transfection assays, and merely one or two analytical techniques such as dynamic light scattering (DLS) and zeta potential measurements. However, a recent push has been made for a more in depth analytical approach at characterizing polyplexes to gain a deeper understanding of the physical interactions taking place between the polymer and nucleic acids.[18-20] Knowing the transfection efficiency of the polymers is only one-half of the bigger picture. By understanding the structure-property relationships through thermodynamic and structural analysis, we can correlate these results with those from the biological assays and direct the findings toward making even better therapeutics in the future.

Numerous analytical techniques are employed in the study of polymeric-nucleic acid interactions. Two common thermodynamic techniques are isothermal titration calorimetry (ITC) and UV-Vis thermal melt curves. Structural analysis of the nucleic acids upon binding with polymers is also important to understanding the structure-property relationships. The two most common structural characterization techniques used in this field that we will focus on are circular dichroism (CD) and Fourier Transform infrared (FT-IR) spectroscopies.

An ITC contains an identical sample and reference cell. As the polycation is injected into the sample cell, which contains the nucleic acid, the heat given off or absorbed during the reaction causes minute temperature changes within the sample cell, which is constantly and accurately measured throughout the reaction. The sample cell temperature is then compared to that of the reference cell, which usually contains buffer or water, and a feedback mechanism alters the amount of heat provided to the sample cell in order to maintain a constant temperature between the cells. This heat is then representative of the heats of each injection and can be integrated and fit to a suitable binding model. From this fit, the values for the enthalpy of binding (ΔH), binding affinity (K), and stoichiometry of binding (*n*) can be calculated. Likewise, if the exact experimental parameters are fixed within certain limits, the Gibbs free energy (ΔG) and entropy of reaction (ΔS) can also be calculated, providing a complete thermodynamic profile for the binding event of interest. In addition to providing such a vast amount of information about a particular binding system of interest, ITC is also an extremely sensitive technique, being able to measure values in the micro- to nanowatt range.[21-23]

UV-vis thermal melt curves utilize typical UV-Vis spectrophotometers that are attached to a thermocycler that can heat and cool the sample holder while monitoring the absorption. The nucleotides found in native double-stranded DNA or siRNA exhibit a natural absorbance in the near-ultraviolet range at 260 nm.[24] Heating the sample causes denaturation of the nucleic acid that breaks the hydrogen bonds and base stacking within the double helix, causing it to unwind or "melt" from double strands to single strands. In the native double-helix structure, the paired nucleotides interact strongly with each other, trapping a large number of the electrons that would normally absorb at 260 nm if they were actually free in solution. Therefore, when "melted" into

single strands of DNA, the base-pair bonds are broken and the absorption increases. This phenomenon is termed "hyperchromicity."[25] Hyperchromic effects result in a very characteristic melting curve, as illustrated in Figure 1.2. The inflection point of this curve corresponds to the melting temperature (T_m) of the nucleic acid.[26]

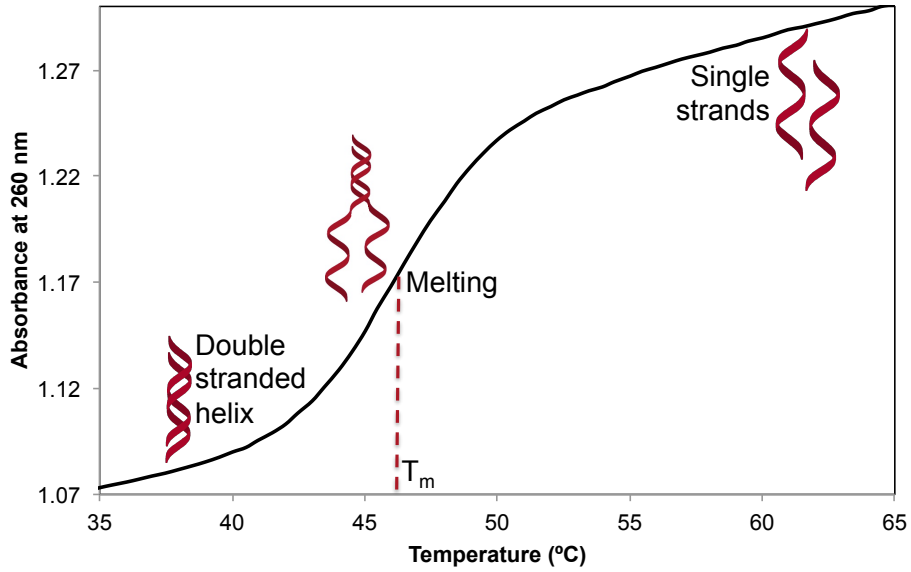

Figure 1.2 Illustration of a typical DNA melt curve

In CD spectroscopy, the key phenomenon being monitored is the difference in absorption of left and right circularly polarized light. Therefore, the secondary structure seen in nucleic acids, such as the double-helix of DNA makes it a prime candidate for CD spectroscopic measurements. If an optically active sample, such as DNA, is exposed to circularly polarized light, the left and right circularly polarized lights will be absorbed differently based upon their respective extinction coefficients. This results in a distinct CD spectrum for a particular optically active sample.[27] For DNA in the native B-conformation, the characteristic CD peaks

are seen at 210 nm (negative), 220 nm (positive), 245 nm (negative), and 280 nm (positive).[28-30] By observing the CD spectra for a sample of DNA as it is binding to a polymer of interest, changes in secondary structure can indirectly be monitored by the peaks shifting and/or changing in intensity.

Table 1.1 Characteristic FTIR vibrational frequencies for DNA

Stretch	Wavenumber (cm^{-1})
Guanine carbonyl	1715
Thymine carbonyl	1663
Adenine C-N	1609
Guanine/Cytosine C-N	1492
Asymmetric phosphate	1222
Symmetric phosphate	1086

The second structural analysis technique that is frequently employed in polyplex studies utilizes an instrument that is more commonly found in everyday laboratories: FT-IR spectroscopy. By utilizing a special attenuated total reflectance (ATR) attachment that is comprised of a ZnSe crystal residing at the bottom of a trough, liquid solutions of polyplex formations can be analyzed by FT-IR as well.[19-20, 31] Similar to the CD spectra, DNA also has characteristic peaks in FT-IR spectra, as listed in Table 1.1.[19-20, 32-33] By monitoring these specific peaks of interest for shifts in wavelength and changes in intensities, inferences can be made regarding the location of binding between a polymer and DNA.[33]

There are numerous reports in the literature that utilize some combination of these techniques to study various polycations that complex nucleic acids, including, but not limited to, spermine and lipospermine,[34] chitosan,[35] PEO-based polymers,[18] polyethylenimine (PEI),[31] and sugar-based polycations.[19-20] All of these publications illustrate not only the progress that has been made in this field over the past decade, but also the extreme importance of thorough bio-physical characterization in these therapeutic delivery systems. In order to truly understand the fundamental physical interactions taking place between nucleic acid therapeutics and polymeric delivery vehicles, a number of analytical techniques should be combined to obtain the most complete thermodynamic and structural profile as possible. Only then can we begin to understand at a molecular level why certain vehicles deliver better than others, and hopefully from this we can continue to modify and adjust the synthesis of future polymeric vehicles for the most efficient therapeutic delivery possible. These analytical methods will be applied to several different DNA-polymer systems in Chapters 3 and 4.

1.2.3 Exploring Hydrogen-Bonding Interactions in Polymers with Variable Temperature FTIR

FTIR spectroscopy is an extremely useful analytical technique for investigating the hydrogen-bonding behavior of polymers. Numerous studies have been conducted using FTIR to explore hydrogen bonding in polymers, such as polyamides and polyurethanes.[36-41] There is widespread hydrogen bonding present in most polyurethanes and it is the driving force behind microphase separation in polyurethane samples.[37, 42] Frequency shifts to lower wavenumbers in the N-H and carbonyl stretching regions, which correspond to the hydrogen bond donators and

acceptors, respectively, are indicative of hydrogen bonding within a sample.[38] In addition, the carbonyl-stretching region of the infrared absorbance is highly sensitive to ordering within the sample. Typically three discernable peaks are present in this region: ordered hydrogen-bonding carbonyls, disordered hydrogen-bonding carbonyls, and non-bonding, or "free," carbonyl groups. Disordered hydrogen bonding refers to hydrogen bonds that occur between hard segment urethane carbonyls found in the amorphous region, while ordered hydrogen bonds occur in the highly ordered regions of the hard segment domain that are potentially crystalline. The distinction between these two is attributed to dipole-dipole coupling of the carbonyls.[41]

Variable temperature FTIR offers the additional advantage of monitoring hydrogen bond dissociation at elevated temperatures, providing insight into the temperature-dependent behavior of these interactions. As hydrogen bonds are broken with increasing temperatures, the carbonyl peaks shift toward higher frequencies as the free carbonyl population increases.[37] Previous literature has reported that hydrogen bond dissociation is not dependent on the extent of ordering within the polyurethane sample, but rather, rapidly increases at temperatures above the hard segment T_g because of increased polymer chain mobility. [42]

Several studies have been published regarding the effects of various nanofillers in polyurethane composites on their hydrogen-bonding properties. These nanofillers have included multi-walled carbon nanotubes (MWCNTs),[43] starch nanocrystals,[44] silver nanoparticles,[45] silica nanoparticles,[46] and dopamine-modified clay.[47] However, no other investigations have thoroughly studied the temperature-dependent effects of hydrogen bonding in polyurethane-CNT composites.[48] This is addressed with variable temperature FTIR studies in Chapter 5.

1.3 References

1. Dominguez, A.; Fernandez, A.; Gonzalez, N.; Iglesias, E.; Montenegro, L. *Journal of Chemical Education* **1997,** *74* (10), 1227.
2. Tong, W.; Zheng, Q.; Shao, S.; Lei, Q.; Fang, W. *J. Chem. Eng. Data* **2010,** *55*, 3766-3771.
3. Zana, R.; Xia, J. Applications of Gemini Surfactants. In *Gemini surfactants: synthesis, interfacial and solution-phase behavior, and applications*, Marcel Dekker Inc.: New York, 2004; pp 296-313.
4. Moroi, Y. 4.3 Critical Micelle Concentration. In *Micelles: Theoretical and Applied Aspects*, Springer Science+Business Media: New York, 1992; p 47.
5. Pérez-Rodríguez, M.; Prieto, G.; Rega, C.; Varela, L. M.; Sarmiento, F.; Mosquera, V. *Langmuir* **1998,** *14* (16), 4422-4426.
6. Bouchemal, K.; Agnely, F.; Koffi, A.; Djabourov, M.; Ponchel, G. *Journal of Molecular Recognition* **2010,** *23* (4), 335-342.
7. Goddard, E. D.; Harva, O.; Jones, T. G. *Transactions of the Faraday Society* **1953,** *49* (0), 980-984.
8. Kalyanasundaram, K.; Thomas, J. K. *Journal of the American Chemical Society* **1977,** *99* (7), 2039-2044.
9. Paula, S.; Sus, W.; Tuchtenhagen, J.; Blume, A. *Journal of Physical Chemistry* **1995,** *99* (30), 11742-11751.
10. Garidel, P.; Hildebrand, A.; Neubert, R.; Blume, A. *Langmuir* **2000,** *16* (12), 5267-5275.

11. Ohta, A.; Toda, K.; Morimoto, Y.; Asakawa, T.; Miyagishi, S. *Colloids and Surfaces A: Physicochemical and Engineering Aspects* **2008,** *317* (1), 316-322.

12. Liu, Y.; Guo, R. *Journal of Colloid and Interface Science* **2007,** *315* (2), 685-692.

13. Hamberger, A.; Landfester, K. *Colloid Polymer Science* **2011,** *289*, 3-14.

14. Rosen, M.; Tracy, D. *J Surfact Deterg* **1998,** *1* (4), 547-554.

15. Menger, F. M.; Keiper, J. S. *Angewandte Chemie International Edition* **2000,** *39* (11), 1906-1920.

16. Leong, K. *MRS Bulletin* **2005,** *30*, 640-646.

17. Reineke, T. M.; Grinstaff, M. W. *MRS Bulletin* **2005,** *30*, 635-639.

18. Bronich, T.; Kabanov, A. V.; Marky, L. A. *Journal of Physical Chemistry B* **2001,** *105*, 6042-6050.

19. Prevette, L. E.; Kodger, T. E.; Reineke, T. M.; Lynch, M. L. *Langmuir* **2007,** *23*, 9773-9784.

20. Prevette, L. E.; Lynch, M. L.; Kizjakina, K.; Reineke, T. M. *Langmuir* **2008,** *24*, 8090-8101.

21. O'Brien, R.; Ladbury, J. E.; Chowdhry, B. Z. Chapter 10: Isothermal titration calorimetry of biomolecules. In *Protein-Ligand Interactions: hydrodynamics and calorimetry*, Harding, S. E.; Chowdhry, B. Z., Eds. Oxford University Press: New York, 2001; pp 263-286.

22. MicroCal. What is ITC? http://www.microcal.com/technology/itc.asp (accessed September 26, 2010).

23. Microcalorimetry: Introduction to characterizing biopolymer binding and kinetics reactions by ITC. TA Instruments: 2009; pp 1-83.

24. van Holde, K. E. Chapter 8: ABSORPTION AND EMISSION OF RADIATION. In *Physical Biochemistry*, 2nd ed.; Prentice-Hall, Inc.: Englewood Cliffs, NJ, 1985; pp 190-194.

25. Nelson, D. L. C., M. M. Chapter 8: Nucleotides and Nucleic Acids. In *Lehninger Principles of Biochemistry*, 4th ed.; W. H. Freeman and Company: New York, 2005; pp 291-292.

26. Schindler, T.; Nordmeier, E. *Polymer* **1999,** *40*, 7019-7027.

27. van Holde, K. E. Chapter 10: Circular Dichroism and Optical Rotation. In *Physical Biochemistry* 2nd ed.; Prentice-Hall, Inc.: Englewood Cliffs, NJ, 1985; pp 235-252.

28. Baase, W. A. J., W. C. Jr. *Nucleic Acids Research* **1979,** *6* (2), 797-814.

29. Brahms, J. a. M., W. F. H. M. *Journal of Biological Chemistry* **1964,** *10*, 73-88.

30. Tunis-Schneider, M. J. B. a. M., M. F. *Journal of Molecular Biology* **1970,** *52*, 521-541.

31. Choosakoonkriang, S. L., B.; Koe, G.; Koe, J.; Middaugh, C. *Journal of Pharmaceutical Sciences* **2003,** *92* (8), 1710-1722.

32. Arakawa, H. A., R.; Naoui, M.; Tajmir-Riahi, H. *The Journal of Biological Chemistry* **2000,** *275* (14), 10150-10153.

33. Taillandier, E.; Taboury, J. A.; Adam, S.; Liquier, J. *Biochemistry* **1984,** *23* (24), 5703-5706.

34. Patel, M. A., T. *Biophysical Journal* **2005,** *88*, 2089-2103.

35. Lee, K. *Macromolecular Research* **2005,** *13* (6), 542-544.

36. Seymour, R. W.; Estes, G. M.; Cooper, S. L. *Macromolecules* **1970,** *3* (5), 579-&.

37. Seymour, R. W.; Cooper, S. L. *Macromolecules* **1973,** *6* (1), 48-53.

38. Senich, G. A.; MacKnight, W. J. *Macromolecules* **1980,** *13* (1), 106-110.

39. Skrovanek, D. J.; Howe, S. E.; Painter, P. C.; Coleman, M. M. *Macromolecules* **1985,** *18* (9), 1676-1683.

40. Skrovanek, D. J.; Painter, P. C.; Coleman, M. M. *Macromolecules* **1986,** *19* (3), 699-705.

41. Coleman, M. M.; Lee, K. H.; Skrovanek, D. J.; Painter, P. C. *Macromolecules* **1986,** *19* (8), 2149-2157.

42. Lamba, N. M. K.; Woodhouse, K. A.; Cooper, S. L.; Lelah, M. D. *Polyurethanes in biomedical applications*. CRC Press: Boca Raton, 1998.

43. Xia, H. S.; Song, M. *Soft Matter* **2005,** *1* (5), 386-394.

44. Chen, G. J.; Wei, M.; Chen, J. H.; Huang, J.; Dufresne, A.; Chang, P. R. *Polymer* **2008,** *49* (7), 1860-1870.

45. Ciobanu, L. C.; Ciobanu, C.; Dorohoi, D. *High Perform. Polym.* **2010,** *22* (1), 56-68.

46. Bistricic, L.; Baranovic, G.; Leskovac, M.; Bajsic, E. G. *European Polymer Journal* **2010,** *46* (10), 1975-1987.

47. Phua, S. L.; Yang, L.; Toh, C. L.; Huang, S.; Tsakadze, Z.; Lau, S. K.; Mai, Y. W.; Lu, X. H. *ACS Appl. Mater. Interfaces* **2012,** *4* (9), 4571-4578.

48. Inglefield, D. L. Tailoring Intermolecular Interactions for High-Performance Nanocomposites. Dissertation, Virginia Polytechnic Institute and State University, Blacksburg, VA, 2014.

Chapter 2 : Isothermal Titration Calorimetric Method to Determine Low Micelle Concentrations for Surfactants with Low Water-Solubility

2.1 Introduction

Surfactants can be found throughout the broad range of scientific literature, with far-reaching applications in fields such as detergents, petroleum production, cosmetics and hygiene, and even pharmaceuticals.[1-3] For these applications, a principal parameter for any novel surfactant is the critical micelle concentration (CMC). The CMC is defined as the concentration, or very narrow concentration range, of surfactant at which micelles begin to form.[4] It is also associated with the concentration at which there is a significant change in a physical properties of the solution, such as surface tension, density, or conductivity. The CMC is a fundamental characteristic among surfactants and amphiphiles when investigating their self-assembly behavior in solution.[5] There are numerous analytical methods currently available to determine critical micelle concentrations, including, but not limited to, UV-Vis spectroscopy, electronic conductivity, fluorescence spectroscopy, surface tension measurements, and isothermal titration calorimetry (ITC).[1, 6-9]

Due to its high sensitivity and the vast amount of information that can be gleaned from a single experiment, ITC is quickly gaining popularity as a means to measure critical micelle concentrations.[6] In a typical ITC experiment to determine the CMC, small amounts of a concentrated micellar solution are titrated into the solvent of interest, and the resultant heats accompanying demicellization, micellization, and dilution are measured. As the CMC of the surfactant is reached within the cell, an abrupt change in the measured heat is observed and

reflected in the resulting enthalpogram. In addition to determining the CMC of a surfactant, a single titration can also yield thermodynamic parameters associated with that micellization, such as the enthalpy, entropy, and Gibb's free energy of micellization.[6]

The sample of interest in this investigation is an ionic gemini surfactant. Where typical ionic surfactants include a hydrophobic tail attached to a single ionic head-group, gemini surfactants contain two ionic head-groups, connected by a linker, and usually two hydrophobic tails.[10-11] One application of gemini surfactants that has been of interest in the literature is for nonviral gene delivery vehicles.[12] Along with biological and medical applications, gemini surfactants have also been studied as electrospinning materials in recent years.[13-14] One notable characteristic of gemini surfactants is that they tend to have very low critical micelle concentrations.[11] With these low CMC values, gemini surfactants are prone to forming large supramolecular assemblies, which have been shown to entangle and stabilize electrospinning jets to form uniform fibers.[13-14] Due to the vital role that solution parameters, such as concentration and surface tension, play in successful electrospinning, the CMC is critical in establishing a useful concentration range for this application.[15] Consequently, a sensitive technique, such as ITC, is required to measure these low (micromolar) CMC values.

Another potential challenge in CMC determination is when the surfactant exhibits limited water solubility. In these cases, the addition of a less polar co-solvent may prove useful in solubilizing the surfactant. For example, Long *et al*. reported using a mixed solvent of water and methanol in ITC to successfully measure the CMC of a phosphonium gemini surfactant (12-2-12P) that exhibits low water solubility.[14] While knowing the CMC of a surfactant in a mixed-

solvent system can be useful for certain applications, it is still desirable to ascertain the more commonly reported value of the CMC in pure water for aqueous applications, such as pharmaceuticals and cosmetics. In this study, the CMC of surfactants was observed as a function of decreasing molar fractions of methanol in aqueous solution. The data obtained were then used to mathematically extrapolate, using a linear relationship, to a predicted CMC value in pure water. The method was first tested with two well-known surfactants that served as standards: sodium dodecyl sulfate (SDS), an anionic surfactant, and cetyltrimethylammonium bromide (CTAB), a cationic surfactant. The same titration procedure was repeated for 12-2-12P and the subsequent linear relationship was used to predict a CMC value in pure water as a follow-up to the previously reported mixed-solvent CMC.[14]

2.2 Experimental

2.2.1 Materials

The phosphonium gemini surfactant with a spacer comprised to two methylene groups, 12-2-12P, was prepared as previously reported.[14] The chemical structure of 12-2-12P is shown in Figure 2.1. High-purity SDS (≥ 98.5%) and CTAB (≥ 99%) were purchased from Sigma-Aldrich, and used without further purification. HPLC grade methanol was purchased from Spectrum Chemicals. Ultrapure water was obtained from a Millipore-DQ3 filtration system, at a resistivity of 18.2 MΩ·cm.

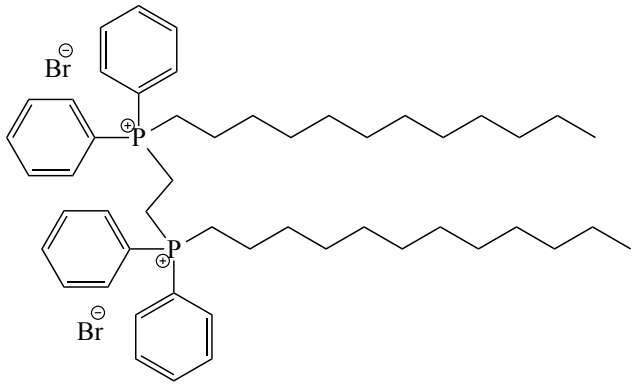

Figure 2.1 Chemical structure of phosphonium gemini surfactant 12-2-12P

2.2.2 Isothermal Titration Calorimetry (ITC)

The instrument used for the titration experiments was a TA Instruments Low Volume NanoITC. The gold sample and reference cells in the ITC have a working volume of 170 μL, and the burette is a 50 μL gas-tight syringe with a stainless steel needle. All titrations were performed at 25 °C with a stir rate of 350 rpm and 300 s intervals between each injection. Before starting each titration, the instrument was allowed to equilibrate until a stable baseline was obtained. Furthermore, a 300 s baseline was collected before and after the first and last injections. Depending on the heat generated, all titrations involved either 1.96 μL per injection (25 total injections) or 1.43 μL per injection (35 total injections).

For experiments involving SDS, mixtures were made with water and methanol in a range of methanol molar fractions ($x_{MeOH} = n_{MeOH}/n_{tot}$) between 0.023 and 0.31. For each titration, the sample and reference cells were both filled with the same water-methanol mixture used to prepare the SDS titrant. SDS titrant concentrations ranged from 85 to 170 mM. The surfactant solution was then titrated into the water-methanol mixture and the thermodynamic data was

collected. This procedure was completed in duplicate for each SDS solution prepared from the concentration range given. Similar experiments were conducted in the range of 9.0 to 15 mM CTAB with solvent compositions ranging between molar fractions of methanol from 0.011 and 0.073. The phosphonium gemini surfactant (12-2-12P) at concentrations between 0.73 and 8.0 mM was titrated in the range of methanol molar fractions from 0.023 to 0.13. ITC data were analyzed with the TA Instruments NanoAnalyze™ software.

2.2.3 Refractive Index (RI)

Refractive index measurements were performed with a Thermo Spectronic ABBE Refractometer. Water-methanol mixtures were prepared in methanol molar fractions ranging from 0.023 to 0.31. Each of the eight mixtures was analyzed at room temperature and their respective refractive indices were recorded and corrected to 20 °C with the following equation[16]:

$$n^{20} = n^{observed} + (T - 20) \times 0.00045 \quad (1)$$

where n^{20} is the corrected refractive index and $n^{observed}$ is the observed refractive index at T, the temperature in degrees Celsius.

2.2.4 Dynamic Light Scattering (DLS)

A Malvern Zetasizer Nano ZS was used for DLS measurements. Samples were analyzed in disposable polystyrene cuvettes and compared to a polystyrene latex reference. DLS measurements were performed at 25 °C. Two sets of experiments were conducted. In the first

set, ultrapure water was filtered through a 2 μm syringe filter and used to prepare a 0.081 mM solution of 12-2-12P. A DLS measurement was taken initially, and then additional filtered water was added as a titrant, with mixing, until a concentration of 0.023 mM 12-2-12P was achieved. DLS measurements were repeated after each addition of water. In the second set of experiments, ultrapure water was filtered through a 0.45 μm filter and used to prepare two solutions of 12-2-12P, one at 0.080 mM and one at 0.027 mM. Three DLS measurements were taken for each of the two concentrations.

2.3 Results and Discussion

2.3.1 ITC Results for Sodium Dodecylsulfate (SDS)

Control experiments were performed with SDS as a surfactant standard. Initially, SDS was titrated into aqueous solutions containing decreasing methanol molar fractions over the range of 0.31 to 0.023. This broad range of methanol molar fractions was used to determine the optimal concentrations at which a correlation between CMC and methanol concentration could be observed. As a representative example of these control experiments, Figure 2.2(a) shows the titration of an aqueous 100 mM SDS solution (x_{MeOH} = 0.1) into the same mixture of water and methanol at 25 ºC. Figure 2.2(b) shows the resulting isotherm from the integral heats per injection versus the concentration of SDS in the cell.

Standard with CMC titrations, the concentration of the surfactant (SDS) in the injection syringe was significantly greater than its reported CMC value. Therefore, throughout the course of the titration the concentration of SDS within the sample cell continued to increase until it eventually passed through the CMC. Referring back to Figure 2.2(b), the titration can be broken

up into three distinct regions. In the beginning of the titration, shown as the initial plateau region from 0 to 7 mM, the micelles contained in the concentrated solution being injected into the cell are dissociating into surfactant unimers. This plateau is due to the enthalpy of demicellization of the dissociating micelles. As the titration progresses and the surfactant concentration within the cell continues to increase from approximately 7 to 15 mM, the heat due to micelle dissociation sharply drops off in the next portion of the graph. This is because the CMC of SDS has been reached and the equilibrium between dissociation and association of micelles shifted to the latter. Thus, micelles are no longer dissociating upon injection. The final plateau region at the end of the titration, from approximately 15 to 25 mM, exhibits greatly reduced heats due to the dilution of micelles. The CMC can be determined as the concentration of surfactant that corresponds to the inflection point in the observed sigmoidal curve, which is obtained by taking the first derivative of the data.[6, 17] The CMC for this titration was determined to be 9.92 mM SDS. The overlaid enthalpograms and corresponding isotherms for the duplicate trials at each methanol molar fraction can be seen in Figure 2.3 – Figure 2.8 and the full set of CMC data can be found in Table 2.1. From the overlaid plots, it was observed that these titrations were quite reproducible, especially at lower molar fractions of methanol.

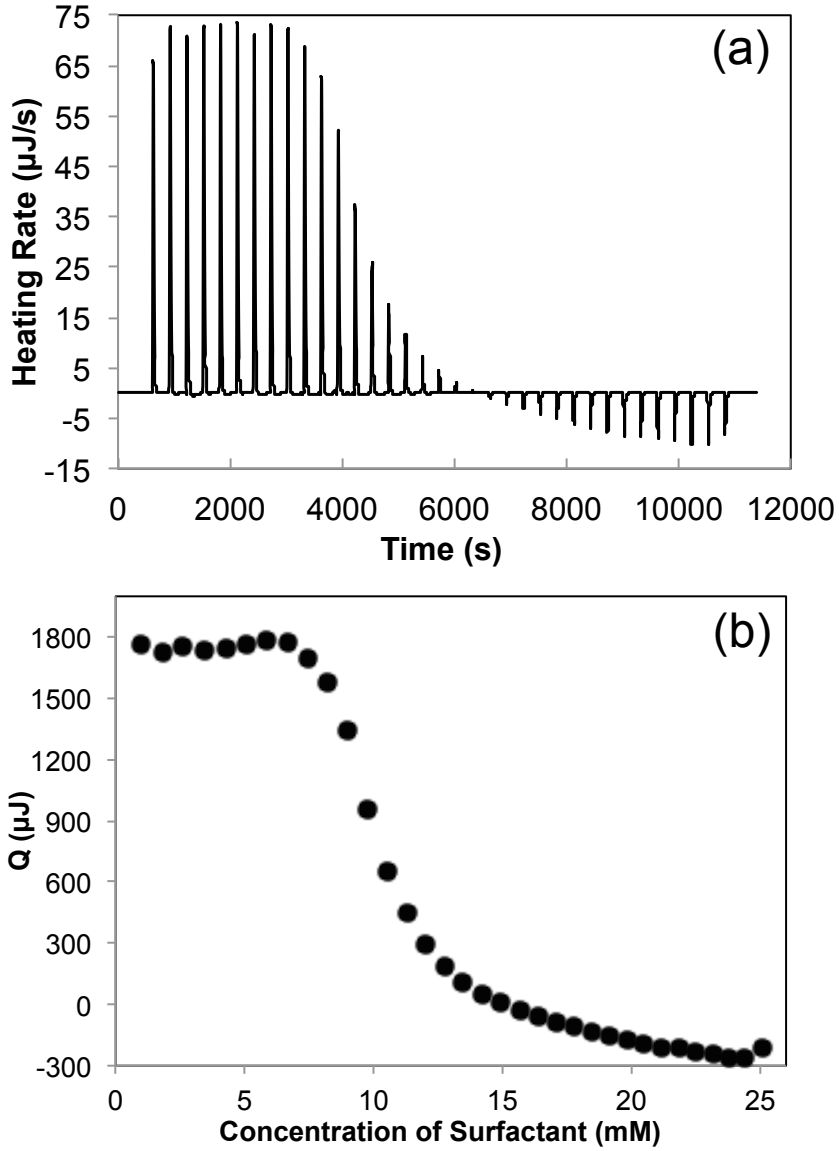

Figure 2.2 (a) ITC enthalpogram of 1.00×10^2 mM SDS being titrated into a water-methanol mixture ($X_{MeOH} = 0.1$) at 25 °C and (b) the resultant integrated heat per injection.

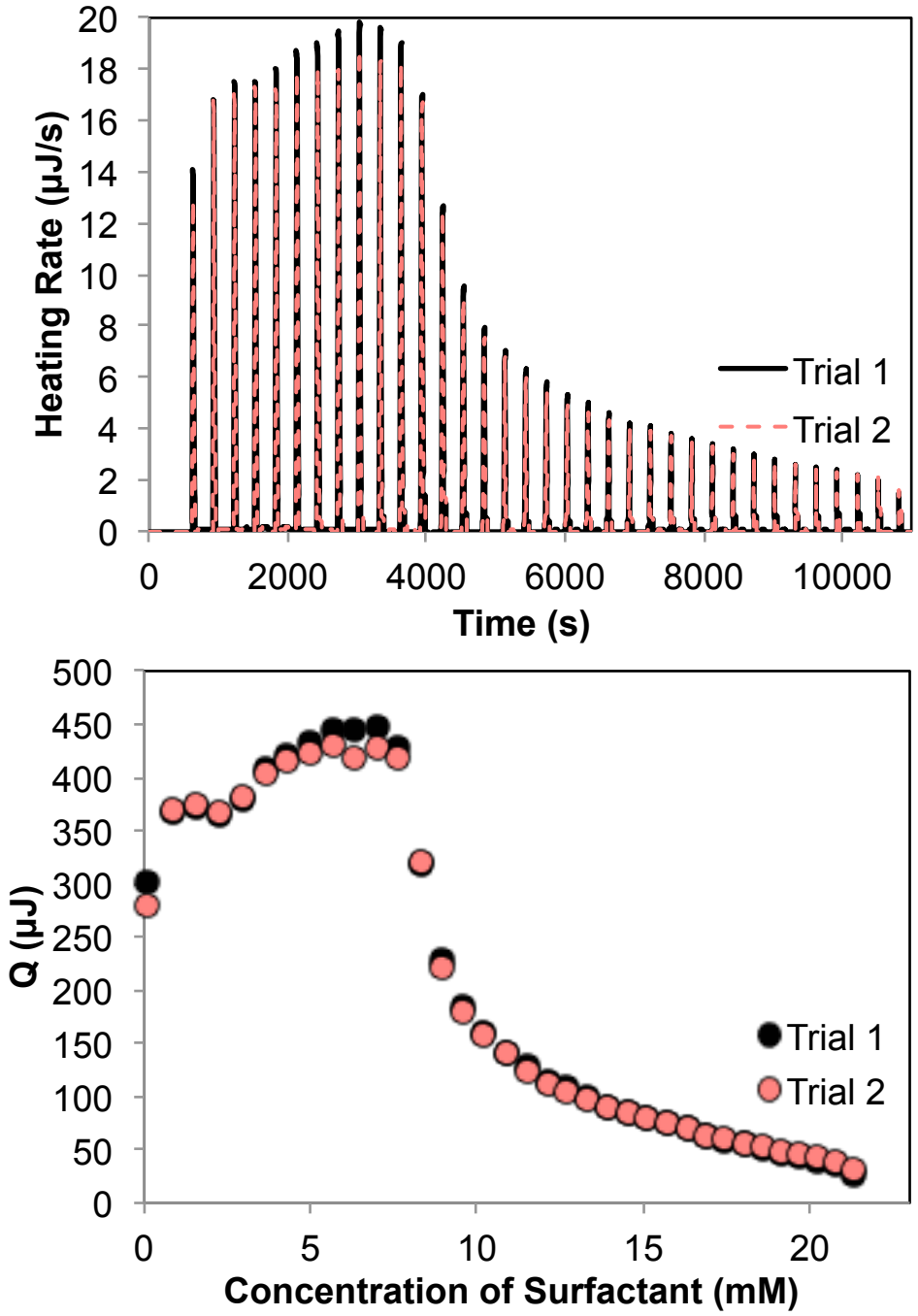

Figure 2.3 (top) ITC enthalpograms for duplicate titrations of SDS being titrated into a water-methanol mixture (X_{MeOH} = 0.023) at 25 °C and (bottom) the resultant integrated heat per injection.

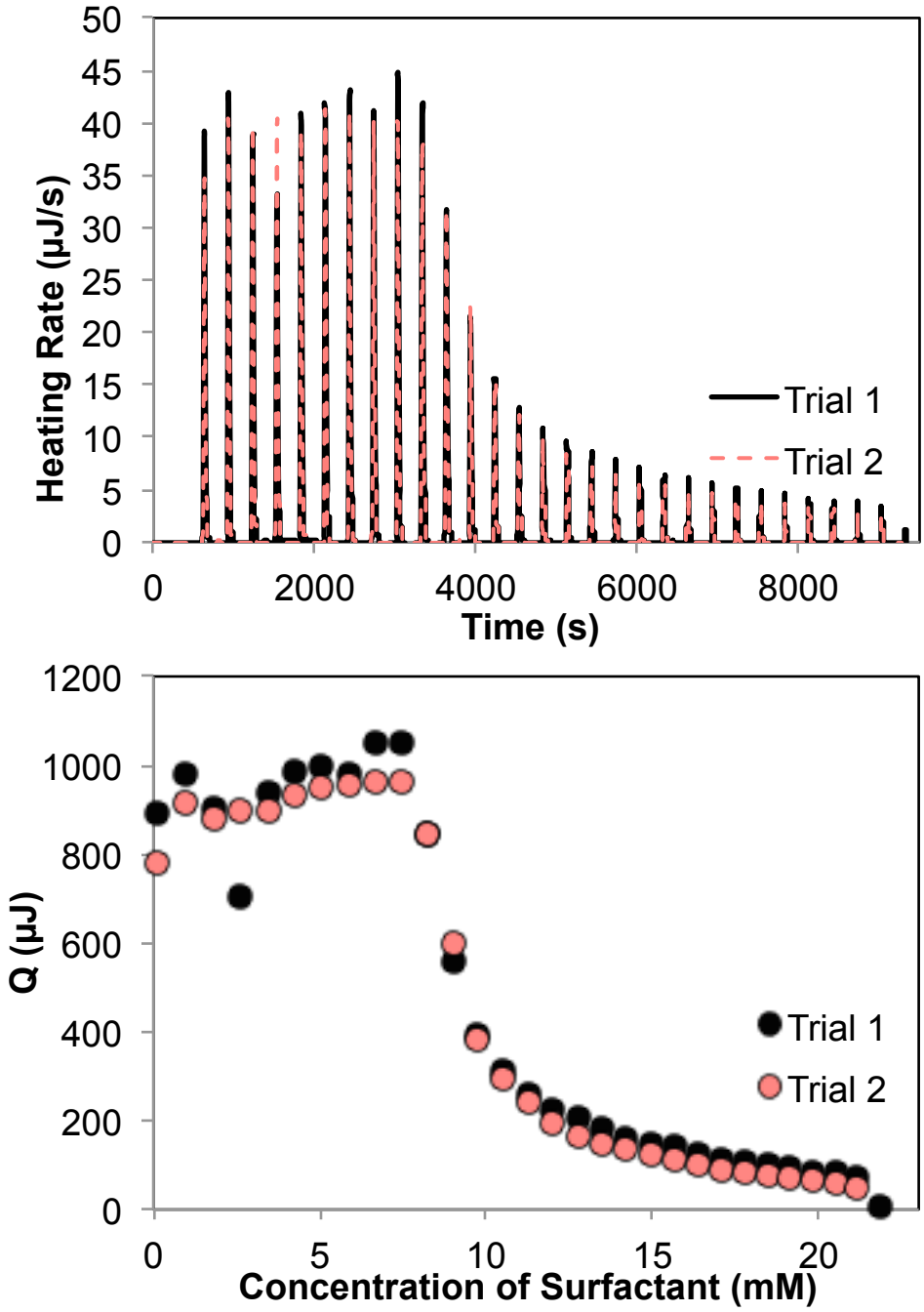

Figure 2.4 (top) ITC enthalpograms for duplicate titrations of SDS being titrated into a water-methanol mixture (X_{MeOH} = 0.047) at 25 °C and (bottom) the resultant integrated heat per injection.

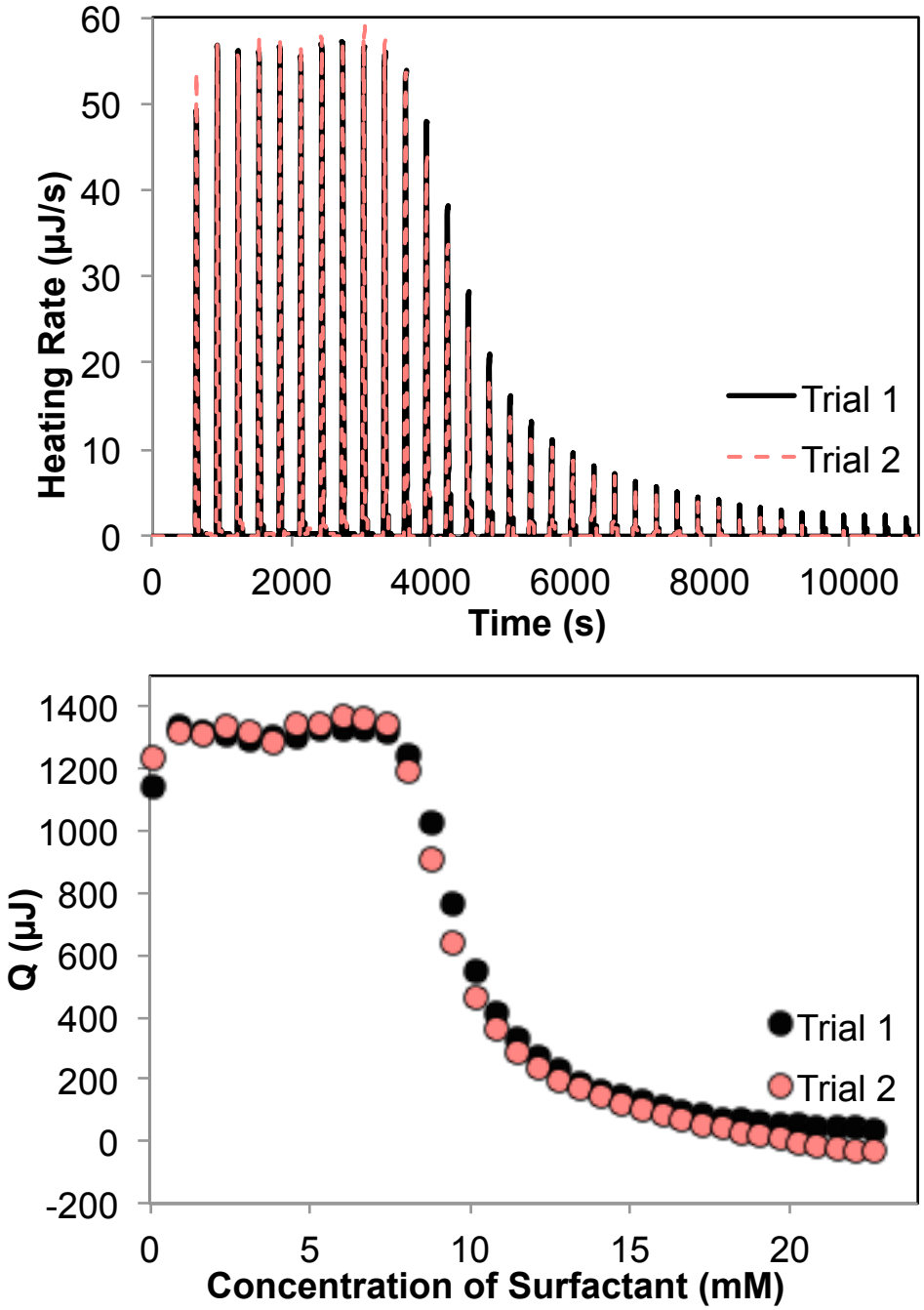

Figure 2.5 (top) ITC enthalpograms for duplicate titrations of SDS being titrated into a water-methanol mixture (X_{MeOH} = 0.073) at 25 °C and (bottom) the resultant integrated heat per injection.

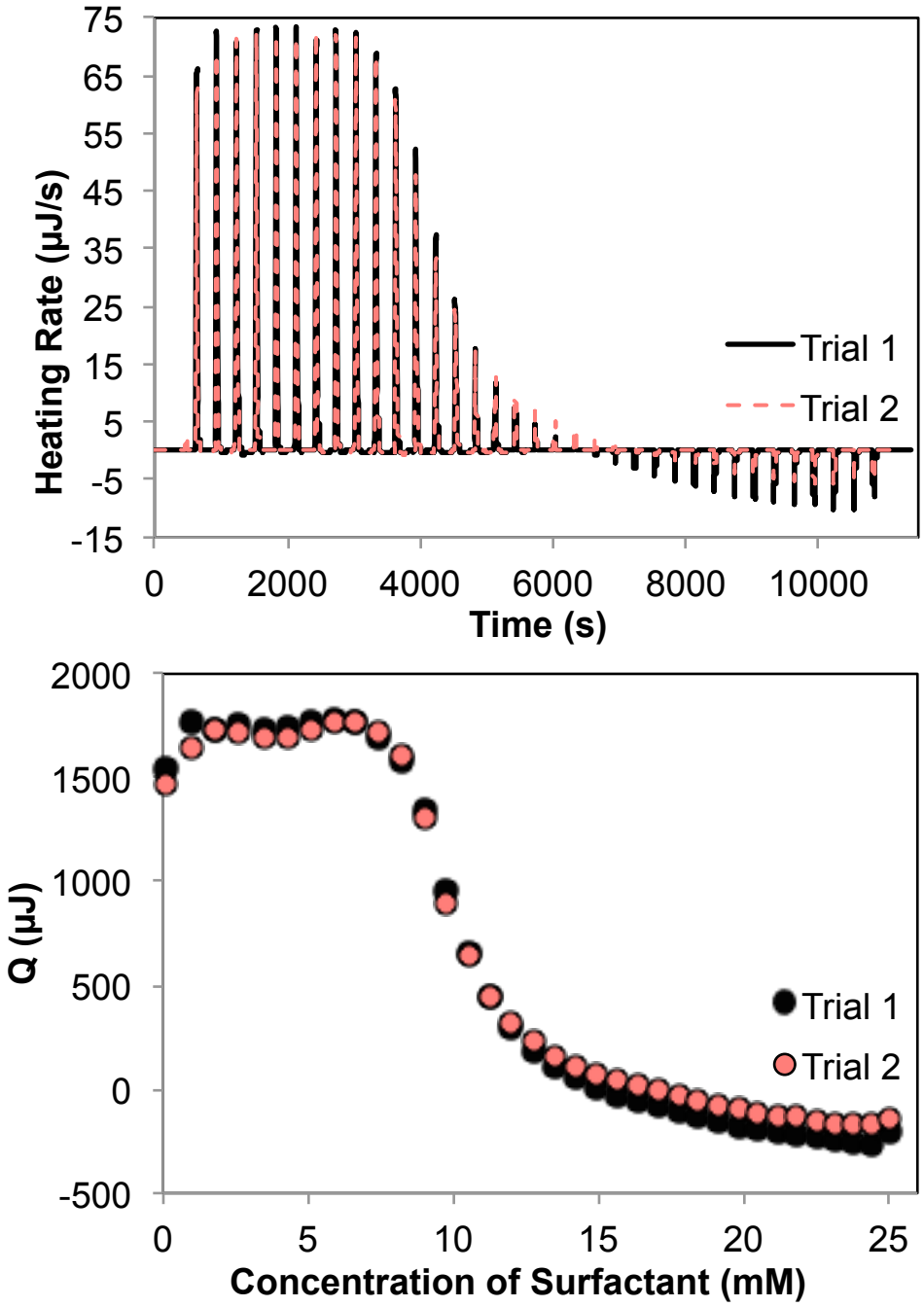

Figure 2.6 (top) ITC enthalpograms for duplicate titrations of SDS being titrated into a water-methanol mixture (X_{MeOH} = 0.10) at 25 °C and (bottom) the resultant integrated heat per injection.

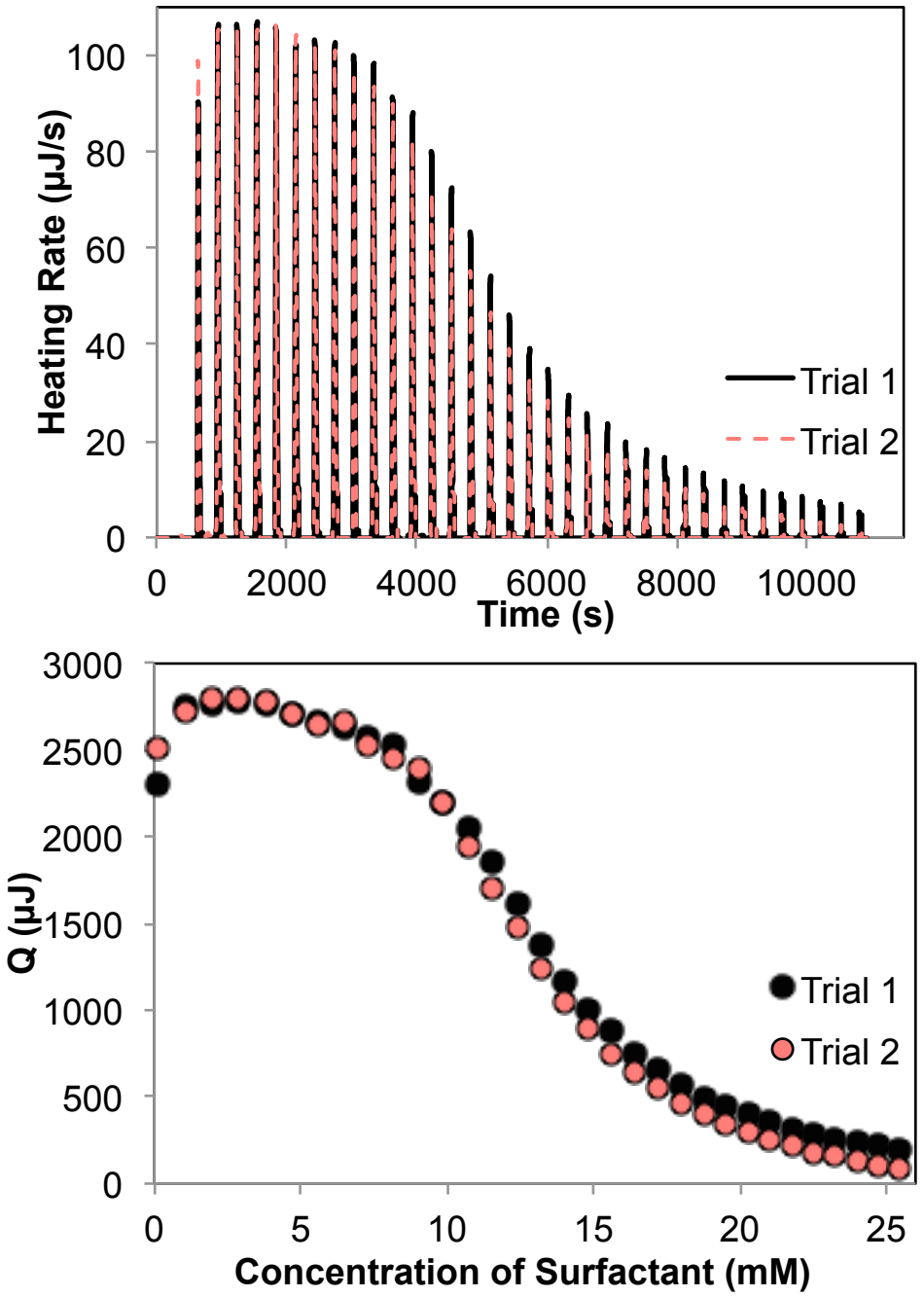

Figure 2.7 (top) ITC enthalpograms for duplicate titrations of SDS being titrated into a water-methanol mixture (X_{MeOH} = 0.16) at 25 °C and (bottom) the resultant integrated heat per injection.

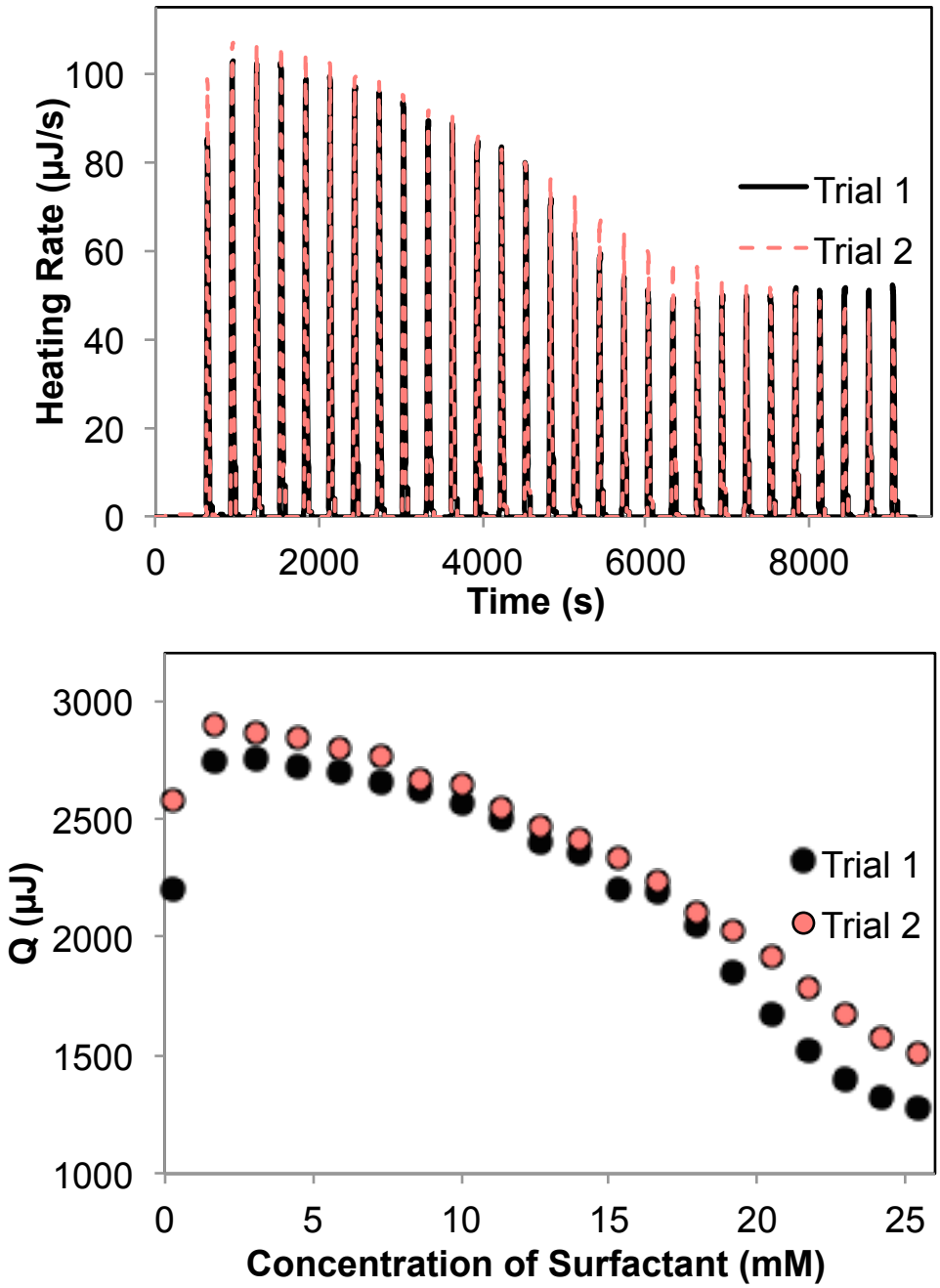

Figure 2.8 (top) ITC enthalpograms for duplicate titrations of SDS being titrated into a water-methanol mixture (X_{MeOH} = 0.31) at 25 °C and (bottom) the resultant integrated heat per injection.

Table 2.1 CMC data for SDS duplicate trials

x_{MeOH}	Trial 1 CMC (mM)	Trial 2 CMC (mM)	Average (mM)	Standard Deviation	Relative Standard Deviation (%)
0.023	8.58	8.55	8.57	0.02	0.2
0.047	8.76	8.97	8.87	0.15	1.7
0.073	9.47	9.16	9.32	0.22	2.4
0.1	9.92	9.77	9.85	0.11	1.1
0.16	12.92	12.50	12.71	0.30	2.3
0.308	18.41	20.10	19.26	1.20	6.21

As shown in Figure 2.9, with increasing molar fractions of methanol there is also an increase in the CMC of SDS. This result was expected due to the cosolvent effect.[18-19] The high end of this range, X_{MeOH} = 0.31, is the same concentration that was used previously to find a CMC in methanol and water.[14] However, lower methanol concentrations were also tested as methanol-water mixtures are non-ideal and have been shown to follow Henry's Law at low methanol concentrations.[20-22] Previous literature observed that the partial pressure of methanol increases linearly with molar fraction up to approximately X_{MeOH} = 0.1 at a temperature of 25 °C.[20] We hypothesized that if an appropriate fit could be found for the data, then the y-intercept of the fit (x_{MeOH} = 0.0) would represent the CMC for the surfactant in pure water. Furthermore, we anticipated that a linear relationship between CMC and molar fraction of methanol was also possible in the Henry's Law regime.

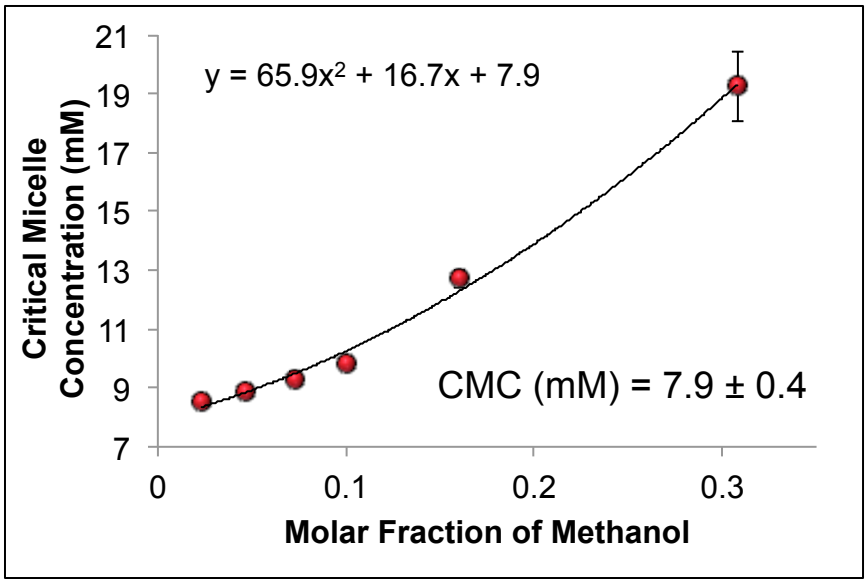

Figure 2.9 Observed CMC of SDS versus molar fraction of methanol, exhibiting a nonlinear relationship

Across the full range that was tested, it was noted that at higher molar fractions of methanol the trend deviated from linearity and predicted a CMC in pure water of 7.9 ± 0.4 mM SDS. This is slightly lower than previously reported literature values.[23-25] However, if only the lower molar fractions of methanol are considered, as shown in Figure 2.10, then the data displays a clear linear relationship that corresponds nicely with the aforementioned Henry's Law regime. Furthermore, extrapolation with this linear fit estimates the CMC in pure water to be 8.13 ± 0.07 mM SDS, which is in excellent agreement with the literature values of 8.1 to 8.4 mM.[23-25] Statistically, both of the predicted CMC values for SDS are actually in good agreement with the literature. However, as higher concentrations of methanol are considered, the trend starts to deviate from linearity to compensate for the more non-ideal behavior of the mixture and there is a loss in precision with the nonlinear fit. This is evident in the standard deviation associated with the CMC predicted from the nonlinear fit, which is more than six times greater than the error for

the linear fit prediction. Based upon these results, we believe that using a linear fit for these extrapolations is the better approach.

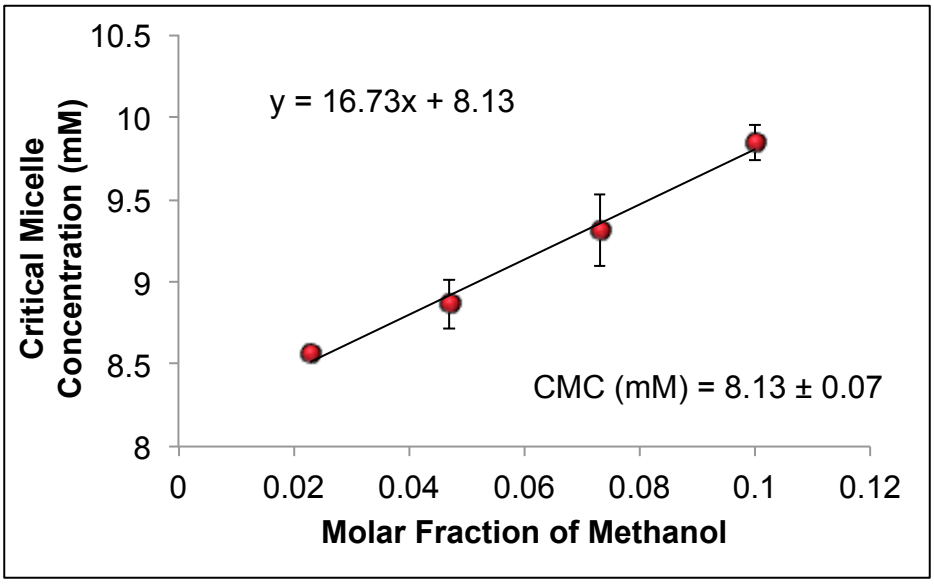

Figure 2.10 Observed CMC of SDS versus molar fraction of methanol, exhibiting a linear relationship at low x_{MeOH}

2.3.2 RI Measurements

After observing the linear behavior in Figure 2.10 for the CMCs at lower concentrations of methanol, it was essential to investigate the solvent intermolecular interactions over the same range of molar fractions. For mixtures that obey Henry's Law, at very dilute concentrations of the "solute," which in this case would be methanol, the solvent molecules are in an environment that is only slightly altered from what is normal, and thus the behavior of the solvent should not be drastically different from that of the pure liquid. However, as you increase the concentration of methanol, the environment of both the water and the methanol start to change, causing

variations in solution behavior and eventual deviation from Henry's Law.[26] Furthermore, mixtures of water and methanol have actually been shown to be significantly more complex than just a simple binary mixture. Katz *et al.* illustrated that because of the strong interactions between methanol and water, due to hydrogen-bonding, there are actually three "phases" to the system: methanol associated with methanol, water associated with water, and methanol associated with water.[27-28] As a result of this complex relationship, a mixture of these two solvents will vary quite differently from pure methanol or water in its solvation capabilities.[29]

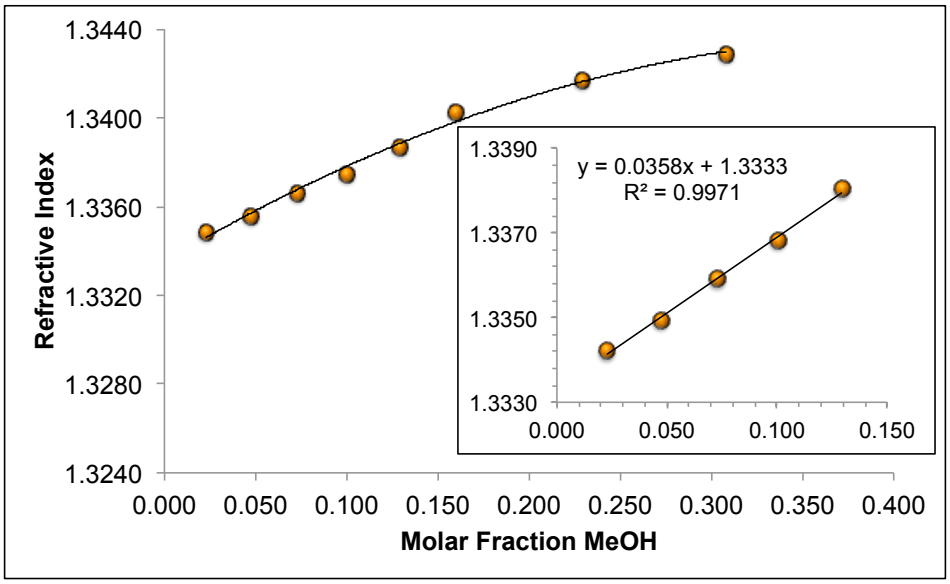

Figure 2.11 Corrected refractive index (n_D^{20}) versus molar fraction of methanol

For these reasons, refractive index (RI) measurements were taken for a series of water-methanol mixtures over the range of methanol molar fractions tested in the SDS titrations, as shown in Figure 2.11. Similar to the CMC results for SDS, the RI measurements taken above a methanol molar fraction of 0.13 begin to deviate from linearity. This is consistent with previous literature for similar mixtures.[30-32] Furthermore, it has been shown that as you increase the

methanol content of a water-methanol mixture, you will eventually reach a maximum value for excess refractive index, at approximately $x_{MeOH} = 0.4$, which represents the mixture with the highest solvent-solvent interactions.[31] However, in the previously noted range of lower molar fractions, the linear trend is quite evident and provides further evidence that we were operating the Henry's Law regime for water-methanol mixtures. These results confirmed that within this lower concentration range, the intermolecular interactions between the methanol and water were invariant; which is crucial for the consistent solubilizing of the surfactant within these mixtures. At higher concentrations of methanol, however, there is more "free" methanol available that is not associated with water, significantly increasing the solubility of the surfactant.[28, 33] This would explain the sharp increase in CMC value for SDS above $x_{MeOH} > 0.1$. Consequently, all remaining CMC titrations were performed at these lower molar fractions of methanol, staying within the linear range of Figure 2.11.

2.3.3 ITC Results for Cetyltrimethylammonium Bromide (CTAB)

In addition to testing this new method on an anionic surfactant like SDS, we felt that it was also necessary to evaluate the performance with a common cationic surfactant. Therefore, cetyltrimethylammonium bromide (CTAB) was also tested. A similar experimental setup to that seen with SDS was used in the CTAB titrations. Furthermore, the range of lower methanol molar fractions that exhibited a linear relationship, both in the SDS CMC values and the refractive index plots (see Figure 2.10 and Figure 2.11), was also employed for the CTAB titrations. The overlaid enthalpograms and corresponding isotherms for the duplicate trials at each methanol molar fraction for the CTAB titrations can be seen in Figure 2.12 – Figure 2.17

and the complete set of CMC data can be found in Table 2.2. Similar to the results for SDS, the overlaid plots for CTAB also show good reproducibility for the sloped region, which is where the critical micelle concentration is determined. For some of the duplicates, the overall heats of reaction do not match up perfectly; however, as this does not affect the CMC calculations, we were not concerned with these slight discrepancies. As shown in Figure 2.18, at these low molar fractions of methanol a positive linear trend is also observed for the CMC values of CTAB. An extrapolated value for the CMC in pure water of 0.95 ± 0.01 mM CTAB was obtained using the linear fit. This value is in excellent agreement with previous CMC values seen in the literature for CTAB micellization in the range of 0.92 to 1.0 mM;[34-35] thus, providing encouraging evidence that this method would be applicable to both positively and negatively ionic charged surfactants.

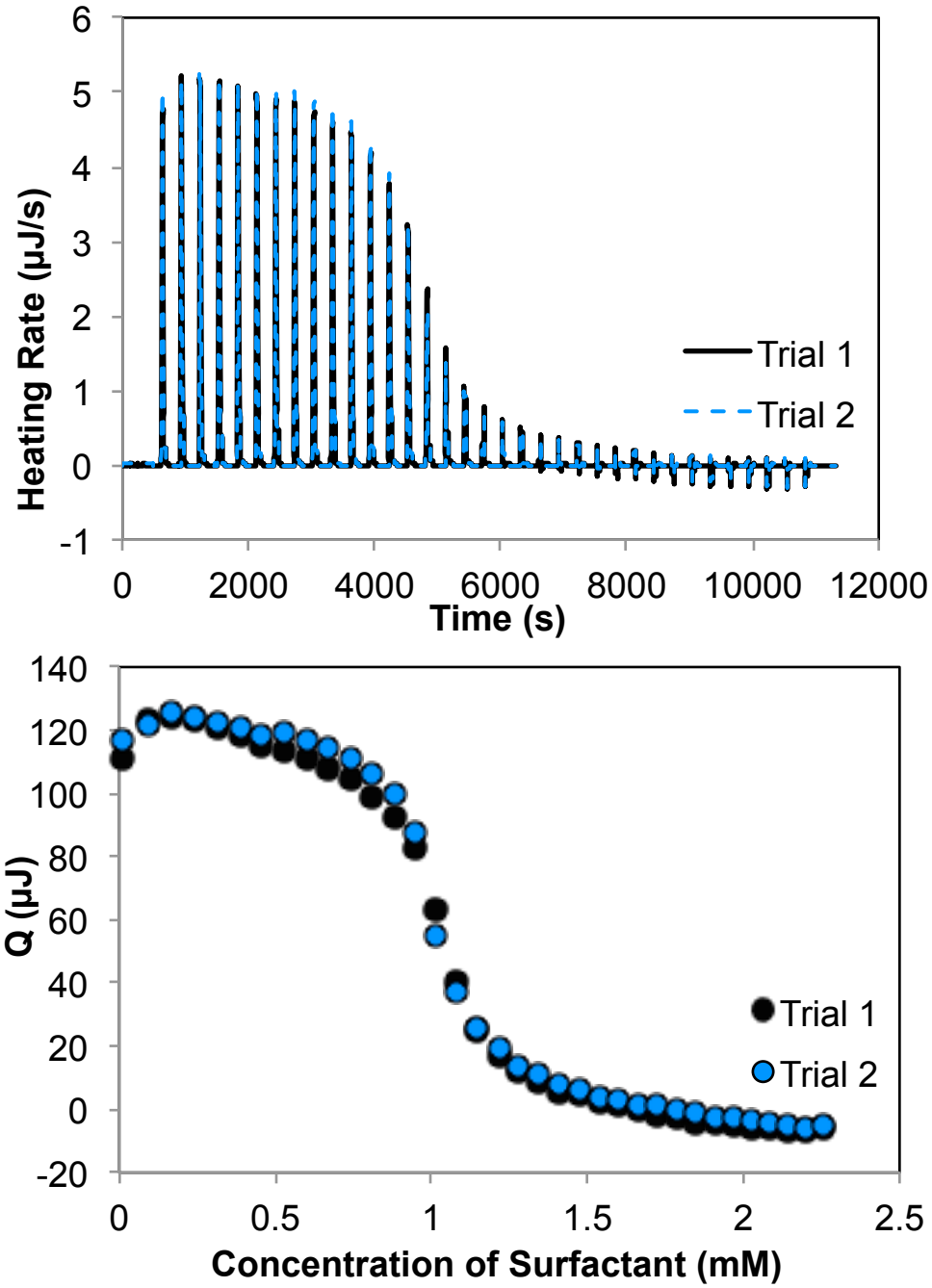

Figure 2.12 (top) ITC enthalpograms for duplicate titrations of CTAB being titrated into a water-methanol mixture (x_{MeOH} = 0.011) at 25 °C and (bottom) the resultant integrated heat per injection.

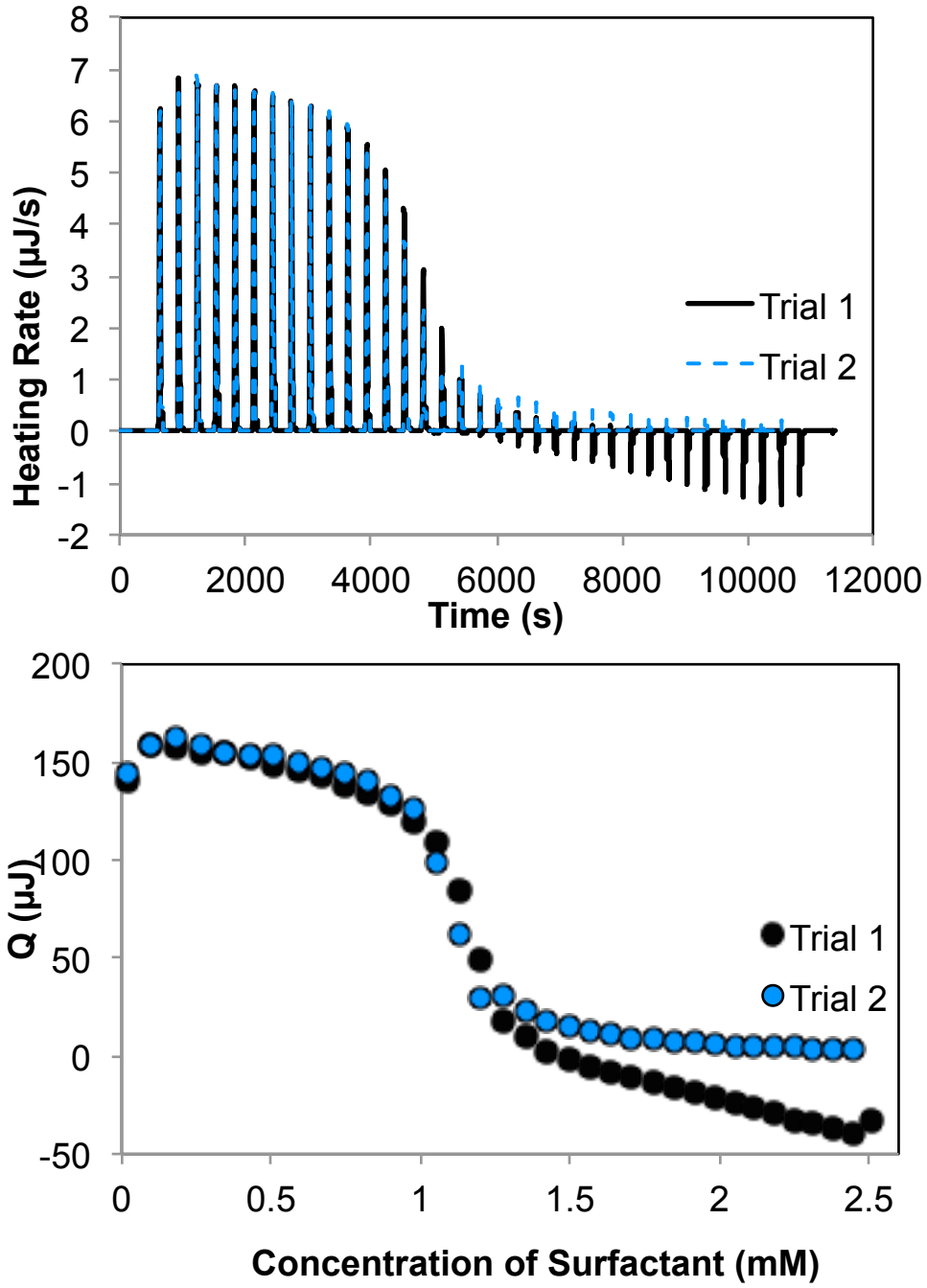

Figure 2.13 (top) ITC enthalpograms for duplicate titrations of CTAB being titrated into a water-methanol mixture (x_{MeOH} = 0.023) at 25 °C and (bottom) the resultant integrated heat per injection.

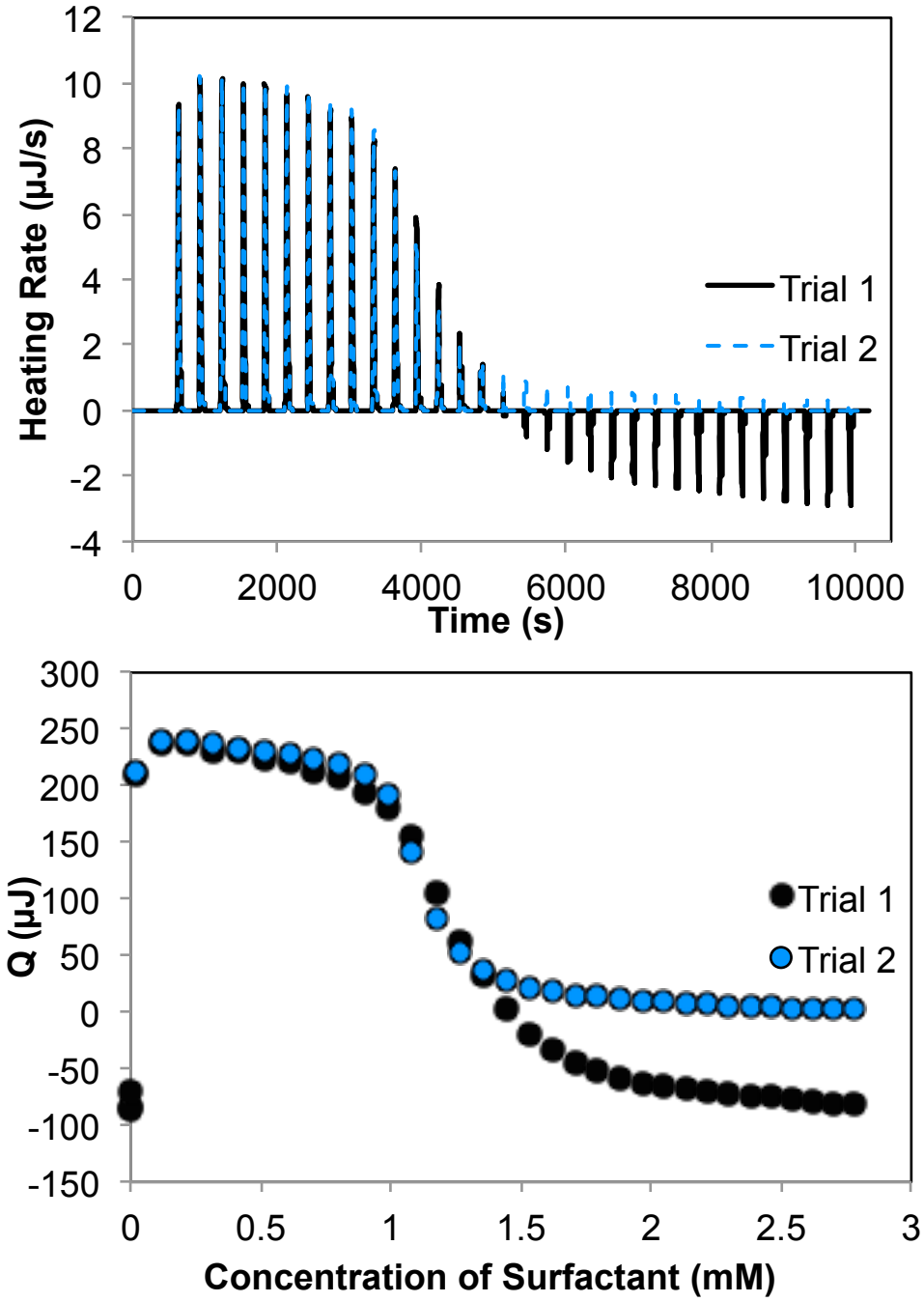

Figure 2.14 (top) ITC enthalpograms for duplicate titrations of CTAB being titrated into a water-methanol mixture (x_{MeOH} = 0.035) at 25 °C and (bottom) the resultant integrated heat per injection.

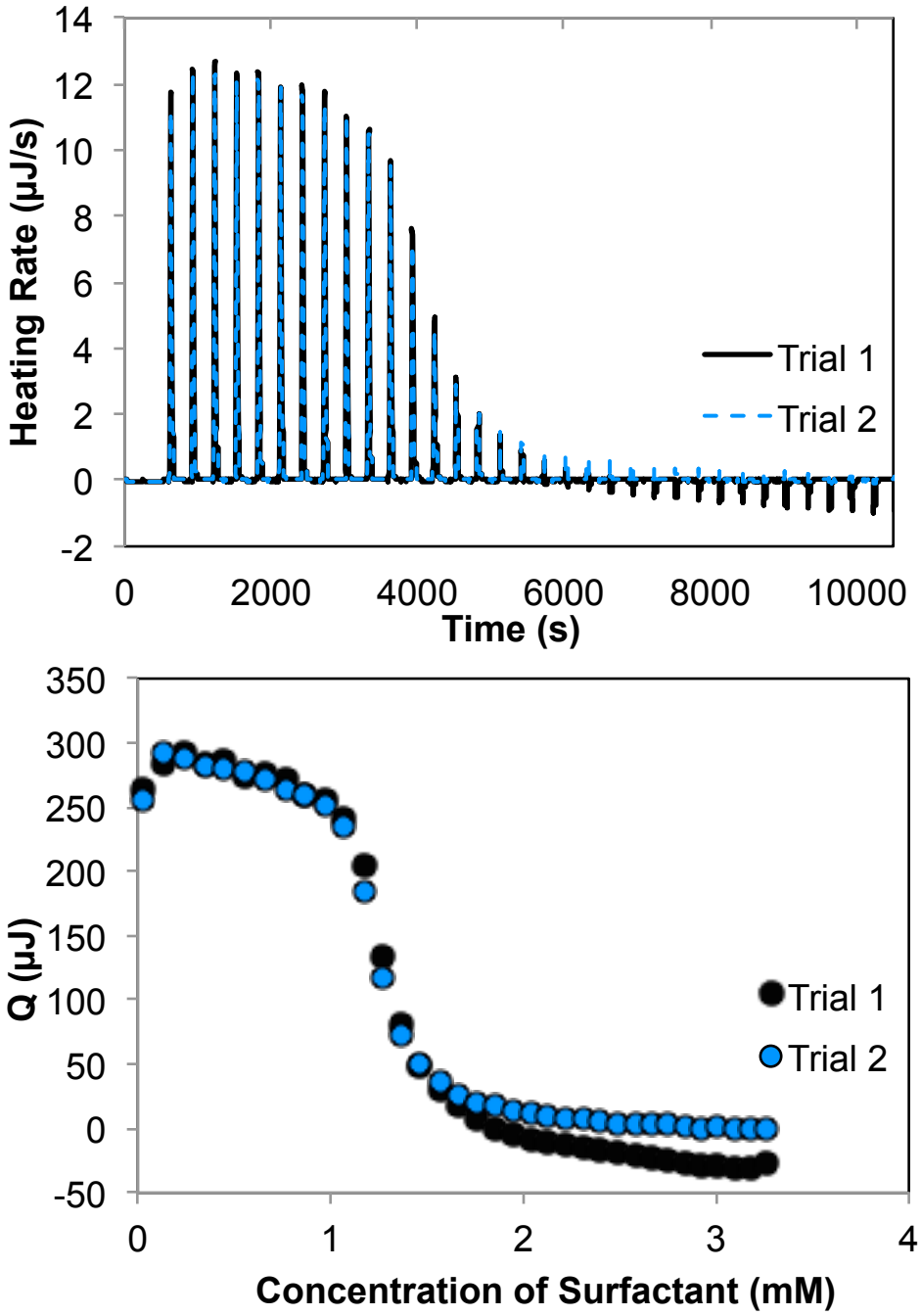

Figure 2.15 (top) ITC enthalpograms for duplicate titrations of CTAB being titrated into a water-methanol mixture (x_{MeOH} = 0.047) at 25 °C and (bottom) the resultant integrated heat per injection.

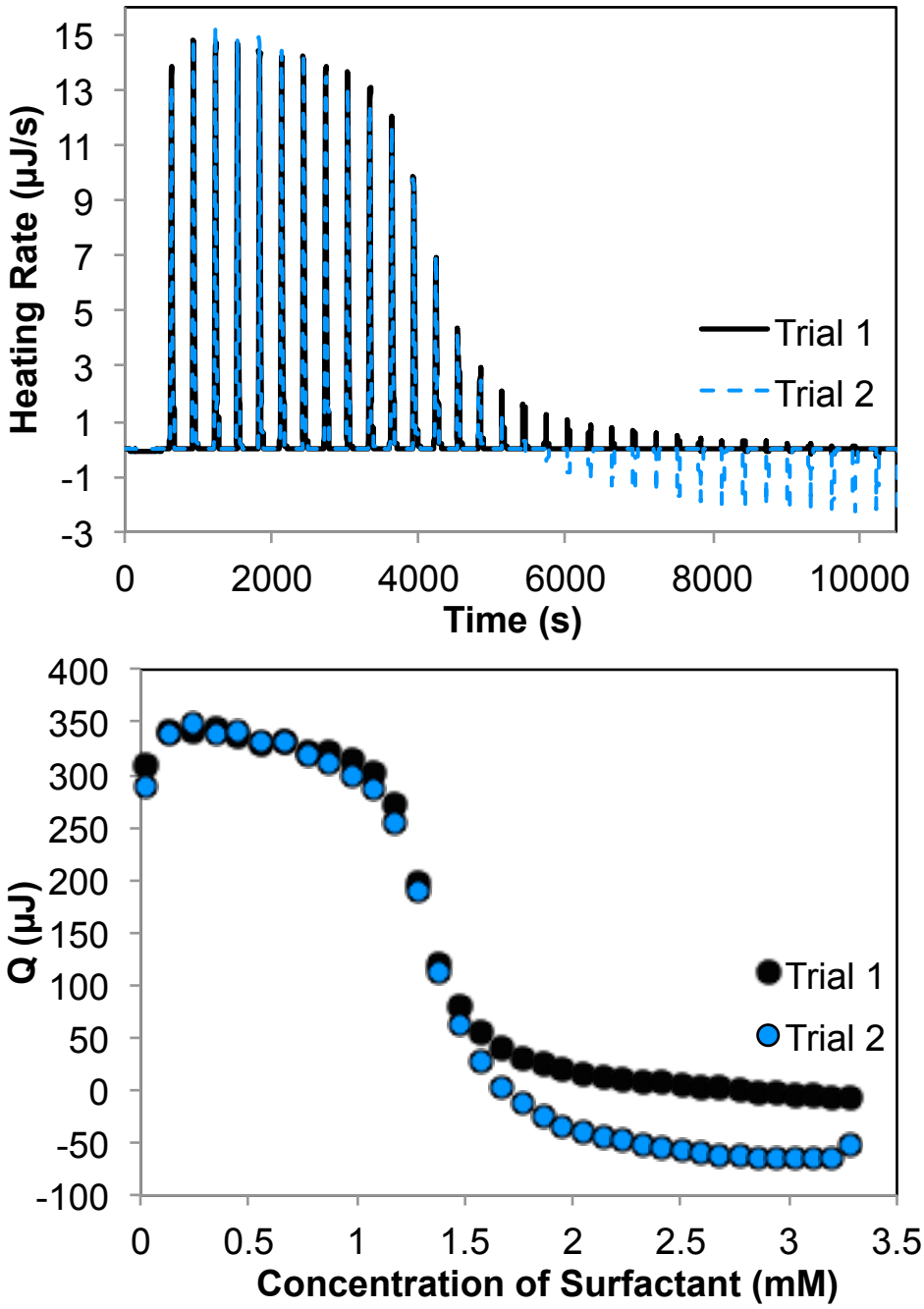

Figure 2.16 (top) ITC enthalpograms for duplicate titrations of CTAB being titrated into a water-methanol mixture (x_{MeOH} = 0.060) at 25 °C and (bottom) the resultant integrated heat per injection.

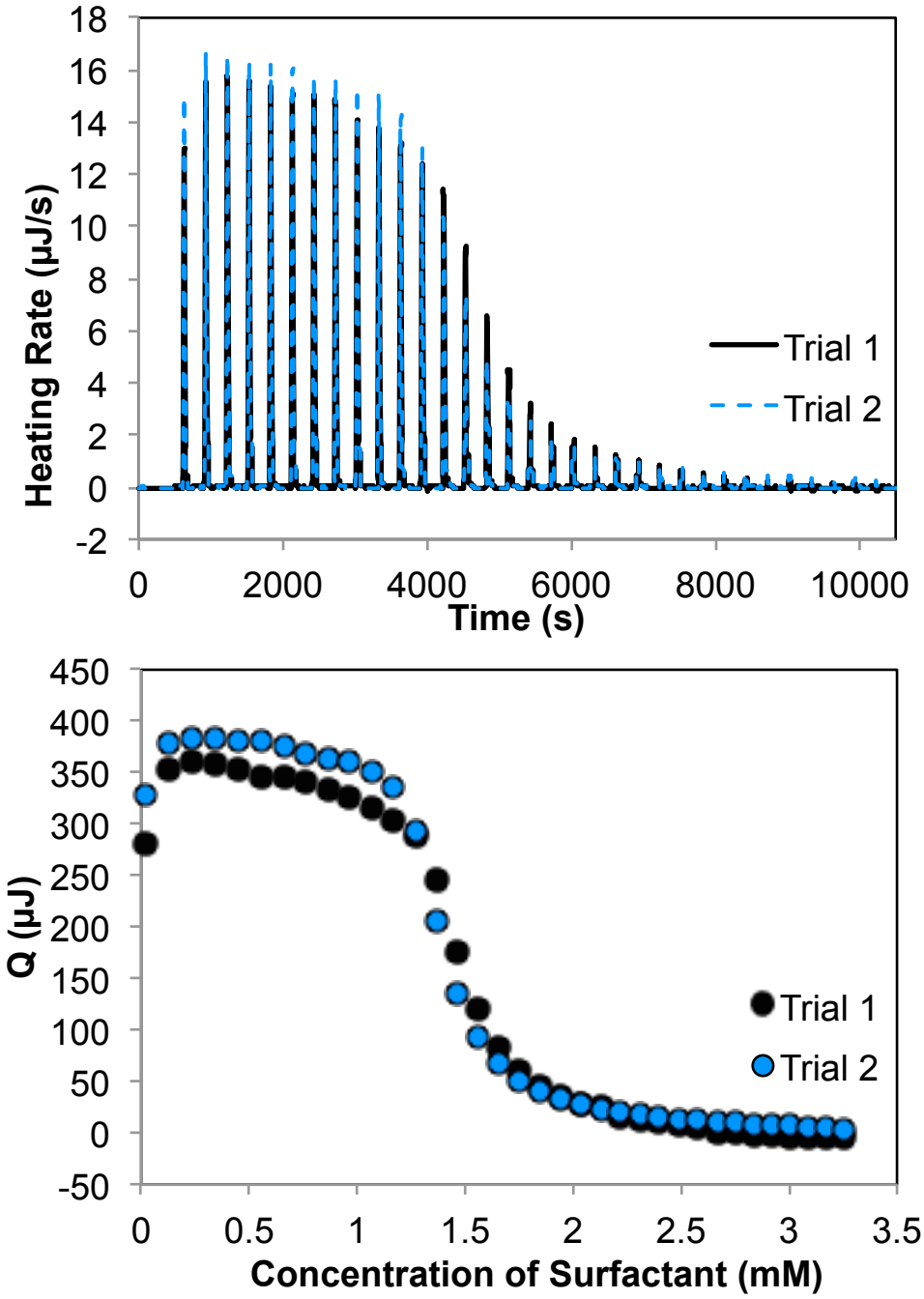

Figure 2.17 (top) ITC enthalpograms for duplicate titrations of CTAB being titrated into a water-methanol mixture (x_{MeOH} = 0.073) at 25 °C and (bottom) the resultant integrated heat per injection.

Table 2.2 CMC data for CTAB duplicate trials

x_{MeOH}	Trial 1 CMC (mM)	Trial 2 CMC (mM)	Average (mM)	Standard Deviation	Relative Standard Deviation (%)
0.011	1.01	1.00	1.01	0.01	0.7
0.023	1.15	1.07	1.11	0.06	5
0.035	1.09	1.23	1.16	0.10	9
0.047	1.26	1.21	1.24	0.04	3
0.060	1.28	1.32	1.30	0.03	2
0.073	1.45	1.36	1.41	0.06	5

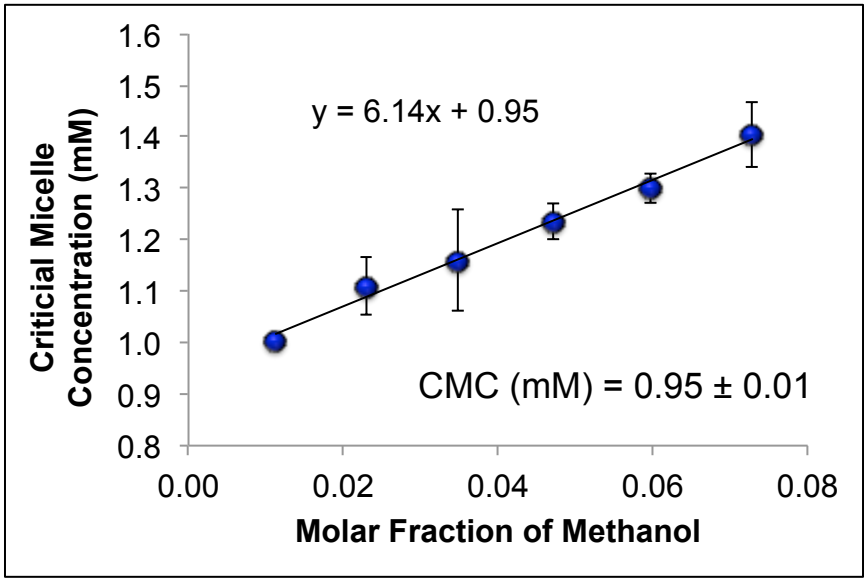

Figure 2.18 Observed CMC of CTAB versus molar fraction of methanol

2.3.4 ITC Results for Phosphonium Gemini Surfactant 12-2-12P

After evaluating the accuracy of the proposed ITC method with both an anionic and cationic standard surfactant, the procedure was repeated for the phosphonium gemini surfactant

12-2-12P. The overlaid enthalpograms and corresponding isotherms for the duplicate trials at each methanol molar fraction for the phosphonium gemini titrations can be seen in Figure 2.19 – Figure 2.22 and the complete set of CMC data can be found in Table 2.3. As observed in the CTAB plots, the gemini surfactant also showed irreproducible heats of reaction for several of the experiments. However, as stated earlier, these enthalpies of reaction bared no effect on the CMC values, which were very reproducible, and were therefore of little concern. Also of interest, in Figure 2.19, it is noted that one trial consists of 35 injections, just like all of the previous experiments with SDS and CTAB; however, this resulted in very small heats per injection, due to the very low concentration of surfactant. Therefore, the other trial, and subsequent titrations with the gemini afterward, were conducted as titrations of 25 injections. With fewer injections of larger volumes, the heats per injection were improved.

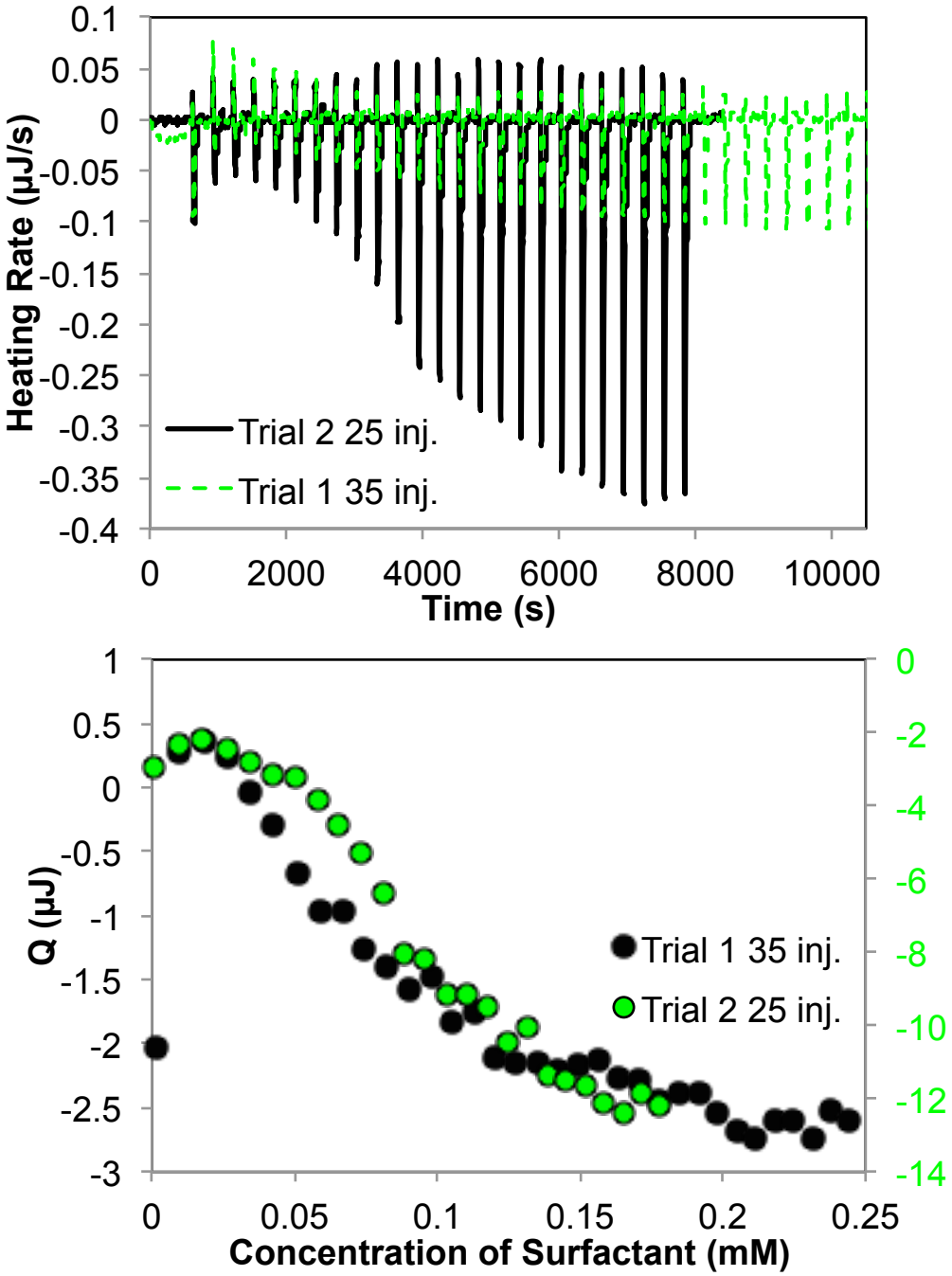

Figure 2.19 (top) ITC enthalpograms for duplicate titrations of 12-2-12P (gemini) being titrated into a water-methanol mixture (x_{MeOH} = 0.023) at 25 °C and (bottom) the resultant integrated heat per injection.

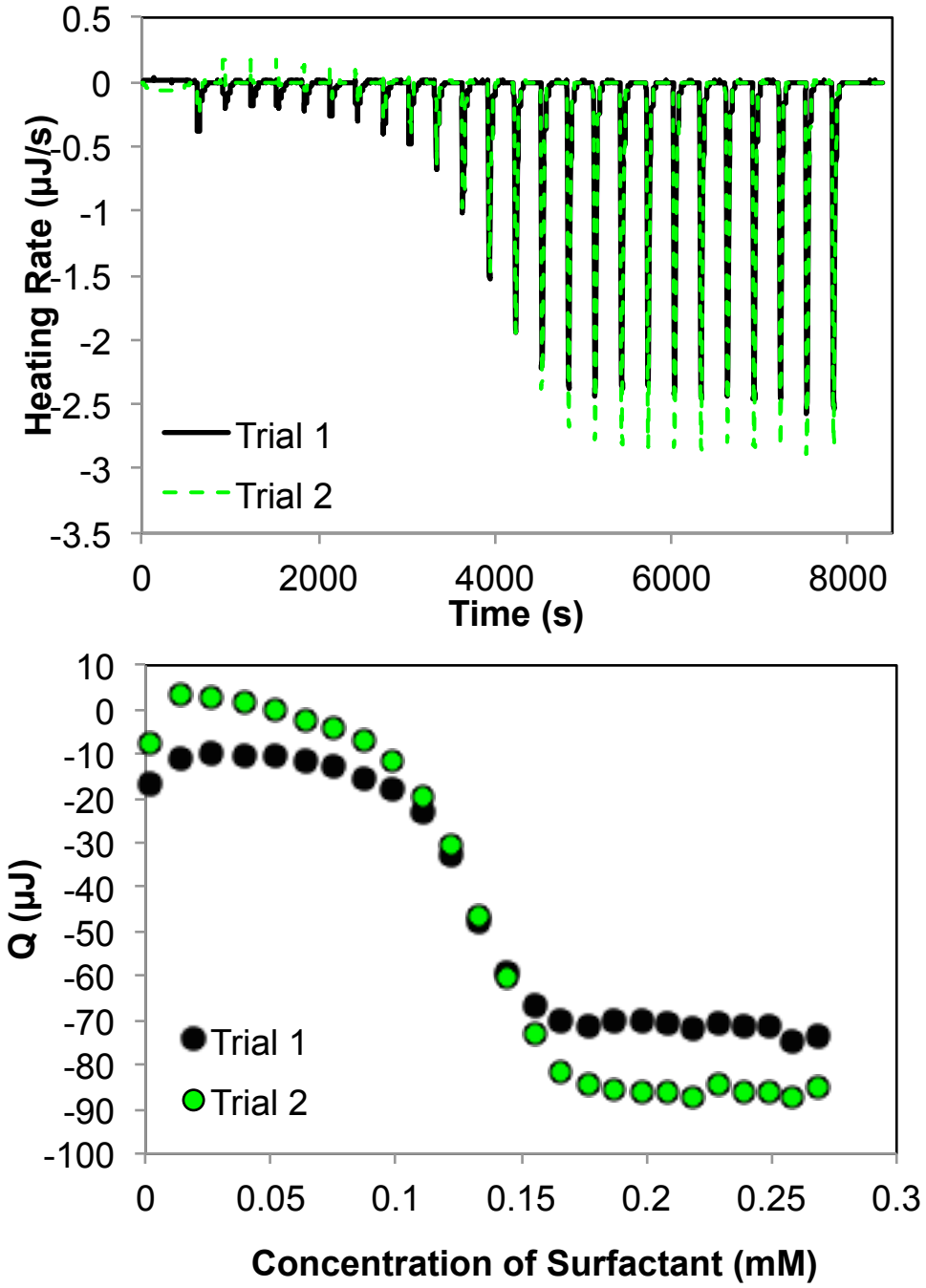

Figure 2.20 (top) ITC enthalpograms for duplicate titrations of 12-2-12P (gemini) being titrated into a water-methanol mixture (x_{MeOH} = 0.047) at 25 °C and (bottom) the resultant integrated heat per injection.

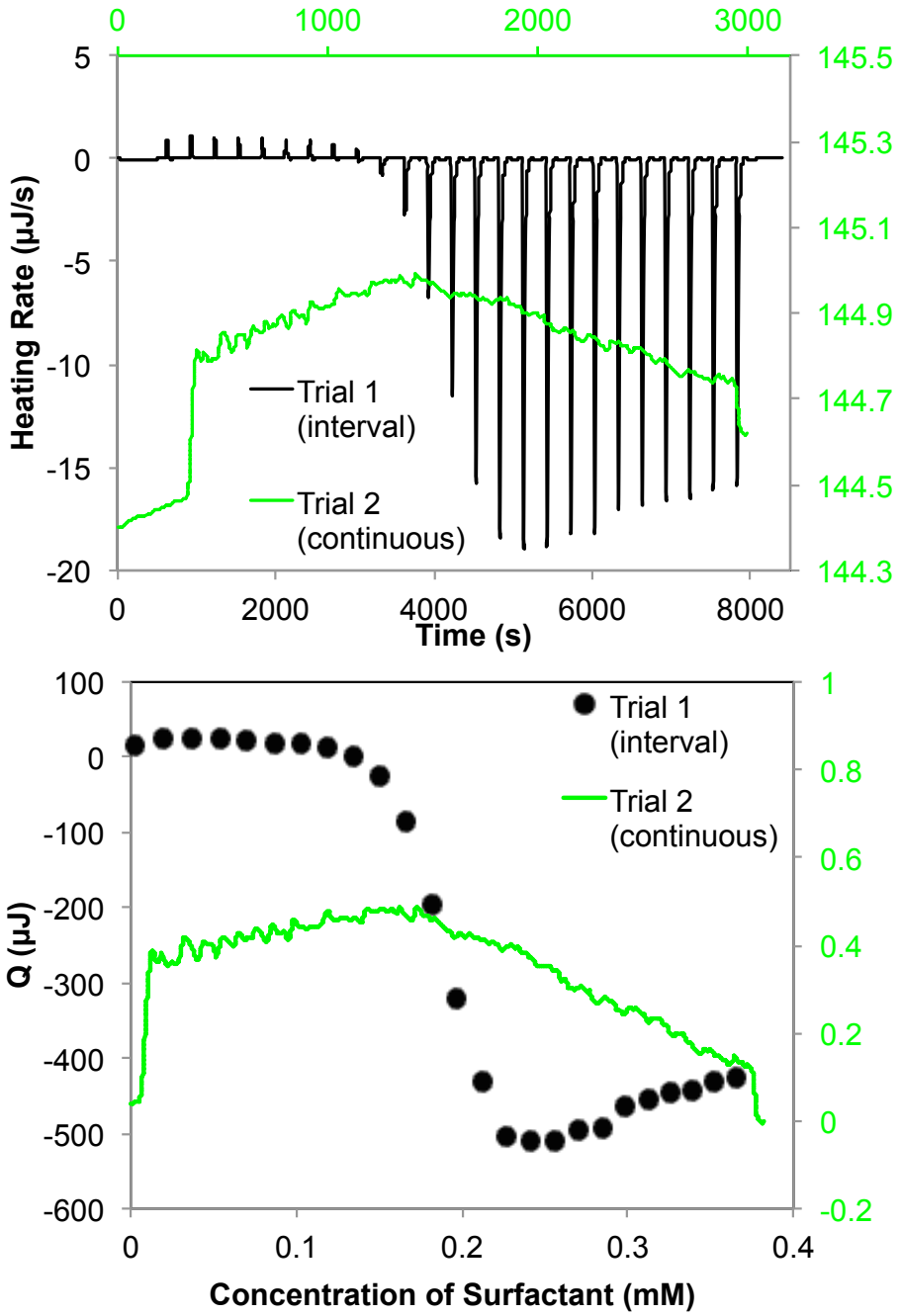

Figure 2.21 (top) ITC enthalpograms for duplicate titrations of 12-2-12P (gemini) being titrated into a water-methanol mixture (x_{MeOH} = 0.073) at 25 °C and (bottom) the resultant integrated heat per injection.

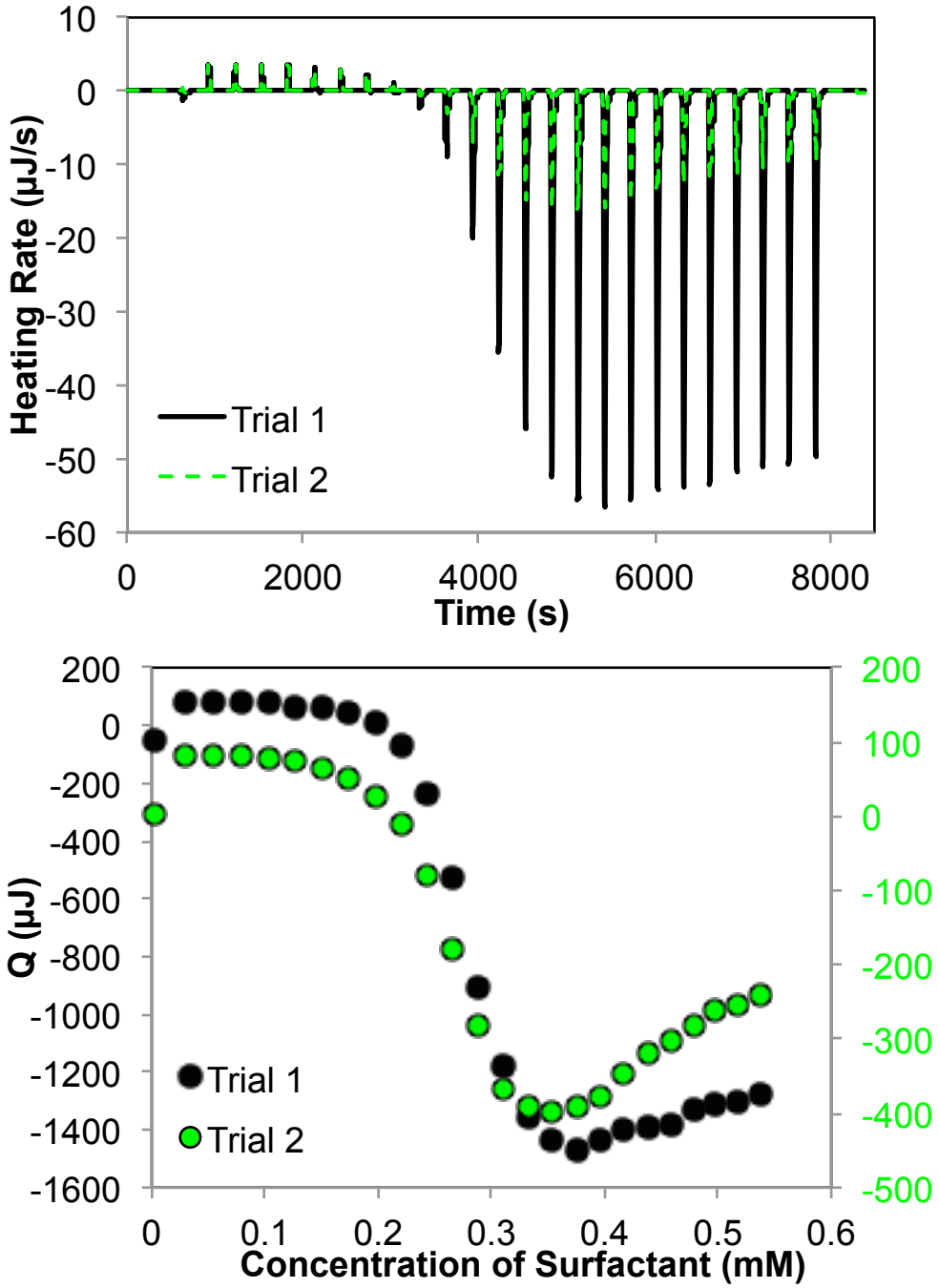

Figure 2.22 (top) ITC enthalpograms for duplicate titrations of 12-2-12P (gemini) being titrated into a water-methanol mixture (x_{MeOH} = 0.13) at 25 °C and (bottom) the resultant integrated heat per injection.

Table 2.3 CMC data for the 12-2-12P duplicate trials

x_{MeOH}	Trial 1 CMC (mM)	Trial 2 CMC (mM)	Average (mM)	Standard Deviation	Relative Standard Deviation (%)
0.023	0.091	0.070	0.081	0.015	18
0.047	0.12	0.12	0.12	0.00	0
0.073	0.18	0.17	0.18	0.01	4
0.13	0.25	0.30	0.28	0.04	13

It should also be noted that as a proof of concept, a continuous titration was conducted for the gemini surfactant at x_{MeOH} = 0.073. In these titrations, surfactant is constantly, and very slowly, added to the sample cell, rather than in interval injections. In this experiment, seen in Figure 2.21, the enthalpogram and isotherm shapes are the same, as there are no peaks which correspond to individual injections, just one steady flow of heat. Consequently, the maximum of this isotherm, or the point at which the slope dramatically changes, corresponds to the CMC value, which coincides nicely with the CMC observed in the normal interval titration (Figure 2.21 Trial 1).

Consistent with the surfactant standards, a linear trend is observed between the CMC value of 12-2-12P and the increasing concentration of methanol from x_{MeOH} = 0.023-0.13. This is illustrated in Figure 2.23. After extrapolation with the linear fit, a CMC of 0.037 ± 0.004 mM was obtained for 12-2-12P in pure water. This noticeably low CMC value was not unexpected, due to the highly hydrophobic nature of the surfactant. In addition, it has been noted in the literature that the critical micelle concentrations for ionic gemini surfactants are characteristically

1 to 2 orders of magnitude lower than that of the analogous surfactant containing only one ionic head-group.[10-11, 36-38] A CMC value of 0.037 mM for this gemini surfactant is therefore not unreasonable, given that the literature CMC value for the monofunctional counterpart to 12-2-12P (dodecyltriphenylphosphonium bromide) is 1.81 mM.[39]

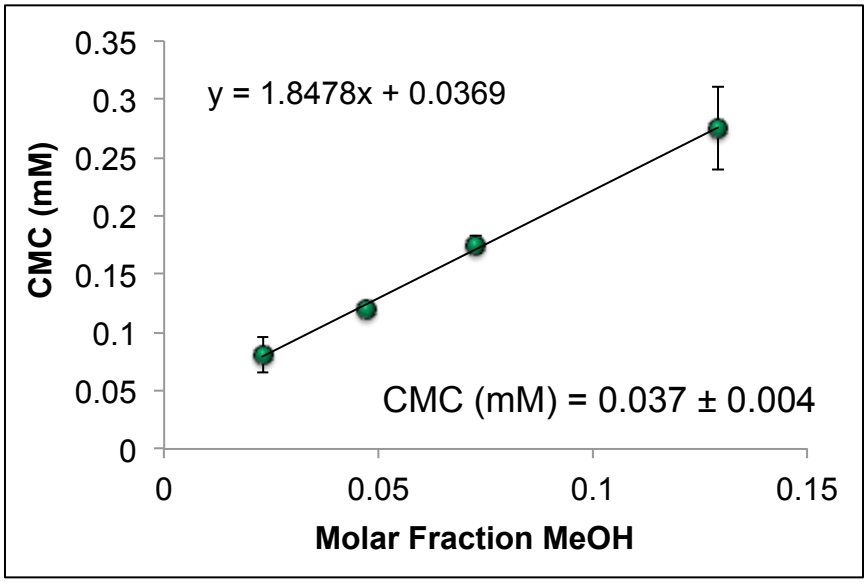

Figure 2.23 Observed CMC of 12-2-12P versus molar fraction of methanol

2.3.5 DLS Results for Phosphonium Gemini Surfactant 12-2-12P

In an effort to confirm the predicted CMC in pure water for the gemini surfactant, DLS measurements were performed to investigate aggregate size above and below the CMC value. In previous literature, Hemp *et al.*[14] reported that 12-2-12P exhibited a hydrodynamic radius of 117 ± 2 nm at a concentration of 0.11 mM. This large aggregate size is not unexpected, given the relatively high concentration of 12-2-12P, considering its low water-solubility, and its extremely hydrophobic nature. Initially, a reverse CMC titration was conducted in the DLS cuvette as an attempt to observe a reduction in aggregate size after passing back through the CMC with

adequate dilution. While this experiment exhibited a nice monomodal distribution by intensity, as shown in Figure 2.24, there was negligible variation in aggregate size, regardless of concentration. Given that this surfactant was designed for electrospinning, due to its propensity to form entanglements, one possible explanation for the unchanging hydrodynamic diameter is that once entangled, these aggregates are difficult to pull back apart without adequate agitation and time.

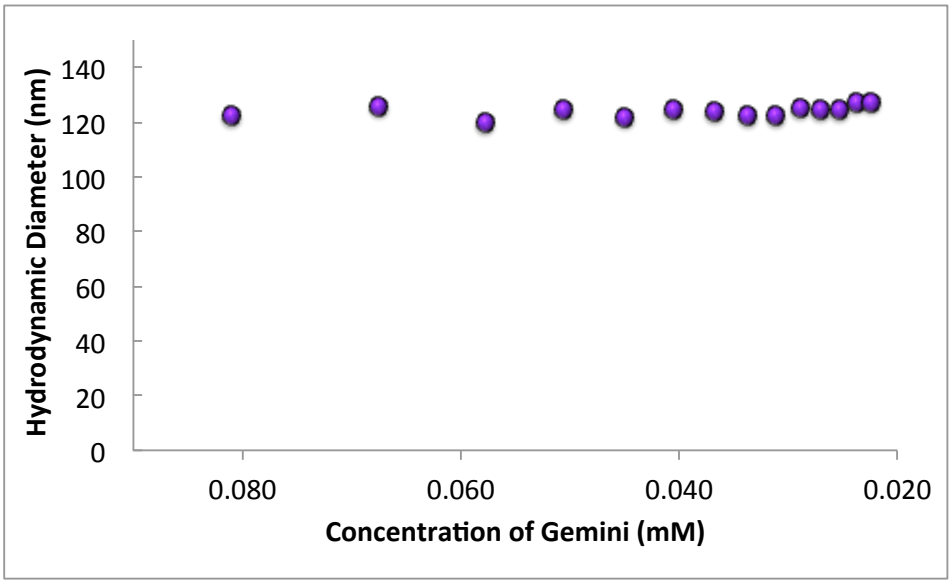

Figure 2.24 DLS results for the reverse titration of 0.081 mM 12-2-12P with water to a final concentration of 0.023 mM 12-2-12P

Because a standard critical micelle concentration ITC titration would be impossible to replicate in a DLS cuvette, due to volume and stirring restrictions, a second experiment was performed using only two concentrations. These two concentrations were prepared prior to the DLS measurements, with elevated temperature and stirring for several hours to ensure that everything was homogeneously mixed. After cooling back to room temperature, DLS

measurements were taken of each concentration. Neither sample exhibited monomodal distributions; in fact, both samples showed an unusual, but small peak at very high diameter sizes (approximately 5000 nm) with tailing. However, the peaks with greater than 10% relative intensity are shown in Table 2.4. The sample containing 0.080 mM 12-2-12P, which is well above the predicted CMC value, showed one notable peak at 289 nm, while the 0.027 mM sample shows two prominent peaks, of almost equal intensity, at 101 nm and 592 nm. While there is a distinct difference in distribution and size between the two samples, suggesting that concentration does play a critical role, the results are inconclusive overall. This is most likely due to the very hydrophobic nature of this gemini surfactant, and consequently its incredibly low water solubility. It is probable that completely homogenous solutions in pure water are not easily obtained or studied from this surfactant, therefore producing DLS results that are not well-defined or explained.

Table 2.4 DLS measurements for 0.080 mM and 0.027 mM 12-2-12P in ultrapure water

Sample	Diameter Mean Intensity Peak 1	Percent Relative Intensity for Peak 1 (%)	Diameter Mean Intensity Peak 2	Percent Relative Intensity for Peak 2 (%)
0.027 mM 12-2-12P	101 nm	42.18%	592 nm	49.96%
0.080 mM 12-2-12P	289 nm	97.60%	-	-

2.4 Additional ITC Experiments

2.4.1 Original Titrations in Water

Prior to any experiments in the water-methanol mixtures, ITC titrations were attempted with the gemini surfactant in neat water to measure the CMC. Due to its low water solubility, the maximum concentration of 12-2-12P that could be solubilized in water was 0.11 mM. This solution was titrated into pure water at 25 ºC, as shown in Figure 2.25 (a) and (b). The resulting heats per injection were extremely low and almost identical to the heats of dilution that are observed when water is titrated into water. Additional titrations with the same solution were performed at 60 and 75 ºC to explore the possibility of temperature effects on the CMC. However, the results were almost identical in shape and magnitude to the titration at 25 ºC. The fact that dilution was the only observable phenomenon in any of these initial experiments suggested that the concentration of 0.11 mM 12-2-12P was not large enough to obtain the actual CMC from the ITC over the course of the titration.[14] (This was, in fact, the case as the final concentration of 12-2-12P reached in the sample cell was approximately 0.02 mM, and our later experiments with extrapolation predicted a CMC value of 0.037 mM.)

As a quick proof of concept, an approximate 50/50 v/v mixture of methanol and water (x_{MeOH} = 0.31) was used to prepare a much more concentrated (8.05 mM) solution of the gemini surfactant, which was then titrated into the same ~50/50 mixture of water and methanol. The results of this experiment are shown in Figure 2.25 (c) and (d). With the addition of methanol we were able to observe the expected sigmoidal curve that is typical of CMC titrations and calculate the CMC of the surfactant in this mixture to be 1.0 mM. These results were published

by Hemp *et al*. in 2014.[14] However, they also served as the catalyst for the idea of measuring the CMCs at various methanol molar fractions and extrapolating to a value for pure water.

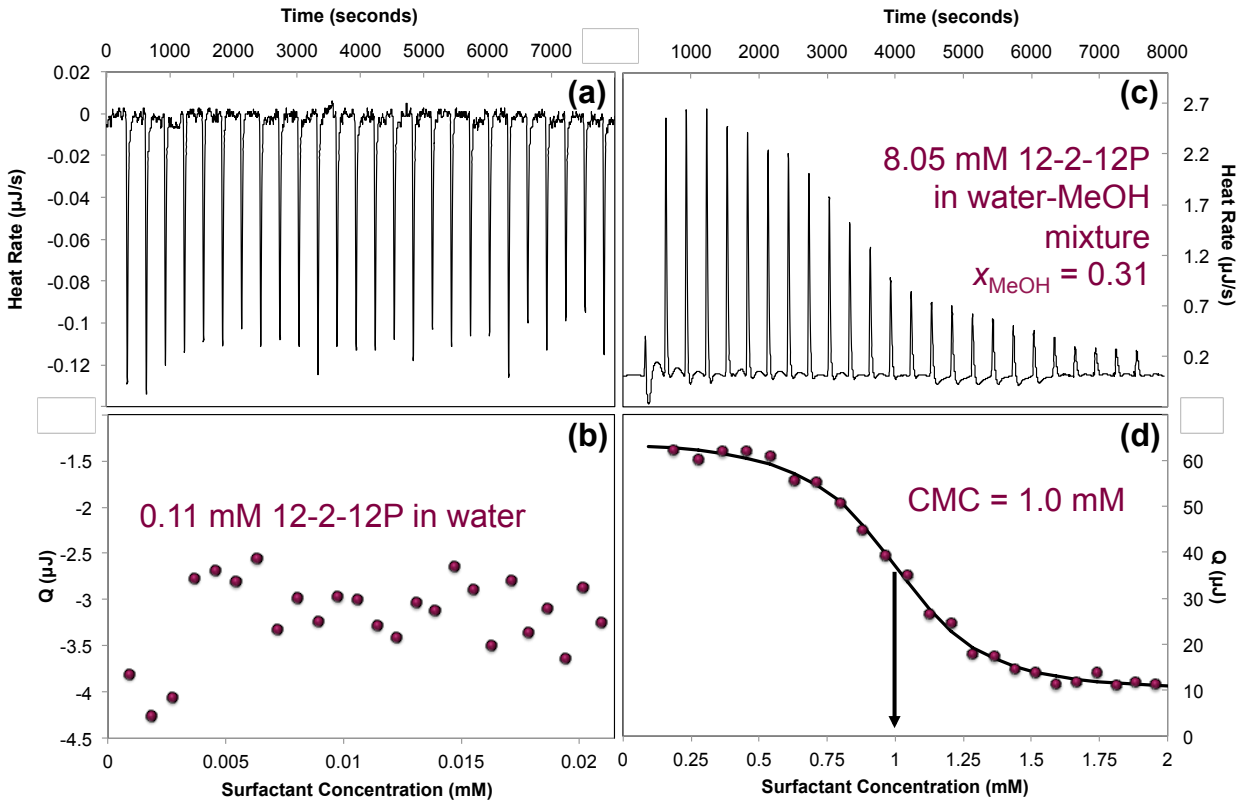

Figure 2.25 (a) The ITC enthalpogram of 0.11 mM 12-2-12P (gemini) being titrated into pure water at 25 °C, (b) the resultant integrated heat per injection for the pure water titration, (c) the enthalpogram of 8.05 mM 12-2-12P being titrated into a water-methanol mixture (x_{MeOH} = 0.31) at 25 ºC, and (d) the resultant integrated heat per injection for the mixture titration

2.4.2 ITC Results for Blank Titrations

As is typical with most ITC experiments, blank titrations of the solvent mixture into itself were performed in an effort to subtract any heat effects that were artifacts of the solvents mixing. In Figure 2.26, a water-methanol mixture at X_{MeOH} = 0.073 was titrated into the identical mixture, shown in purple, and overlaid with the equivalent titrations for SDS. The heats of this blank

titration are relatively small in comparison to that of the SDS. This is further emphasized in Figure 2.27, which shows the overlay of the raw data for the SDS titration compared to the same data that has been corrected by subtracting the blank. While the two curves are not identical, they are quite similar and overlay very nicely in the midpoint region, which corresponds to the critical micelle concentration. The CMC for the raw data was determined to be 9.47 mM SDS and the CMC value after subtracting the blank was 9.52 mM SDS. While these values are not identical, they are within error of each other compared to the other duplicate trials.

There was, however, a noticeable problem with the blank titration process. Similar blanks were run, like the one in Figure 2.26, but reproducible heats could not be achieved between duplicate titrations, even over the course of five replicates. For a system like SDS, where the heats per injection are relatively large due to high concentrations of surfactant, some amount of variation in the enthalpy of micellization is not of great concern. However, for the other systems, in which much lower concentrations of surfactants were used, like CTAB and the phosphonium gemini surfactant, these variations result in severe discrepancies between trials. Therefore, since the primary focus of this study was the critical micelle concentration value, which remains fairly constant before and after the blank is subtracted, correction for a blank titration was not deemed necessary for the rest of the ITC experiments.

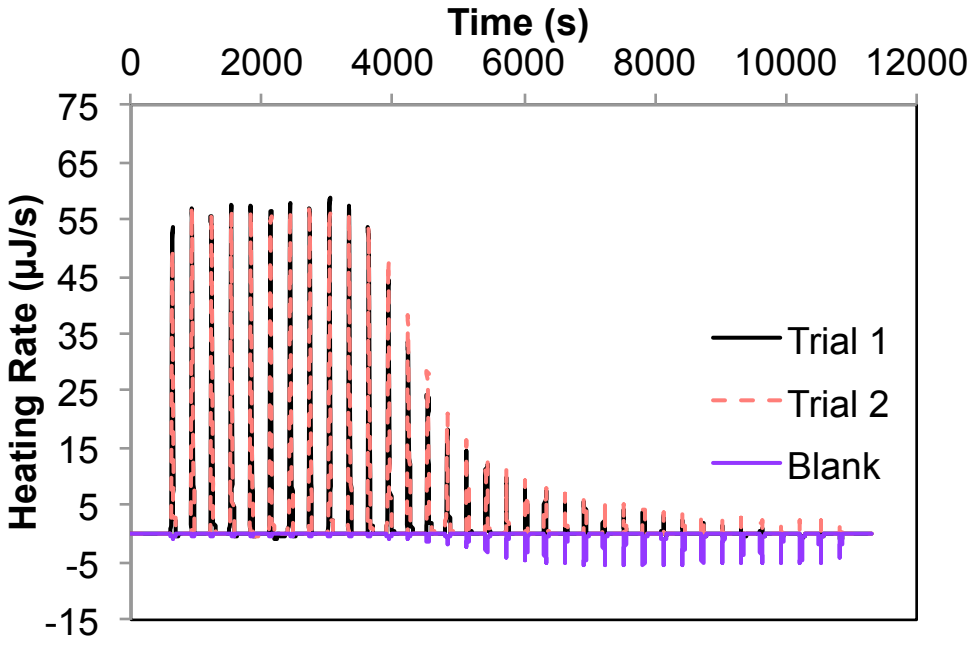

Figure 2.26 Comparison of the blank titration of a water-methanol mixture (X_{MeOH} = 0.073) to the ITC enthalpograms for duplicate titrations of 90 mM SDS being titrated into the same water-methanol mixture.

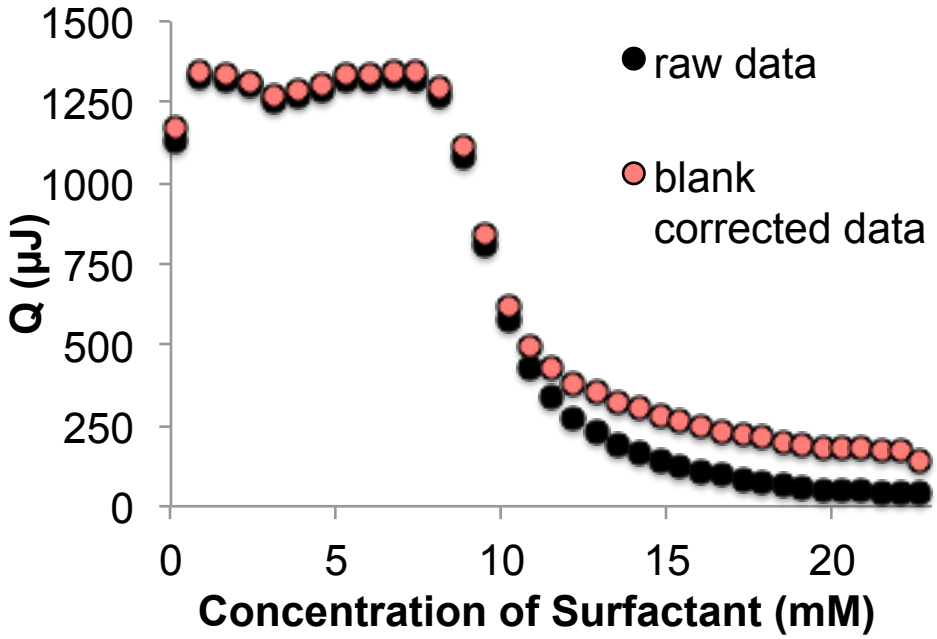

Figure 2.27 Comparison of the isotherms for the titration of 90 mM SDS in a water-methanol mixture (X_{MeOH} = 0.073) with and without blank correction.

While obtaining a complete thermodynamic profile of micellization was not required for the purposes of this investigation, it is one of the principal advantages to using isothermal titration calorimetry for CMC determination. The irreproducibility of these methanol-water blanks could be attributed to the complexity of water-methanol mixtures and their strong hydrogen-bonding interactions, as discussed earlier. However, further work is needed to explore this phenomenon in more detail. Ideally, we would like a system in which the blanks could be optimized and used for accurate data correction, so that not only CMC values could be reported, but also enthalpies and entropies of micellization. Moreover, it would be interesting to explore if these thermodynamic parameters also display the same linear and nonlinear relationships as the CMC values do with increasing molar fractions of methanol.

2.4.3 ITC Results for Dodecyltriphenylphosphonium Bromide and TWEEN® 80

Originally, dodecyltriphenylphosphonium bromide (C_{12}TPPBr), which is essentially one half of the gemini surfactant, was investigated as the standard cationic surfactant with literature CMC values. However, after several repeated titrations at various concentrations, it was evident that reproducible and accurate results would be extremely difficult and time consuming to obtain. There were fairly large inconsistencies between titrations and the overall extrapolation was significantly higher than the noted literature values for C_{12}TPPBr. One probable explanation is the limited purity of the commercially available surfactant. At the start, the highest purity C_{12}TPPBr sample that we were able to locate commercially was only 98%. In addition, over a relatively short amount of time, color change, and most likely degradation, was noted in the bottle, which was being stored in dry conditions. Due to all of these difficulties, the decision was

made to use CTAB, which is also well studied and available at much higher purities, for the cationic surfactant standard.

Additionally, after the extrapolation for the 12-2-12P predicted an low CMC in pure water at 0.037 mM, TWEEN® 80 was also used to test the method in these very low concentration ranges as a surfactant that had previously published CMC results. TWEEN® 80 is a commercially available nonionic surfactant, and Chou *et al.*[40] reported its CMC in water as 0.012 mM. Similar titrations were performed for TWEEN® 80 as had been done for the gemini surfactant, in the same linear range of methanol concentrations, however, severe irreproducibility issues were observed. Critical micelle concentration values were very inconsistent between duplicate titrations, and there was not a clear trend, linear or nonlinear, for the CMC values as a function of X_{MeOH}. These complications are attributed to sample preparation. TWEEN® 80 is a very viscous liquid, and accurate measurements, of either volume or mass, in these very low concentration ranges, were exceedingly difficult to obtain with any real certainty. As ITC calculations are dependent upon knowing the solution concentrations with absolute certainty, this presented a problem that is not easily corrected. It is also possible that because TWEEN® 80 is a nonionic surfactant, its solution behavior may be very different than that of the ionic surfactants tested in these experiments. As a result of these observations, the experiments with TWEEN® 80 were abandoned for the time being. However, in future work, it would be advantageous to find another commercially available ionic surfactant with a published low CMC to further validate this method.

2.4.4 Comparison of ITC Results in Deionized Water and Ultrapure Water

Initially, all of the ITC experiments were completed with mixtures made from methanol and deionized (DI) water obtained from the laboratory's house filtration system. While the results from this DI water were consistent and reproducible, with calculated CMC values in the expected ranges, these experiments are still measuring interactions on the interfacial level, where purity plays a very large role. Therefore, several experiments were repeated, in duplicate, with ultrapure water. These results can be seen in Figure 2.28 and Figure 2.29. These replicate experiments in ultrapure water overlay very nicely with the original data, and are all within experimental error. This confirms that the purity of the water in the original solutions was adequate for accurate CMC determinations.

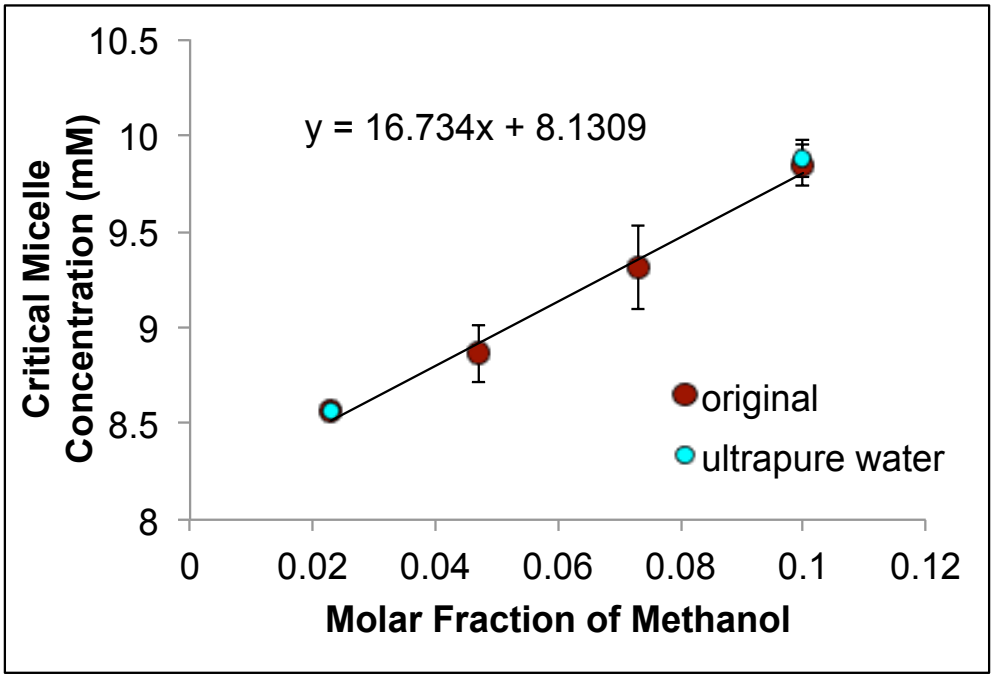

Figure 2.28 Overlay of the original data observed for the CMC of SDS using DI water and methanol with the replicate trials using ultrapure water and methanol.

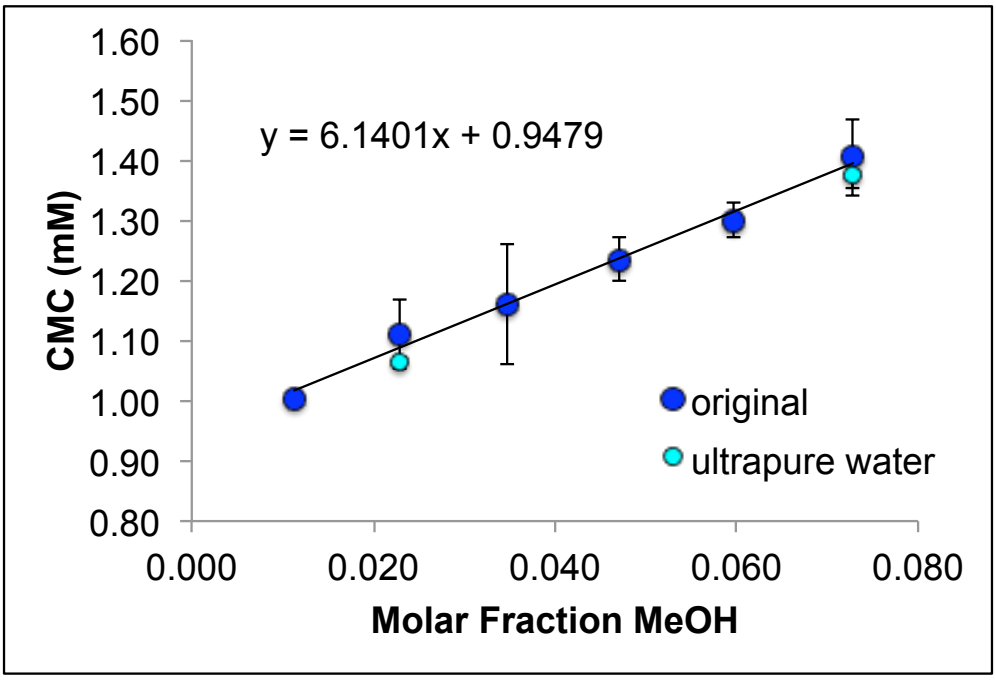

Figure 2.29 Overlay of the original data observed for the CMC of CTAB using DI water and methanol with the replicate trials using ultrapure water and methanol.

2.5 Conclusions

In this study, a method was developed to predict low CMC values for surfactants with limited water-solubility using isothermal titration calorimetry. The method was first tested on two well-characterized ionic surfactants, which served as standards: SDS and CTAB. A positive, linear correlation was found by measuring the CMC of the surfactants in aqueous solutions with increasing methanol molar fractions within an optimized range. These linear trends were then utilized to mathematically extrapolate back to a predicted CMC value for the surfactant in pure water. The results for both SDS (CMC = 8.13 ± 0.007 mM) and CTAB (CMC = 0.95 ± 0.01 mM) were in excellent agreement with previous literature.[23-25, 34-35] This procedure was then repeated to determine a previously unattainable critical micelle concentration[14] for the novel

gemini surfactant, 12-2-12P, in pure water. This resulted in a predicted CMC for 12-2-12P of 0.037 ± 0.004 mM that was approximately 50 times lower than that of its monomeric surfactant counterpart, which was also in good agreement with the literature findings for other gemini surfactants.[10-11, 36-38]

2.5 References

1. Dominguez, A.; Fernandez, A.; Gonzalez, N.; Iglesias, E.; Montenegro, L. *Journal of Chemical Education* **1997,** *74* (10), 1227.
2. Tong, W.; Zheng, Q.; Shao, S.; Lei, Q.; Fang, W. *J. Chem. Eng. Data* **2010,** *55*, 3766-3771.
3. Zana, R.; Xia, J. Applications of Gemini Surfactants. In *Gemini surfactants: synthesis, interfacial and solution-phase behavior, and applications*, Marcel Dekker Inc.: New York, 2004; pp 296-313.
4. Moroi, Y. 4.3 Critical Micelle Concentration. In *Micelles: Theoretical and Applied Aspects*, Springer Science+Business Media: New York, 1992; p 47.
5. Pérez-Rodríguez, M.; Prieto, G.; Rega, C.; Varela, L. M.; Sarmiento, F.; Mosquera, V. *Langmuir* **1998,** *14* (16), 4422-4426.
6. Bouchemal, K.; Agnely, F.; Koffi, A.; Djabourov, M.; Ponchel, G. *Journal of Molecular Recognition* **2010,** *23* (4), 335-342.
7. Goddard, E. D.; Harva, O.; Jones, T. G. *Transactions of the Faraday Society* **1953,** *49* (0), 980-984.
8. Kalyanasundaram, K.; Thomas, J. K. *Journal of the American Chemical Society* **1977,** *99* (7), 2039-2044.
9. Paula, S.; Sus, W.; Tuchtenhagen, J.; Blume, A. *Journal of Physical Chemistry* **1995,** *99* (30), 11742-11751.
10. Rosen, M.; Tracy, D. *J Surfact Deterg* **1998,** *1* (4), 547-554.

11. Menger, F. M.; Keiper, J. S. *Angewandte Chemie International Edition* **2000,** *39* (11), 1906-1920.

12. Wettig, S. D.; Verrall, R. E.; Foldvari, M. *Current gene therapy* **2008,** *8* (1), 9-23.

13. Cashion, M. P.; Li, X.; Geng, Y.; Hunley, M. T.; Long, T. E. *Langmuir* **2010,** *26* (2), 678-683.

14. Hemp, S. T.; Hudson, A. G.; Allen, M. H.; Pole, S. S.; Moore, R. B.; Long, T. E. *Soft Matter* **2014,** *10* (22), 3970-3977.

15. Li, Z.; Wang, C. Effects of Working Parameters on Electrospinning. In *One-Dimensional nanostructures*, Springer Berlin Heidelberg: 2013; pp 15-28.

16. Pavia, D. L. *Introduction to Organic Laboratory Techniques: A Small Scale Approach*. Thomson Brooks/Cole: 2005.

17. Hamberger, A.; Landfester, K. *Colloid Polymer Science* **2011,** *289*, 3-14.

18. Gharibi, H.; Razavizadeh, B. M.; Rafati, A. A. *Colloids and Surfaces A: Physicochemical and Engineering Aspects* **1998,** *136* (1–2), 123-132.

19. Huang, J. B.; Mao, M.; Zhu, B. Y. *Colloids and Surfaces A: Physicochemical and Engineering Aspects* **1999,** *155* (2–3), 339-348.

20. Butler, J. A. V.; Thomson, D. W.; Maclennan, W. H. *J. Chem. Soc.* **1933**, 674-86.

21. Butler, J. A. V.; Ramchandani, C. N.; Thomson, D. W. *Journal of the Chemical Society (Resumed)* **1935,** (0), 280-285.

22. Eastman, R. *Science* **1960,** *131* (3393), 97-98.

23. Goddard, E. D.; Benson, G. C. *Canadian Journal of Chemistry* **1957,** *35* (9), 986-991.

24. Paredes, S.; Tribout, M.; Ferreira, J.; Leonis, J. *Colloid & Polymer Sci* **1976,** *254* (7), 637-642.

25. Helenius, A.; McCaslin, D. R.; Fries, E.; Tanford, C. [63] Properties of detergents. In *Methods in Enzymology*, Sidney Fleischer, L. P., Ed. Academic Press: 1979; Vol. Volume 56, pp 734-749.

26. Atkins, P.; Paula, J. d. Ideal-dilute solutions. In *Physical Chemistry Volume 1: Thermodynamics and Kinetics*, 8th ed.; W. H. Freeman and Company: New York, 2006; pp 145-146.

27. Katz, E. D.; Ogan, K.; Scott, R. P. W. *Journal of Chromatography A* **1986,** *352* (0), 67-90.

28. Katz, E. D.; Lochmuller, C. H.; Scott, R. P. W. *Analytical Chemistry* **1989,** *61* (4), 349-355.

29. Hemmateenejad, B. *Journal of Chemometrics* **2005,** *19* (11-12), 657-667.

30. Herraez, J. V.; Belda, R. *J. Solution Chem.* **2006,** *35* (9), 1315-1328.

31. El-Dossoki, F. I. *J. Chin. Chem. Soc. (Taipei, Taiwan)* **2007,** *54* (5), 1129-1137.

32. Wohlfarth, C. Refractive index of the mixture (1) water; (2) methanol. In *Refractive Indices of Pure Liquids and Binary Liquid Mixtures (Supplement to III/38)*, Lechner, M. D., Ed. Springer Berlin Heidelberg: 2008; Vol. 47, pp 564-566.

33. Cazes, J.; Scott, R. P. W. Mixed Phases. In *Chromatography Theory*, Marcel Dekker, Inc.: New York, 2002; pp 131-132.

34. Neugebauer, J. M. [18] Detergents: An overview. In *Methods in Enzymology*, Murray, P. D., Ed. Academic Press: 1990; Vol. Volume 182, pp 239-253.

35. Harris, E. L. V.; Angal, S. Protein Purification Applications: A Practical Approach. IRL Press at Oxford University Press: New York, NY, 1990; p 71.

36. Zana, R.; Benrraou, M.; Rueff, R. *Langmuir* **1991,** *7* (6), 1072-1075.

37. Menger, F. M.; Littau, C. A. *Journal of the American Chemical Society* **1993,** *115* (22), 10083-10090.

38. Tehrani-Bagha, A. R.; Holmberg, K. *Materials* **2013,** *6* (2), 580-608.

39. Owoyomi, O.; Ige, J.; Soriyan, O. *Chemical Sciences Journal* **2011,** *CSJ-25*, 1-13.

40. Chou, D. K.; Krishnamurthy, R.; Randolph, T. W.; Carpenter, J. F.; Manning, M. C. *Journal of Pharmaceutical Sciences* **2005,** *94* (6), 1368-1381.

Chapter 3 : Unlocking the Thermodynamics of Polycation-DNA Complexation with Isothermal Titration Calorimetry

3.1 Introduction

In recent years, nucleic acid therapeutics have gained considerable attention in the medical field as possible treatments for various genetic and acquired diseases. However the obstacles preventing successful delivery of these therapeutics into the body are many-fold.[1] Unfortunately, DNA by itself is difficult to deliver to the cell. A delivery vehicle is needed to protect the DNA from degradation by enzymes during transport, compact it so that it is small enough to be take up by the cell, neutralize the negative charge, and potentially target it to a specific diseased cell.[2] Traditionally, viral vectors have been used to this end; however, they typically have a fairly low loading capacity and can illicit immunogenic responses. In an effort to solve this problem without the use of viral vectors, researchers have moved toward the study of biocompatible and nontoxic cationic polymers as alternative nucleic acid delivery vehicles.[1, 3]

Typically, polymers developed for gene delivery vehicles are characterized through biological assays, such as cytotoxicity and transfection assays. However, knowing the transfection efficiency of the polymers is only one-half of the bigger picture. By understanding the structure-property relationships through thermodynamic and structural analysis, we can correlate these results with those from the biological assays and direct the findings toward making even better therapeutics in the future. It is for this reason that many researchers are turning toward more in depth analytical characterization methods to gain a deeper understanding of the physical interactions taking place between the polymer and nucleic acids.[4-6]

One analytical technique that is used throughout the polyplex, and greater pharmaceutical, literature is isothermal titration calorimetry (ITC).[7-10] ITC allows for the determination of thermodynamic binding parameters, such as enthalpy (ΔH), binding affinity (K), and stoichiometry (n_{bind}) all in a single experiment. This also allows for the calculation of the Gibb's free energy (ΔG) and entropy (ΔS) of binding.[11-13] This thermodynamic information allows us to better understand the types and strengths of different interactions (electrostatic, hydrogen bonding, van der Waals, etc.) taking place between the polymer and DNA, as shown in Figure 3.1.

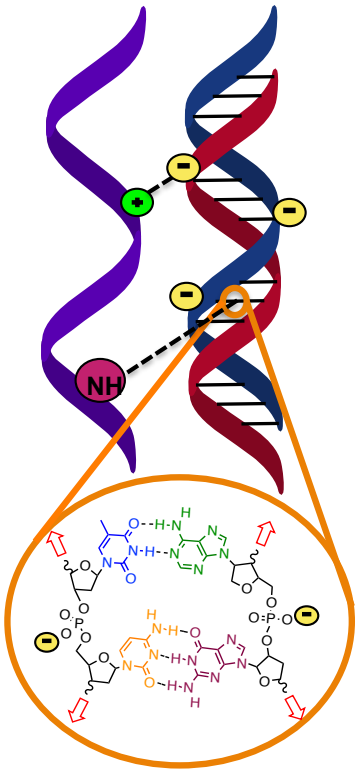

Figure 3.1 Schematic of possible intermolecular interactions in polymer-DNA complexation

In this work we will be applying characterization by ITC to three different polymer systems. In 2011, Allen *et al*. reported on the synthesis and transfection efficiency of a novel series of imidazolium copolymers with varying degrees of charge density.[14] Here, we will describe in full detail the ITC results for the fully charged polycation from this series. In addition, Hemp *et al*. published the synthesis of another polycation system containing poly(2-dimethylaminoethyl methacrylate) (pDMAEMA) and vinyl benzyl adenine for applications in electrospinning.[15] However, given the previous success seen in DNA complexation with pDMAEMA and its derivatives,[16-17] as well as the possible hydrogen bonding interactions available from adenine unit, this polycation was also investigated with ITC. Finally, Wang *et al*. reported on a new NMR technique for the quantitation of free polymer in polyplex systems.[18] The results presented in this study describe complementary experiments using ITC to confirm the binding stoichiometry for PEI and plasmid DNA (pDNA) that was determined with the new NMR technique.

3.2 Experimental

3.2.1 Materials for Preliminary Experiments and System Optimization

The two copolymers used in these experiments were prepared as previously reported.[14-15] The first is a fully quaternized imidazolium containing polymer (approximate number average molar mass (M_n) of 23,000 g/mol and a polydispersity index (PDI) of 1.89, as determined by size exclusion chromatography (SEC) in reference to poly(ethylene oxide) standards) with the chemical structure shown in Figure 3.2 (a). The second is a copolymer (M_n = 253,000 g/mol with a PDI of 1.61, as determined by SEC) of 2-(dimethylamino)ethyl methacrylate (DMAEMA)

and 22 mol % vinylbenzyladenine (VBA), with the structure shown in Figure 3.2 (b). Plasmid DNA, or pDNA, (pcmv-lacz, 7.5 kbp) was purchased from Aldevron at 1.0 mg/mL in water. Ultrapure water was obtained from a Millipore-DQ3 filtration system, at a resistivity of 18.2 MΩ·cm. Phosphate buffered saline (PBS) was purchased from Fisher Scientific.

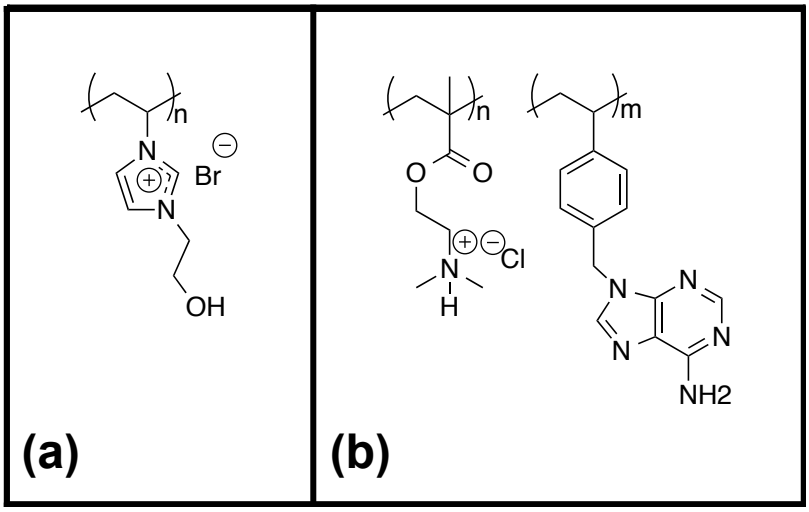

Figure 3.2 Chemical structures of (a) fully quaternized imidazolium containing polymer and (b) copolymer of DMAEMA and 22 mol % vinylbenzyladenine.

3.2.2 Materials for ITC Experiments to Confirm NMR Free Polymer Results

Linear PEI with a molecular weight of 25,000 g/mol was purchased from Alfa Aesar and used as received. Plasmid DNA (pcmv-lacz, 7.5 kbp) was purchased from Aldevron at 1.0 mg/mL in water. Ultrapure water was obtained from a Millipore-DQ3 filtration system, at a resistivity of 18.2 MΩ•cm. Tris was purchased from Fisher Scientific. Tris buffer was prepared at 10 mM using ultrapure water and titrated to pH 7.4 with 0.1 M HCl or NaOH.

It should be noted that all concentrations given for DNA and polymer solutions are based off the phosphate and charged nitrogen group concentrations, respectively. This allows the

results to be reported in terms of the charge ratio N/P, or moles of charged nitrogen group to moles of phosphate.

3.2.3 Initial ITC Experiments – System Optimization

Prior to all experiments, the pDNA solutions were prepared by thoroughly dialyzing against a solvent, either ultrapure water or PBS buffer. The resulting dialysates were used to prepare the corresponding polymer solutions. The instrument used for these titration experiments was a TA Instruments Low Volume NanoITC. The gold sample and reference cells in the ITC have a working volume of 170 μL, and the burette is a 50 μL gas-tight syringe with a stainless steel needle. For each titration, the sample cell was filled with the pDNA solution and the reference cell with ultrapure water. The burette syringe was filled with polymer solution. All titrations were performed at 25 °C with a stir rate of 350 rpm and 300 s intervals between each injection. Before starting each titration, the instrument was allowed to equilibrate until a stable baseline was obtained. Furthermore, a 300 s baseline was collected before and after the first and last injections. Depending on the heat generated, the injection volume and number of total injections was adjusted accordingly. All titrations for these experiments were either 20 or 25 injections total. TA Instruments NanoAnalyze™ software was used to fit the data with the standard independent binding sites model.

3.2.4 ITC Experiments to Confirm NMR Free Polymer Results

A TA Instruments low volume NanoITC was used to perform all of the titration experiments. The pDNA solution was dialyzed thoroughly against Tris buffer and the remaining

dialysate was used to prepare the PEI solutions. The 50 μL burette syringe was filled with 172 μg/mL PEI solution and the sample cell was filled with 132 μg/mL pDNA. The reference cell was filled with ultrapure water. Titrations were performed at 37 ºC in triplicate. (It should be noted that the Tris buffer was prepared at 25 ºC, so the pH of these solutions is likely lower during the titrations at 37 ºC. However, the NMR experiments were also performed at 37 ºC, so the change in pH, and consequently changes in polyplex formation due to pH, should be consistent.) A stirring rate of 350 rpm was used. Each titration was a total of 25 injections with an interval of 300 s per injection. Each injection was 1.96 μL, and the final approximate N/P was 5. TA Instrument NanoAnalyze™ software was used to fit the data with the standard independent binding sites model.

3.3 Results & Discussion

3.3.1 Preliminary Titrations and Aggregation Concerns

Preliminary experiments were conducted with relatively high concentrations of pDNA and polymer based on previous literature for polycation binding in a standard volume ITC instrument.[5-6] Initial experiments with the imidazolium-containing polymer did result in an observed binding, as shown in Figure 3.3; however, there was also significant polyplex aggregation at these concentrations. This aggregation was physically visible as a sticky, white coating on the end of the buret when it was removed from the ITC at the conclusion of the titration. Furthermore, the aggregation resulted in a biphasic enthalpogram, which is a common problem seen in the literature[6, 19] for polyplex binding. Therefore, the data corresponding to aggregation was omitted and only half of the binding data was used to obtain the binding

parameters seen in the bottom portion of Figure 3.3. While this is not an ideal way to fit the data, it did result in thermodynamic binding parameters that were not unreasonable compared to other DNA binding studies.[4-6, 19-20] The aggregation at these high concentrations of pDNA and polymer also made it extremely difficult to obtain reproducible data. Regardless of these initial obstacles, the data was still analyzed and we were able to make preliminary observations regarding the thermodynamics of binding.

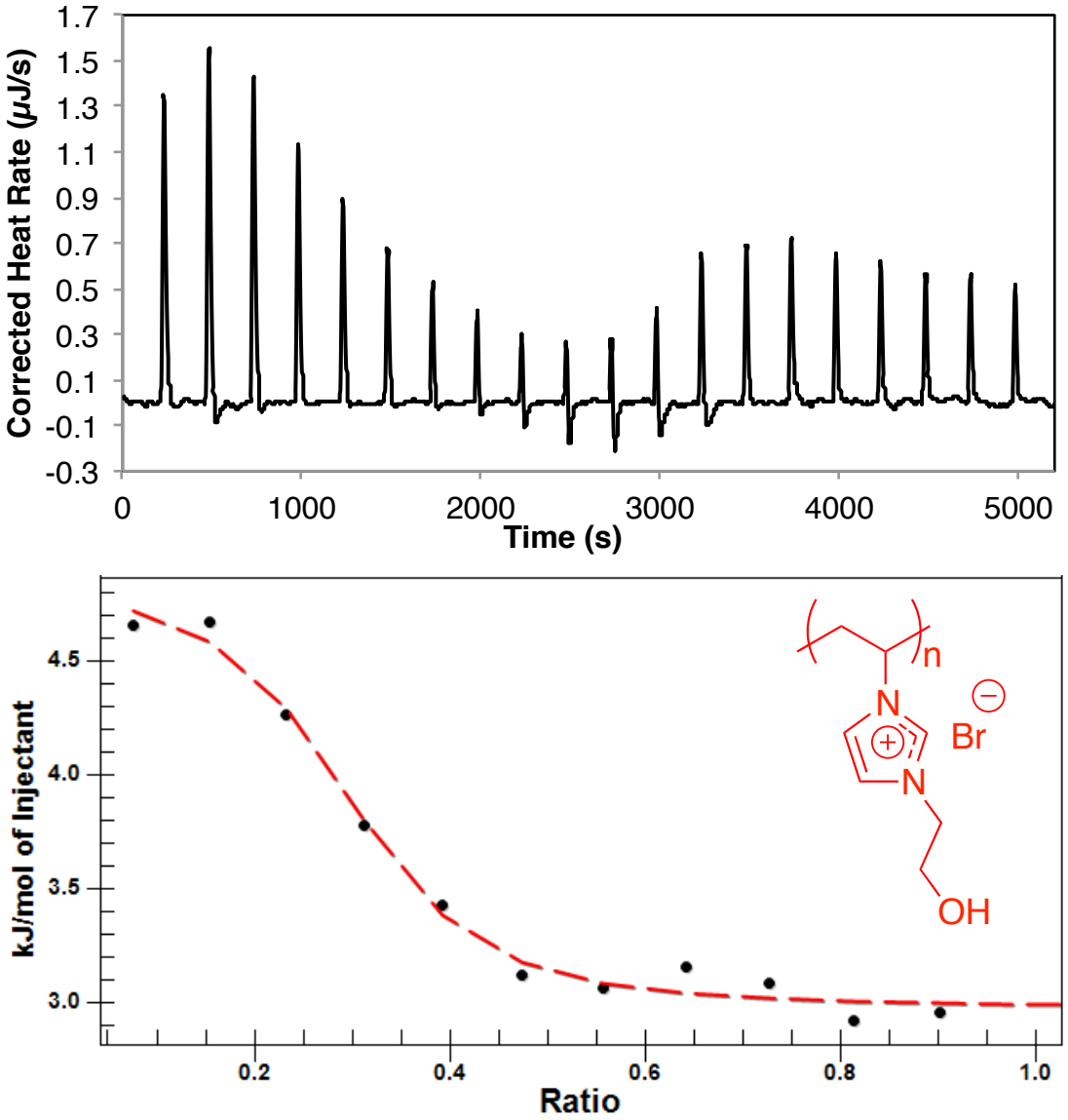

Figure 3.3 (top) ITC enthalpogram of 4.6 mM imidazolium-containing polymer being titrated into 0.86 mM pDNA at 25 ºC (solvent: water, 20 injections) and (bottom) the resultant integrated heat per injection and fitting isotherm

The complexation of DNA with the imidazolium-containing polymer is a spontaneous process at room temperature, and this was confirmed by the negative Gibb's free energy value, shown in Table 3.1. The binding affinity, K, is slightly lower than expected for a polycationic

system; however, the n_{bind} value is quite comparable to other polycation binding studies.[20-21] Given the values for ΔH and ΔS, we can see that the binding of the imidazolium-containing polymer to pDNA is completely driven by entropy and is a slightly endothermic process. Low enthalpy values, which are close to zero, are expected for purely electrostatic interactions;[22-23] therefore, it is likely that other minor enthalpic contributions, besides electrostatic interactions, are involved in this binding system. However, interpreting the ΔH data for these polyplex complexation events is difficult, as there are many possible contributors to the observed heats: electrostatic interactions, hydrogen bonds breaking and/or forming, proton uptake, etc.[6] This enthalpically unfavorable behavior is common in many highly charged polycation-DNA systems.[6-7, 24-25] Most researchers attribute this increase in entropy, which drives the binding event, to be a combination of counterion and water molecule release,[7, 26] as well as possible conformational changes in the polymer upon binding.[27]

Table 3.1 Thermodynamic binding parameters for **Figure 3.3**

K (M^{-1})	**ΔH (kJ/mol)**	**n_{bind}**	**ΔS (kJ/mol•K)**	**ΔG (kJ/mol)**
6.82×10^4	1.89	0.27	0.10	-27.6

These initial experiments were also performed for the adenine-containing polymer, in an effort to compare the binding thermodynamics of two copolymers that were different in structure. While it is still a positively charged polymer, it also has the added adenine functionality to promote more hydrogen bonding between the polymer and the pDNA base pairs. Similar aggregation behavior was seen for this polymer as well, as shown in Figure 3.4; therefore, the data was treated in the same manner, and the heats attributed to aggregation were

omitted from fitting. The thermodynamic parameters obtained from the fitting procedure are shown in Table 3.2, along with the previously shown data for the imidazolium-containing polymer for comparison.

The Gibb's free energy and n_{bind} values for the adenine-containing polymer are quite similar to that of the imidazolium-containing polymer. The binding affinity is slightly lower than that of the imidazolium-containing polymer, but it is still on the same order and lower, in general, than what is expected for polycations. Perhaps the most notable features of this data are the strikingly different enthalpy and entropy of binding values. Figure 3.5 uses the equation for the change in Gibb's free energy to mathematically compare the enthalpic and entropic contributions to binding from both polymers. (Note: due to rounding differences in the fitting procedure, these are approximate, not exact, equalities.) As mentioned previously, Figure 3.5 (a) illustrates the enthalpically unfavorable binding of the imidazolium-containing polymer to pDNA being completely driven by the much larger and negative contribution that the entropy makes to ΔG, facilitating the spontaneous binding event ($\Delta G < 0$). While Figure 3.5 (b) shows a near equal contribution from enthalpy and entropy in the spontaneous complexation of pDNA and the adenine-containing polymer.

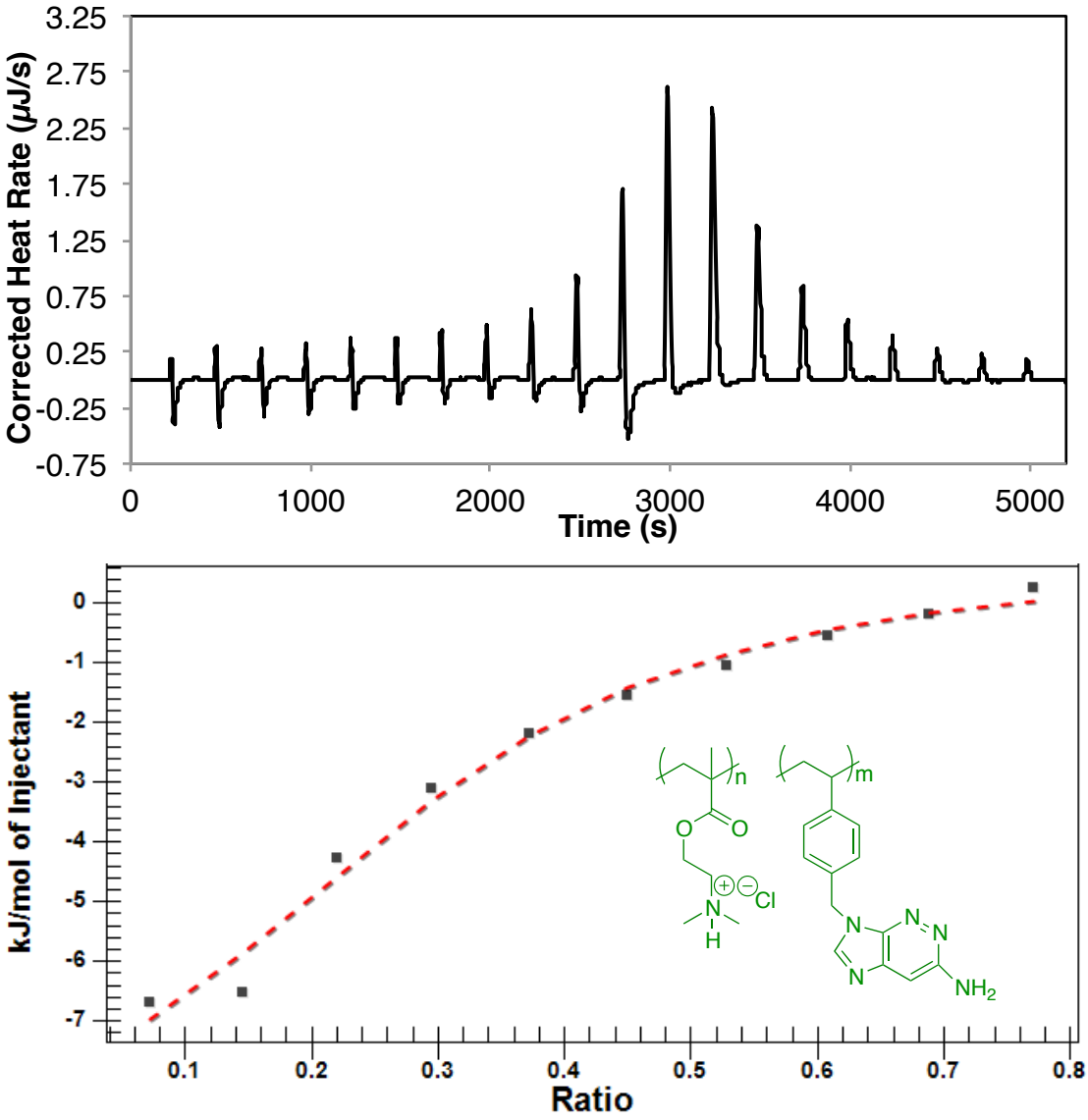

Figure 3.4 (top) ITC enthalpogram of 3.8 mM adenine-containing polymer being titrated into 0.75 mM pDNA at 25 ºC (solvent: water, 20 injections) and (bottom) the resultant integrated heat per injection and fitting isotherm

Table 3.2 Comparison of thermodynamic binding parameters for imidazolium- and adenine-containing polymers in **Figure 3.3** and **Figure 3.4**, respectively

	K (M^{-1})	**ΔH (kJ/mol)**	**n_{bind}**	**ΔS (kJ/mol•K)**	**ΔG (kJ/mol)**
Imidazolium-containing polymer	6.82×10^4	1.89	0.27	0.10	-27.6
Adenine-containing polymer	1.35×10^4	-11.2	0.31	0.041	-23.5

(a)

$$\Delta G = \Delta H - T\Delta S$$

$$-27.6\ \frac{kJ}{mol} \cong 1.89\ \frac{kJ}{mol} - (298K)\left(0.1\ \frac{kJ}{mol \cdot K}\right)$$

$$-27.6\ \frac{kJ}{mol} \cong 1.89\ \frac{kJ}{mol} - 29.8\ \frac{kJ}{mol}$$

(b)

$$\Delta G = \Delta H - T\Delta S$$

$$-23.6\ \frac{kJ}{mol} \cong -11.2\ \frac{kJ}{mol} - (298K)\left(0.04\ \frac{kJ}{mol \cdot K}\right)$$

$$-23.6\ \frac{kJ}{mol} \cong -11.2\ \frac{kJ}{mol} - 11.9\ \frac{kJ}{mol}$$

Figure 3.5 Mathematical representations of contributions from enthalpy and entropy in the overall binding thermodynamics of **Figure 3.3** and **Figure 3.4** for (a) the imidazolium-containing and (b) the adenine-containing polymers, respectively

Initially we hypothesized that this large enthalpic contribution to the hydrogen-bonding functionality of the adenine block of the copolymer. While more experiments were needed to explore this exothermic complexation further, the negative enthalpy value was very encouraging. Previous literature has shown that enthalpically favored binding is a good indicator of specific binding interactions, whereas endothermic complexation is usually seen with nonspecific interactions. With the end goal of optimizing and fine-tuning polycations for DNA binding, it

has been shown to be more difficult to fix the problem of nonspecific, endothermic binding, than it is to improve the entropy contribution for a specific interaction.[26]

3.3.2 Solution Preparation Concerns

Before going further with the previous experiments, several adjustments were made to the experimental setup in an effort to eliminate the aggregation and to rule out any heat effects other than the actual polymer-DNA complexation. To address the aggregation concerns, the concentrations of polymer and pDNA were greatly reduced to accommodate the smaller sample cell volume in this particular instrument. In addition, the preliminary binding experiments had been conducted in ultrapure water. This led to concerns that without any buffering capacity, a large majority of the heat signal we were getting could be due to proton exchange within the water. Therefore, subsequent solutions were prepared in PBS buffer (7.4 pH) to alleviate these concerns and to make the titrations comparable to physiological pH conditions.

As shown in Figure 3.6, by lowering the concentrations of the adenine-containing polymer and pDNA, by approximately 65% and 85%, respectively, the enthalpograms were no longer biphasic, indicative of aggregation-free binding. In addition, aggregates were no longer visible clinging to the side of the buret syringe at the conclusion of these titrations. The overall heat generated in these two titrations suggests reproducibility. A new concern presented itself, however, in these two very different binding stoichiometry values. For these two titrations, the exact same solutions and experimental conditions were used, with the exception of being performed on different days. The first titration was performed directly after the solutions were

prepared, on day 0. Afterward, the solutions were stored at 4 ºC until day 3, when the second titration was performed. Due to the binding stoichiometry almost doubling in the second titration, with no other experimental differences besides the age of the solutions, it became evident that there were potential problems with the solution stability of the polymers. Therefore, all subsequent polymer solutions were used for titration experiments immediately after being prepared.

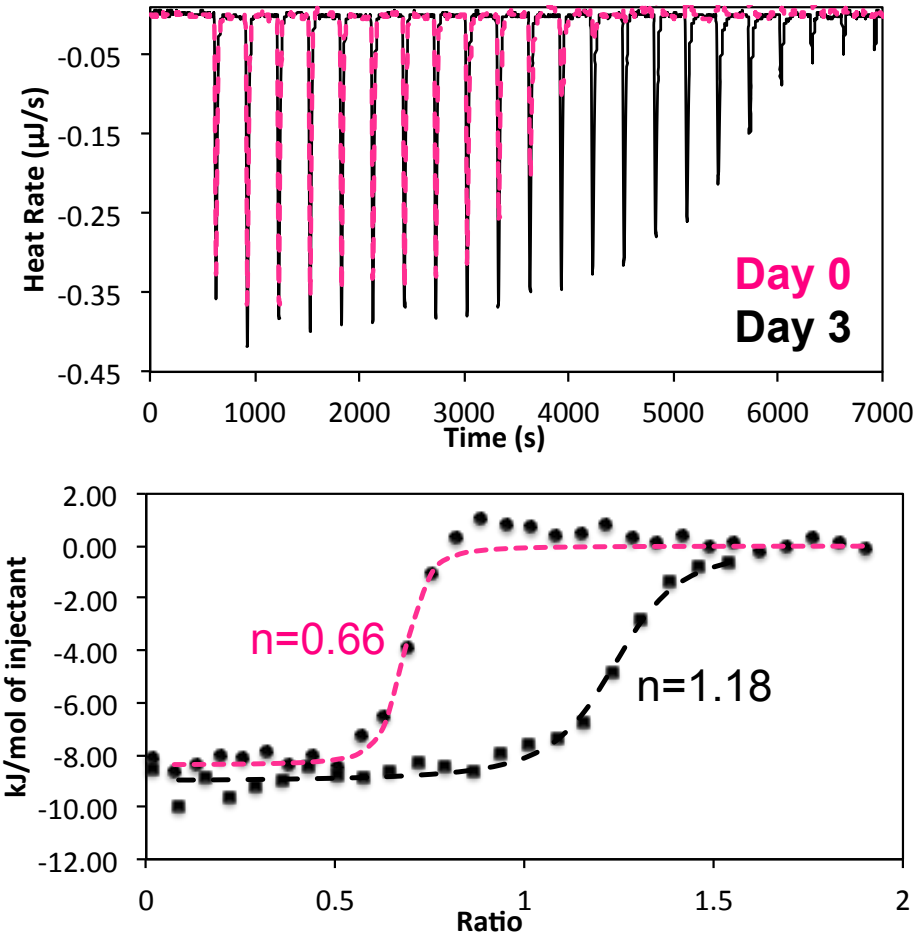

Figure 3.6 (top) ITC enthalpograms of 1.4 mM adenine-containing polymer being titrated into 0.1 mM pDNA at 25 ºC (solvent: PBS buffer, 26 injections) at day 0 and day 3 of the solutions being prepared, and (bottom) the resultant integrated heat per injection and fitting isotherms

3.3.3 Optimized Experimental Conditions and Reproducible Data

Figure 3.7 shows three consecutive titrations performed at the lower concentrations of pDNA and the adenine-containing polymer in PBS buffer, in which the solutions were prepared immediately before use in the ITC. The three trials overlay quite nicely and confirmed that these new experimental conditions were essential in obtaining reproducible data. An example of the model fitting is shown in Figure 3.8, where we observe a much cleaner sigmoidal shape and fit than in the preliminary experiments with half of the data omitted from aggregation. The average thermodynamic parameters from the triplicate titrations are provided in Table 3.3. The errors associated with each of these values are comparable to those seen in similar ITC studies of DNA complexation.[6, 25]

These titrations exhibited an average binding affinity that was two orders of magnitude greater than the previous result, which is more in-line with the expected K for polycation-DNA complexation. The Gibb's free energy and binding stoichiometry are also slightly greater in magnitude than before, but remain comparable to the literature.[4-6, 19-20] The previous values may have been low as a result of fitting partial data that was skewed by aggregation; however, there is no way to confirm this with certainty. This set of experiments still observed exothermic binding as before, but the ΔH value is slightly less negative and the ΔS is slightly greater than previously observed in the preliminary experiments. Returning to the Gibb's free energy equation in Figure 3.9, the entropic term is now more clearly the dominant driving force for binding under these optimized experimental conditions. However, the binding between the adenine-containing polymer and pDNA is still exothermic and enthalpically favorable, as anticipated. This substantial contribution from enthalpy suggests that the adenine within the VBA component of

the copolymer is providing a significant amount of complimentary hydrogen bonding with the pDNA base pairs, in addition to whatever electrostatic interactions are also occurring.

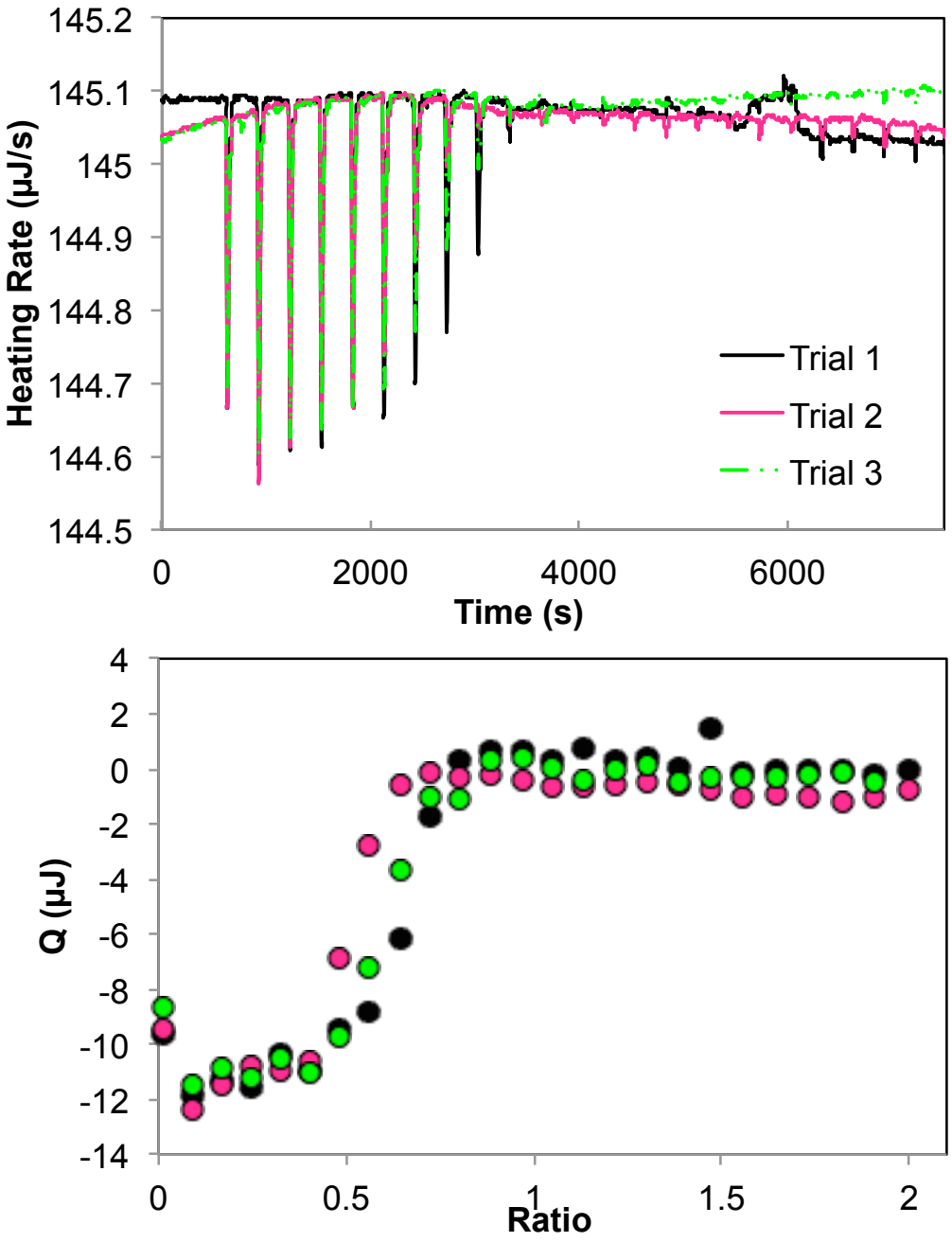

Figure 3.7 (top) overlaid ITC enthalpograms for 3 trials of 1.14 mM adenine-containing polymer being titrated into 0.1 mM pDNA at 25 ºC (solvent: PBS buffer, 26 injections) and (bottom) the resultant integrated heats per injection

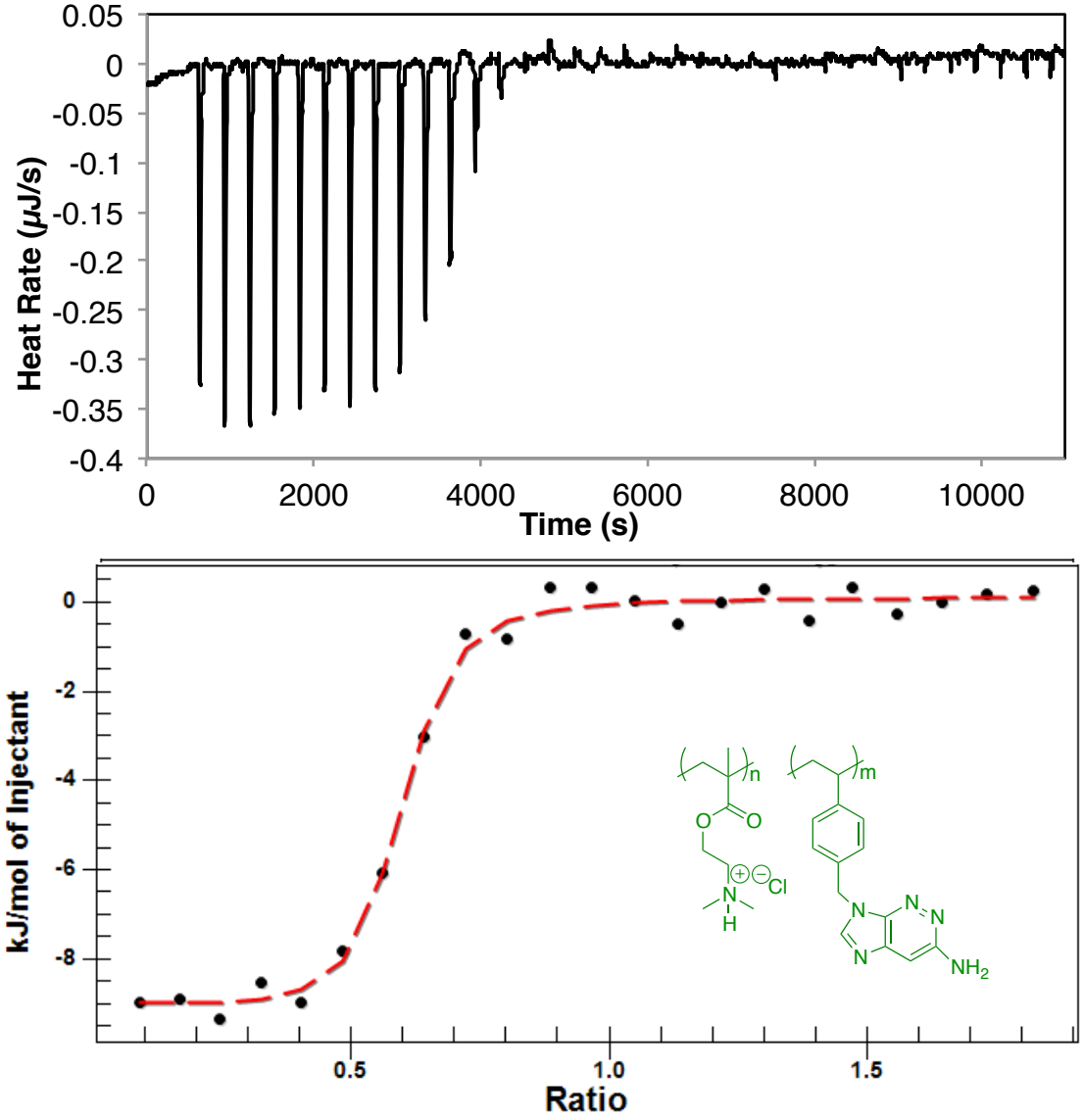

Figure 3.8 (top) ITC enthalpogram of 1.14 mM adenine-containing polymer being titrated into 0.1 mM pDNA at 25 ºC (solvent: PBS buffer, 26 injections) and (bottom) the resultant integrated heat per injection and fitting isotherm

Table 3.3 Average binding thermodynamics for the titrations represented by **Figure 3.8**

$K \times 10^{-6}$ (M^{-1})	ΔH (kJ/mol)	n_{bind}	ΔS (kJ/mol•K)	ΔG (kJ/mol)
2.8 ± 0.6	-9.2 ± 0.2	0.54 ± 0.08	0.093 ± 0.002	-36.8 ± 0.5

$$\Delta G = \Delta H - T\Delta S$$

$$-36.8\ \frac{kJ}{mol} \cong -9.20\ \frac{kJ}{mol} - (298K)\left(0.09\frac{kJ}{mol \cdot K}\right)$$

$$-36.8\ \frac{kJ}{mol} \cong -9.20\ \frac{kJ}{mol} - 26.8\ \frac{kJ}{mol}$$

Figure 3.9 Mathematical representation of contributions from enthalpy and entropy in the overall binding thermodynamics for the imidazolium-containing polymer at optimized experimental conditions in **Figure 3.8**

3.3.4 Comparison of Copolymer to pDMAEMA Homopolymer

To test the hypothesis that this enthalpic contribution to binding was a result of substantial hydrogen bonding between the adenine units and the pDNA base pairs, an identical experiment was also performed to study the binding of the pDMAEMA homopolymer, from which the copolymer was made, and pDNA. While the pDMAEMA homopolymer does have some hydrogen-bonding functionality in the amine group, similar to the hydroxyl groups on the imidazolium-containing polymer, its main function is to provide the electrostatic interactions. By removing the adenine portion of the copolymer, a substantial amount of potential hydrogen-bonding sites are lost. The results of this titration are shown in Figure 3.10.

Given the loss of the adenine hydrogen-bonding sites, we were expecting a very different binding profile for the pDMAEMA, as compared to that of the adenine-containing polymer. In fact, it was assumed probable that another endothermic pDNA complexation event, driven by entropy, would be observed like the imidazolium-containing polymer exhibited. However, the results in Figure 3.10 are completely contrary to these expectations. Compared to Figure 3.8, these two enthalpograms and fitting isotherms look almost identical. Furthermore, the thermodynamic binding parameters listed in Table 3.4 are very similar to those seen for the adenine-containing polymer in Table 3.3. The values for the binding affinity, n_{bind}, and the Gibb's free energy of the pDMAEMA titration are actually all within error of the copolymer titration results. The entropy value for the pDMAEMA binding is slightly higher than that seen in the copolymer, but they are still within 10% of each other.

The main difference between the two sets of data is seen in the enthalpy values, where the ΔH observed for the adenine-containing copolymer is still more exothermic than that of the homopolymer, by approximately 3 kJ/mol. While the pDMAEMA is about 30% less exothermic than the adenine-containing copolymer, we were still surprised that the binding was exothermic. It became evident that our earlier assumptions regarding the adenine functionality as the primary enthalpic contributor were not accurate. Therefore, the dramatic difference between the endothermic binding for the imidazolium-containing polymer and the exothermic binding of the adenine-containing copolymer must instead originate from some other structural difference(s) between the two. More specifically, it is likely that the variability in the arrangements and quantities of counterions and solvent molecules associated with the two polycations before and after binding are significantly different, as the release of these counterions and solvent molecules

is very often credited with being the entropic binding force of polyplex binding.[7, 26] In addition, the small ~3 kJ/mol difference in ΔH values may still be a result of the adenine functionalities, however more experiments are needed to gain a better understanding of all the enthalpic contributions to complexation in these systems. Currently, due to the lack of available sample, this one comparison is all that has been collected thus far.

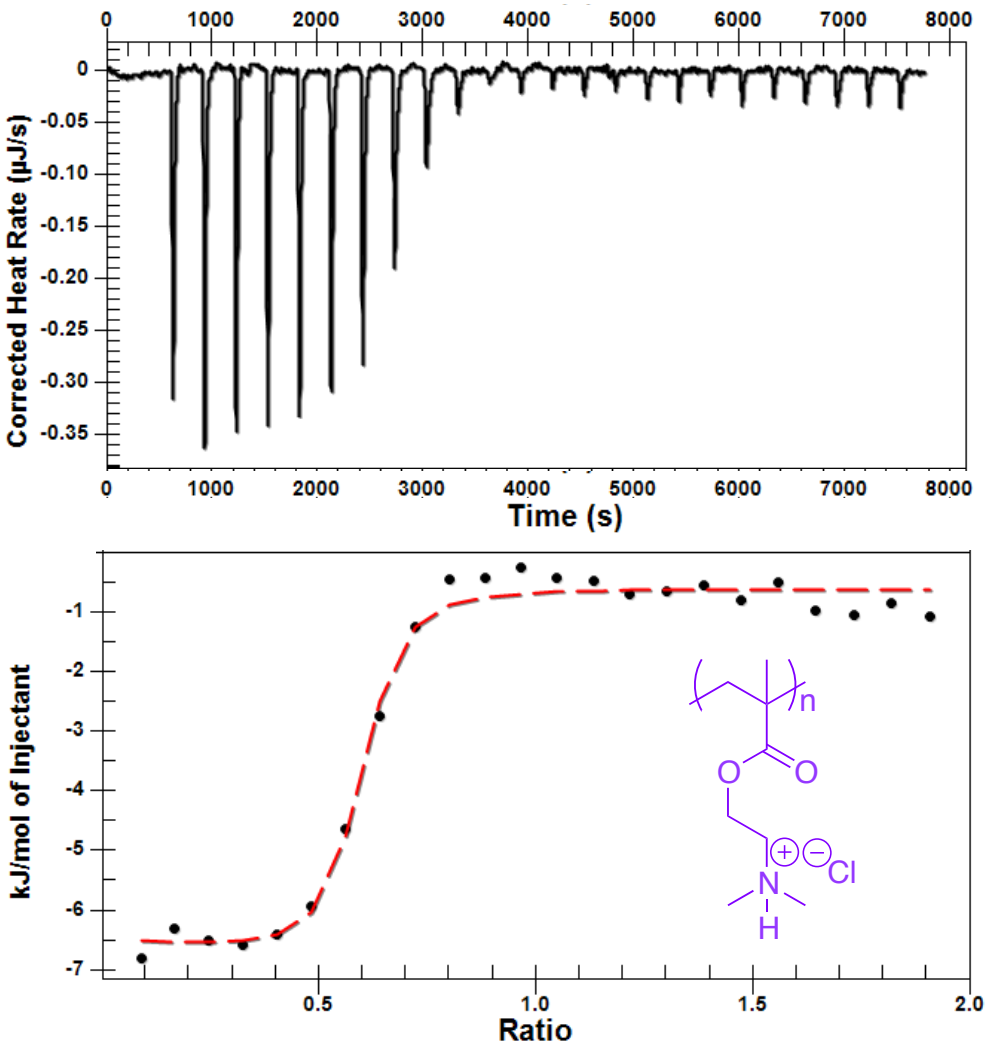

Figure 3.10 (top) ITC enthalpogram of 1.14 mM pDMAEMA-HCl homopolymer being titrated into 0.1 mM pDNA at 25 ºC (solvent: PBS buffer, 26 injections) and (bottom) the resultant integrated heat per injection and fitting isotherm

Table 3.4 Thermodynamic binding parameters for **Figure 3.10**

K (M^{-1})	ΔH (kJ/mol)	n_{bind}	ΔS (kJ/mol•K)	ΔG (kJ/mol)
2.70×10^6	-6.00	0.56	0.103	-36.7

Previous studies in the literature of DNA complexation may help to explain some of the exothermic binding behavior seen for the adenine-containing polymer. Stolnik *et al*. also reported exothermic enthalpy values when studying the effects of pH on the complexation of DNA and pDMAEMA. Overall, they observed higher degrees of ionization for the polymer and increased binding affinities at lower pH values. Nevertheless, even at the high end of the tested pH range (6.6 – 8.0), at which the degree of ionization is much lower, significant heat release was still observed during complexation. Stolnik *et al*. attribute this to the neutral, unprotonated polymer abstracting protons from the buffer so that it may interact with the negatively charged DNA. Therefore, they concluded that the observed enthalpy was not due to the binding event alone, but rather that the buffer ionization enthalpy was also a large contributing factor.[16] This proton exchange behavior has been seen in previous binding studies for proteins and other polycations.[21, 28-29]

The average pKa value for PDMAEMA reported in the literature is 7.5.[17, 30] Given that our titrations, for both the adenine-containing polymer and the pDMAEMA homopolymer, were carried out in pH 7.4 PBS buffer, approximately half of the DMAEMA residues were likely unprotonated during the titrations. Therefore it is highly probable that some, if not most, of the observed heat released in these titrations was due to proton exchange with the

buffer. Future work, if more samples become available, should involve doing similar titrations with the adenine-containing polymer in multiple buffers with varying ionization energies to confirm the contributions of buffer ionization to the overall complexation enthalpy. This also raises the additional awareness of pH in general during polyplex formation. Given that the charge on many of these polycations is due to protonated amines, the pH is a critical factor in polyplex formation. For example, while the pKa of the PDMAEMA amine is approximately 7.5, the pKa for adenine at the N1 position is only around 4.[15] Preparing the polyplex solutions at a lower pH would result in a higher percentage of overall protonation and charge density, possibly decreasing the binding stoichiometry. Therefore, in addition to exploring buffers with differing ionization energies, it would also be beneficial to investigate these binding thermodynamic experiments in buffers of various pH as well.

3.3.5 ITC Experiments to Confirm NMR Free Polymer Results

Although studies on the imidazolium-containing and adenine-containing polymers had to be suspended due to sample issues, we were able to take what we had learned from these investigations, regarding optimal experimental conditions for these polycation systems in our low volume ITC, and apply it to another polymer-DNA binding project. Wang *et al.*[31] had developed a new method using NMR to quantify the concentration of free polymer remaining in solution after polyplexes are formed. The amount of free polymer is typically difficult to characterize, but an important parameter, nonetheless, as it affects toxicity,[32] cellular uptake,[33-34] and delivery efficiency.[35-36] This new NMR method allowed for not only the quantitation of free polymer, but also the stoichiometric ratio (N/P) of bound polymer to DNA in the polyplexes

themselves.[31] In this investigation, isothermal titration calorimetry was used to verify the N/P ratio for PEI-DNA complexes that had previously been determined with this new NMR method.

Using low concentrations of polymer and pDNA, both in pH 7.4 Tris buffer, triplicate titrations were conducted. Figure 3.11 shows an example of one of the titrations and the average thermodynamic parameters from all three titrations are shown in Table 3.5. The standard deviations listed for these parameters are typical compared to other polycationic studies,[6, 21] and indicate good reproducibility between titrations. However, the only parameter of interest in this study is n_{bind}, or the binding stoichiometry, which was observed to be 3.5 ± 0.3. This value was in perfect agreement with the N/P value of 3.5 determined by NMR.[31]

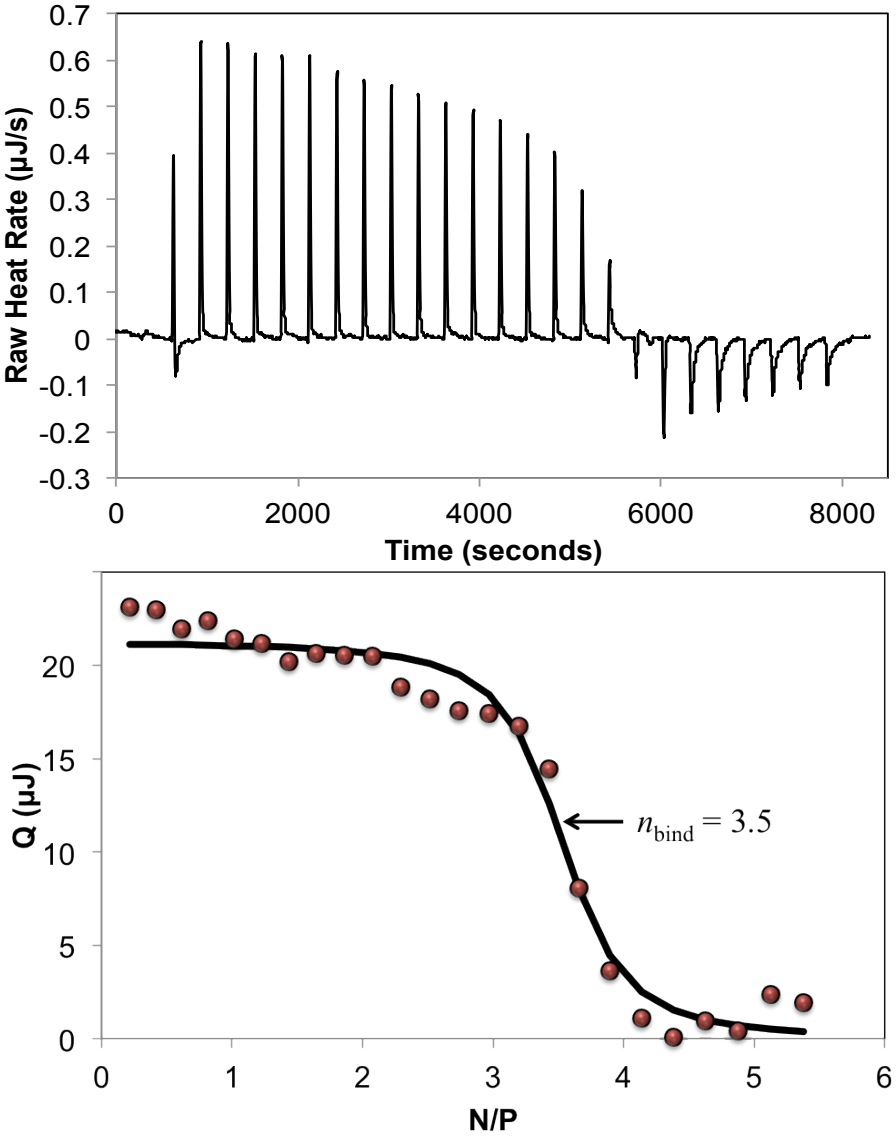

Figure 3.11 (top) ITC enthalpogram of 172 µg/mL PEI titrated into 132 µg/mL pDNA in 10 mM Tris buffer pH 7.4 at 37 ºC and (bottom) the resultant integrated heat per injection and fitting isotherm

Table 3.5 Thermodynamic binding parameters for **Figure 3.11**

	Trial 1	**Trial 2**	**Trial 3**	**Average**	**Std. Dev.**	**%RSD**
K (M^{-1})	2.66×10^5	6.43×10^5	5.75×10^5	4.94×10^5	2.01×10^5	40.6
ΔH (kJ/mol)	2.71	2.18	1.58	2.16	0.56	26
n_{bind}	3.4	3.3	3.8	**3.5**	**0.3**	8

3.4 Conclusions & Future Work

In conclusion, experimental conditions were optimized for the successful study of polycation-DNA complexation in a low volume ITC among several different polymer structures. Early titrations demonstrated the need for the preparation of buffered solutions at low polymer and DNA concentrations, and that these solutions should be prepared immediately before experimentation to obtain reproducible binding results. Preliminary results showed that the imidazolium-containing polymer has an entropically driven binding, which is enthalpically unfavorable. However, these results were obtained in non-ideal conditions, where aggregation of the polyplexes may have produced incorrect data. In addition, the adenine-containing polymer and the pDMAEMA homopolymer both exhibited exothermic binding, with strong contributions from enthalpy and entropy. The observed ΔH for the copolymer is slightly more negative than for the pDMAEMA, which may be attributed to the added hydrogen-bonding capabilities of the adenine groups of the copolymer; however, this has not been confirmed. Furthermore, the heat release seen for both of these polycations may be a result of proton abstraction from the buffer by unprotonated residues of the polycations, as seen in previous literature.[16] Further experiments are needed to test this theory. Finally, this low volume ITC system was successfully utilized to determine the stoichiometric ratio of PEI-DNA binding to confirm novel NMR results.[31]

If more samples become available, several experiments should be completed in the future for the imidazolium-containing and adenine-containing polymers to solve numerous unanswered questions. For example, more replicates should be performed under optimized conditions (freshly made, buffered solutions at low concentrations) to ensure reproducibility for both polymers. The accuracy of these titrations would also benefit from blank titrations, to subtract

out any heat effects from the mixing of each component, polymer and DNA, with the buffer. For the time being, blank models that came with the fitting software were used instead of blank titrations, due to the lack of actual samples. Furthermore, all of the binding data analyzed in this chapter were fit with the independent binding sites model, which has been used extensively throughout the polyplex binding literature.[4-6, 19-20] However, while this model will fit the data and give reasonable thermodynamic values, it is not the most accurate model to fit polycation-DNA binding, as it assumes a 1:1 binding stoichiometry, which is not always, or even usually, the case with polyplex systems. Future work should be directed toward finding and/or writing a better, more appropriate binding model for these polyplex systems. The need for such models has also been expressed in recent literature as well.[16, 25, 37-38]

In addition, both of the polycations studied here were each part of a series of polymers, looking at varying structures, charge densities, etc. It would also be advantageous to compare thermodynamic data across the different series to gain a better understanding of the polymer-DNA complexation mechanism. In addition, dynamic light scattering experiments would be useful for testing the ratios at which aggregation occurs. Finally, titrations carried out in buffers with varying ionization energies, pH values, and different salt concentrations are needed to decipher the actual contributions from buffer ionization enthalpy, degree of protonation, and electrostatic interaction, respectively, to the overall enthalpy of complexation.

3.5 References

1. Reineke, T. M.; Grinstaff, M. W. *MRS Bulletin* **2005,** *30*, 635-639.
2. Leong, K. *MRS Bulletin* **2005,** *30*, 640-646.
3. Duncan, R. *Nature Reviews* **2003,** *2*, 347-360.
4. Bronich, T.; Kabanov, A. V.; Marky, L. A. *Journal of Physical Chemistry B* **2001,** *105*, 6042-6050.
5. Prevette, L. E.; Kodger, T. E.; Reineke, T. M.; Lynch, M. L. *Langmuir* **2007,** *23*, 9773-9784.
6. Prevette, L. E.; Lynch, M. L.; Kizjakina, K.; Reineke, T. M. *Langmuir* **2008,** *24*, 8090-8101.
7. Bouchemal, K. *Drug Discovery Today* **2008,** *13* (21/22), 960-972.
8. Wettig, S. D.; Verrall, R. E.; Foldvari, M. *Current gene therapy* **2008,** *8* (1), 9-23.
9. Falconer, R. J.; Penkova, A.; Jelesarov, I.; Collins, B. M. *J. Mol. Recognit.* **2010,** *23* (Copyright (C) 2011 American Chemical Society (ACS). All Rights Reserved.), 395-413.
10. Falconer, R. J.; Collins, B. M. *J. Mol. Recognit.* **2011,** *24* (Copyright (C) 2011 American Chemical Society (ACS). All Rights Reserved.), 1-16.
11. O'Brien, R.; Ladbury, J. E.; Chowdhry, B. Z. Chapter 10: Isothermal titration calorimetry of biomolecules. In *Protein-Ligand Interactions: hydrodynamics and calorimetry*, Harding, S. E.; Chowdhry, B. Z., Eds. Oxford University Press: New York, 2001; pp 263-286.

12. MicroCal. What is ITC? http://www.microcal.com/technology/itc.asp (accessed September 26, 2010).

13. Microcalorimetry: Introduction to characterizing biopolymer binding and kinetics reactions by ITC. TA Instruments: 2009; pp 1-83.

14. Allen, M. H.; Green, M. D.; Getaneh, H. K.; Miller, K. M.; Long, T. E. *Biomacromolecules* **2011,** *12* (Copyright (C) 2012 American Chemical Society (ACS). All Rights Reserved.), 2243-2250.

15. Hemp, S. T.; Hunley, M. T.; Cheng, S.; DeMella, K. C.; Long, T. E. *Polymer* **2012,** *53* (7), 1437-1443.

16. Rungsardthong, U.; Ehtezazi, T.; Bailey, L.; Armes, S. P.; Garnett, M. C.; Stolnik, S. *Biomacromolecules* **2003,** *4*, 683-690.

17. Samsonova, O.; Pfeiffer, C.; Hellmund, M.; Merkel, O. M.; Kissel, T. *Polymers* **2011,** *3* (2), 693-718.

18. Wang, X.; Kelkar, S. S.; Hudson, A. G.; Moore, R. B.; Reineke, T. M.; Madsen, L. A. *ACS Macro Letters* **2013,** *2* (11), 1038-1041.

19. Patel, M. A., T. *Biophysical Journal* **2005,** *88*, 2089-2103.

20. Choosakoonkriang, S. L., B.; Koe, G.; Koe, J.; Middaugh, C. *Journal of Pharmaceutical Sciences* **2003,** *92* (8), 1710-1722.

21. Ma, P. L.; Lavertu, M.; Winnik, F. M.; Buschmann, M. D. *Biomacromolecules* **2009,** *10* (Copyright (C) 2011 American Chemical Society (ACS). All Rights Reserved.), 1490-1499.

22. Privalov, P. L.; Dragan, A. I.; Crane-Robinson, C. *Nucleic Acids Research* **2011,** *39* (7), 2483-2491.

23. Ruso, J. M.; Piñeiro, Á. *Proteins in Solution and at Interfaces: Methods and Applications in Biotechnology and Materials Science*. Wiley: 2013.

24. Ross, P. D.; Shapiro, J. T. *Biopolymers* **1974,** *13* (2), 415-416.

25. Matulis, D.; Rouzina, I.; Bloomfield, V. A. *Journal of Molecular Biology* **2000,** *296* (4), 1053-1063.

26. Campoy, A. V.; Freire, E. *Biophysical Chemistry* **2005,** *115*, 115-124.

27. Turgeon, S. L.; Schmitt, C.; Sanchez, C. *Current Opinion in Colloid & Interface Science* **2007,** *12* (4–5), 166-178.

28. Murphy, K. P.; Xie, D.; Garcia, K. C.; Amzel, L. M.; Freire, E. *Proteins-Structure Function and Genetics* **1993,** *15* (2), 113-120.

29. Srivastava, D. K.; Wang, S.; Peterson, K. L. *Biochemistry* **1997,** *36* (21), 6359-6366.

30. Arigita, C.; Zuidam, N. J.; Crommelin, D. J. A.; Hennink, W. E. *Pharmaceutical Research* **1999,** *16* (10), 1534-1541.

31. Wang, X.; Kelkar, S. S.; Hudson, A. G.; Moore, R. B.; Reineke, T. M.; Madsen, L. A. *ACS Macro Lett.* **2013,** *2* (11), 1038-1041.

32. Lv, H. T.; Zhang, S. B.; Wang, B.; Cui, S. H.; Yan, J. *Journal of Controlled Release* **2006,** *114* (1), 100-109.

33. Behr, J. *Chimia* **1997,** *51*, 34-36.

34. Haensler, J.; Szoka, F. C. *Bioconjugate Chemistry* **1993,** *4* (5), 372-379.

35. Sonawane, N. D.; Szoka, F. C.; Verkman, A. S. *Journal of Biological Chemistry* **2003,** *278* (45), 44826-44831.

36. Akinc, A.; Thomas, M.; Klibanov, A. M.; Langer, R. *J. Gene. Med.* **2005,** *7* (5), 657-663.

37. Kim, W.; Yamasaki, Y.; Kataoka, K. *J. Phys. Chem. B* **2006,** *110* (Copyright (C) 2011 American Chemical Society (ACS). All Rights Reserved.), 10919-10925.

38. Ball, V.; Maechling, C. *International Journal of Molecular Sciences* **2009,** *10*, 3283-3315.

Chapter 4 : Analytical Characterization of Polymer-DNA Binding: Thermodynamics, Intermolecular Interactions, Size, and Thermal Stability

4.1 Introduction

Here, we present a continuation into the study of polyplex structure-property relationships that began in Chapter 3. This work will focus on a different polycation: a trehalose-based polymer[1], Tr5, that is the next in a series of polymeric delivery vehicles that was previously studied.[2] In 2008, Reineke's group published thermodynamic and structural studies on a series of polycations that contained a trehalose sugar moiety and an oligoethyleneamine unit with varying numbers of secondary amines (1-4) per repeat unit. These polycations are referred to as Tr1-Tr4, respectively. In addition to characterizing the thermodynamic binding parameters of the polyplexes with isothermal titration calorimetry (ITC), analyses were also performed with circular dichroism (CD) and Fourier transform infrared (FTIR) spectroscopies to probe the structural changes exhibited by DNA upon binding with the polymers.[2]

In conjunction with results from potentiometric titrations and previous biological assays,[3-4] Reineke's group was able to hypothesize from the ITC results that the longer amine spacers, as seen in Tr3 and Tr4, may allow a higher degree of hydrogen bonding activity, as opposed to electrostatic interactions alone. In addition, the typical hydration layer usually found around trehalose sugars in solution[5] may be preserved in polymers such as Tr3 and Tr4 because of the longer spacers, potentially reducing aggregation among the polyplexes and increasing efficacy.[2]

CD spectra revealed that the polymers with shorter amine spacers, Tr1 and Tr2, showed minimal shift or intensity changes; whereas Tr3 and Tr4 showed significant red shifts in the spectra, as well as decreased intensities. Reineke's group was able to conclude from the spectra that Tr1- and Tr2-DNA interactions were more electrostatic in nature, as this would explain the lack of a secondary structural change. Conversely, Tr3 and Tr4 appeared to be interacting with DNA via increased hydrogen bonding interactions, causing the shift in the spectra. In this study, shifts in the FTIR spectra for the polyplexes were also monitored, specifically for the guanine carbonyl stretch and the symmetric phosphate stretch. The resulting spectra showed large shifts in the symmetric phosphate peak for Tr1, with continually decreasing shifts as the number of amine spacers decreased. This supported the hypothesis that DNA complexation with Tr1 and Tr2 is driven primarily by electrostatic interactions, while Tr3 and Tr4 involve more hydrogen bonding with the DNA backbone.[2]

In the previous study, Reineke's group provided a nice example of the substantial amount of information that can be gathered from various analytical techniques in order to better understand the structure-activity relationships between polymeric delivery vehicles and nucleic acid therapeutics. In this work, we present similar characterizations of the next polymer in the series with five secondary amines per repeat unit: Tr5. In addition to ITC, CD spectroscopy, and FTIR spectroscopy analyses, this work also includes results from dynamic light scattering (DLS) and zeta potential measurements, as well as thermal curves obtained with UV-Vis spectroscopy.

4.2 Experimental

4.2.1 Materials

The polycation Tr5 was synthesized as reported previously,[1] and is shown in Figure 4.1. The plasmid DNA (pDNA) used was pCMV-technical grade DNA (7.2 kb) and was purchased from PlasmidFactory. A 20 bp NF-κB oligonucleotide decoy DNA was purchased from Integrated DNA Technologies. Ultrapure water was obtained from a Millipore-DQ3 filtration system, at a resistivity of 18.2 MΩ•cm. Tris was purchased from Fisher Scientific. A 10 mM Tris buffer was prepared at 25 ºC using ultrapure water and titrated to pH 7.4 with 0.1 M HCl or NaOH.

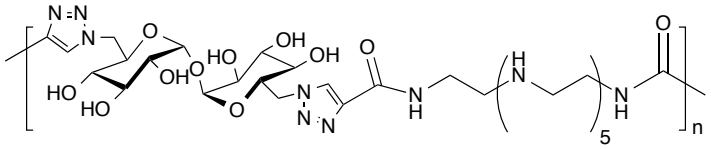

Figure 4.1 Chemical structure of Tr5 (adapted from Prevette, *et al*., 2008)

It should be noted that all concentrations given for DNA and polymer solutions are based off the phosphate and secondary amine concentrations, respectively. This allows the results to be reported in terms of the charge ratio N/P, or moles of amine to moles of phosphate.

4.2.2 ITC Binding Thermodynamics

Prior to all experiments, the pDNA solutions were prepared by thoroughly dialyzing against 10 mM Tris buffer (pH 7.4). The resulting dialysates were used to prepare the corresponding Tr5 solutions. The instrument used for these titration experiments was a TA

Instruments Low Volume NanoITC. The gold sample and reference cells in the ITC have a working volume of 170 μL, and the burette is a 50 μL gas-tight syringe with a stainless steel needle. For each titration, the sample cell was filled with the pDNA solution and the reference cell with ultrapure water. The burette syringe was filled with Tr5 solution. All titrations were performed at 25 °C with a stir rate of 350 rpm and 300 s intervals between each injection. Before starting each titration, the instrument was allowed to equilibrate until a stable baseline was obtained. Furthermore, a 300 s baseline was collected before and after the first and last injections. Depending upon the heat generated, the injection volume and number of total injections was adjusted accordingly. All titrations for these experiments were in the range of 10 to 25 injections total, with the total volume delivered always being 50 μL. TA Instruments NanoAnalyze™ software was used to fit the data with the standard independent binding sites model.

4.2.3 DLS & Zeta Potential

A Malvern Zetasizer Nano ZS was used for DLS measurements. Samples were analyzed in disposable polystyrene cuvettes and compared to a polystyrene latex reference. Measurements were performed at 25 °C and one measurement of three runs each was collected for each sample after a 5 minute equilibration. Hydrodynamic diameters are reported from the z-average results. Three sets of experiments were conducted. In the first set, polyplex size and charge were measured at increasing N/P ratios by titrating 5.5 mM Tr5 (based on moles of secondary amine) into 0.31 mM pDNA (based on moles of phosphate) with 13 μL aliquots. Both solutions were prepared in 10 mM Tris buffer (pH 7.4). In the second set of experiments 5 separate

formulations of varying N/P ratios were prepared prior to measurement, instead of being titrated into the DLS cuvette. These formulations were prepared by equal volume mixing from 0.31 mM pDNA, 1.55 mM Tr5, and appropriate amounts of 10 mM Tris buffer (pH 7.4) to bring each solution to the correct volume and concentration. The third set of experiments used the same equal volume formulation procedure, but two trials were performed with more N/P ratios.

4.2.4 FTIR Spectroscopy

FTIR measurements were performed with a Perkin-Elmer Spectrum One instrument equipped with a horizontal ZnSe crystal ATR attachment. All solutions were prepared in 10 mM Tris buffer (pH 7.4). Consequently, a background spectrum of this buffer was subtracted from each set of data, using a flat baseline at 2200 cm^{-1} for reference.[2, 6-7] All spectra collected were an average of at least 100 scans at a resolution of 4 cm^{-1}. Three sets of experiments were performed. Initially, polyplexes were measured at increasing N/P ratios by titrating 27 mM Tr5 into 12.12 mM pDNA directly on the ATR attachment. For the second set of experiment equal volume formulations were prepared and incubated 5 minutes before running them separately on the instrument. These formulations were prepared with 8.3 mM pDNA, 33.7 mM Tr5, and appropriate amounts of 10 mM Tris buffer (pH 7.4) to bring each solution to the correct volume and concentration. In the final set of experiments, polyplexes were again prepared by titrating directly onto the ATR crystal. The solution concentrations were 12.0 mM pDNA and 44.0 mM Tr5.

4.2.5 CD Spectroscopy

Circular dichroism measurements were made with a Jasco J-815 CD Spectropolarimeter. Each spectrum was an average of 3 iterations from 350-225 nm at a resolution of 0.5 nm. All measurements were taken at ambient room temperature with a nitrogen purge. Polyplex solutions were measured at varying N/P ratios by titrating 5.5 mM Tr5 into 0.24 mM pDNA, both in 10 mM Tris buffer (pH 7.4). A background spectrum for Tris buffer was also collected and subtracted from each of the other spectra.

4.2.6 UV-Vis Thermal Melts

A Cary 100 Bio UV-Vis with temperature control was used to collect melting curves at 260 nm in appropriate solution conditions for various Tr5 polyplex samples. Tris buffer dialysate (10 mM, pH 7.4) was used to prepare solutions for polyplexes made with pDNA and 5 mM Tris buffer (5 mM NaCl, pH 7.4) was used to prepare solutions for polyplexes made with decoy DNA. Background absorbance from the appropriate buffer was subtracted from each measurement. Samples were allowed to incubate for 30 minutes at room temperature after mixing and then were ramped at a heating rate of either 0.1 or 0.5 ºC/min. Data was collected in corresponding 0.1 or 0.5 ºC increments, with temperatures ranging from 5 to 90 ºC. The melting temperatures, T_m, were determined using the WinUV software (Agilent Technologies) from the inflection point of the absorbance versus temperature profiles. Polyplexes made with both pDNA and decoy DNA were investigated. For experiments with decoy DNA, set volumes (10 µL) of a stock solution were added to buffer and then a full UV-Vis scan was performed to determine the concentration of decoy DNA in the cuvette (approximately 5 to 10 mM). Afterward, appropriate amounts of Tr5 stock solution and buffer were added to achieve the desired N/P ratio.

4.3 Results & Discussion

4.3.1 ITC Binding Thermodynamics

Initial experiments were first conducted analogously to those reported for Tr1-Tr4 to test the thermodynamics of binding between Tr5 and pDNA.[2] The same concentrations of pDNA and polycation (based on moles of phosphate and secondary amine, respectively) were used, however these experiments were performed in an ITC with a much smaller sample cell volume. In these preliminary titrations, solutions were prepared and used for one titration, and then reused for an additional trial(s) later after the instrument had been cleaned. As shown in Table 4.1, these results were quite variable and displayed poor reproducibility, rendering it difficult to make definitive or accurate conclusions about the data. This irreproducibility also suggests solution instability over time like the early results reported in Chapter 3 for other polycations. In addition, aggregation was also visible in the solution mixture after the titration, which is further evidence for the instability of these polymer solutions over time. Therefore, all future titrations were conducted within one hour of solution preparation.

Table 4.1 Thermodynamic binding parameters for replicate trials of 3 mM Tr5 titrated into 0.31 mM pDNA (25 injections; 25 ºC); times listed correspond to the length of time that lapsed between solution preparation and the beginning of the titration

	Trial 1 (1-2 hrs)	**Trial 2 (24 hrs)**	**Trial 3 (1 hr)**	**Trial 4 (4-5 hrs)**	**Average**	**Std. Dev.**	**% RSD**
K ($\times 10^{-5}$ M^{-1})	12.1	6.10	9.21	2.74	**7**	**4**	**54**
ΔH (kJ/mol)	1.53	1.71	1.63	1.91	**1.7**	**0.2**	**10**
n_{bind}	0.95	1.10	0.98	1.13	**1.0**	**0.1**	**9**

Table 4.2 presents the thermodynamic binding data for five consecutive titrations in which all of the solutions were prepared and then used immediately within the next hour (slight variability in the wait for baseline equilibration). While the data for the binding affinity is slightly more consistent in these titrations, the values for enthalpy and stoichiometry of binding both display considerably greater standard deviations than those seen in Table 4.1. Furthermore, a large amount of visible aggregation on the end of the buret syringe was still visible at the end of the titrations. Considering the much lower volume of the sample cell in the NanoITC instrument (170 μL) compared to that of a standard volume instrument used (1.5 mL) used for Tr1-Tr4[2], it became apparent that the concentrations of the polymer and pDNA solutions also needed to be scaled down to accommodate the change in volume.

Table 4.2 Thermodynamic binding parameters for replicate trials of 3 mM Tr5 titrated into 0.31 mM pDNA (25 injections, 25ºC); all titrations performed within 1 hour of solution preparation

	Trial 1	**Trial 2**	**Trial 3**	**Trial 4**	**Trial 5**	**Average**	**Std. Dev.**	**% RSD**
K ($\times 10^{-5}$ M^{-1})	6.71	4.93	3.00	4.77	2.54	**4**	**2**	**38**
ΔH (kJ/mol)	1.97	2.72	2.38	2.85	3.72	**2.7**	**0.7**	**24**
n_{bind}	2.15	2.12	2.36	1.82	1.53	**2.0**	**0.3**	**16**

After reducing the concentrations of both the pDNA and Tr5 solutions by approximately 50%, three consecutive, reproducible titrations were performed as shown in Figure 4.2. While there was a significant reduction in the amount of aggregate material visible on the buret at the

end of the titrations, a small amount was still present. This is also visible in the biphasic enthalpograms. Therefore, the last four points of each binding isotherm, which were attributed to heats of aggregation, were omitted during fitting in accordance with the literature.[2, 8] The overlaid heats per injection and fitting curves for the three titrations can be seen in Figure 4.3. Table 4.3 provides the thermodynamic binding parameters obtained from the fitting curves. The standard deviations associated with each of these values are much improved from the initial experiments and are also on the order of those seen in previous literature for Tr1-Tr4. In addition, the values for binding affinity, enthalpy, and entropy observed here for Tr5 are quite similar to those seen previously for Tr4, while the binding stoichiometry is just slightly lower.[2]

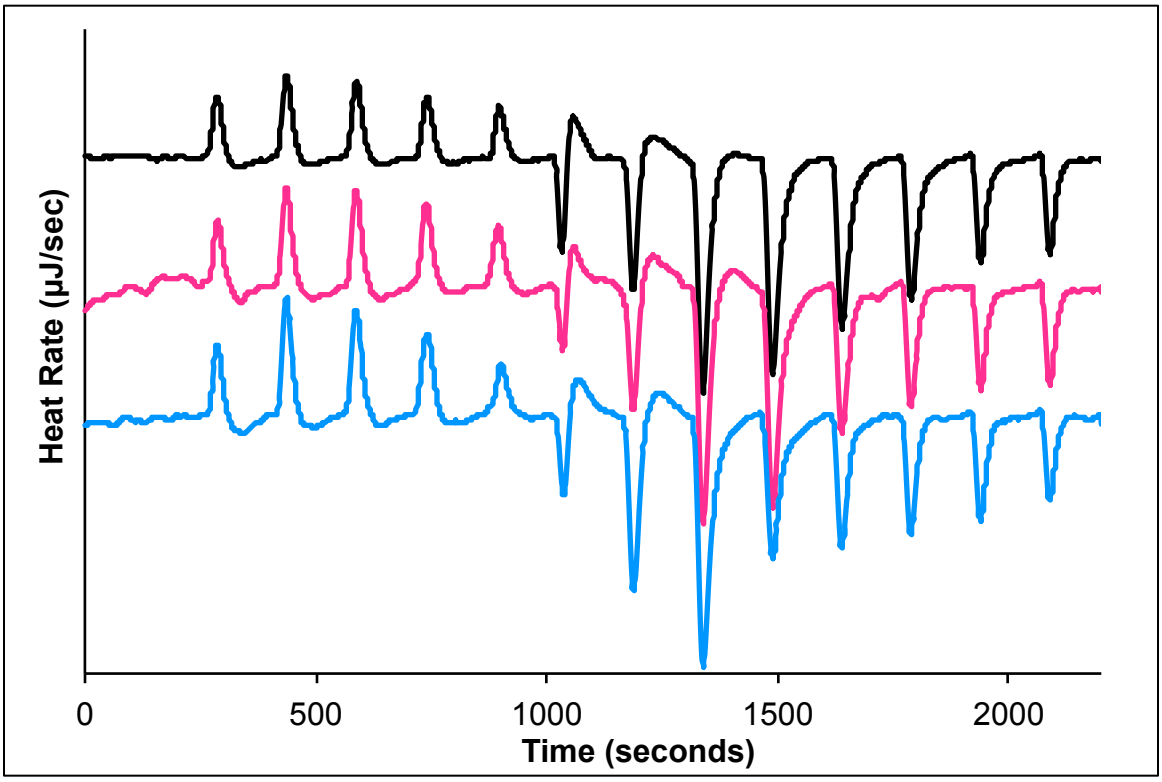

Figure 4.2 Overlaid enthalpograms for triplicate titrations of 13 injections of 1.4 mM Tr5 into 0.16 mM pDNA at 25 ºC (heat rate values are omitted because the data is vertically offset)

While the addition of one more secondary amine unit into the polymer backbone did not make a substantial difference in the thermodynamic binding parameters, these data still provide several important pieces of information. To begin with, new information was obtained for the binding thermodynamics of a polycation-DNA complex that had not previously been studied and augments the published series of Tr1-Tr4.[2] In addition, the binding observed here is endothermic and entropically driven, most likely because of counterion and water molecule release upon binding. This is consistent with other polycation systems, including the imidazolium-containing polymer in Chapter 3 and the Tr1-Tr4 series.[2, 9] Finally, the work here, in conjunction with the experiments in Chapter 3, was vital in making improvements to the experimental procedures for studying polyplex binding with a low volume ITC. To our knowledge, a low volume instrument has never been used for analyzing polycation-DNA complexation prior to these studies.

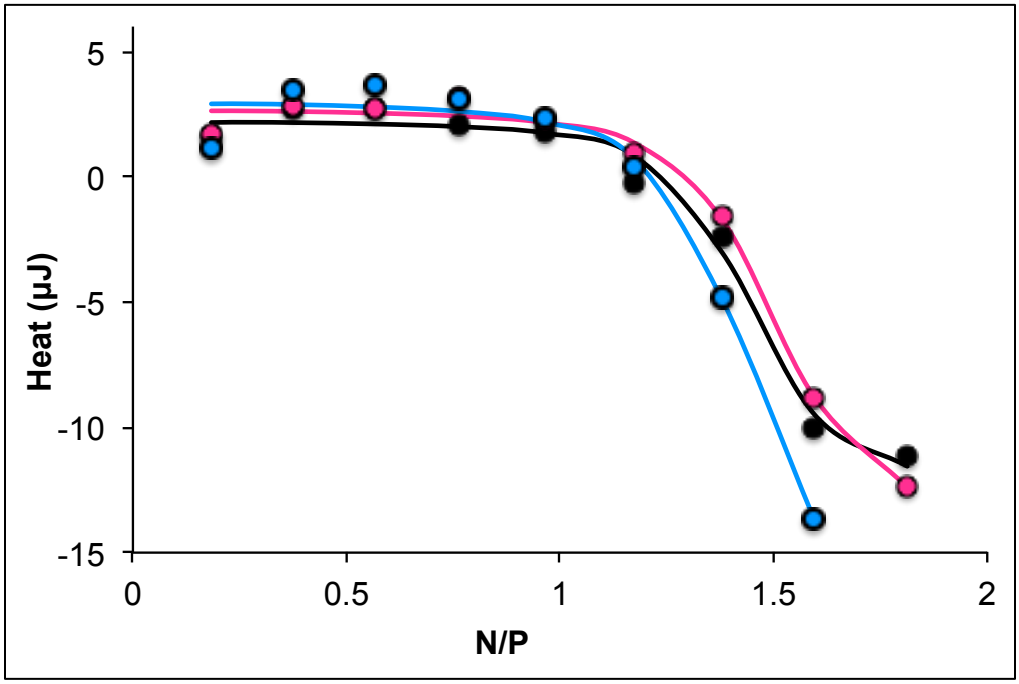

Figure 4.3 Overlay of resulting heats per injection for **Figure 4.2**

Table 4.3 Thermodynamic binding parameters for titrations in **Figure 4.2** and **Figure 4.3**

	Trial 1	Trial 2	Trial 3	Average	Std. Dev.	% RSD
K ($\times 10^{-5}$ M^{-1})	11.7	9.89	9.93	**10**	**1**	**10**
ΔH (kJ/mol)	2.72	3.08	3.91	**3.2**	**0.6**	**20**
n_{bind}	1.34	1.40	1.34	**1.36**	**0.03**	**3**
ΔG (kJ/mol)	-34.62	-34.20	-34.21	**-34.3**	**0.2**	**0.7**
ΔS (kJ/mol•K)	0.125	0.125	0.128	**0.126**	**0.002**	**1**

4.3.2 DLS & Zeta Potential

Dynamic light scattering (DLS) and zeta potential measurements were taken to determine the size and charge of the Tr5 polyplexes. In addition, these measurements were used to determine the N/P ratio at which aggregation occurs to verify the suspected region of aggregation observed with ITC. In an effort to remain consistent with the ITC experiments, initial DLS measurements were taken for polyplex solutions with increasing N/P ratios by titrating Tr5 into pDNA. Figure 4.4 shows the results for two consecutive trials of DLS measurements performed with this titration method. Overall, the data were very inconsistent and no definitive conclusions about trends can be drawn. Aggregation does seem to occur at higher N/P ratios, but the onset is very different between trials.

The inconsistencies observed in the preliminary data suggested that the mixing used in this titration method might not be adequate or uniform between the additions of Tr5. Stirring within the cuvette was not an option and the only means of mixing was by pumping the solution up and down with the pipette after each addition. Typically, the polyplexes that are used for *in*

vitro assays are prepared by premixing 50/50 volume formulations of polymer and pDNA with the appropriate concentrations to achieve a desired N/P ratio. The polyplex solutions are then incubated at a set temperature for a certain amount of time before being added to the cells.[3] We decided to try the same equal volume formulation approach to address the non-uniformity seen in the DLS titration experiments.

The first set of DLS data for equal volume formulated polyplexes is shown in Figure 4.5. In this experiment, only four different N/P ratios, along with a pDNA only control, were used to quickly determine the effectiveness of this mixing method. For each sample, equal volumes of pDNA and Tr5 solutions were mixed (for the pDNA only control, an equal volume of buffer was added to the pDNA solution) by inversion and then incubated at room temperature for 15 minutes before DLS measurement. Although this experiment was performed with a limited sample set, the results were encouraging. A consistent trend that makes sense is seen across the N/P ratios. At the lowest N/P ratio, a decrease in size is seen in comparison to the pDNA only (N/P = 0) sample. This is consistent with the concept of polycations compacting DNA upon complex formation.[10-11] The size of the polyplexes remains fairly consistent with increasing N/P ratios until N/P = 2.5, where a dramatic jump in size is observed. This 300% increase is attributed to aggregation of the polyplexes. This is similar to the suspected N/P ratio for the onset of aggregation in the ITC data, however more trials with an extended range of N/P ratios were needed for validation.

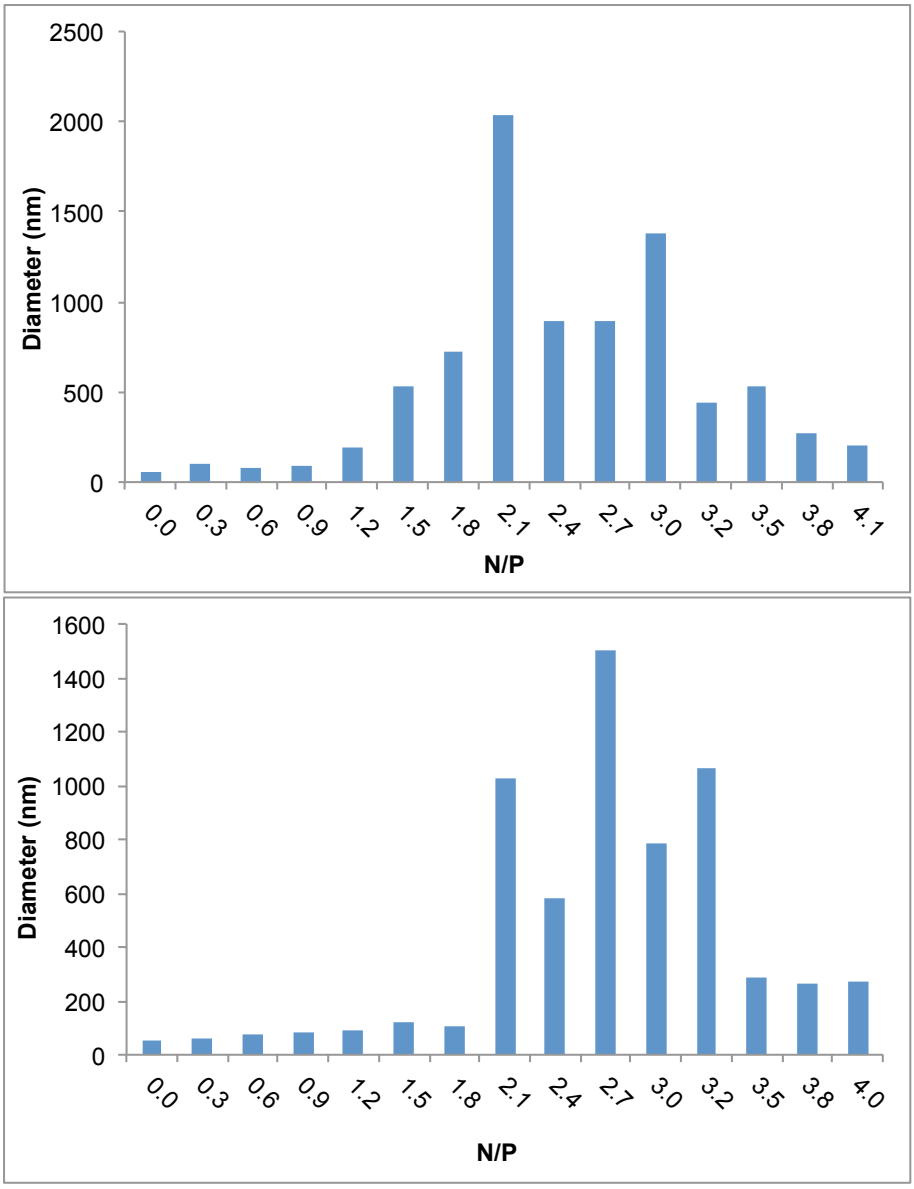

Figure 4.4 Two consecutive trials of DLS measurements as 5.5 mM Tr5 was titrated into 0.31 mM pDNA at 25 ºC

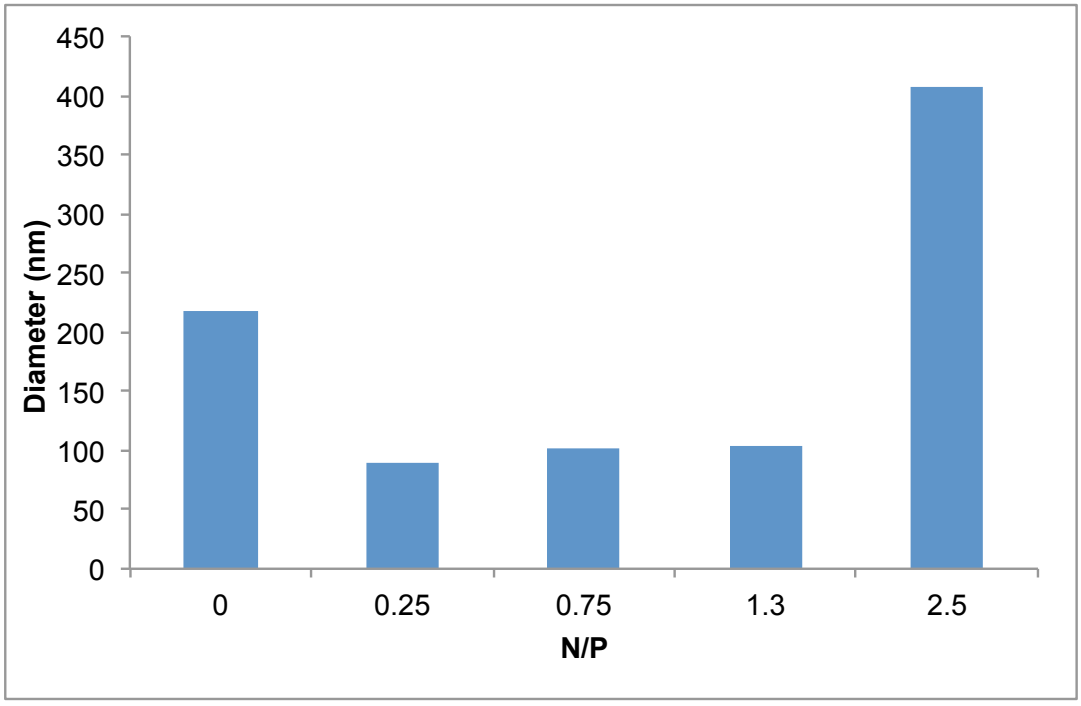

Figure 4.5 DLS measurements for Tr5 polyplexes prepared in 50/50 formulations

Figure 4.6 displays the results for duplicate trials of DLS and zeta potential measurements for the equal volume formulation of polyplexes at seven different N/P ratios and a pDNA only control. The pattern exhibited by these data is very similar to the one seen in Figure 4.5. Upon complexation and pDNA compaction we observe a decrease in the diameter from approximately 160 nm to 100 nm. The polyplex sizes remain fairly constant until an N/P ratio of 1.5, where it starts to slowly increase and then a dramatic jump to over 4,000 nm is seen at N/P = 2. However, at a N/P ratio of 2.5 the size drops back down to approximately 250 nm. The zeta potential measurements of the polyplex surface charges provide additional insight into the size variations. Within error, the zeta potential values are fairly consistent, and negative, until N/P = 2 where charge neutralization occurs. Upon neutralization of the negatively charged pDNA, the

polyplexes begin to aggregate due to van der Waals forces,[2] as seen by the drastic increase in polyplex diameter at this ratio. Furthermore, at an N/P ratio of 2.5, the zeta potential continues to increase due to the addition of more positively charged polymer.

Overall, there is good agreement between the sizes and surface charges of the polyplexes studied here and the other trehalose-based polycations. In fact, Tr4 also showed charge neutralization around N/P = 2, and a similar decrease in diameter after neutralization was seen for Tr1 and Tr2.[2] Furthermore, these results confirmed the onset of polyplex aggregation at an N/P ratio of 2, which had been suspected in the biphasic enthalpograms previously collected in ITC experiments. In addition, the 50/50 polyplex formulation results, as compared to the titration method, yielded much-improved reproducibility and confidence in the obtained data.

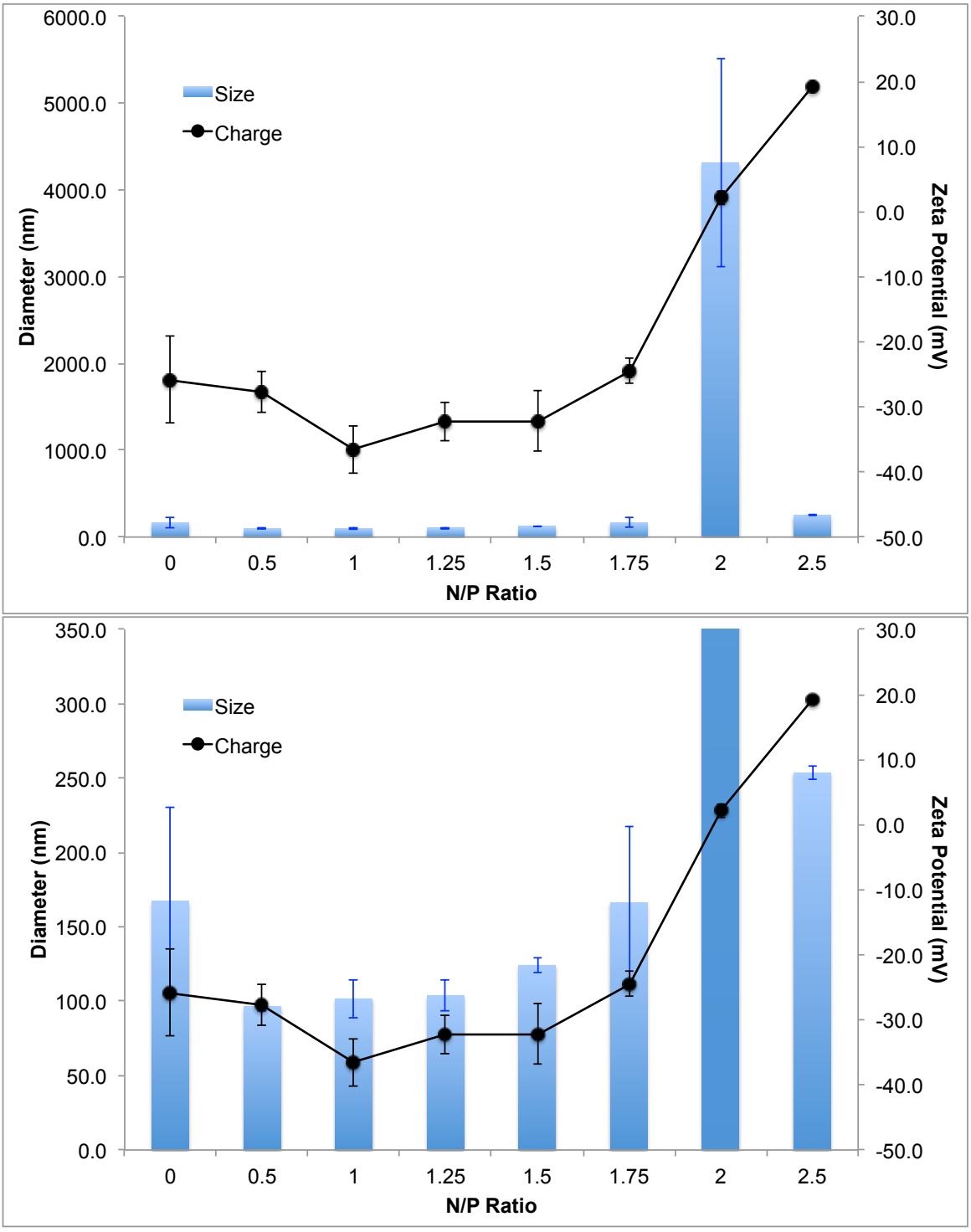

Figure 4.6 (top) DLS and zeta potential measurements for Tr5 polyplexes prepared in 50/50 formulations and (bottom) the same plot with an expanded y-axis to emphasize the results at lower N/P ratios

4.3.3 FTIR Spectroscopy

FTIR spectroscopy was utilized to explore the specific locations of binding between Tr5 and pDNA by monitoring shifts in characteristic pDNA band frequencies as well as any spectral intensity changes. Figure 4.7 shows the overlaid spectra at several N/P ratios from the titration of 27 mM Tr5 into 12 mM pDNA. Several of the characteristic vibrational frequencies for DNA are visible in the pDNA only spectrum (shown in black). The peak at 1715 cm^{-1} corresponds to the guanine carbonyl, while the broad peak centered around 1640 cm^{-1} is attributed to overlapping contributions from the thymine carbonyl and adenine C-N stretching bands. The peaks at 1222 and 1086 cm^{-1} are assigned to the asymmetric and symmetric phosphate stretches, respectively.[2, 12-15] Very few changes are noted in the spectra as Tr5 is added to the pDNA. There is an overall increase in intensity with increasing N/P ratios, which has previously been linked to changes in the DNA nucleobase pairing and stacking upon binding.[2, 12-18] In addition, a small peak starts to develop around 1150 cm^{-1}, which is attributed to the aliphatic C-N stretching in Tr5.[19]

Although some useful information was gleaned from the first FTIR experiment, there was some concern with the accuracy of the mixing process. After the addition of Tr5, especially at higher N/P ratios, there was a significant amount of visible aggregation within the sample solution on the ATR crystal. This made mixing the solution after aliquot additions exceedingly difficult, and was most likely not uniform throughout the mixture. Therefore, a second set of experiments was performed with equal volume formulations of polyplexes, similar to the DLS experiments. In addition, a Tr5 only control spectrum was also collected to look for overlapping peaks with the pDNA. These results are shown in Figure 4.8. In general, very comparable

results were obtained using the 50/50 volume formulations as compared to the titration method. However, the spectrum collected for Tr5 only is suspiciously similar to that of the polyplexes, creating a new concern for the efficiency of the cleaning method used in between samples.

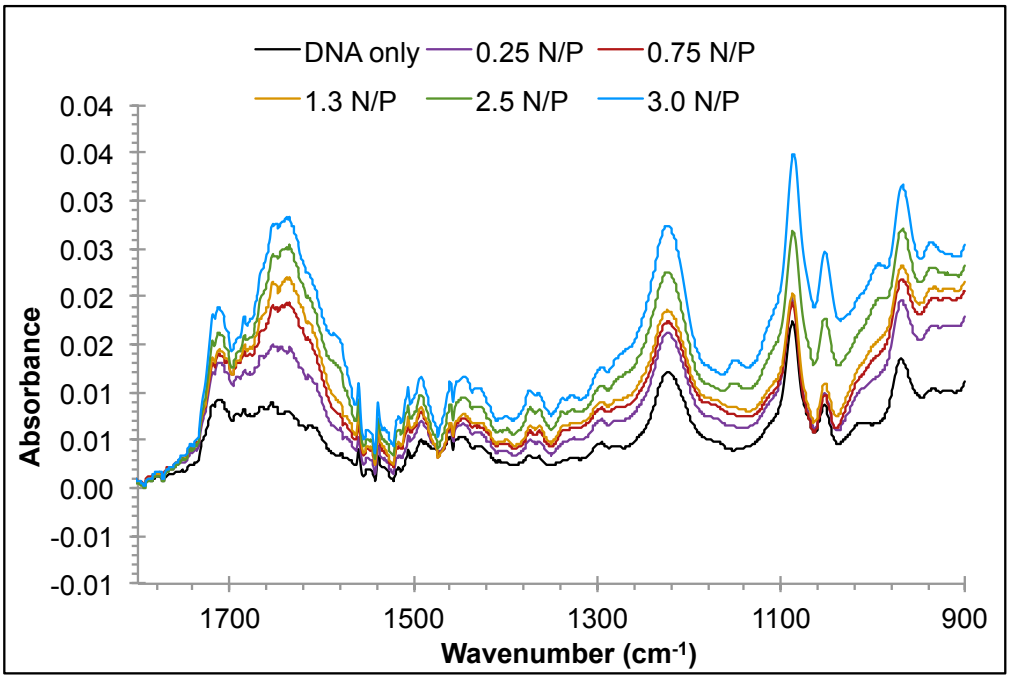

Figure 4.7 FTIR spectra for the titration of 27 mM Tr5 into 12 mM pDNA

Considering the cleaning concerns, and the large amounts of both polymer and pDNA that are consumed with equal volume formulations, a final trial repeating the titration method was performed to confirm the results from the first experiment. Efforts were made to carefully and thoroughly mix each addition of Tr5, regardless of the aggregation that occurred. Furthermore, this set of data was also collected over the full detectable wavenumber range (4000-900 cm^{-1}) of the instrument. The first two experiments only focused on the truncated range used to probe Tr1-Tr4.[2] Figure 4.9 shows the overlaid spectra from this experiment.

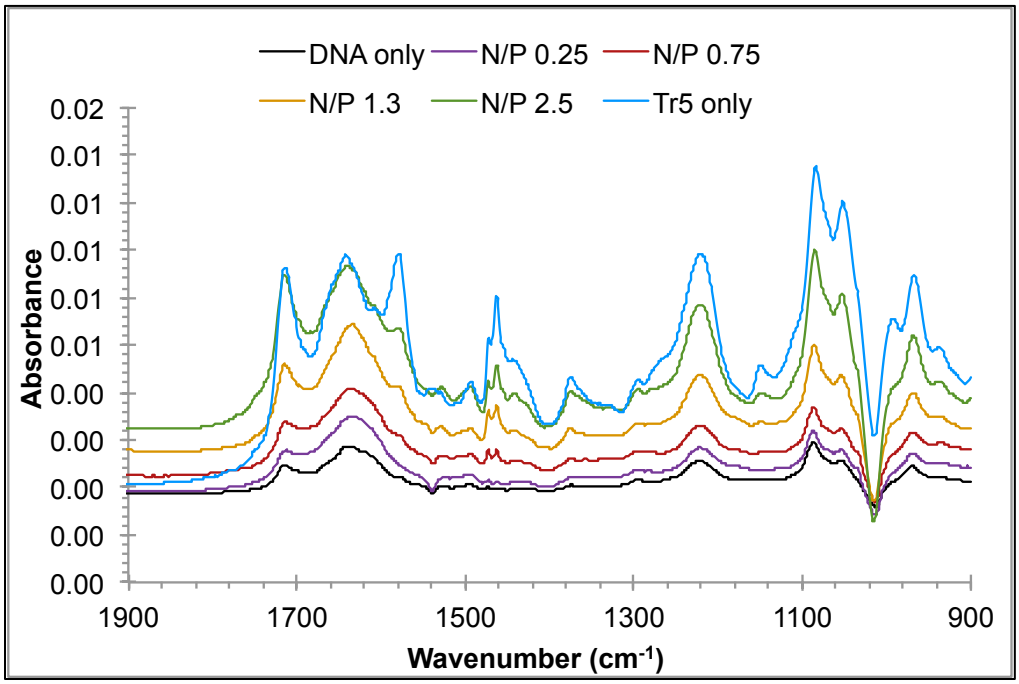

Figure 4.8 FTIR spectra for equal volume formulations (300 µL of 33.7 mM Tr5 and the 300 µL of pDNA at the appropriate concentration) of polyplexes

The graph in the top of Figure 4.9 displays the same truncated region that was probed in the first two experiments. Again, very few changes are noticed with increasing N/P ratios, other than the previously mentioned increasing intensity and developing peak at 1150 cm^{-1}. However, it is important to note that the Tr5 only spectrum, which was collected first after thoroughly cleaning the ATR crystal, shows only one overlapping peak with the pDNA at 1640 cm^{-1}. This peak is attributed to the carbonyl groups in Tr5 and unfortunately makes it difficult to track changes in the thymine carbonyl and adenine C-N stretches of the pDNA.

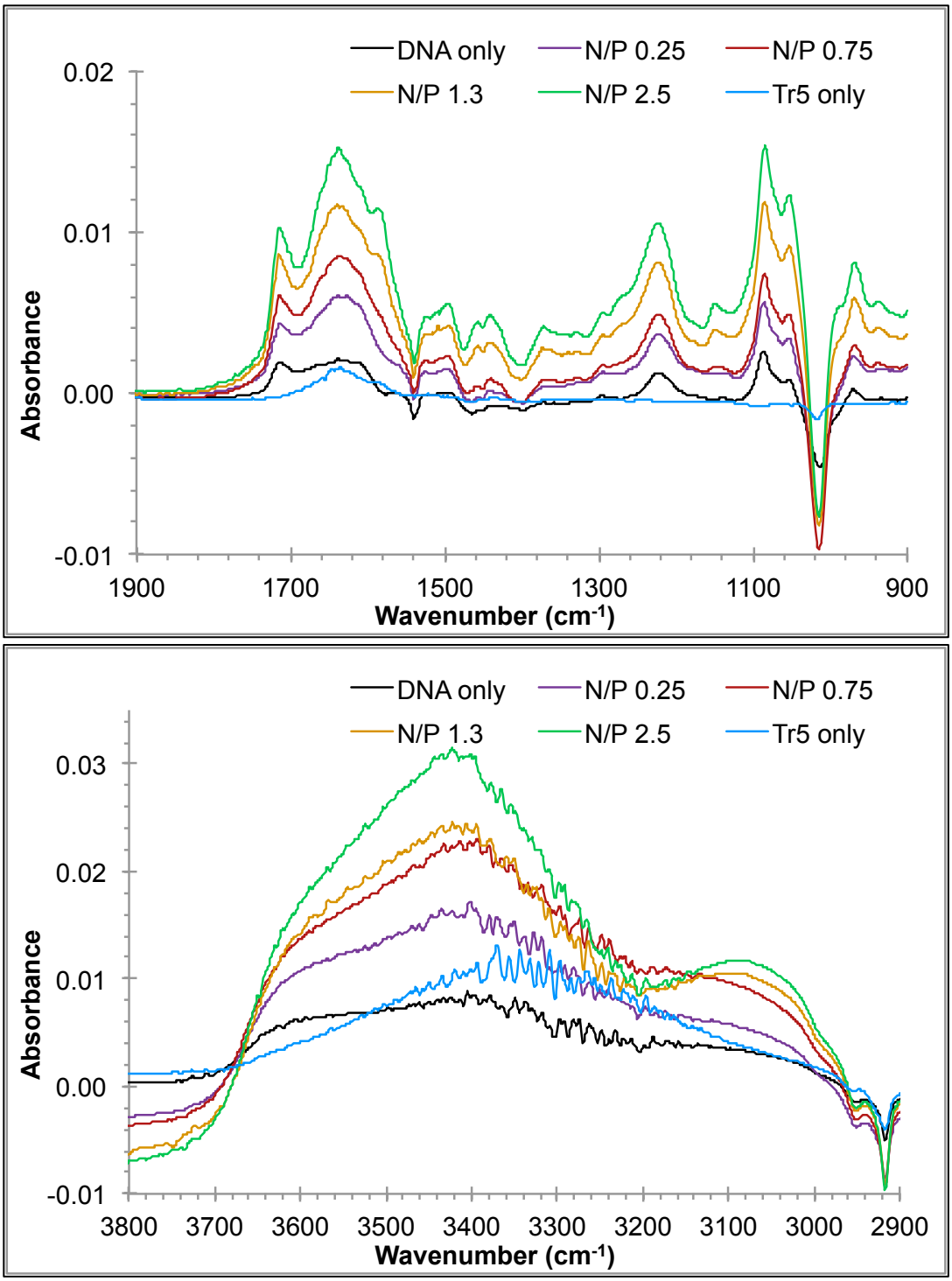

Figure 4.9 FTIR spectra for the titration of 44 mM Tr5 into 12 mM pDNA for the (top) 1900-900 cm^{-1} region and (bottom) 3800-2900 cm^{-1} region

The bottom graph in Figure 4.9 shows the higher wavenumber regions of the spectra that were not previously explored. Both the pDNA and the Tr5 show a very broad peak in this region. This is likely due to water that was not fully subtracted out with the buffer background, as well as possible contributions from hydroxyl O-H stretching and secondary amine N-H stretching in the case of Tr5.[20] As polyplexes are formed and the N/P ratios increase, there is a shift in the broad band from approximately 3350 to 3450 cm^{-1}, which is likely due to the increased secondary amine content as more Tr5 is added. There is also a distinct shoulder that develops at 3080 cm^{-1}, which may be attributed to intramolecular hydrogen-bonding hydroxyl groups or aromatic C-H stretching in Tr5.[20] However, due to the extreme overlap and complex nature of this broad peak, it is extremely challenging to make any conclusive inferences about these data.

In general, very few changes were observed in the spectra with increasing N/P ratios for any of the FTIR experiments conducted. Intensity increases were seen throughout all of the data, which may correlate to changes within the pDNA structure upon binding,[2, 12-18] but is more likely due to concentration effects as more and more sample is added to the ATR crystal. In addition, two small peaks develop at 1150 and 3080 cm^{-1} at higher N/P ratios, but these are also attributed to structural groups within Tr5 and the increase correlates with higher concentrations of polymer in the sample mixture. Although negligible shifting was seen in the characteristic stretching frequencies for pDNA, this is still in good agreement with the published results for Tr4. In that study, no conclusive spectral changes were observed with increasing N/P ratios other than at 1086 cm^{-1}. A very noticeable shift in this symmetric phosphate stretch was observed for Tr1, which also exhibited the highest degree of electrostatic interaction with pDNA out of all four

polymers tested. However, the extent of shifting decreased with increasing numbers of secondary amine. For Tr4 there was essentially no shift in the symmetric phosphate band, and this was attributed to its comparably lower electrostatic interactions with pDNA.[2] In view of the other similarities between Tr5 and Tr4 that have been observed with ITC and DLS, these FTIR results are not unexpected.

4.3.4 CD Spectroscopy

Circular dichroism (CD) was used to explore any changes in the pDNA secondary structure upon binding with Tr5 as shown in Figure 4.10. The spectra shown in this wavelength range correspond to the ellipticity of pDNA only, as trehalose polycations do not absorb in this region.[2] The positive and negative peaks observed in the pDNA only spectrum (dark green line) are consistent with the $\pi \rightarrow \pi^*$ transition of native B-form DNA.[2, 21-23] As the N/P ratio increases, there is a distinct red shift and decrease in intensity of the spectra. These results are very similar to those reported for Tr3 and Tr4. The noticeable spectral changes for the polymers with a greater quantity of secondary amines, as compared to the minimal changes seen with Tr1 and Tr2, were attributed to enhanced hydrogen bonding interactions between the pDNA base pairs and the polymer that altered the tilt of the helix and resulted in a modified B-form pDNA.[2, 24] Given the repeated similarities that have been observed for Tr4 and Tr5 throughout this investigation, it is also probable that hydrogen bonding plays a significant role in the Tr5-pDNA complexation process.

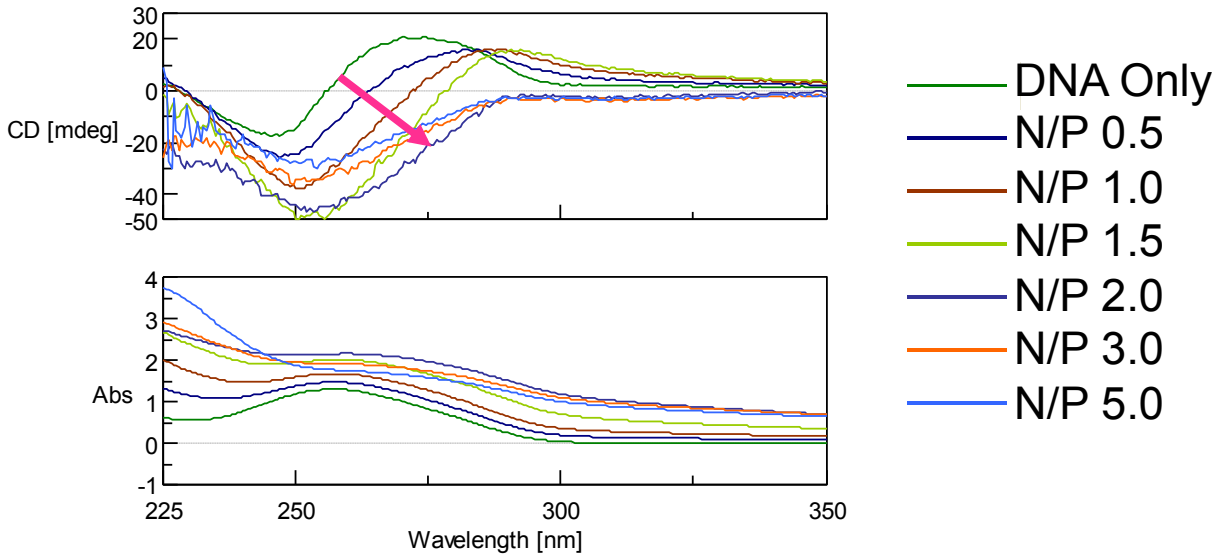

Figure 4.10 CD spectra for increasing N/P ratios of polyplexes formed from pDNA and Tr5

4.3.5 UV-Vis Thermal Melts

UV-Vis thermal curves are commonly collected for polyplex systems to investigate the stabilization afforded to DNA molecules upon binding with polycations.[25-26] As a tool that had not been applied to the trehalose-based polymer series prior to this investigation, this technique was attempted with the DNA-Tr5 polyplexes to investigate any possible DNA thermal stability enhancement. A preliminary experiment was conducted with plasmid DNA at a concentration that was comparable to that used in the ITC experiments, as shown in Figure 4.11. A melting temperature (T_m) of approximately 76 ºC was observed for all three samples, including the pDNA control. No thermal stability was seemingly gained from the addition of Tr5 to the pDNA; however, this initial experiment was carried out with only two very low N/P ratios, at which the pDNA may not have been fully complexed.

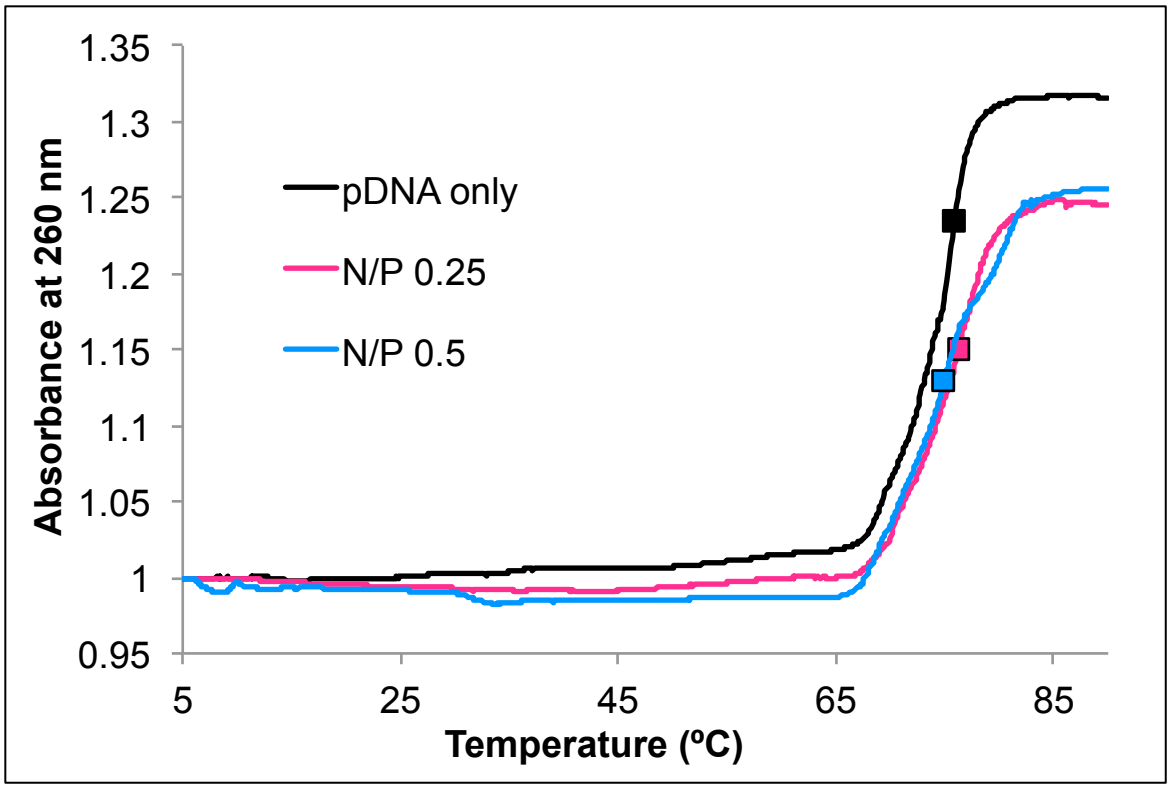

Figure 4.11 Overlaid thermal curves for increasing N/P ratios of pDNA (0.31 mM) and Tr5 polyplexes, ramped from 5-90 ºC at a ramping rate of 0.1 ºC/min

It was necessary to complete additional thermal curve experiments across a range of N/P ratios to determine if Tr5 provided any thermal stability to the DNA, however pDNA is fairly expensive and quite susceptible to degradation. In an effort to circumvent these issues while optimizing a new technique for the Tr5 polyplexes, decoy DNA was purchased as a more robust and cost-effective model system. The initial thermal curves collected for the decoy DNA were very irreproducible. Numerous trials were attempted in which decoy DNA would be exposed to repeated heat-cool-heat cycles, but the T_m values were never consistent between trials. This led us to believe that the decoy DNA had not been properly annealed when it was first received.

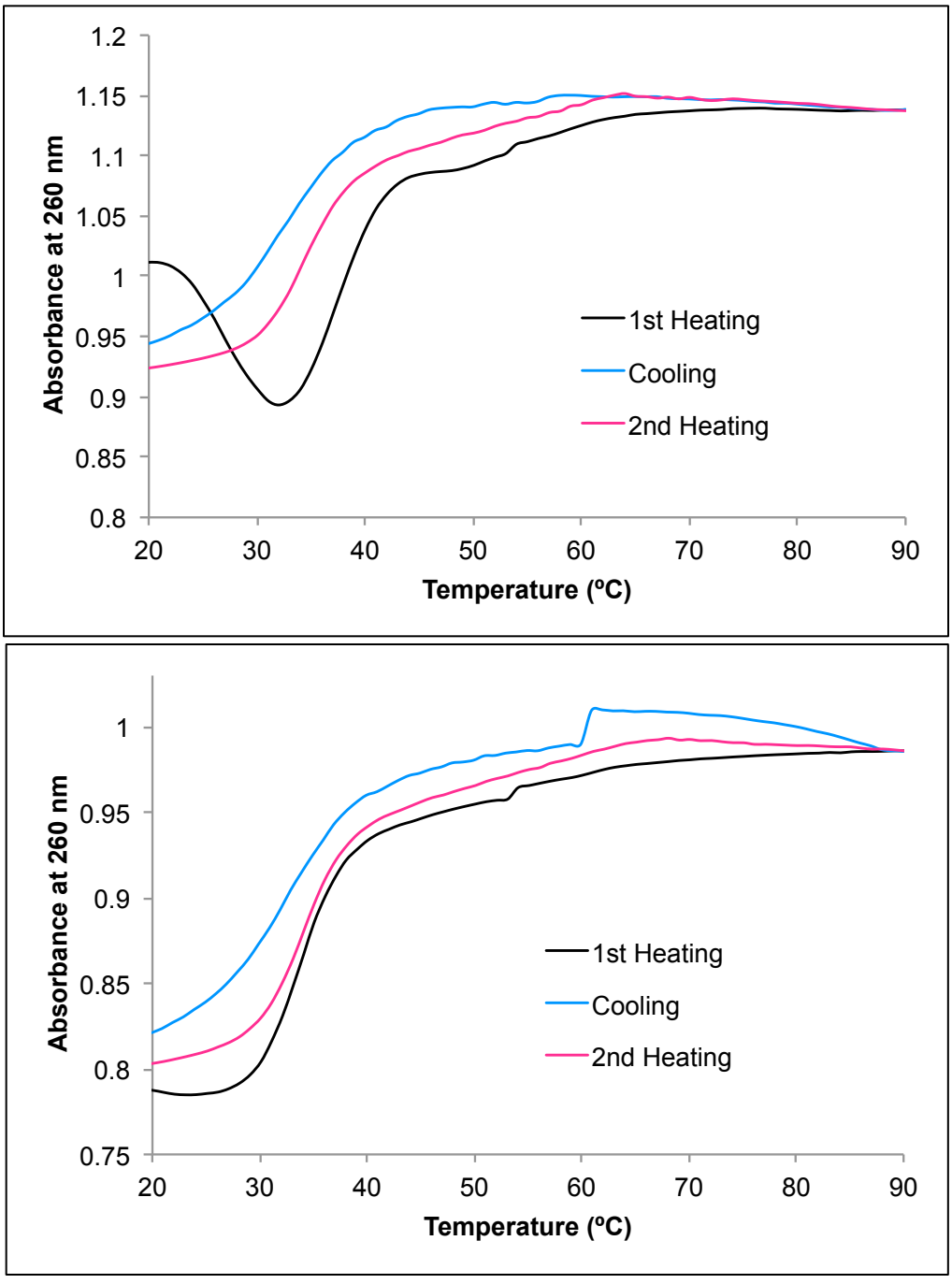

Figure 4.12 Overlaid UV-Vis thermal curves for a heat-cool-heat cycle (heating from 5-90 ºC at 0.5 ºC/min with a 3 minute hold, cooling from 90-5 ºC at 0.5 ºC/min with a 3 minute hold) for (top) the originally annealed sample of decoy DNA and (bottom) the same sample after being re-annealed

Originally, the decoy DNA was received as two solid samples, the sense and antisense strands. These had each been dissolved in buffer, mixed together, and then subjected to an annealing cycle (ramped from 5 to 90ºC at 1 ºC/min, held for 30 minutes, and then cooled back to 25 ºC at 0.1 ºC/min with a 12 hour hold time) in the UV-Vis. To ensure proper annealing of the two strands, a portion of the originally annealed sample was heated to 90 ºC in a water bath on a hot plate and held for 30 minutes. The hot plate was then turned off and allowed to cool at ambient conditions and the sample was left in the water bath to cool and anneal slowly, over the course of 24 hours. Afterward, samples from each of the originally annealed and re-annealed decoy DNA strands were analyzed simultaneously with a heat-cool-heat cycle in the UV-Vis. The results in Figure 4.12 clearly indicate a more reproducible melt curve for the decoy DNA after being re-annealed at a slower rate.

Due to the successful achievement of reproducible thermal curves after the re-annealing procedure, all future analyses on the UV-Vis were performed with this sample of decoy DNA. Furthermore, each aliquot of decoy DNA that was being prepared for a polyplex experiment was first put through one (or more, if necessary to obtain a smooth, reproducible thermal curve), thermal cycles before adding any polymer. This extra step in the procedure was added to ensure adequately annealed DNA for each individual UV-Vis experiment. This proved to be the best method for obtaining accurate and reproducible thermal curves for the decoy DNA as well as polyplex solutions. Figure 4.13 shows a representative example of this reproducibility for a solution of polyplexes at N/P = 0.5.

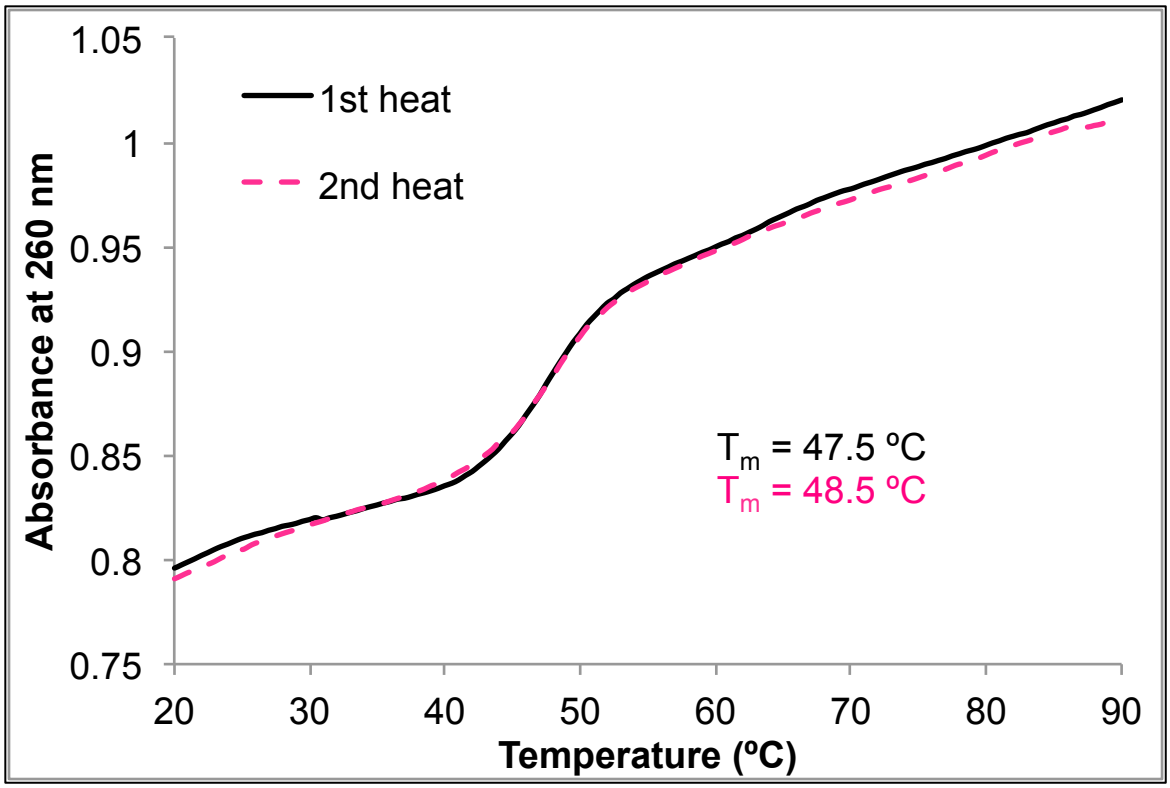

Figure 4.13 Overlaid UV-Vis thermal curves for two heating cycles (20-90 ºC at 0.5 ºC/min) of a N/P = 0.5 polyplex solution from decoy DNA and Tr5

After addressing all of the reproducibility issues with the decoy DNA, thermal curves were collected for decoy DNA-Tr5 polyplex solutions at increasing N/P ratios, as shown in Figure 4.14. All four curves in this figure are very similar and exhibit T_m values around 45 ºC, which did not suggest any added thermal stability from the presence of Tr5. However, these N/P ratios were on the low end of polyplex formation, considering the maximum N/P ratio measured here was 1.2 and the n_{bind} value determined from ITC was 1.36. Therefore, we decided to complete another set of experiments under the exact same conditions with higher N/P ratios.

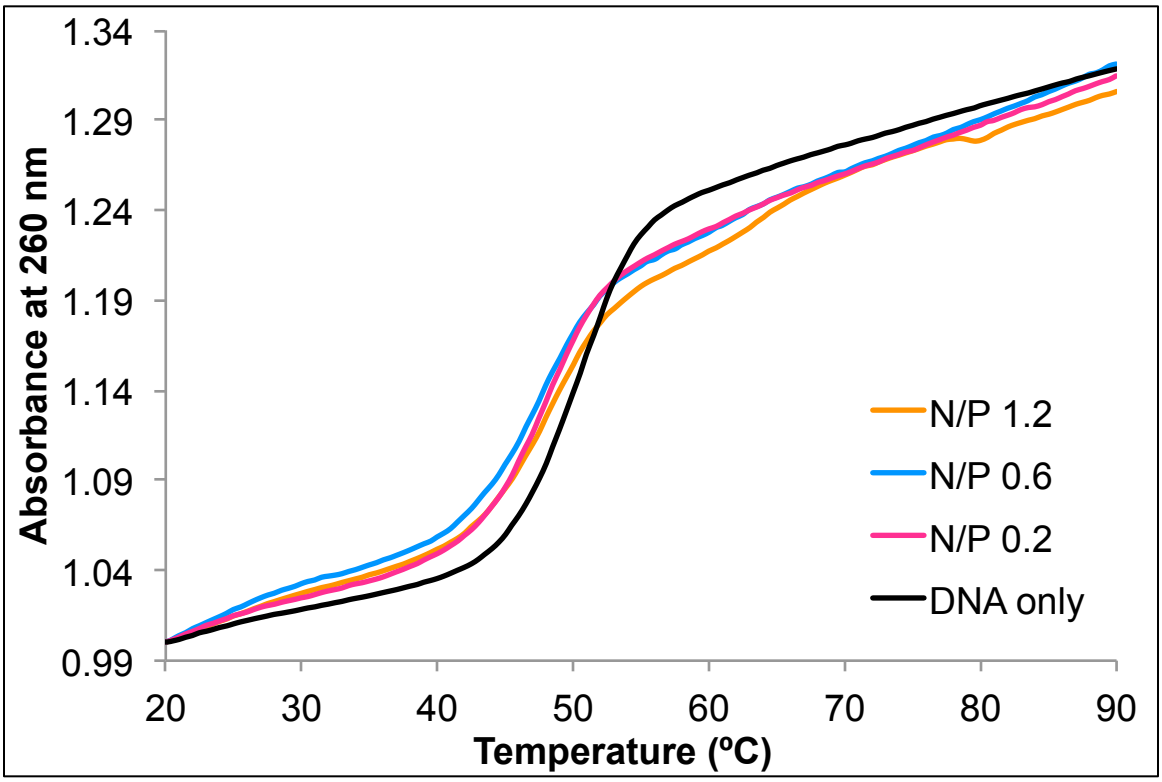

Figure 4.14 Overlaid thermal curves for increasing N/P ratios of decoy DNA and Tr5 polyplexes, ramped from 20-90 ºC at a ramping rate of 0.5 ºC/min

Figure 4.15 shows the thermal curves collected with the same experimental conditions at higher N/P ratios. Here we observed a noticeable shift in the T_m for the polyplex solutions compared to the decoy DNA only. On average, the decoy DNA complexed with Tr5 melts around 18 ºC higher than that of the naked DNA, and supports the hypothesis of greater thermal stability in the presence of polymer. However, other than the apparent threshold of reaching an N/P ratio that is high enough to provide any thermal stabilization, there is no appreciable difference in T_m values among the varying concentrations of Tr5. This suggests that the improved thermal stability is independent of polymer concentration above that initial threshold.

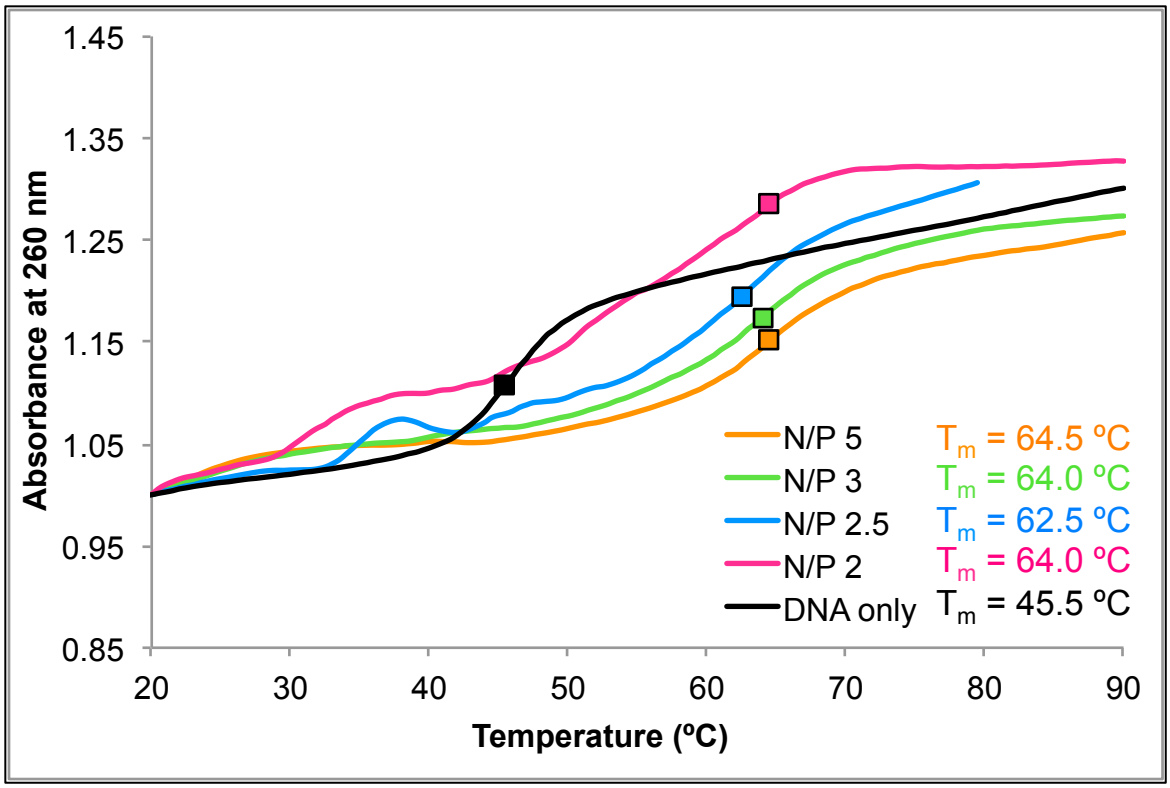

Figure 4.15 Overlaid thermal curves for greater N/P ratios of decoy DNA and Tr5 polyplexes, ramped from 20-90 ºC at a ramping rate of 0.5 ºC/min

Despite the exciting improvements in thermal stability that were noted for Figure 4.15, one additional experiment was performed to explore the effects of polyplex formulations on T_m. For all of the preceding thermal curve experiments, small amounts (typically less than 100 µL) of a concentrated Tr5 solution were added into a much larger volume of decoy DNA and mixed by pipette pumping and then inversion after the cuvette was capped. Concerns over inadequate mixing from this procedure, especially with the poor results seen in DLS measurements from similar solution preparation, led us to repeat the thermal curve experiments with equal volume formulations of polyplex solutions.

Figure 4.16 shows the thermal curves collected for several polyplex mixtures that were prepared with equal volumes of polymer and decoy DNA solutions. In this figure we still see increased thermal stability in the presence of Tr5. The major difference, however, is that now this enhancement is seen even at very low N/P ratios. In fact, we only went as high as N/P = 1.25 for this experiment, because the T_m had already leveled off to the same values seen in Figure 4.15. In addition, two transition temperatures are observed in these data. For the lowest N/P of 0.5, there is only a slight increase in T_m from the DNA only curve by 3.5 ºC. The solution at N/P 0.75 shows the same T_m at 47.5 ºC and also the higher melting temperature at 65.5 ºC. Both of the higher N/P ratios then exhibit only the high T_m around 63 ºC. This biphasic melting behavior seen for the solution at an N/P ratio of 0.75 may be a result of varying degrees of decoy DNA complexation, however more tests are needed to test this hypothesis. One additional observation is that although T_m is affected by the concentration of Tr5 in this experiment, it is not a gradual increase. There still appears to be threshold values of polymer concentration to achieve a certain melting temperature.

In conclusion, this technique was successfully utilized to assess the thermal stability of decoy DNA in the presence of Tr5. Overall, at sufficient concentrations of Tr5 thermal stability of the decoy DNA was improved. This was observed for both formulation procedures, although the threshold concentration values were quite different. These results made it very apparent that the way in which the polyplexes are prepared has a very large effect on the ability of Tr5 to thermally stabilize the DNA. Future experiments should explore additional N/P ratios to determine if additional transition temperatures are detectable, especially at much higher N/P ratios such as 5 to 20. In addition, the thermal stability of DNA is highly dependent upon the

environment, including pH, ionic activity, etc.[25] These experiments were conducted in a very controlled and buffered environment, but future experiments could be designed around conditions that are more analogous to that of the human body and comparable to their intended application.

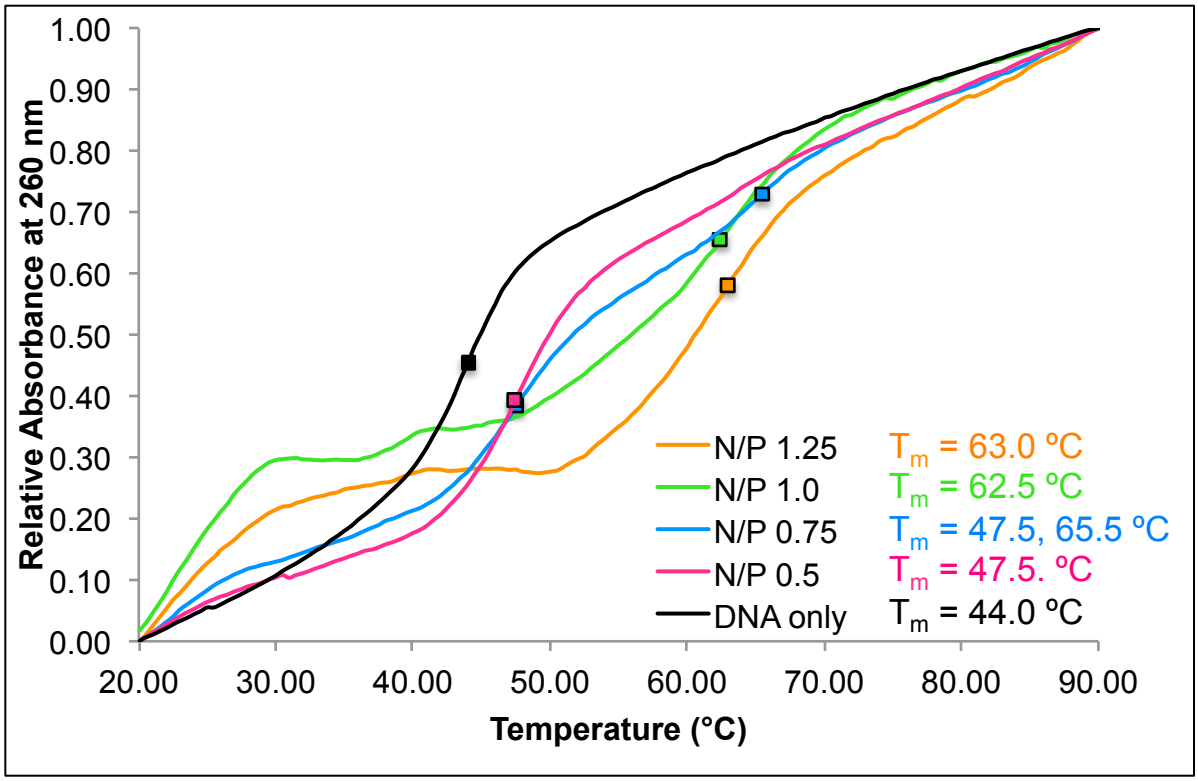

Figure 4.16 Overlaid thermal curves for increasing N/P ratios of decoy DNA and Tr5 polyplexes (made with equal volume formulations), ramped from 20-90 ºC at a ramping rate of 0.5 ºC/min

4.4 Conclusions & Future Work

In conclusion, Tr5 was investigated as the next in a series of previously published[2] trehalose-based polycations that bind with pDNA to form polyplex gene delivery vehicles. Thermodynamic binding parameters were determined with isothermal titration calorimetry and

showed the complexation between Tr5 and pDNA to be endothermic and entropically driven. DLS and zeta potential measurements revealed charge neutralization and polyplex aggregation at N/P = 2, which is consistent with the results seen in ITC. Furthermore, FTIR and CD spectroscopies were utilized to explore the changes experienced by DNA upon binding with Tr5. The FTIR results were not very conclusive due to problems with overlapping peaks and polyplex aggregation. However the results obtained here for Tr5 were very similar to those seen for Tr4, which was shown to have weaker electrostatic and stronger hydrogen bonding interactions with DNA than its counterparts that contained fewer secondary amine groups.[2] Supporting this assessment, the CD results obtained in this study suggested that hydrogen bonding interactions occur between Tr5 and the DNA base pairs upon complexation. In addition, a new technique was also applied to probe Tr5-DNA complexation. UV-Vis thermal melt curves were obtained for several polyplex formations, and in general showed improved thermal stability for decoy DNA that was complexed with Tr5.

There are several additional experiments that should be performed to expand our understanding of these polyplex systems. Future work with isothermal titration calorimetry should explore titrations that are comprised of more injections at smaller volumes to address the issue of polyplex aggregation in the sample cell. Lower concentrations of the polymer and pDNA solutions may also be required. Also, as expressed in Chapter 3, future work should address the need for a better model to fit the ITC data collected for polycation-DNA binding, as opposed to the independent binding sites model, which assumes 1:1 binding stoichiometry. Furthermore, it may also prove beneficial to repeat these experiments in different buffers of various pH to determine the effects of pH on polyplex formation. While the exact pKa of the

secondary amines in Tr5 were not measured here, previous literature reported Tr4 to exhibit approximately 12% of the secondary amines protonated at biological pH.[2] Performing additional titrations in buffers of lower pH could afford lower binding stoichiometries, due to higher charge densities, and other interesting heat effects in the polyplex formation process.

In addition, further improvements are required to optimize the FTIR experiments to ensure thorough sample mixing and accurate results. It may also prove beneficial to attempt these analyses with a liquid transmission cell to obtain bulk FTIR spectra instead of ATR experiments to obtain surface spectra. Further UV-Vis thermal studies are required for the exploration of different polyplex preparations, additional N/P ratios, and solution conditions that are comparable to physiological environments. Also, the studies presented here were done with decoy DNA as a less expensive, more robust model. After method optimization, repeated experiments with pDNA would provide a better comparison to the other analytical studies. Finally, there are several other trehalose-based polycations that could be explored in addition to the Tr5 sample. Kizjakina *et al*. have also published syntheses of analogous polymers with six secondary amine groups per repeat unit, Tr6, as well as Tr4 analogs with PEG end group functionalities.[1]

4.5 References

1. Kizjakina, K.; Bryson, J. M.; Grandinetti, G.; Reineke, T. M. *Biomaterials* **2012,** *33* (6), 1851-1862.
2. Prevette, L. E.; Lynch, M. L.; Kizjakina, K.; Reineke, T. M. *Langmuir* **2008,** *24*, 8090-8101.
3. Srinivasachari, S.; Liu, Y.; Prevette, L. E.; Reineke, T. M. *Biomaterials* **2007,** *28*, 2885-2898.
4. Srinivasachari, S. L., Y.; Zhang, G.; Prevette, L.; Reineke, T. *Journal of the American Chemical Society* **2006,** *128*, 8176-8184.
5. Engelsen, S. P., S. *Journal of Physical Chemistry B* **2000,** *104*, 9301-9311.
6. Prevette, L. E.; Kodger, T. E.; Reineke, T. M.; Lynch, M. L. *Langmuir* **2007,** *23*, 9773-9784.
7. Alex, S.; Dupuis, P. *Inorganica Chimica Acta* **1989,** *157* (2), 271-281.
8. Patel, M. A., T. *Biophysical Journal* **2005,** *88*, 2089-2103.
9. Ross, P. D.; Shapiro, J. T. *Biopolymers* **1974,** *13* (2), 415-416.
10. Leong, K. *MRS Bulletin* **2005,** *30*, 640-646.
11. Reineke, T. M.; Grinstaff, M. W. *MRS Bulletin* **2005,** *30*, 635-639.
12. Taillandier, E.; Taboury, J. A.; Adam, S.; Liquier, J. *Biochemistry* **1984,** *23* (24), 5703-5706.
13. Taillandier, E.; Liquier, J.; Taboury, J. A. *Advances in Infrared and Raman Spectroscopy*. Heyden & Sons, Inc.: London, 1985; Vol. 12.

14. Taillandier, E.; Liquier, J. *Spectroscopic Methods for Analysis of DNA*. Academic Press, Inc.: New York, 1992; Vol. 211.

15. Arakawa, H. A., R.; Naoui, M.; Tajmir-Riahi, H. *The Journal of Biological Chemistry* **2000,** *275* (14), 10150-10153.

16. Benevides, J. M.; Stow, P. L.; Ilag, L. L.; Incardona, N. L.; Thomas, G. J. *Biochemistry* **1991,** *30* (20), 4855-4863.

17. Ruiz-Chica, J.; Medina, M. A.; Sánchez-Jiménez, F.; Ramıírez, F. J. *Biochemical and Biophysical Research Communications* **2001,** *285* (2), 437-446.

18. Ouameur, A. A.; Tajmir-Riahi, H.-A. *Journal of Biological Chemistry* **2004,** *279* (40), 42041-42054.

19. Stewart, J. E. *The Journal of Chemical Physics* **1959,** *30* (5), 1259-1265.

20. Lin-Vien, D.; Colthup, N. B.; Fateley, W. G.; Grasselli, J. G. *The Handbook of Infrared and Raman Characteristic Frequencies of Organic Molecules*. Elsevier Science: 1991.

21. Bloomfield, V. A.; Crothers, D. M.; Tinoco, I. *Physical Chemistry of Nucleic Acids*. Harper & Row Publishers, Inc.: New York, 1974.

22. Gray, D. M.; Ratliff, R. L.; Vaughan, M. R. *Spectroscopic Methods for Analysis of DNA*. Academic Press, Inc.: New York, 1992; Vol. 211.

23. Rodger, A.; Norden, B. *Circular Dichroism and Linear Dichroism*. Oxford University Press: Oxford, 1997.

24. Tunis-Schneider, M. J. B. a. M., M. F. *Journal of Molecular Biology* **1970,** *52*, 521-541.

25. Schindler, T.; Nordmeier, E. *Polymer* **1999,** *40*, 7019-7027.

26. Nisha, C. K.; Manorama, S. V.; Ganguli, M.; Maiti, S.; Kizhakkedathu, J. N. *Langmuir* **2004,** *20* (6), 2386-2396.

Chapter 5 : Hydrogen Bonding in Polyurethane – Carbon Nanotube Composites

5.1 Introduction

The extraordinary mechanical, electrical, and thermal properties of carbon nanotubes (CNTs) have generated a great deal of interest for potential use in polymer-matrix composites.[1-3] However, because of the nonpolar graphene surfaces found on CNTs in their natural state, aggregation commonly occurs due to hydrophobic interactions. Aggregation causes a less effective composite because of reduced interactions between the CNTs and the actual polymer.[4-6] This is particularly concerning in polyurethane systems, such as the one used in this investigation, because of the polar nature of the polymer matrix.[7-8] To reduce these aggregation effects, one method to increase dispersion of the CNTs in the polymer matrix is to functionalize the CNT surface with polar moieties.[9-10] In addition, multi-walled carbon nanotubes (MWCNTs) serve as excellent candidates, maintaining their outstanding mechanical properties, even after extensive functionalization, because their inner walls are not affected.[11] Having a better understanding of the intermolecular interactions taking place within these composites, for example hydrogen-bonding, is essential for optimizing the CNT-polymer interactions and, as a result, the overall composite properties.

One extremely useful analytical technique for investigating the hydrogen-bonding behavior of polymers is FTIR spectroscopy. Numerous studies have been conducted using FTIR to explore hydrogen bonding in polymers, like polyamides and polyurethanes.[12-17] There is widespread hydrogen bonding present in most polyurethanes and it is the driving force behind microphase separation in polyurethane samples.[13, 18] The presence of hydrogen bonding within a

sample can be observed by monitoring the frequency shifts of the hydrogen bond donators and acceptors, the amine and carbonyl stretches, respectively. Frequency shifts to lower wavenumbers can indicate the presence of hydrogen bonding within a sample.[14] In addition, the carbonyl-stretching region of the infrared absorbance is highly influenced by ordering within the sample. Typically three discernable peaks are present in this region: carbonyls that are not hydrogen-bonded, or "free"; disordered hydrogen-bonding carbonyls; and ordered hydrogen-bonding carbonyls. Disordered hydrogen bonding refers to hydrogen bonds that occur between hard segment urethane carbonyls found in the amorphous region, while ordered hydrogen bonds occur in the highly ordered regions of the hard segment domain that are potentially crystalline. The distinction between these two is attributed to dipole-dipole coupling of the carbonyls.[17] Variable temperature FTIR offers the additional advantage of observing the temperature-dependent behavior of hydrogen bonds by monitoring their dissociation at elevated temperatures. As hydrogen bonds are broken with increasing temperatures, the carbonyl peaks shift toward higher frequencies as the free carbonyl population increases.[13] Previous studies have shown that hydrogen bond dissociation is not dependent on the extent of ordering within the polyurethane sample, but rather, rapidly increases at temperatures above the hard segment T_g. This phenomenon was attributed to disruption of hydrogen bonds as the polymer chain mobility increased.[18]

The potential for changes in the hydrogen-bonding behavior of polyurethanes is always present when nanofillers are incorporated to form nanocomposites. The extent of these effects is greatly dependent upon the type of nanofiller – nanoparticles, nanoclays, CNTs, etc. – and any surface functionality that may be present. While interactions between the polymer and nanofiller

may be improved with surface functionalities, the polymer-polymer interactions may also be affected. Looking at the big picture, these hydrogen-bonding effects will play a key role in the proccessability and tunability of the end composite properties.[19] While a small number of studies[20-25] have been published regarding the effects of nanofillers in polyurethane composites on their hydrogen-bonding properties, no other investigations have thoroughly studied the temperature-dependent effects of hydrogen bonding in polyurethane-CNT composites.[19]

In this investigation, we examine the temperature-dependent effects of surface functionalization and weight percent loading of MWCNTs on hydrogen bonding in MWCNT-polyurethane composites. Composites containing purified, acid-oxidized, amide-amine functionalized, and amide-urea functionalized MWCNTs at loadings from 0.18 to 10 wt. % were characterized with variable temperature FTIR. Peak fitting was used to further analyze the data and quantify the extent of hydrogen bonding throughout the samples. It was hypothesized that the combination of MWCNT surface functionalities with increased hydrogen-bonding capacities at higher loadings would increase the hydrogen bonding content within the polyurethane hard segment by enabling more efficient dispersion of MWCNTs throughout the polyurethane matrix and enhancing polymer-MWCNT interactions. Furthermore, the added rigidity from the incorporation of MWCNTs was expected to reduce the overall polymer chain mobility and raise the required hydrogen bond dissociation temperature.

5.2 Experimental

5.2.1 Materials

A segmented polyurethane and MWCNTs with various functionalizations, as shown in Figure 5.1, were used to prepare polymer-matrix composites at varying weight percent loadings of MWCNTs as previously reported.[19] In summary, the polyurethane was prepared from dicyclohexylmethane-4,4'-diisocyante, poly(tetramethylene oxide) (~2,000 g/mol) as the soft segment, and butanediol as the chain extender. The resulting segmented polyurethane was 45 wt.% hard segment and had a M_w of 50,200 g/mol. Four different types of MWCNTs were used in the composites. MWCNTs with no functionalization were washed in hydrochloric acid and used as a control group that had minimal hydrogen bonding capacity. Three other functionalized MWCNTs were prepared using the acid oxidation route:[26-28] acid oxidized MWCNTs (AO-MWCNTs), amide-amine functionalized MWCNTs (AA-MWCNTs), and amide-urea functionalized MWCNTs (AU-MWCNTs). Composites were formed from the polyurethane and each of the four different kinds of MWCNT in a range of 0.18 to 10 wt.% loadings.

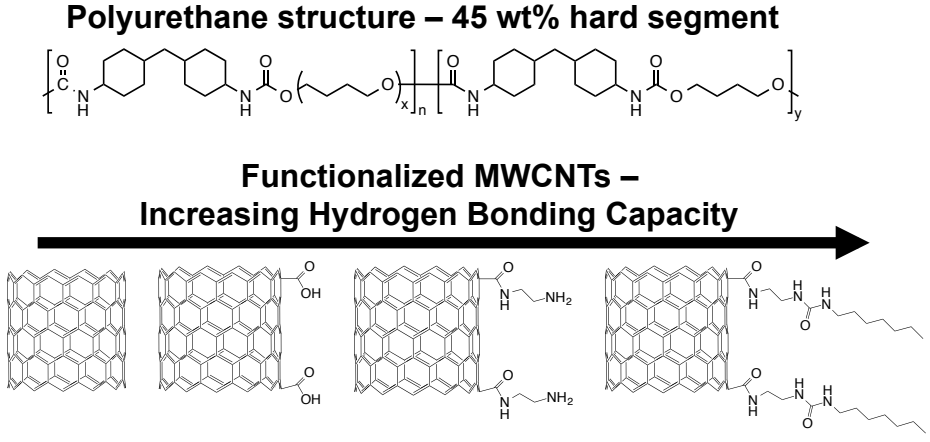

Figure 5.1 Chemical structures of the polyurethane and varying MWCNTs used to form the composites; adapted from Reference 19.

5.2.2 Variable Temperature FTIR-ATR Analysis

Experiments were performed with a Varian 670-IR, using a PIKE GladiATR™ heated diamond stage. Spectra were collected from 4000 to 400 cm^{-1} at a resolution of 4 cm^{-1}, and each spectrum was an average of 32 scans. Samples were heated at a rate of 1 ºC/min from 35 to 185 ºC, and spectra were collected every 10 ºC. Prior to collection for each sample, a background of the laboratory air was collected at room temperature; this background is automatically subtracted from each spectrum collected afterward. The air background over the full range from room temperature to 185 ºC was also studied and shown to be effectively invariant. This is shown in Figure 5.2. Due to this invariance and the applied temperature ramping process applied to the samples, a single background of air at room temperature was subtracted from each experimental spectrum.

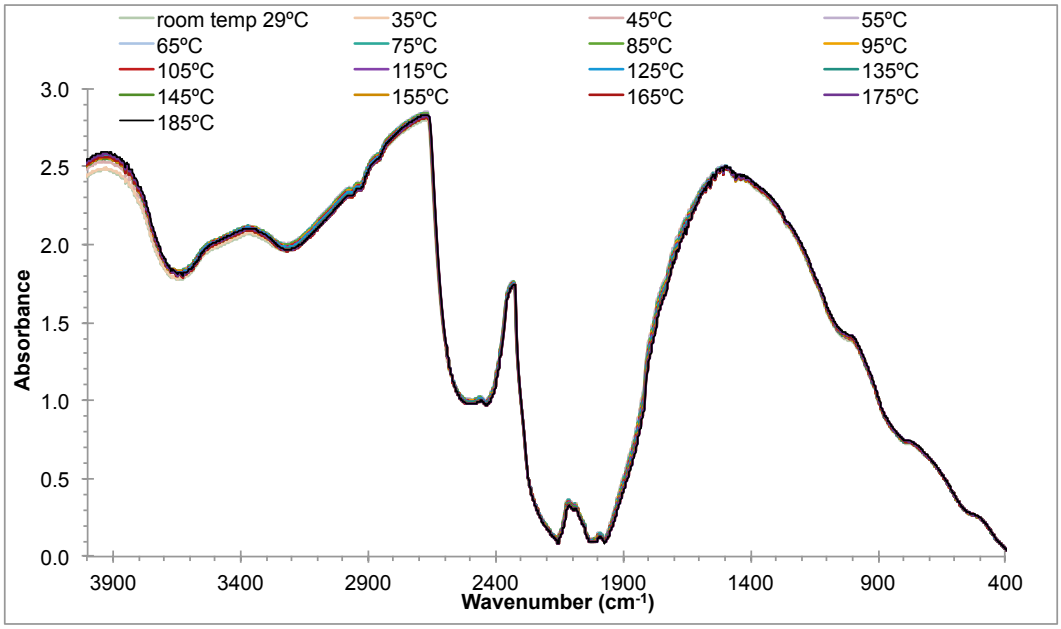

Figure 5.2 Variable temperature spectra of the air background

5.2.3 Peak Fitting Procedure

Peak fitting was used to quantitatively compare the three peaks seen in the carbonyl-stretching region of the data, corresponding to two different states of hydrogen bonding bands and one "free," or nonbonding, carbonyl band, as previously seen in literature.[17] ATR correction was performed for each spectrum before adjusting with linear baseline correction. The baseline correction points were selected at regions in the spectra that correspond to minima where no visible absorptions were detected, with specific emphasis on either side of the carbonyl-stretching region near 1780 and 1565 cm^{-1}. The specific wavenumbers corresponding to the minima adjacent to either side of the carbonyl band were noted and also used as the upper and lower limits for peak fitting.

The three carbonyl bands present were all Gaussian in shape, and were each fit with a Gaussian peak using nonlinear least squares fitting in Microsoft® Excel. Fitting iterations were repeated until the residuals were within ± 0.005. Preliminary estimates were made for the amplitude, width, and frequency (ν) of each peak, and then the software was used to perform fitting iterations until constant values for the three parameters were reached. Afterward, Wolfram Mathematica® was utilized to calculate the area under each peak using the fit values of the three parameters. Since the coefficient for absorption is characteristically larger in hydrogen bonding carbonyl bands than that of the free carbonyl, a correction factor (k = 1.71) was used to normalize the total carbonyl region with respect to changing temperature, in accordance with the literature.[17, 29] In an effort to simplify the comparison of hydrogen bonding across different temperatures, weight percent loadings of CNTs, different functional groups, etc., the areas of the

two peaks corresponding to different hydrogen bonding forms were combined. Therefore, the relative areas of total hydrogen bonding and free carbonyl peaks were compared for each sample.

5.3 Results & Discussion

5.3.1 Spectroscopic Results for Variable Temperature FTIR-ATR

The variable temperature FTIR spectra collected for the neat polyurethane samples are shown in Figure 5.3. Several characteristic IR peaks common to polyurethanes can be identified in these spectra. The large peak, and the focus of this study, at 1710 cm^{-1} is due to C=O stretching,[30-31] with the shoulder around 1685 cm^{-1} corresponding to carbonyl groups involved in hydrogen bonding.[17] The peak at 3315 cm^{-1} corresponds to the N-H stretching region. The peaks present at 2918 and 2848 cm^{-1} are due to the alkane C-H stretch. The 1521 and 1220 cm^{-1} peaks are due to the CHN vibration of secondary urethane groups and the coupled C-N and C-O stretching region, respectively. The large peak at 1095 cm^{-1} is due to the C-O-C symmetric stretch.[30-31] As the temperature increases, the large "peaks" that grow in throughout the 2200-1900 cm^{-1} region are actually noise, associated with the diamond on the heated stage. This is due to the fact that we are limited, by the instrumentation, to subtracting an initial background at the lowest temperature from all of the subsequent spectra, regardless of temperature effects that may also be occurring with the diamond. Fortunately, these noise peaks did not interfere with the region of interest for this investigation.

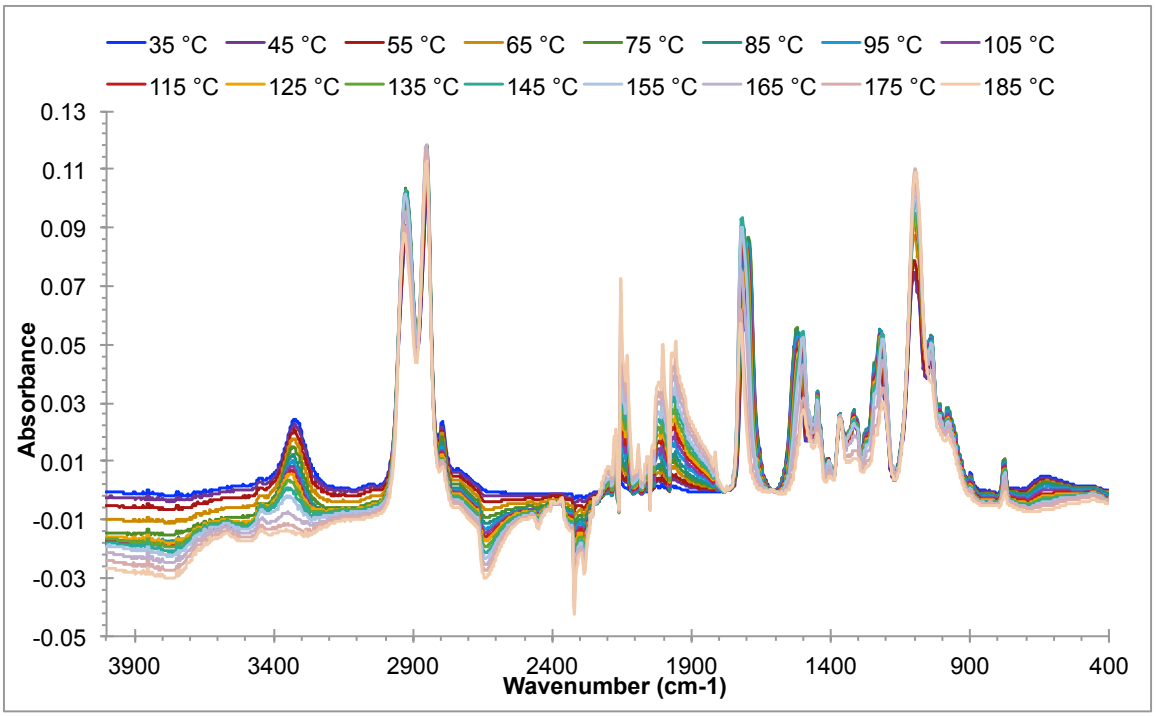

Figure 5.3 Variable temperature FTIR-ATR spectra for the neat polyurethane sample.

Figure 5.4 shows the same spectra for the neat polyurethane, but specifically focused in on the carbonyl-stretching region. As stated previously, there appear to be at least two peaks in this region, and upon closer inspection, there is a clear shift in peak ratios as the temperature increases. Initially at 35 ºC, the principal contribution to the spectrum is a peak centered around 1685 cm^{-1}, with a second, smaller peak centered around 1710 cm^{-1}. As the temperature increases up to 185 ºC, the 1685 cm^{-1} peak gradually diminishes, while the 1710 cm^{-1} component becomes the prominent peak and shifts slightly higher to 1725 cm^{-1}. This peak shifting behavior is due to hydrogen bond dissociation. When a carbonyl oxygen is hydrogen-bonded to the hydrogen of a neighboring amine, the vibrational frequency of the carbonyl bond is restricted. This results in the carbonyl absorbing infrared radiation at lower frequencies than identical carbonyl structures

that are not hydrogen-bonded, or "free". The type and strength of the hydrogen bond will also play a role in defining the lower frequency at which the carbonyl absorbs.[17, 29, 32] In a polymer system such as this polyurethane, as the sample is heated, the chain mobility increases and disrupts the hydrogen bonds, generating larger populations of free carbonyls and a shift in absorbance to higher wavenumbers.[19] Similar peak shifting behavior with increasing temperature can be seen in Figures 5.5 through 5.8 for all of the composite samples, as well. However, there are noticeable differences for different weight percent loadings of the CNTs, as well as differences between functional groups.

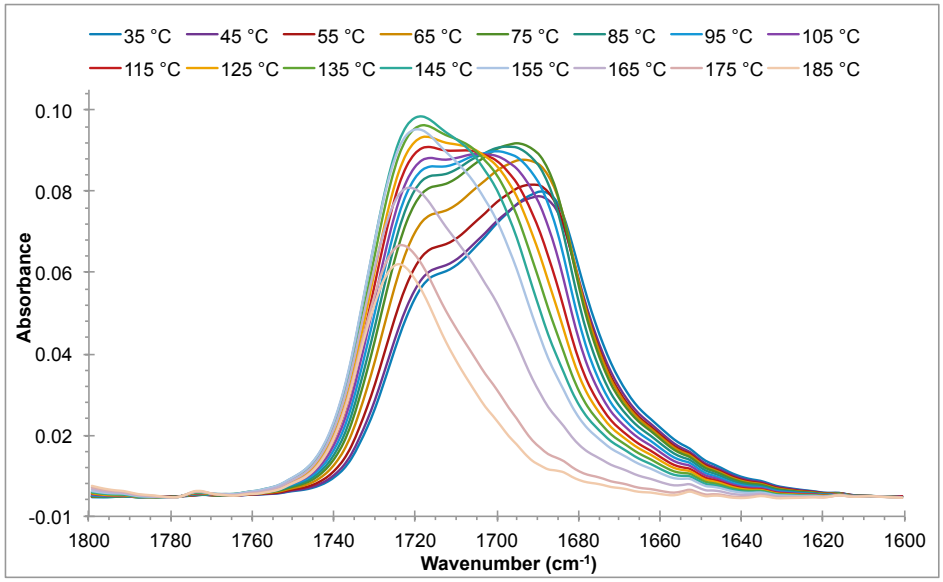

Figure 5.4 Variable temperature FTIR-ATR spectra of the carbonyl-stretching region for the neat polyurethane sample.

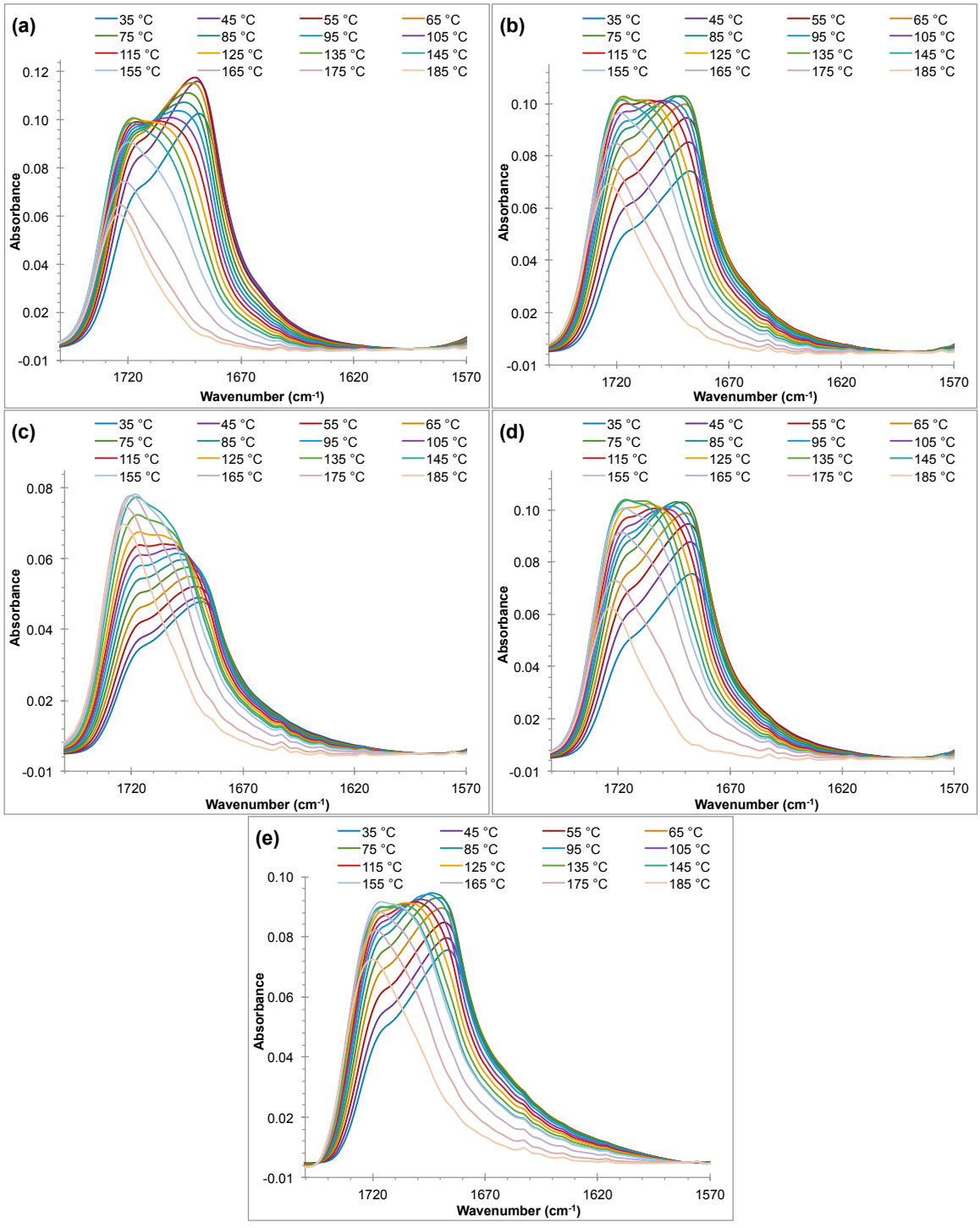

Figure 5.5 Variable temperature FTIR-ATR spectra of the carbonyl-stretching region for the composites with: (a) 0.18, (b) 1.8, (c) 2.4, (d) 5, and (e) 10 wt. % loading of the purified MWCNTs.

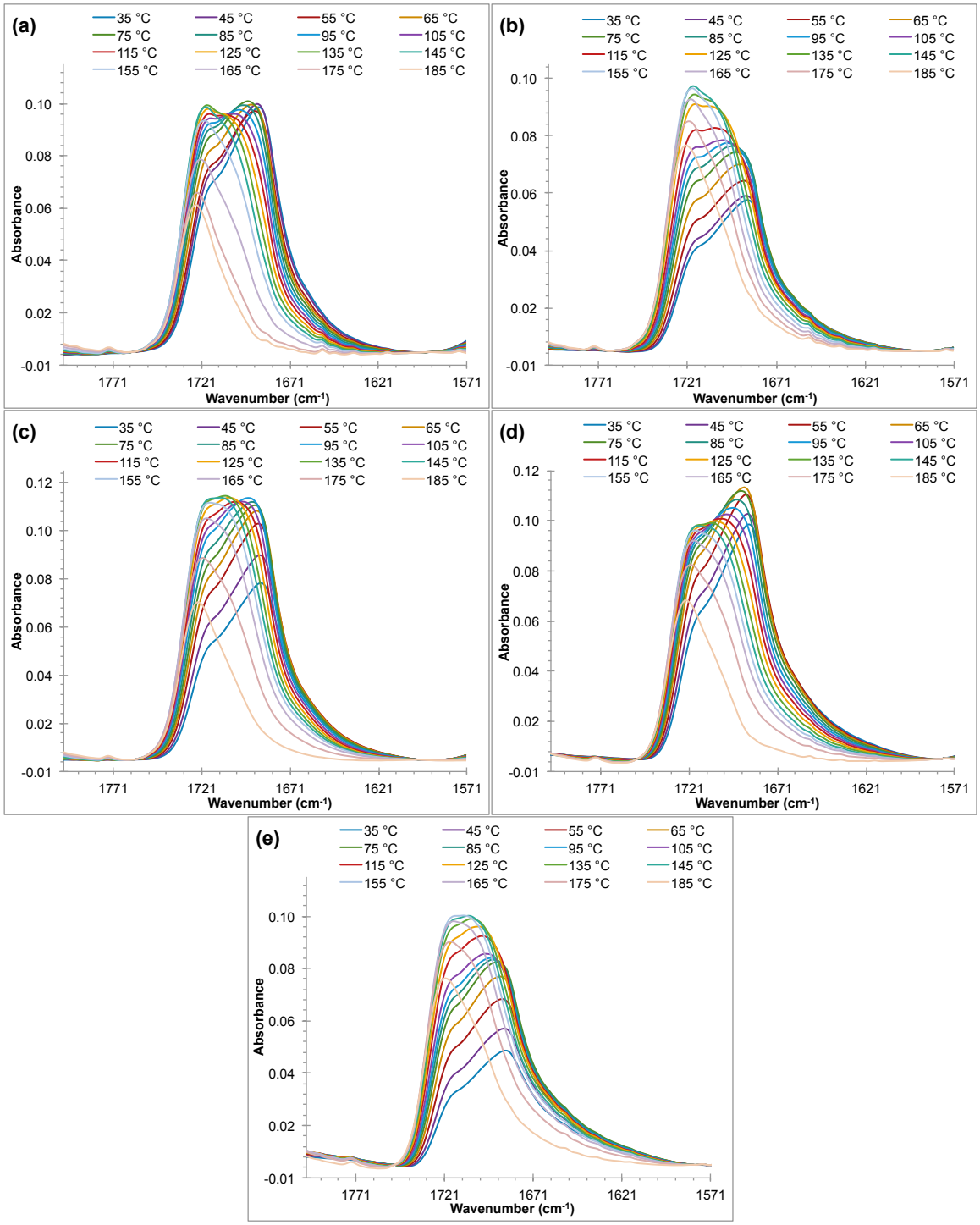

Figure 5.6 Variable temperature FTIR-ATR spectra of the carbonyl-stretching region for the composites with: (a) 0.18, (b) 1.8, (c) 2.4, (d) 5, and (e) 10 wt. % loading of the AO-MWCNTs.

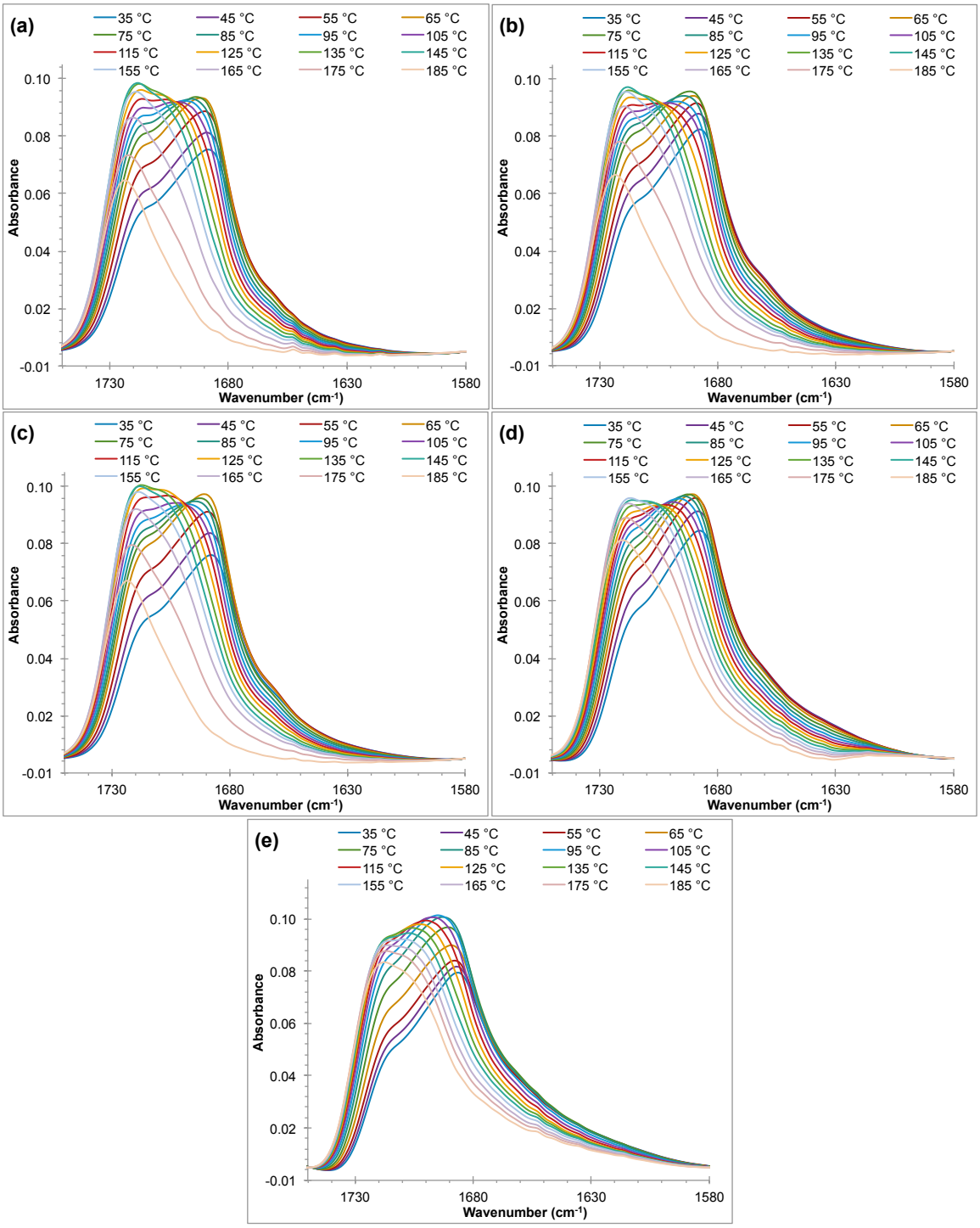

Figure 5.7 Variable temperature FTIR-ATR spectra of the carbonyl-stretching region for the composites with: (a) 0.18, (b) 1.8, (c) 2.4, (d) 5, and (e) 10 wt. % loading of the AA-MWCNTs.

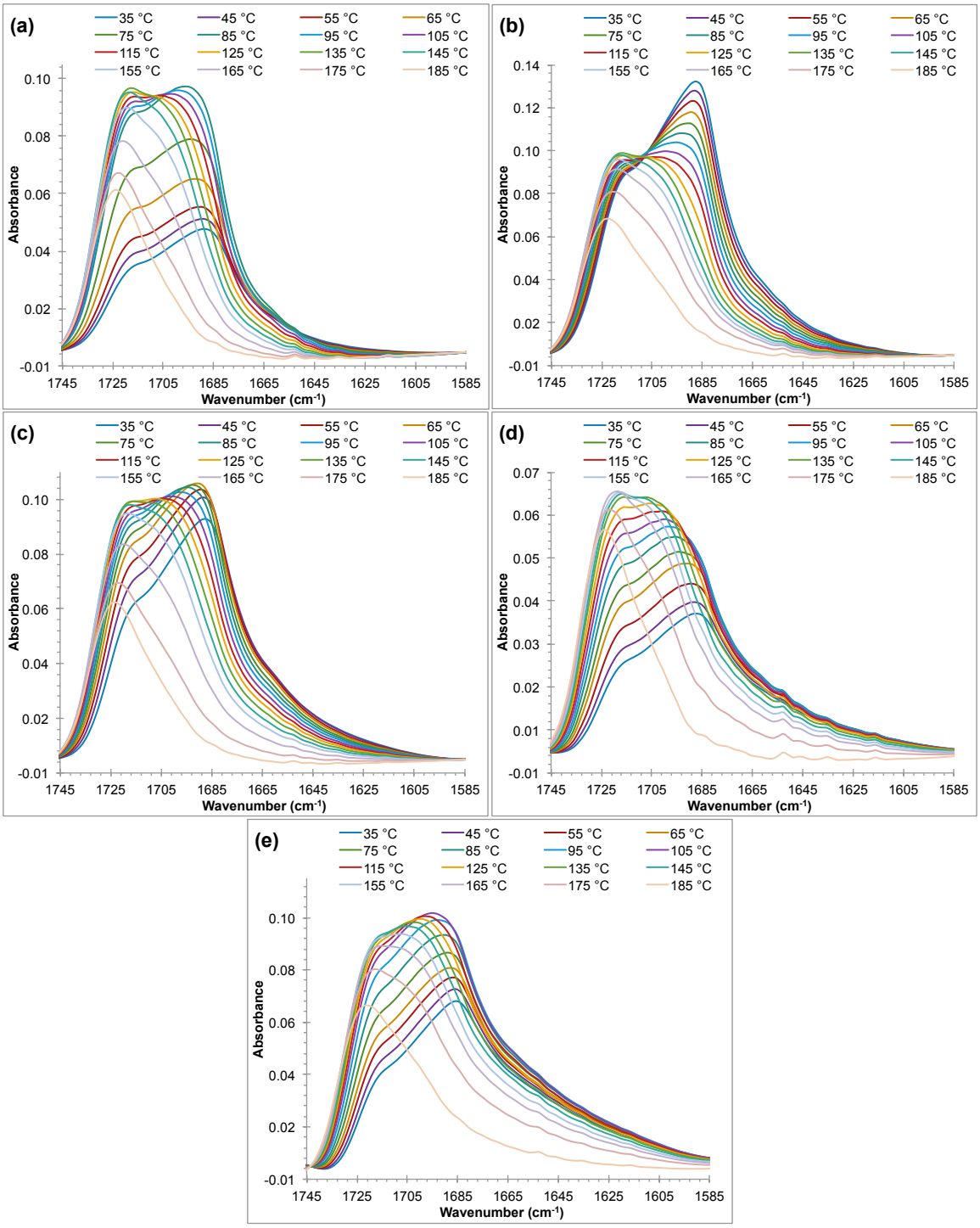

Figure 5.8 Variable temperature FTIR-ATR spectra of the carbonyl-stretching region for the composites with: (a) 0.18, (b) 1.8, (c) 2.4, (d) 5, and (e) 10 wt. % loading of the AU-MWCNTs.

5.3.2 Peak Fitting Results

While the spectra for different functionalized CNTs at different weight percent loadings and temperatures are all obviously different to some extent, it is difficult to make an accurate comparison or conclude about trends qualitatively with so much data. Therefore, peak fitting was used to attempt a quantitative comparison of hydrogen bonding content among the different samples as a function of temperature. After several attempts with multiple peak fitting software programs and numerous combinations of peak shapes and quantity, it was ultimately determined that the carbonyl region data was best fit with three Gaussian peaks, as shown in Figure 5.9. Previous literature has reported that the overlapping peaks in the carbonyl region of hydrogen bonding samples correspond to various hydrogen-bonding states, and that the different IR bands are the result of how the carbonyl is affected by each kind and strength of hydrogen bond. More specifically, the order of the hydrogen-bonding domains plays a key role in the different states of carbonyl hydrogen bonding.[17, 29, 32]

According to Coleman and Painter,[17] the peaks at 1670, 1690, and 1710 may correspond to ordered hydrogen bonding, disordered hydrogen bonding, and free carbonyl groups, respectively. Ordered hydrogen bonding refers to regions of the hard segment domain that exhibit highly ordered, and potentially crystalline, behavior, while disordered bonding occurs between hard segment urethane carbonyls found in the amorphous domains of the polymer. While a third peak in the ordered hydrogen bonding position is present for all of the samples, its peak area is considerably smaller compared to the disordered hydrogen bonding and free carbonyl peaks. While previously reported wide-angle X-ray diffraction (WAXD) studies did not confirm the presence of crystallinity in these samples, the peak fitting results would suggest

that a small amount of hard segment crystallization is occurring. Inglefield *et al.* suggested that this potentially minimal crystallization was perhaps below the limits of detection or hidden under the amorphous halo of the WAXD data.[19]

Regardless of the ordered versus disordered argument, there is still a distinct shift from hydrogen-bonded carbonyls to free carbonyl groups. As shown in Figure 5.9 (a) and (b), there is a dramatic change in peak ratios over the total temperature range of these experiments. As the samples are heated, hydrogen bonds are broken, resulting in a significantly larger percentage of free carbonyls at 185 ºC than were originally present in the sample at 35 ºC. Table 5.1 gives the absolute areas of the three different carbonyl peaks that were fit in Figure 5.9. Additional peak fitting data can be found in Appendix B. As mentioned previously, the population of ordered hydrogen bonds is comparatively low in these samples, and hard segment crystallinity was not detected in previous analytical characterization by WAXD.[19] Consequently, fitting and reporting the two hydrogen-bonded carbonyl peaks as ordered versus disordered does not conclusively provide any additional depth of understanding to the overall hydrogen-bonding behavior of the samples. Thus, in an effort to simplify and more accurately compare the total hydrogen bonding content among the samples, the areas of order and disordered hydrogen-bonding peaks were added together for further analysis. In addition to the previously mentioned absorption coefficient correction, k, the data was also normalized by reporting the relative, rather than absolute, areas of hydrogen bonding and free carbonyl peaks, to account for temperature-induced intensity variations, different sample thicknesses, etc.

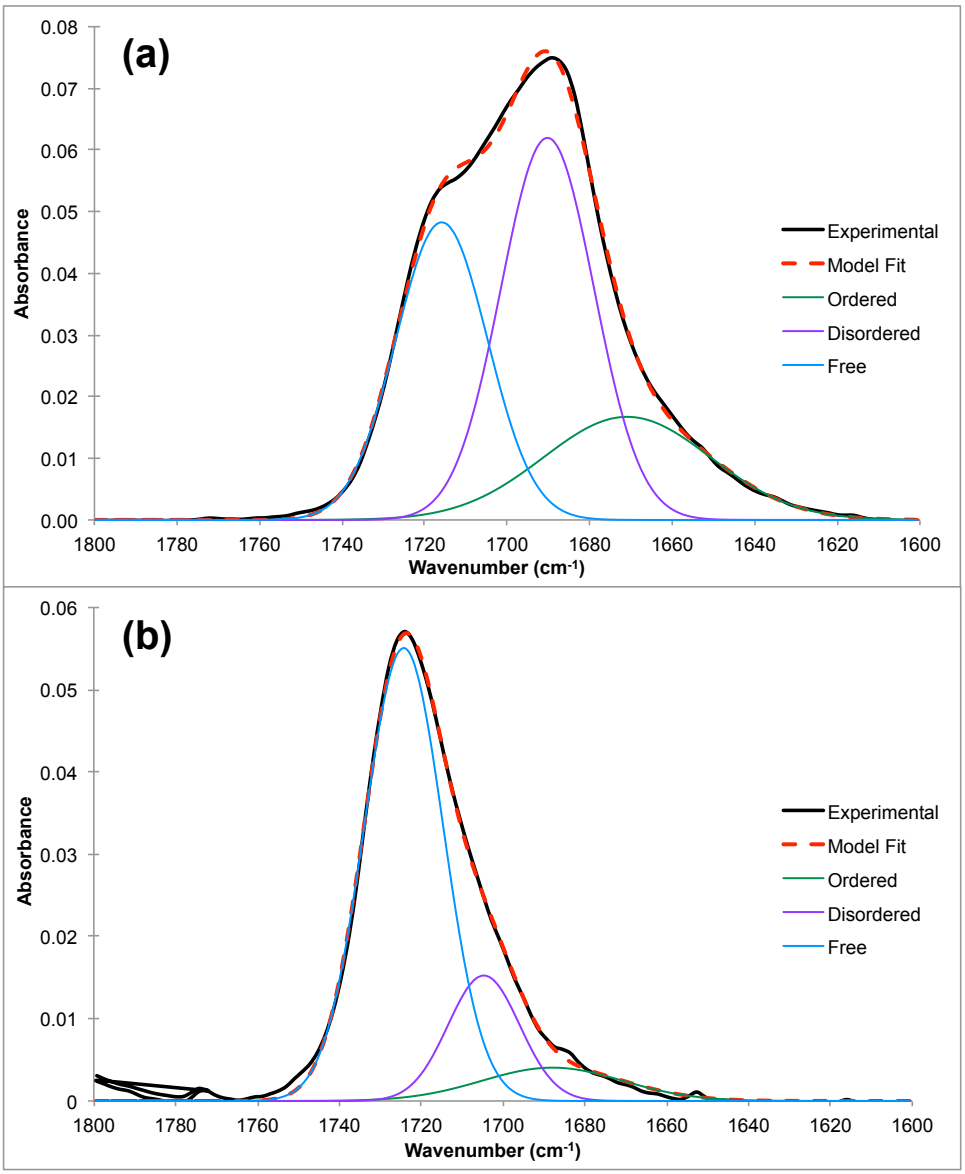

Figure 5.9 Peak fitting results for the neat polyurethane sample at (a) 35 ºC and (b) 185 ºC

Table 5.1 Peak fitting results for the neat polyurethane sample

	Absolute Areas			Relative Areas			
	Ordered H-bonding	**Disordered H-bonding**	**Free Carbonyl**	**Total H-bonding**	**Free Carbonyl**	**% H-bonded**	**R_{index}**
35 °C	1.19	2.48	1.90	0.66	0.58	53.03	1.13
185 °C	0.25	0.47	1.89	0.28	1.24	18.22	0.22

Furthermore, Table 5.1 also provides the comparison of hydrogen bonding to free carbonyl groups as represented in two numerical values: the hydrogen bonding index,[12, 20] R_{index}, and % H-bonded. R is the ratio of the relative areas of the hydrogen bonding carbonyls to the free carbonyls, where R = 1 corresponds to equal populations of free and hydrogen-bonding carbonyl groups. This presents a convenient way to report the crossover point, or the temperature at which the population of free carbonyls is now greater than that of hydrogen bonding. Similarly, the % H-bonded values are another useful way to present the same data, indicating what percentage of the total population of carbonyls in a sample are participating in hydrogen bonding at any one temperature.

5.3.3 Comparison of Hydrogen-Bonding vs Free Carbonyl Groups

The peak fitting procedure demonstrated in Figure 5.9 and Table 5.1 was repeated for all of the spectra collected for each sample. Figure 5.10 shows a plot of relative area versus temperature for the neat polyurethane, and gives a clear illustration of the hydrogen bonding behavior as the temperature increases. Initially, at 35 ºC, there are slightly fewer free carbonyls than those involved in hydrogen bonding. As the temperature increases, hydrogen bonds start to

dissociate and the free carbonyl content begins to increase in the range of 50 to 100 ºC, which happens to coincide with the hard segment T_g temperature range.[19] At 55 ºC, we observe the crossover point, at which the relative area of the free carbonyl is now higher than that of the hydrogen-bonded carbonyl groups. This trend continues to grow as the temperature is increased further throughout the experiment; however, there are some noteworthy differences in slope across the higher temperatures. From approximately 110 to 150 ºC, the slope almost plateaus and very minimal increases in the free carbonyl content are observed. However, above 155 ºC, there is a dramatic change in slope, and the free carbonyl population starts to rapidly increase as hydrogen bonds are dissociated. This onset temperature for rapid hydrogen-bond dissociation is also in good agreement with the previously reported flow temperature determined by dynamic mechanical analysis (DMA).[19]

By plotting the hydrogen-bonding and free carbonyl populations as a function of temperature for each type of composite, we can start to see the effects of MWCNTs on the hydrogen-bonding behavior of the polyurethane. As shown in Figures 5.11 through 5.14, there are distinct changes to the shapes of these plots with various weight percent loadings of MWCNTs and different surface functionalities on the MWCNTs. However, generally speaking, some universal trends are observed. For example, regardless of functionalization, adding any amount of MWCNTs to the polyurethane increased the overall hydrogen-bonding content.

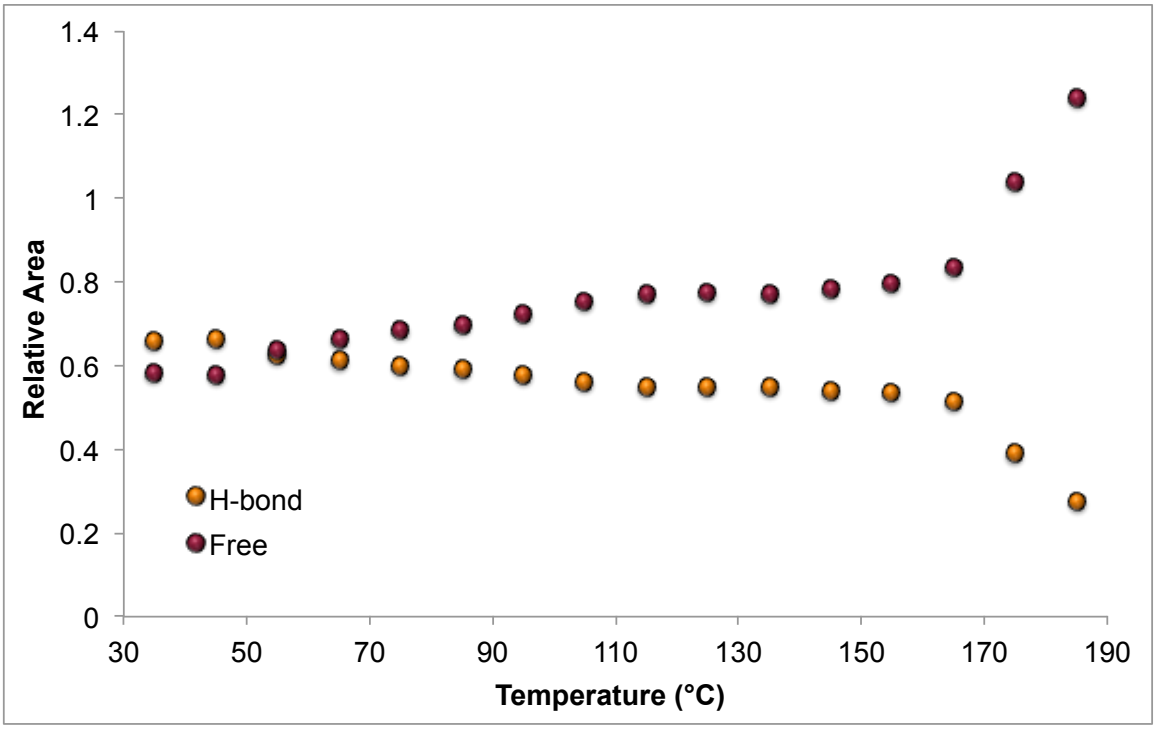

Figure 5.10 Relative areas for total hydrogen-bonding and free carbonyl bands after peak fitting for the neat polyurethane sample.

The addition of any MWCNTs also affected the temperature required for hydrogen bond dissociation. The aforementioned crossover point, is at a higher temperature, by at least 10 ºC, for every sample containing MWCNTs, compared to that of the neat polyurethane. Even the lowest weight percent loading of the purified MWCNTs, with no functionalization, starts crossing over around 55 ºC, but doesn't complete the crossover until 75 ºC. This would indicate that the presence of MWCNTs, in general and regardless of functional groups, plays some role in the hydrogen-bonding mechanism of these composites.

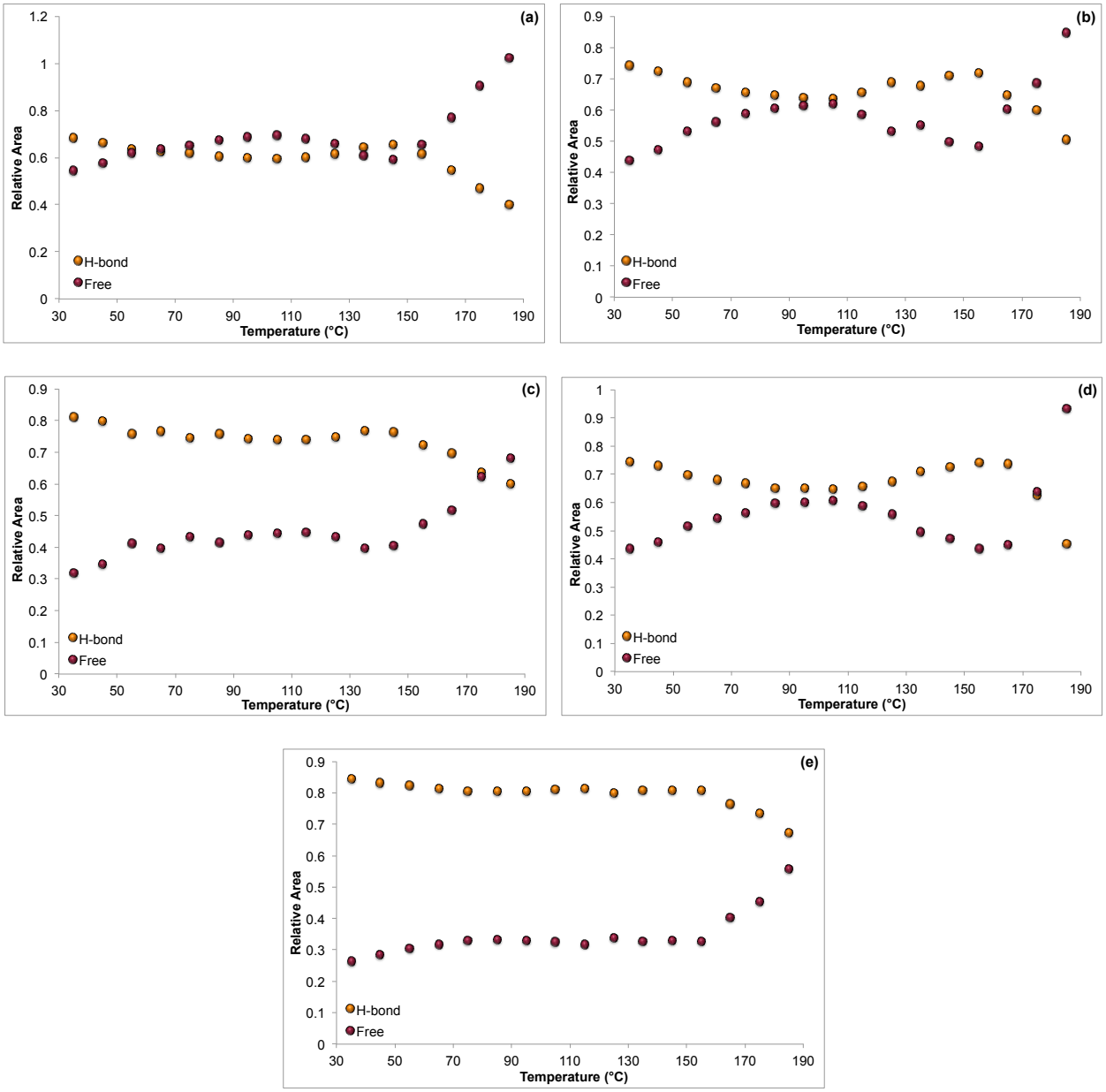

Figure 5.11 Relative areas for total hydrogen-bonding and free carbonyl bands after peak fitting for the composites with: (a) 0.18, (b) 1.8, (c) 2.4, (d) 5, and (e) 10 wt. % loading of the purified MWCNTs.

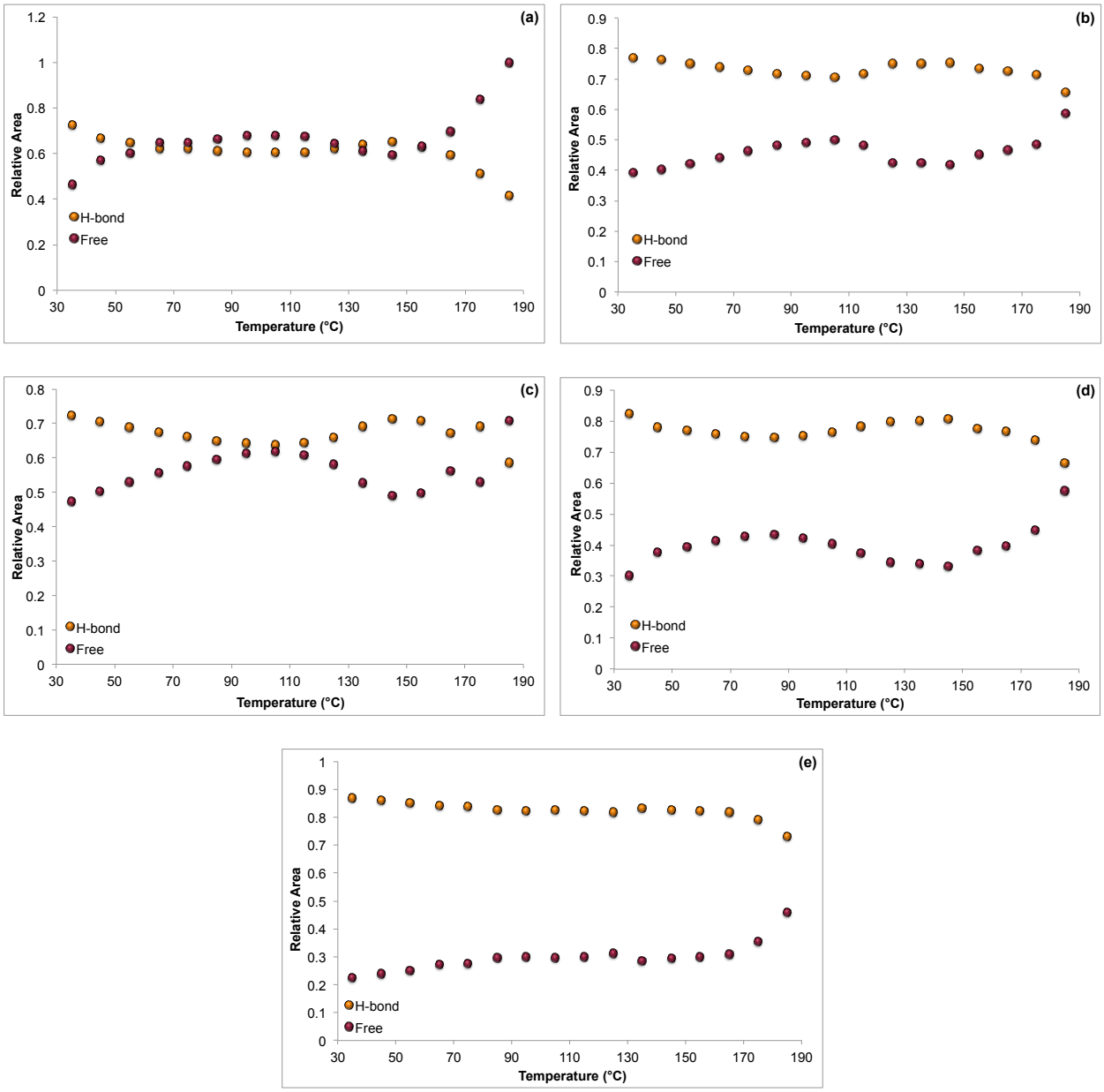

Figure 5.12 Relative areas for total hydrogen-bonding and free carbonyl bands after peak fitting for the composites with: (a) 0.18, (b) 1.8, (c) 2.4, (d) 5, and (e) 10 wt. % loading of the AO-MWCNTs.

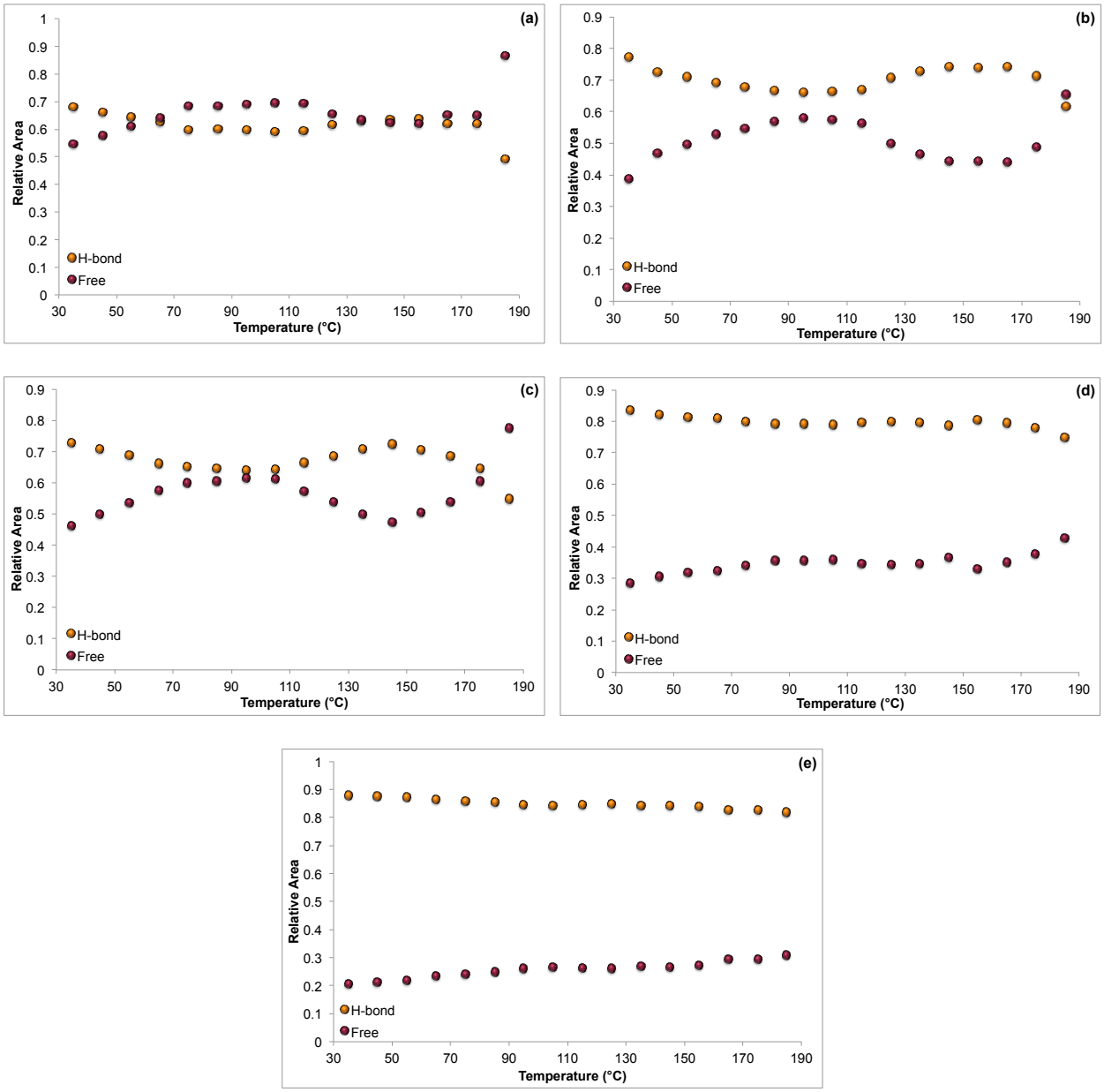

Figure 5.13 Relative areas for total hydrogen-bonding and free carbonyl bands after peak fitting for the composites with: (a) 0.18, (b) 1.8, (c) 2.4, (d) 5, and (e) 10 wt. % loading of the AA-MWCNTs.

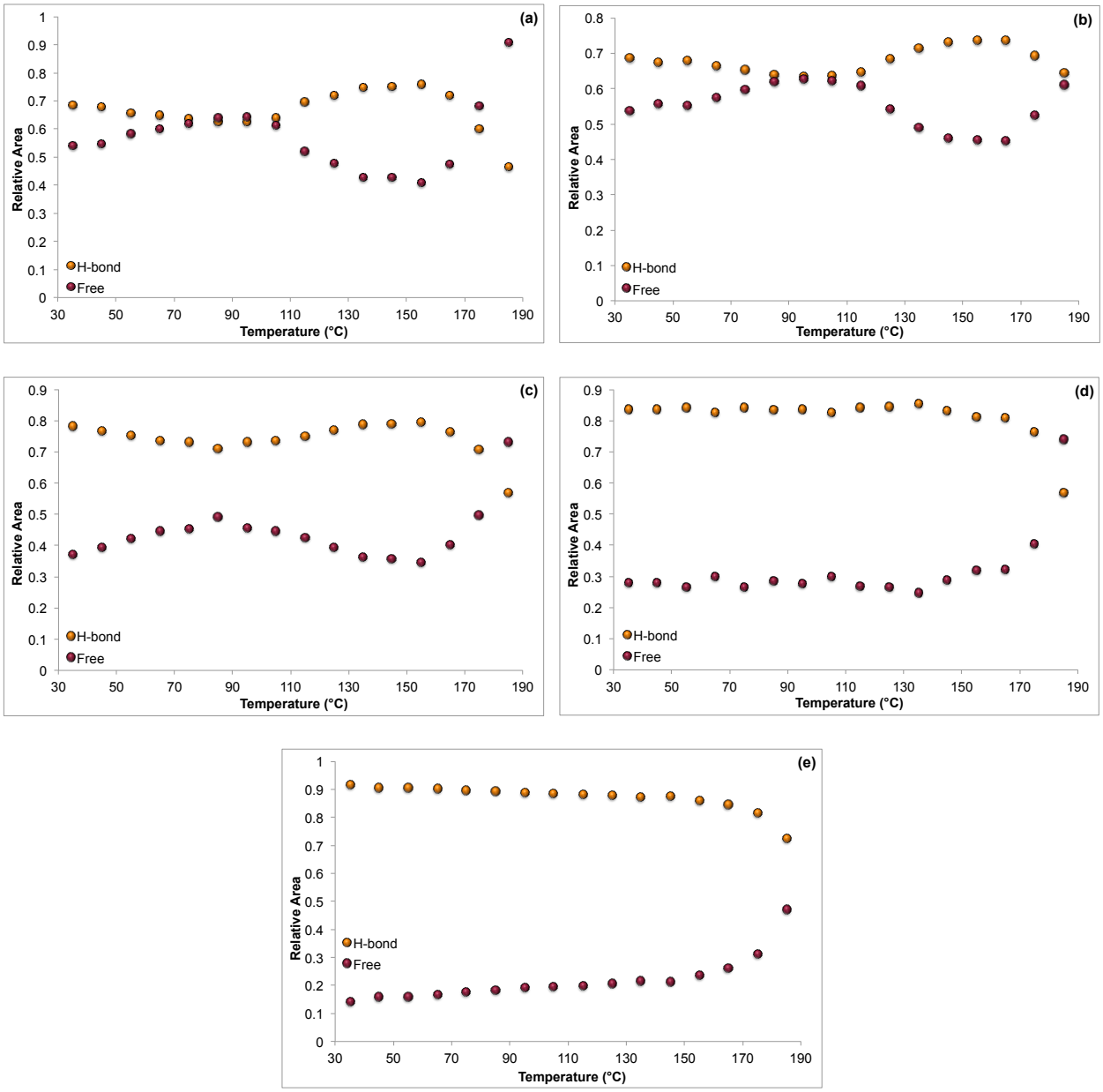

Figure 5.14 Relative areas for total hydrogen-bonding and free carbonyl bands after peak fitting for the composites with: (a) 0.18, (b) 1.8, (c) 2.4, (d) 5, and (e) 10 wt. % loading of the AU-MWCNTs.

In addition, at higher weight percent loadings of the different MWCNTs, the crossover point trend continues to increase with temperature, or is never actually reached. This suggests

that stronger hydrogen bonds are formed with increased concentrations of MWCNTs. Furthermore, the functionalizations of the MWCNTs seem to partially follow the general trend that with higher hydrogen-bonding capacity, higher temperatures are required for hydrogen bond dissociation. This is easiest to see at the lower percent loadings. For example, the crossover temperature at 0.18 wt. % for most of the samples is around 55 to 75 ºC, showing a gradual increase with increasing functionalization. However, for the amide urea functionalized MWCNTs, the crossover for the 0.18 wt. % is not totally complete until 105 ºC, which is considerably higher than the other samples.

An additional unexpected trend was observed in this data, specifically in the middle loadings from 1.8 to 5 wt. % MWCNTs, regardless of functionalization. In each of these plots, a dip is seen in the midsection of the graph. These samples initially all show similar behavior to the neat polyurethane, and as the temperature starts to increase, the free carbonyl content also increases. However, after the samples reach approximately 100 ºC, which corresponds to the hard segment T_g, the free carbonyl population starts to go back down as hydrogen bonds start to reform. This reversal continues until temperatures surpass the previously mentioned "rapid dissociation temperature" seen in the neat polyurethane around 150 ºC. At these higher temperatures, hydrogen bond dissociation resumes, and proceeds at a significantly faster rate than before the dip; however, not as rapidly as the dissociation seen in the neat polyurethane. One possible explanation for these dips in the data, compared to the plateau region of the neat polyurethane, is that the samples were undergoing an annealing region from approximately 100 to 150 ºC. Above the hard segment T_g, the increased chain mobility may have allowed for urethane reorganization and an increase in the hydrogen bonding, until high enough temperatures

were reached to continue dissociation.[19] Further investigation is needed to explore this possible annealing and to explain why it only occurs in the composite samples and not the neat polyurethane.

To further explore the content and strength of hydrogen bonding across the samples, two numerical values were also assessed: %H-bonded and R_{index}. In Figure 5.15, the percentage of hydrogen-bonding carbonyls, out of the total carbonyl peaks that were fit, is plotted as a function of temperature for each series of composites. Numerous observations can be made from the data that provide more insight into the effects of functionalization, weight percent loadings, and temperature. For example, all of the samples, at similar weight percent loadings, have fairly similar starting percentages of hydrogen bonding carbonyls at 35 ºC, within the 50 to 80 % range. The only exception is the 10 wt. % loading AU-MWCNT composite, which had an initial %H-bonded value of almost 90%. In general, all of the composites have a higher percentage of hydrogen-bonding carbonyls than the neat polyurethane, with minor overlap from the 0.18 wt. % samples at lower temperatures. The data also seem to follow the anticipated trend, with a few exceptions, that with increasing hydrogen-bonding capacity, the starting percentage of hydrogen bonds increases. This phenomenon is especially apparent at high concentrations of MWCNTs. At 5 and 10 wt. % MWCNT loadings, the AA-MWCNTs have a slightly higher percentage of hydrogen-bonding carbonyls than their AO-MWCNT counterparts. In addition, the %H-bonded shows fewer changes over a more extended temperature range for the AA-MWCNTs versus the AO-MWCNTs. The same is true when comparing AU-MWCNTs and AA-MWCNTs at 5 and 10 wt. % loadings.

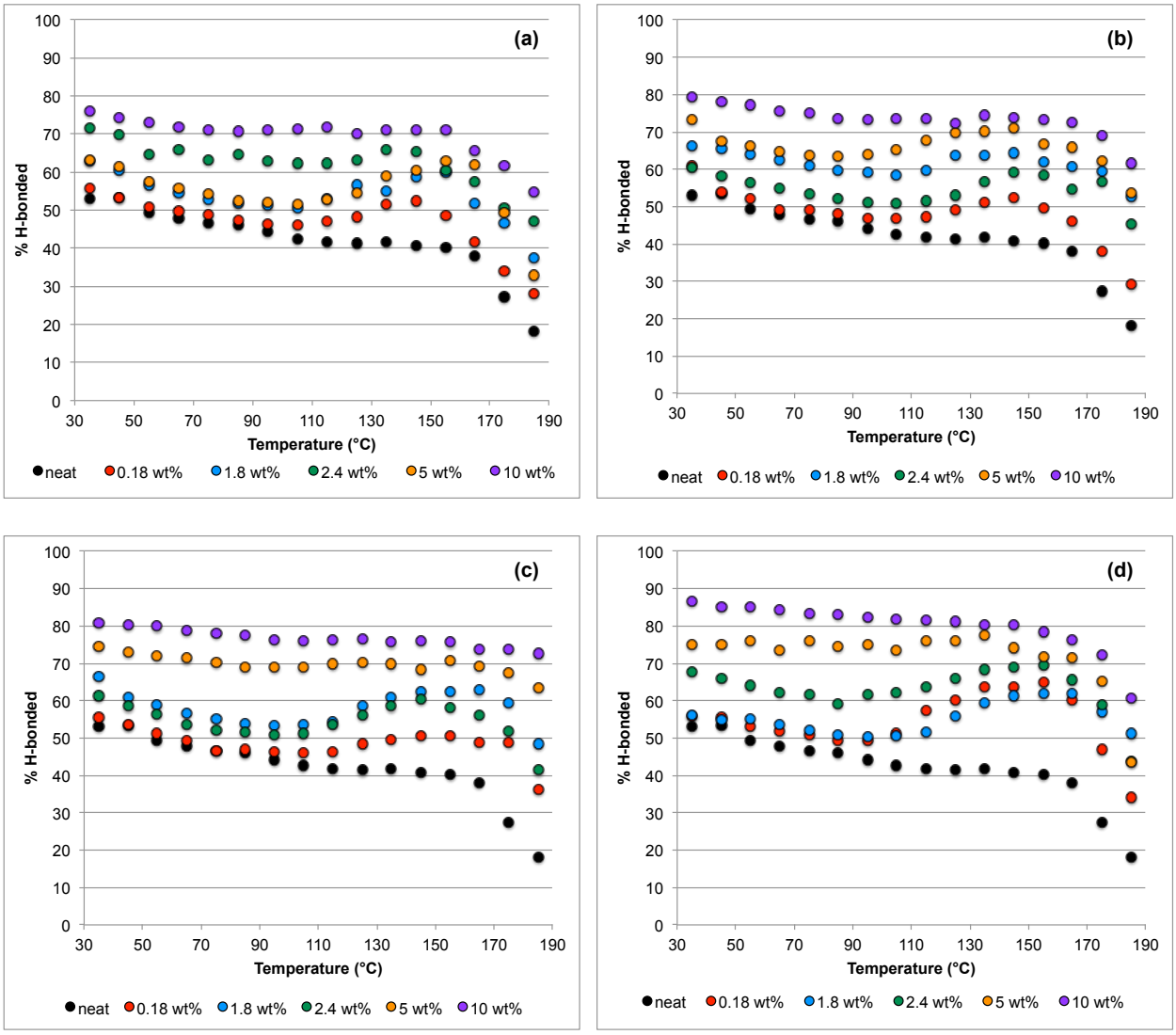

Figure 5.15 Percentage of carbonyls that are hydrogen bonding vs. temperature for (a) purified MWCNTs, (b) AO-MWCNTs, (c) AA-MWCNTs, and (d) AU-MWCNTs

Overall, temperature seems to have a decreased effect on the hydrogen bonding content at the higher weight percent loadings for all of the functionalized MWCNTs, as compared to the purified MWCNTs. The major inconsistency with this trend is the fact that at higher temperatures (~165 to 185 ºC), the percentage of hydrogen bonding carbonyls for the 5 and 10

wt. % loadings of the amide-urea functionalized MWCNTs starts to rapidly decrease due to hydrogen bond dissociation; whereas, the amide-amine functionalized MWCNTs remain fairly constant in the same range of loadings and temperatures. This unexpected drop may be the result of urea degradation at higher temperatures, thus disrupting the hydrogen bonds. However, further experiments are needed to better understand this phenomenon. In addition, the possible annealing behavior, mentioned previously as the dip seen between 100 to 150 ºC for the 1.8 to 5 wt. % loading composites, is also seen in this data.

Another means of looking at the same data in a slightly different perspective is by calculating the R_{index}. Where the %H-bonded is the percentage of hydrogen bonding carbonyls out of the total carbonyls present, the R_{index} is simply the ratio of hydrogen bonding carbonyls to free carbonyls. The R_{index} is frequently used in literature[18, 20] as a numerical value to describe the hydrogen bonding content of a sample, while also providing a reference point to compare multiple samples: $R_{index} = 1$. This is the crossover point, or temperature, mentioned earlier at which the populations of both free and hydrogen-bonding carbonyls are the same. Figure 5.16 shows the comparison of the same data plotted as %H-bonded and R_{index}, for the acid-oxidized composite samples. Because the R_{index} is a ratio, rather than a percentage, and the scale is so much smaller, the slopes of the curves in the R_{index} plot are slightly more exaggerated than in the %H-bonded plot. Generally, these profiles are very similar, and in this comparison, very little additional information can be gleaned by presenting the data in the R_{index} format. However, by plotting the initial and final (35 ºC and 185 ºC, respectively) R_{index} data, grouped by weight percent loadings, for each sample on the same comprehensive plot, as shown in Figure 5.17 and

Figure 5.18, further conclusions can be drawn with regards to the effects of functionalization and concentration on hydrogen bonding.

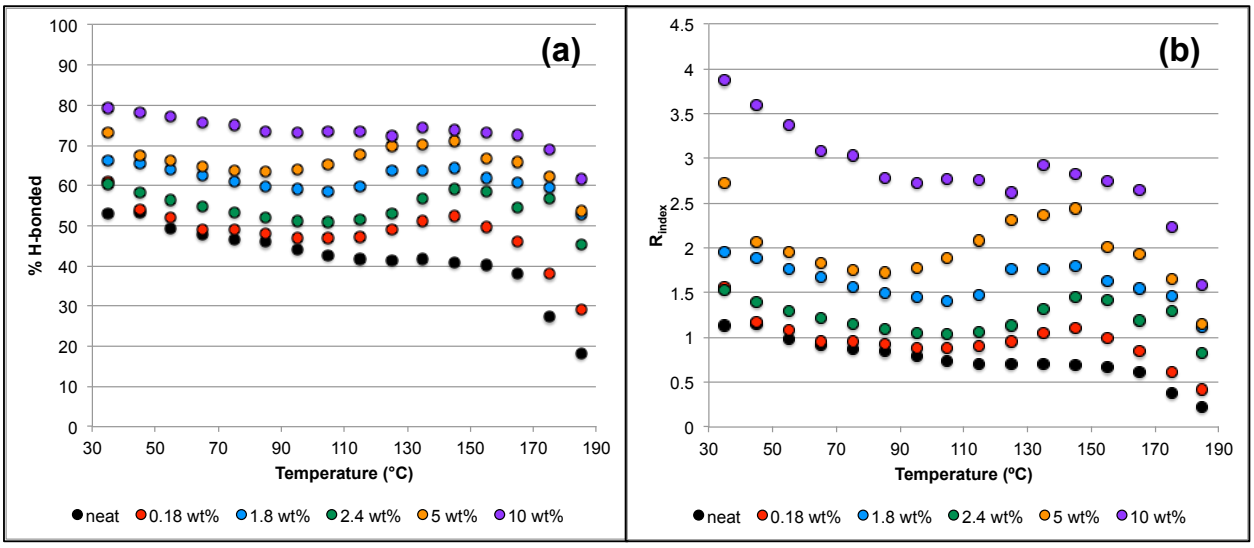

Figure 5.16 Comparison of (a) %H-bonded and (b) R_{index} as functions of temperature for AO-MWCNTs

As shown in Figure 5.17, there is an evident, while not perfect, trend that as the weight percent of MWCNTs increases, the hydrogen bonding also increases. At the lowest loading of 0.18 wt. %, the composite samples are actually still quite similar to the neat polyurethane at 35 ºC; but at 185 ºC, the composites retain more hydrogen bonding content than the neat samples. As the concentration of MWCNTs increases, the gain in hydrogen bonding also continues, with a few exceptions. For example, the composite with 1.8 wt. % AU-MWCNTs actually exhibits a drop in R_{index} from 0.18 wt. %. Also, two of the composites at 2.4 wt. % loadings – the acid-oxidized and amide-amine functionalized MWCNTs – exhibit lower R_{index} values than would be expected with the remainder of the weight percent trend. In general, the data for all of the composites at 2.4 wt. % loadings is fairly inconsistent with the other data; therefore, it has been

removed from Figure 5.18, which is the same temperature data re-plotted as a scatter plot to emphasize trends.

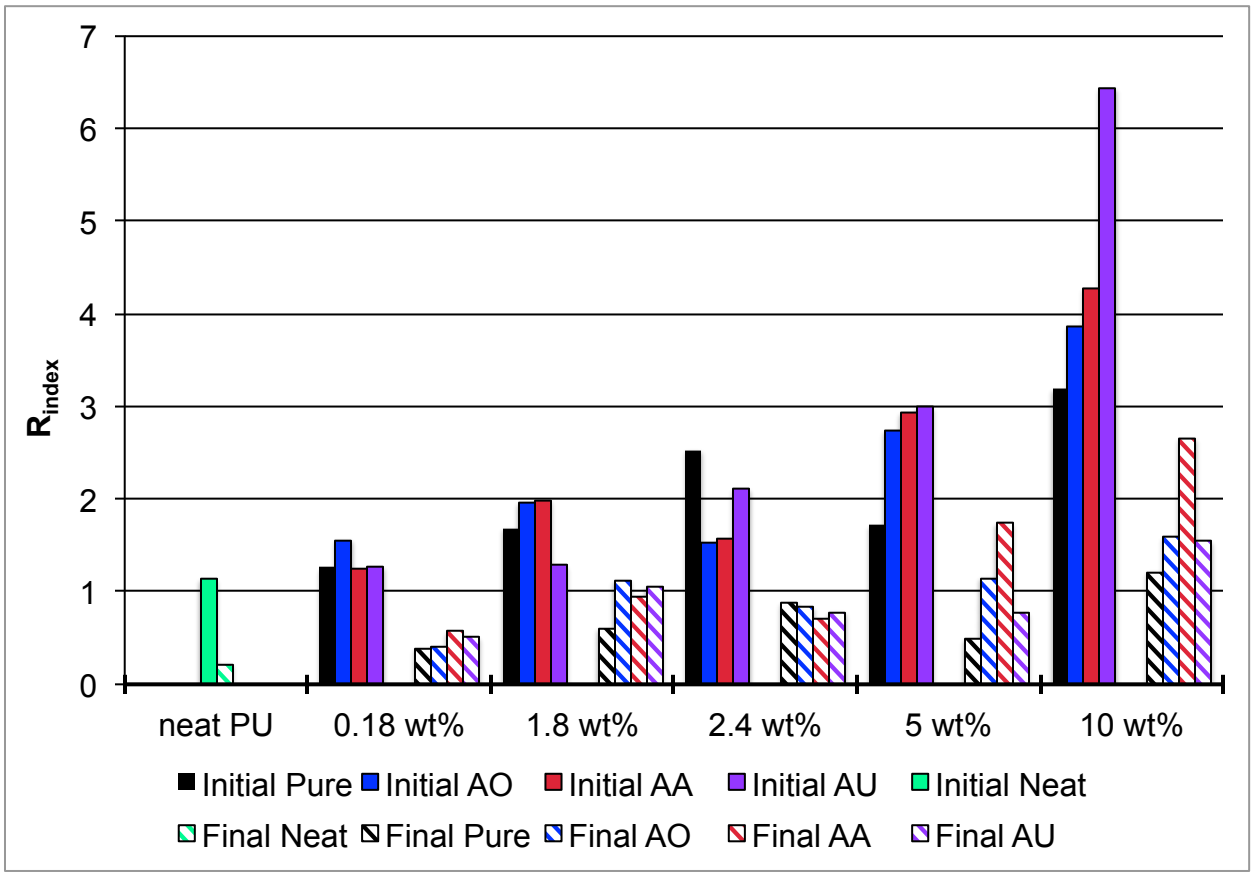

Figure 5.17 R-index vs. wt. % loading of MWCNTs at initial temperature (35 ºC) and final temperature (185 ºC) across the 4 different series of samples and the neat polyurethane (bar graph).

At low temperatures, as shown in Figure 5.17 and Figure 5.18(a), the increasing hydrogen-bonding capacities have a minimal effect on hydrogen bonding at lower weight percent loadings of the MWCNTs. From 0.18 to 2.4 wt. %, the R_{index} values for the different functional groups are somewhat random and follow no recognizable pattern. However, at 5 and 10 wt. %, the R_{index} values increase with hydrogen-bonding capacity perfectly. It is also worth mentioning

that the initial R_{index} value for the 10 wt. % AU-MWCNT composite is remarkably greater than any of the other composites, by approximately 30%. Besides this one very high outlier, the patterns seen in R_{index} for the different MWCNTs, at both temperatures, are strikingly similar for the 5 and 10 wt. % composites, differing only in magnitude, which is to be expected with the change in concentration. This may point to a potential minimum threshold concentration at which the different surface functionalities are actually "seen" by the polyurethane. Even the purified MWCNTs have been shown to influence the hydrogen bonding behavior of the polyurethane; and with higher loadings of the purified MWCNTs, the hydrogen bonding is still typically increased. At lower loadings of the functionalized MWCNTs, there may not be sufficient quantities of functional groups present to make an appreciable difference as compared to the pure MWCNTs. However, at higher loadings, like above 5 wt. %, a pattern starts to immerge, suggesting that the hydrogen bonding capacity of the functional groups is now providing a significant influence to the hydrogen bonding mechanism. This may relate to the abilities of the MWCNTs to interact with and disperse throughout the polyurethane, as discussed earlier.[4-6] In previous experiments with transmission electron microscopy (TEM), the MWCNTs with surface functionalities were well dispersed throughout the polyurethane while the non-functionalized MWCNT composites were not.[19] While the functionalized MWCNTs may have been well dispersed in the polyurethane, at lower loadings the concentration of functional groups may not have been sufficient to make a consistent and noticeable difference in the polymer-CNT interfacial interactions, as compared to the purified MWCNTs. Further experiments are needed to explore this pattern at high weight percent loadings.

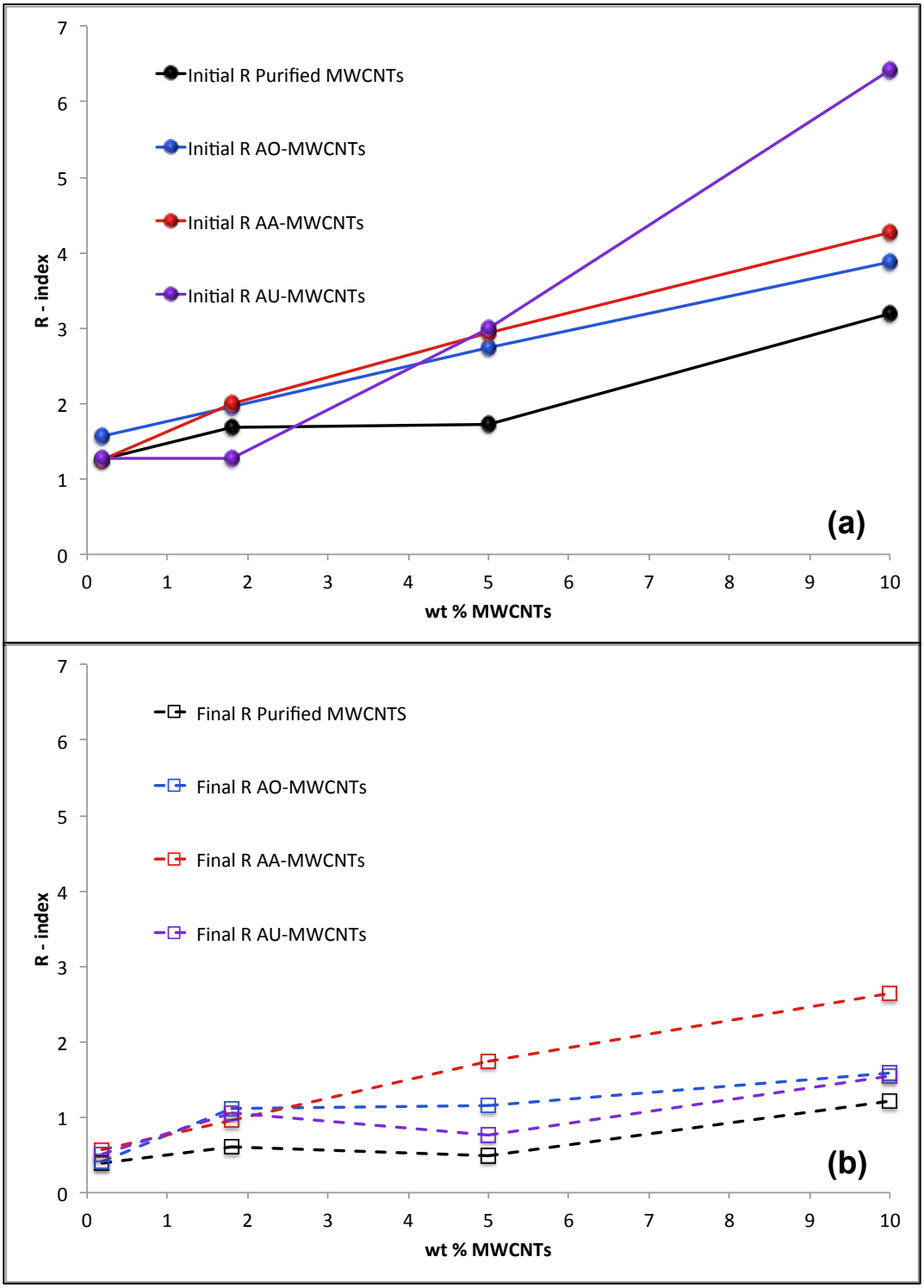

Figure 5.18 R-index vs. wt. % loading of MWCNTs at (a) the initial temperature, 35 ºC, and (b) the final temperature, 185 ºC, across the 4 different series of samples (scatter plot).

The R_{index} plots are also exceedingly useful in looking at the effects on dissociation temperature, by focusing on the reference point of R = 1, or the crossover temperature. In Figure 5.17 we observe that several of the samples never reach this crossover point, meaning that there are still a majority of carbonyls that did not dissociate, even at 185 ºC. This is true for all of the composites at a 10 wt. % loading, which is consistent with the high R_{index} values that all of these composites started with at 35 ºC. The crossover is also never reached for the 5 wt. % loadings of the AO-MWCNTs and AA-MWCNTs, but the AU-MWCNT composite at 5 wt. % is surprisingly well below R = 1 at 185ºC. In addition, the composite samples with 1.8 wt. % loadings of AO-MWCNTs and AU-MWCNTs are just barely above R = 1 at the final temperature. In general, the temperature data is somewhat scattered, however, looking at Figure 5.18 (b), two major conclusions can be drawn from the temperature data. The first surprising observation is that the final R_{index} values for the AU-MWCNT composites are consistently lower than expected, due to the higher hydrogen-bonding capacity of the urea group. As stated earlier, this may be an effect of urea degradation at elevated temperatures, and needs to be explored further for a more conclusive determination. The second major observation that stands out in this data is the profile for the AA-MWCNT composites at the final temperature. The R_{index} values for these composites, specifically at 5 and 10 wt. %, are still well above R = 1 and much higher than the other composites. In addition, referring back to Figure 5.17, most of the composites show a decrease in R across the temperature range that is usually greater than 50% of the starting value. However, for all of the AA-MWCNT composites, the decrease in R_{index} with temperature is 50% or less. While further experimentation is needed to expand on this data, it is

obvious that something about the amide-amine surface functionalities provides added thermal stabilization to the hydrogen bonds, compared to the other MWCNTs.

5.4 Conclusions & Future Work

In conclusion, variable temperature FTIR was successfully utilized to explore the effects of surface functionality and loading of MWCNTs in polyurethane-MWCNT composites. Quantitative analysis of the carbonyl-stretching region was performed using peak fitting and numerically expressed with R_{index} and %H-bonded values. In general, the functionalized MWCNTs had a much larger influence on the R_{index} than the purified MWCNTs. The MWCNTs with surface functionalities also required higher temperatures for hydrogen bond dissociation, which correlated well with the flow temperatures seen in previous DMA experiments.[19] Furthermore, given the patterns that emerged in R_{index} that follow the increase in hydrogen bonding capacity of the functionalized MWCNTs only at the higher loadings (5 and 10 wt. %), the combination of functionality and loading is critical to the idea of making hydrogen bonding behavior tunable in these composites.

However, there are still several unanswered questions that should be explored in future work. Further experimentation is needed to determine why all of the initial R_{index} values, regardless of functionality, are so high for the 10 wt. % loading composites. Furthermore, investigations are needed to explain why the expected pattern of increasing hydrogen bond content with progressively amplified hydrogen-bonding capacities among surface functionalities only occurs at higher concentrations of MWCNTs. Related to this, an explanation is needed for the surprisingly low R_{index} values for the AU-MWCNT composites at 185 ºC.

Additionally, duplicate spectra should be collected from multiple samples to validate the reproducibility of the results seen here. The samples at 2.4 wt. % loadings are of specific concern, as most of these R_{index} values do not follow the same trends as the remainder of the data. It would also be advantageous to repeat the same process of peak fitting analysis in the NH-stretching region for the same set of data. This would provide additional information about the hydrogen bonding behavior of the samples, and possibly offer a route to explore the thermodynamics of hydrogen bond dissociation.[33]

5.5 References

1. Andrews, R.; Weisenberger, M. C. *Curr. Opin. Solid State Mat. Sci.* **2004,** *8* (1), 31-37.
2. Moniruzzaman, M.; Winey, K. I. *Macromolecules* **2006,** *39* (16), 5194-5205.
3. Du, J. H.; Bai, J.; Cheng, H. M. *Express Polym. Lett.* **2007,** *1* (5), 253-273.
4. Bose, S.; Khare, R. A.; Moldenaers, P. *Polymer* **2010,** *51* (5), 975-993.
5. Ma, P. C.; Siddiqui, N. A.; Marom, G.; Kim, J. K. *Compos. Pt. A-Appl. Sci. Manuf.* **2010,** *41* (10), 1345-1367.
6. Rahmat, M.; Hubert, P. *Compos. Sci. Technol.* **2011,** *72* (1), 72-84.
7. Gojny, F. H.; Wichmann, M. H. G.; Kopke, U.; Fiedler, B.; Schulte, K. *Compos. Sci. Technol.* **2004,** *64* (15), 2363-2371.
8. Spitalsky, Z.; Tasis, D.; Papagelis, K.; Galiotis, C. *Progress in Polymer Science* **2010,** *35* (3), 357-401.
9. Balasubramanian, K.; Burghard, M. *Small* **2005,** *1* (2), 180-192.
10. Sahoo, N. G.; Rana, S.; Cho, J. W.; Li, L.; Chan, S. H. *Progress in Polymer Science* **2010,** *35* (7), 837-867.
11. Ventura, D. N.; Stone, R. A.; Chen, K. S.; Hariri, H. H.; Riddle, K. A.; Fellers, T. J.; Yun, C. S.; Strouse, G. F.; Kroto, H. W.; Acquah, S. F. A. *Carbon* **2010,** *48* (4), 987-994.
12. Seymour, R. W.; Estes, G. M.; Cooper, S. L. *Macromolecules* **1970,** *3* (5), 579-&.
13. Seymour, R. W.; Cooper, S. L. *Macromolecules* **1973,** *6* (1), 48-53.
14. Senich, G. A.; MacKnight, W. J. *Macromolecules* **1980,** *13* (1), 106-110.
15. Skrovanek, D. J.; Howe, S. E.; Painter, P. C.; Coleman, M. M. *Macromolecules* **1985,** *18* (9), 1676-1683.

16. Skrovanek, D. J.; Painter, P. C.; Coleman, M. M. *Macromolecules* **1986,** *19* (3), 699-705.

17. Coleman, M. M.; Lee, K. H.; Skrovanek, D. J.; Painter, P. C. *Macromolecules* **1986,** *19* (8), 2149-2157.

18. Lamba, N. M. K.; Woodhouse, K. A.; Cooper, S. L.; Lelah, M. D. *Polyurethanes in biomedical applications*. CRC Press: Boca Raton, 1998.

19. Inglefield, D. L. Tailoring Intermolecular Interactions for High-Performance Nanocomposites. Dissertation, Virginia Polytechnic Institute and State University, Blacksburg, VA, 2014.

20. Xia, H.; Song, M. *Soft Matter* **2005,** *1* (5), 386-394.

21. Chen, G. J.; Wei, M.; Chen, J. H.; Huang, J.; Dufresne, A.; Chang, P. R. *Polymer* **2008,** *49* (7), 1860-1870.

22. Ciobanu, L. C.; Ciobanu, C.; Dorohoi, D. *High Perform. Polym.* **2010,** *22* (1), 56-68.

23. Bistricic, L.; Baranovic, G.; Leskovac, M.; Bajsic, E. G. *European Polymer Journal* **2010,** *46* (10), 1975-1987.

24. Jena, K. K.; Narayan, R.; Raju, K. *Polymer International* **2012,** *61* (8), 1309-1317.

25. Phua, S. L.; Yang, L.; Toh, C. L.; Huang, S.; Tsakadze, Z.; Lau, S. K.; Mai, Y. W.; Lu, X. H. *ACS Appl. Mater. Interfaces* **2012,** *4* (9), 4571-4578.

26. Rosca, I. D.; Watari, F.; Uo, M.; Akasaka, T. *Carbon* **2005,** *43* (15), 3124-3131.

27. Datsyuk, V.; Kalyva, M.; Papagelis, K.; Parthenios, J.; Tasis, D.; Siokou, A.; Kallitsis, I.; Galiotis, C. *Carbon* **2008,** *46* (6), 833-840.

28. Avilés, F.; Cauich-Rodríguez, J. V.; Moo-Tah, L.; May-Pat, A.; Vargas-Coronado, R. *Carbon* **2009,** *47* (13), 2970-2975.

29. Wang, W.; Wang, W.; Chen, X.; Jing, X.; Su, Z. *Journal of polymer Science: Part B: Polymer Physics* **2009,** *47*, 685-695.

30. Lee, H.-T.; Lin, L.-H. *Macromolecules* **2006,** *39* (18), 6133-6141.

31. Dias, R. C. M.; Góes, A. M.; Serakides, R.; Ayres, E.; Oréfice, R. L. *Materials Research* **2010,** *13*, 211-218.

32. Teo, L.-S.; Chen, C.-Y.; Kuo, J.-F. *Macromolecules* **1997,** *30* (6), 1793-1799.

33. Wang, F. C.; Feve, M.; Lam, T. M.; Pascault, J.-P. *Journal of Polymer Science Part B: Polymer Physics* **1994,** *32* (8), 1305-1313.

Chapter 6 : General Conclusions & Suggested Future Work

In this work, we have employed numerous advanced analytical techniques to better understand the intermolecular forces present in various nanostructured materials. Isothermal titration calorimetry (ITC) and Fourier transform infrared (FTIR) spectroscopy, in combination with several other supporting techniques, were utilized to answer fundamental questions about these different nanomaterials. Topics included the self-assembly of surfactants into micelles, structure-property relationships of polymer-DNA complexes, and temperature-dependent hydrogen bonding behaviors in polyurethane-carbon nanotube (CNT) nanocomposites.

Chapter 2

A new ITC method was successfully developed to predict low critical micelle concentration (CMC) values for surfactants with limited water-solubility. The method was first validated with two surfactant standards (sodium dodecyl sulfate and cetyltrimethylammonium bromide), and then applied to a novel gemini surfactant, 12-2-12P. CMC values were determined for solutions with varying molar fractions of methanol. The resulting linear correlation was used to mathematically extrapolate to a predicted CMC value in pure water. All of the deduced CMCs were in excellent agreement with the expected values from literature.[1-10] In the future, efforts should be made to better understand the thermodynamics of mixing for the water-methanol mixtures to enable more accurate collection and subtraction of blank titrations

from the data. This would allow for the determination of micellization enthalpy data in each mixed-solvent titration.

Chapter 3

A low volume ITC was successfully used to study the complexation of DNA by several different polycation samples (refer to Figure 3.2). Preliminary titrations revealed the need for freshly made, buffered solutions of polymer and plasmid DNA (pDNA) at low concentrations, in order to obtain reproducible binding results without aggregation. The imidazolium-containing polymer exhibited endothermic, entropically driven binding with DNA. However, these results are suspect, as they were obtained in earlier titrations when aggregation and irreproducibility were still of concern. The adenine-containing polymer exhibited exothermic binding, which was originally thought to be a result of hydrogen-bonding contributions from the adenine group. However, almost identical thermodynamic binding parameters were obtained for the pDMAEMA homopolymer (refer to Figure 3.10). The slight differences in ΔH may still be related to hydrogen-bonding contributions, but this requires further experimentation to be verified. It is likely that the heat release observed for both of these polymers is due to unprotonated residues of DMAEMA abstracting protons from the buffer,[11] however additional experiments are needed to confirm this. Finally, this ITC system was successfully utilized to determine the stoichiometric ratio of linear polyethylenimine binding to DNA to confirm novel NMR results.[12]

Contingent upon acquiring more samples, future studies should focus on obtaining reproducible results for both polymers in freshly made, buffered solutions at low concentrations.

Blank titrations should also be performed and subtracted from the binding data to eliminate any heat artifacts from mixing, buffer mismatch, etc. In addition, both of the polycations studied here were each part of a series of polymers, looking at varying structures, charge densities, etc. Future studies should investigate the differences in thermodynamic data across the different series to gain a better understanding of the structure-property relationships for the polyplexes.

Furthermore, all of the binding data analyzed in this chapter were fit with the independent binding sites model, which has been used extensively throughout the polyplex binding literature.[13-17] However, while this model will fit the data and give reasonable thermodynamic values, it is not the most accurate model to fit polycation-DNA binding, as it assumes a 1:1 binding stoichiometry, which is not always, or even usually, the case with polyplex systems. Future work should be directed toward finding and/or writing a better, more appropriate binding model for these polyplex systems. The need for such models has also been expressed in recent literature as well.[11, 18-20] Consideration should also be given to performing more titrations in buffers of varying ionization energies and salt concentrations to explore the effects of buffer ionization enthalpies and electrostatic contributions, respectively, on the overall complexation enthalpy. Finally, the additional analytical techniques explored in Chapter 4, such as Fourier transform Infrared (FTIR) spectroscopy, circular dichroism (CD) spectroscopy, dynamic light scattering (DLS), etc., would also provide supplemental data for these polymers that could greatly enhance our understanding of the polyplex formation.

Chapter 4

As a follow-up to previously published reports for polycations containing a trehalose sugar unit and varying lengths of amine spacers, Tr1-Tr4,[15] the binding of Tr5 to DNA was characterized with multiple analytical techniques. In general, the data collected from ITC, FTIR, CD, and DLS for Tr5 were all analogous to what had been observed for Tr4. ITC results indicated that Tr5 binding to pDNA is an endothermic event that is driven by entropy. Aggregation of the polyplexes was also observed in the ITC results around N/P = 2, which was later confirmed with DLS. The FTIR data that was collected did not show any noticeable changes in the DNA upon binding to Tr5, however this was not unexpected. In addition, the CD spectra were indicative of hydrogen-bonding interactions between the DNA base pairs and Tr5. The thermal curves obtained with UV-Vis suggested an overall enhancement of DNA thermal stability when bound to Tr5.

In future work, changes in the ITC procedure should be made to avoid aggregation in the cell, which interferes with the data fitting. This may involve titrations with smaller injections and/or lower concentrations of pDNA and polycation. In addition, aggregation and mixing were also problematic in the FTIR studies. Repeating these experiments with a liquid transmission cell, as opposed to the ATR crystal, may allow for smaller volumes of solution to be used, preventing aggregation. In addition, using a liquid cell would provide a better analysis of bulk solutions, as opposed to ATR, which is only a surface technique. Further thermal curve experiments should investigate higher N/P ratios, as well as physiological solution conditions. It may also be advantageous to repeat some of the experiments with pDNA in comparison to the

decoy DNA. Finally, there are additional trehalosed-based polymers that could be analyzed with these same techniques and compared to Tr5.[21]

Chapter 5

Temperature-dependent hydrogen bonding effects in composites comprised of surface functionalized multi-walled carbon nanotubes (MWCNTs) and a polyurethane were investigated with variable temperature FTIR. By comparing the ratio of the hydrogen bonded peak areas to the free carbonyl peak areas (R_{index}), peak fitting in the carbonyl-stretching region afforded a quantitative comparison across the different series of functionalizations and weight percent loadings of the MWCNTs. Overall, the MWCNTs with surface functionalization showed a much greater influence on R_{index} than purified MWCNTs. Higher temperatures were also required for hydrogen bond dissociation in the functionalized MWCNTs. In addition, at higher loadings (5 and 10 wt. %) and 35 ºC, R_{index} increased with increasing hydrogen-bonding capacity of the functional groups on the MWCNT surface. Further experiments are needed to determine why this pattern is only apparent at higher weight percent loadings of the MWCNTs. However, this pattern was not upheld at elevated temperatures and future work should explore the surprisingly low R_{index} values for the amide urea functionalized MWCNT composites at 185 ºC.

It is also suggested that these experiments be repeated in triplicate to ensure that the reported results are reproducible. Special attention should be given to the 2.4 wt. % loading samples, and almost of the R_{index} values collected at this loading do not follow the trends seen in the rest of the data. Furthermore, a great deal of additional insight into the hydrogen-bonding

behavior of these composites could be gleaned from repeating the peak fitting analysis in the NH-stretching region. This region has also been reported in the literature to provide the thermodynamic parameters associated with hydrogen bond dissociation.[22]

References

1. Goddard, E. D.; Benson, G. C. *Canadian Journal of Chemistry* **1957,** *35* (9), 986-991.
2. Paredes, S.; Tribout, M.; Ferreira, J.; Leonis, J. *Colloid & Polymer Sci* **1976,** *254* (7), 637-642.
3. Helenius, A.; McCaslin, D. R.; Fries, E.; Tanford, C. [63] Properties of detergents. In *Methods in Enzymology*, Sidney Fleischer, L. P., Ed. Academic Press: 1979; Vol. Volume 56, pp 734-749.
4. Neugebauer, J. M. [18] Detergents: An overview. In *Methods in Enzymology*, Murray, P. D., Ed. Academic Press: 1990; Vol. Volume 182, pp 239-253.
5. Harris, E. L. V.; Angal, S. Protein Purification Applications: A Practical Approach. IRL Press at Oxford University Press: New York, NY, 1990; p 71.
6. Rosen, M.; Tracy, D. *J Surfact Deterg* **1998,** *1* (4), 547-554.
7. Menger, F. M.; Keiper, J. S. *Angewandte Chemie International Edition* **2000,** *39* (11), 1906-1920.
8. Zana, R.; Benrraou, M.; Rueff, R. *Langmuir* **1991,** *7* (6), 1072-1075.
9. Menger, F. M.; Littau, C. A. *Journal of the American Chemical Society* **1993,** *115* (22), 10083-10090.
10. Tehrani-Bagha, A. R.; Holmberg, K. *Materials* **2013,** *6* (2), 580-608.
11. Rungsardthong, U.; Ehtezazi, T.; Bailey, L.; Armes, S. P.; Garnett, M. C.; Stolnik, S. *Biomacromolecules* **2003,** *4*, 683-690.
12. Wang, X.; Kelkar, S. S.; Hudson, A. G.; Moore, R. B.; Reineke, T. M.; Madsen, L. A. *ACS Macro Lett.* **2013,** *2* (11), 1038-1041.

13. Patel, M. A., T. *Biophysical Journal* **2005,** *88*, 2089-2103.

14. Prevette, L. E.; Kodger, T. E.; Reineke, T. M.; Lynch, M. L. *Langmuir* **2007,** *23*, 9773-9784.

15. Prevette, L. E.; Lynch, M. L.; Kizjakina, K.; Reineke, T. M. *Langmuir* **2008,** *24*, 8090-8101.

16. Bronich, T.; Kabanov, A. V.; Marky, L. A. *Journal of Physical Chemistry B* **2001,** *105*, 6042-6050.

17. Choosakoonkriang, S. L., B.; Koe, G.; Koe, J.; Middaugh, C. *Journal of Pharmaceutical Sciences* **2003,** *92* (8), 1710-1722.

18. Matulis, D.; Rouzina, I.; Bloomfield, V. A. *Journal of Molecular Biology* **2000,** *296* (4), 1053-1063.

19. Kim, W.; Yamasaki, Y.; Kataoka, K. *J. Phys. Chem. B* **2006,** *110* (Copyright (C) 2011 American Chemical Society (ACS). All Rights Reserved.), 10919-10925.

20. Ball, V.; Maechling, C. *International Journal of Molecular Sciences* **2009,** *10*, 3283-3315.

21. Kizjakina, K.; Bryson, J. M.; Grandinetti, G.; Reineke, T. M. *Biomaterials* **2012,** *33* (6), 1851-1862.

22. Wang, F. C.; Feve, M.; Lam, T. M.; Pascault, J.-P. *Journal of Polymer Science Part B: Polymer Physics* **1994,** *32* (8), 1305-1313.

Chapter 7 : Appendix A – Additional FTIR Data and Collaborations

7.1 Introduction

As discussed earlier in Chapter 5, variable temperature Fourier transform infrared (FITR) spectroscopy is a valuable tool for the analysis of hydrogen-bonding behavior in polymer systems. Here, we will discuss the contributions from variable temperature FTIR to four previously published studies regarding the synthesis and characterization of novel copolymers. In each of these publications, FTIR is used in corroboration with other analytical techniques to provide valuable information concerning the structural effects of various polymer architectures on the hydrogen bonding and overall polymer morphology.

7.2 Variable Temperature FTIR Analysis Hydrogen Bonding in Segmented Polyurethanes with Triptycene-Containing Hard Segments

7.2.1 Background & Experimental Details

In 2013, Chang *et al*. reported on the synthesis of novel segmented polyurethanes from polytetramethylene glycol (PTMG) that contain triptycene in the hard segments.[1] The diisocyantes used were hexamethylene diisocyanate (HDI) and 4,4'-methylenebis(phenyl isocyanate) (MDI). Hydroquinone bis(2-hydroxyethyl)ether (HQEE) and triptycene-1,4-hydroquinone bis(2-hydroxyethyl)ether (TD) were used as the chain extenders. Four final combinations of segmented polyurethanes were achieved: HDI-HQEE, HDI-TD, MDI-HQEE, and MDI-TD. HDI and MDI were both used to explore the effects of their varying flexibilities, and HQEE was used as an analog to the bulky triptycene unit for comparison.[1]

Variable temperature FTIR experiments were performed on each of these samples to assess the hydrogen bonding contents and to observe hydrogen bond dissociation at elevated temperatures. The instrument used in these experiments was a Varian 670-IR equipped with a PIKE GladiATR^{TM} heated diamond stage attachment. Spectra were collected from 4000-400 cm^{-1} at a resolution of 4 cm^{-1}, and each spectrum was an average of 32 scans. Initial spectra were collected at 30 ºC, and then in 10 ºC increments as the temperature increased to 190 ºC at a ramping rate of 1 ºC/min.[1]

7.2.2 Results & Discussion

Hydrogen bonding in polyurethane samples will cause shifts in the stretching frequencies for both the NH and carbonyl regions.[2] Figure 7.1 shows the carbonyl region for each of the four polyurethane samples at 30 ºC. For each of these samples there are two carbonyl bands. The peak at lower wavenumbers corresponds to carbonyl groups participating in ordered hydrogen bonding, and the peak at higher wavenumbers is the free carbonyl peak. In addition, a third peak is observed as a shoulder around 1705 cm^{-1} in the MDI-HQEE sample. This peak is attributed to disordered hydrogen bonding of the carbonyl groups.[3] Literature has previously suggested that the strength of carbonyl hydrogen bonds can be determined from the location of these carbonyl stretching bands. Peaks with lower wavenumbers are indicative of stronger hydrogen-bonding interactions.[4]

At 30 ºC, the polyurethane samples listed in order of decreasing wavenumber absorption for the hydrogen-bonding peak are MDI-TD, MDI-HQEE, HDI-TD, and HDI-HQEE. In

addition, the hydrogen-bonding peak of HDI-HQEE exhibits the highest intensity, while the MDI-TD has the lowest. The weaker hydrogen bonding in the MDI-TD sample is attributed to the bulky triptycene unit and the reduced flexibility of the MDI inhibiting efficient chain packing. Conversely, the increased flexibility of HDI and less sterically hindered HQEE allow for more efficient packing and provide HDI-HQEE with a higher content of stronger hydrogen bonds. It was not unexpected that the absorption wavenumbers for HDI-TD and MDI-HQEE fell in the middle given their mixed combination of bulkiness and chain flexibility.[1]

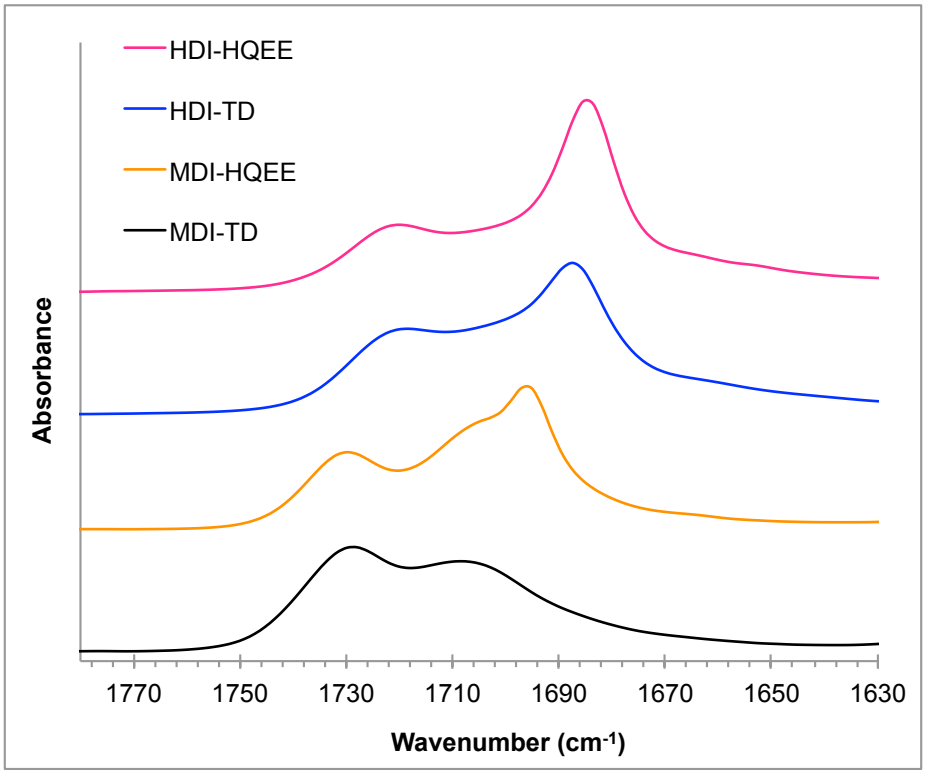

Figure 7.1 Carbonyl-stretching region of FTIR spectra for polyurethane samples at 30 ºC (absorption values omitted because the data is vertically offset)

The NH-stretching region was also examined to gain a better understanding of the hydrogen-bonding behavior. Previous literature has shown that more narrow peaks in the NH-stretching region are indicative of increased hydrogen-bonding content.[5] Figure 7.2 shows the FTIR spectra for the four polyurethanes in the NH-stretching region at 30 ºC. MDI-TD clearly has the broadest peak and HDI-HQEE has the narrowest peak. The widths of the MDI-HQEE and HDI-TD peaks are very similar to each other and fall between the other two. These results confirm our earlier observations in the carbonyl region.[1]

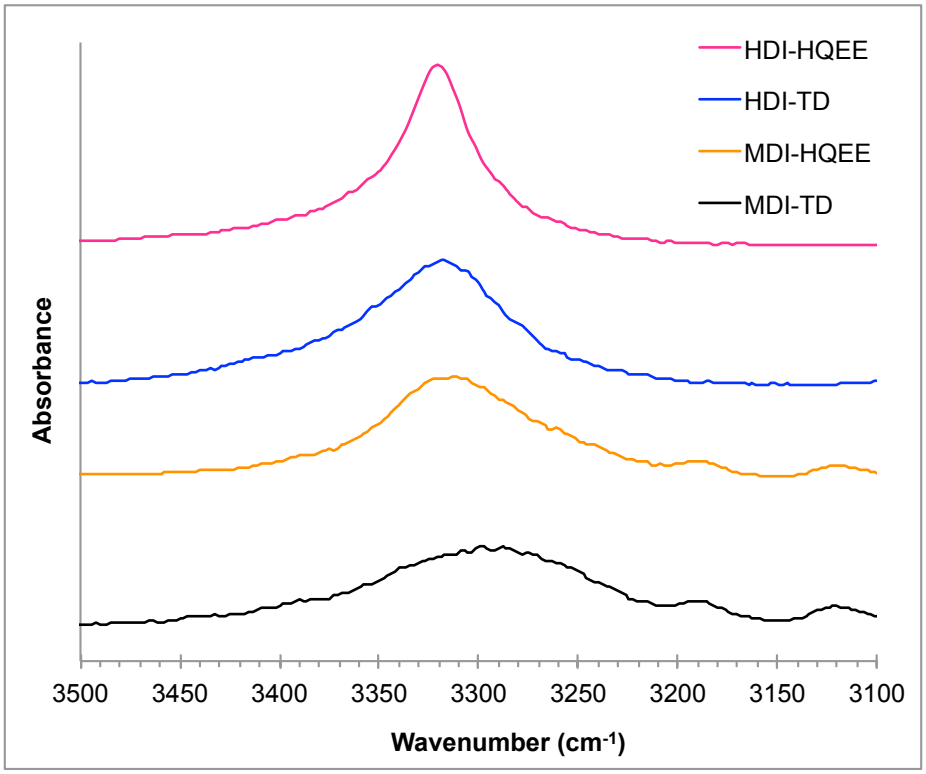

Figure 7.2 NH-stretching region of FTIR spectra for polyurethane samples at 30 ºC (absorption values omitted because the data is vertically offset)

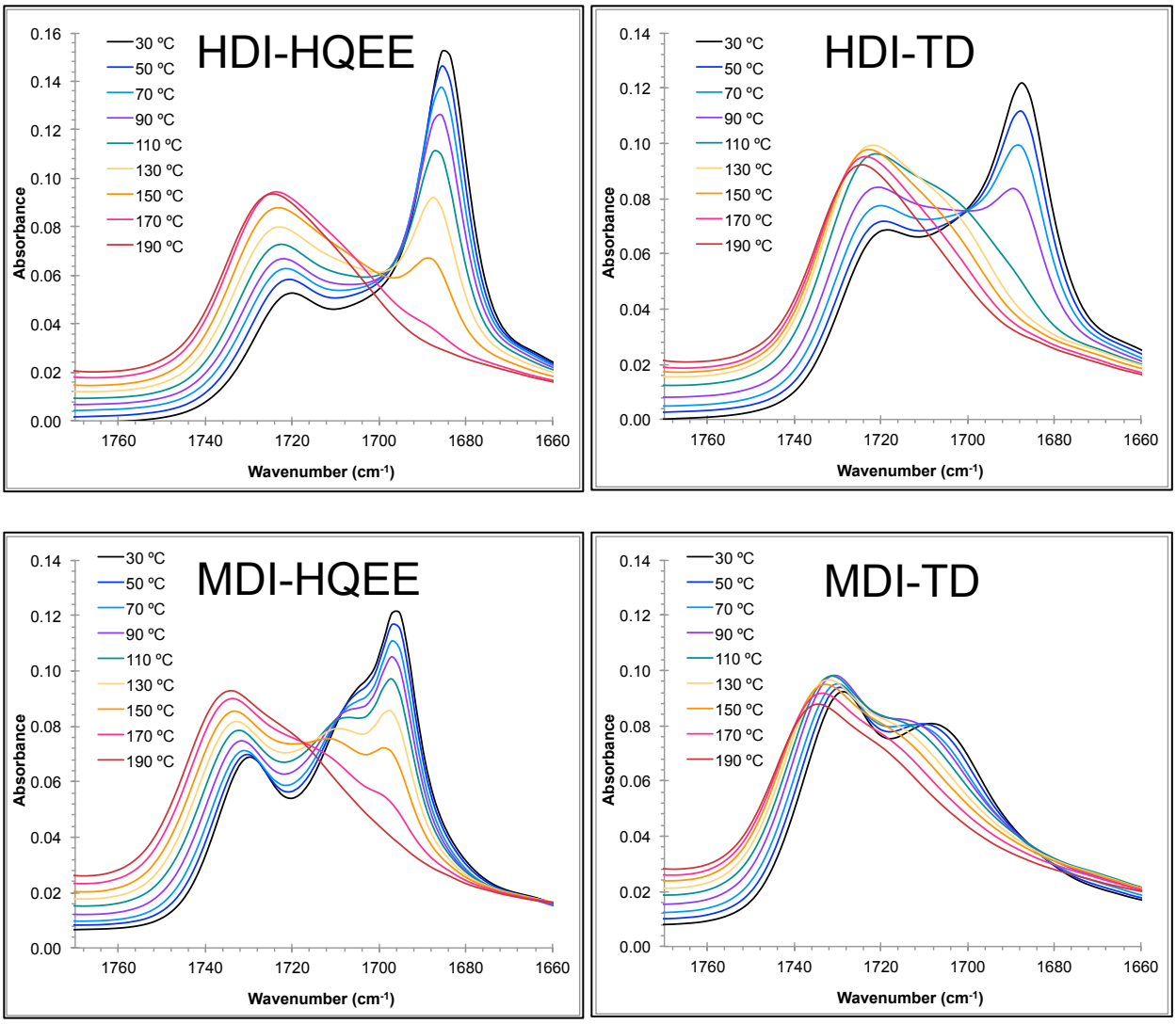

Figure 7.3 Variable temperature FTIR spectra for the polyurethane samples in the carbonyl-stretching region

Figure 7.3 shows the variable temperature spectra (in 20 ºC increments for ease of viewing) of the carbonyl region for each of these polyurethanes. These data provide valuable information regarding the dissociation behavior of the hydrogen bonds for the differing samples. As the temperature increases, more hydrogen bonds are disrupted and a shift toward higher

wavenumbers is observed for all of the samples. However, there is a distinct difference in the hydrogen-bond dissociation temperature among the polymer samples. Hydrogen bond dissociation is not complete until much higher temperatures in the polyurethanes containing HQEE. Complete dissociation is not seen until 170 to 190 ºC for these two samples. The triptycene-containing polyurethanes, however, exhibit hydrogen bond dissociation earlier around 110 to 130 ºC. These results are consistent with the previous hard segment structure-based explanation of hydrogen bonding strengths in these samples. The HQEE polyurethanes required higher temperatures for hydrogen bond dissociation due to their more efficient packing and stronger hydrogen-bonding interactions. Similarly, the bulky triptycene units in the TD polyurethanes allow for weaker hydrogen bonds; therefore, lower temperatures are required for dissociation.[1]

In summary, variable temperature FTIR analysis was able to provide valuable insight into the hydrogen bonding behavior of these polyurethane samples. Copolymers containing bulky triptycene units in the hard segment exhibited weaker hydrogen-bonding interactions that dissociated at lower temperatures than their HQEE counterparts. These results were in good agreement with additional analysis by small angle X-ray scattering (SAXS), atomic force microscopy (AFM), and dynamic mechanical analysis (DMA).[1]

7.3 Variable Temperature FTIR Analysis of Hydrogen Bonding in Poly(dimethyl siloxane) Poly(oxamide) Segmented Copolymers

7.3.1 Background & Experimental Details

Buckwalter *et al*. reported on the synthesis of poly(dimethyl siloxane) polyoxamide (PDMS-Ox) segmented copolymers in 2013.[6] Several series of copolymers were made with 2K, 5K, and 12K g/mol PDMS. For each molecular weight series, the number of methylene groups used as spacers between the oxamide groups varied from 2, 4, 6, or 8. The purpose of this study was to investigate the structure-property relationships of these copolymers; more specifically, to determine the effects of varying molecular weights in the soft segment and oxamide spacing in the hard segment on the thermal and mechanical properties of the copolymers.[6]

Variable temperature FTIR experiments were performed on each of the PDMS2K-Ox samples to assess the effects of oxamide spacing on the hydrogen bonding in the hard segments and to observe hydrogen bond dissociation at elevated temperatures. The instrument used in these experiments was a Varian 670-IR equipped with a PIKE GladiATR™ heated diamond stage attachment. Spectra were collected from 4000 to 400 cm^{-1} at a resolution of 4 cm^{-1}, and each spectrum was an average of 32 scans. Initial spectra were collected at 30 ºC, and then in 5 ºC increments as the temperature increased to 195 ºC at a ramping rate of 1 ºC/min. (Figures are plotted in 20 ºC increments for ease of viewing.) Each sample was dried prior to FTIR analysis.[6]

7.3.2 Results & Discussion

Hydrogen bonding in these copolymers occurs between the carbonyl and NH groups of the oxamides and can be easily monitored through characteristic shifts in the stretch vibrations for the corresponding IR absorption bands. Furthermore, the carbonyl region for semicrystalline polyamides typically exhibits three contributing peaks that are sensitive to order. These include ordered hydrogen bonding in the crystalline regions, disordered hydrogen bonding in the amorphous domains, and free carbonyl groups that are not bonded.[7-8] In addition, ordered hydrogen bonding was expected in these samples, due to the crystallinity of the hard segments that was observed in differential scanning calorimetry (DSC) experiments.[6]

Figure 7.4 shows the variable temperature spectra for the two PDMS2K-Ox samples with the lowest and highest number of methylene spacers between oxamide groups. For all of the samples at 30 ºC, the major contributor to the carbonyl region is the ordered hydrogen-bonding band around 1650 cm^{-1}. A very small peak for the free carbonyl groups is also observed around 1685 cm^{-1}. As the temperature was increased, the contribution from ordered hydrogen bonding decreased, while an increase in disordered bonding (around 1660 to 1670 cm^{-1}) and free carbonyl groups was observed due to hydrogen bond dissociation. This hydrogen bond dissociation is also observed in the NH-stretching region, shown in Figure 7.5. At 30 ºC, the observed peak around 3300 cm^{-1} is attributed to hydrogen bonding. With increasing temperature this peak diminishes while the free N-H band around 3400 cm^{-1} gradually grows. However, the peak at higher wavenumbers is difficult to distinguish from noise because the signal is so low in this region.[6]

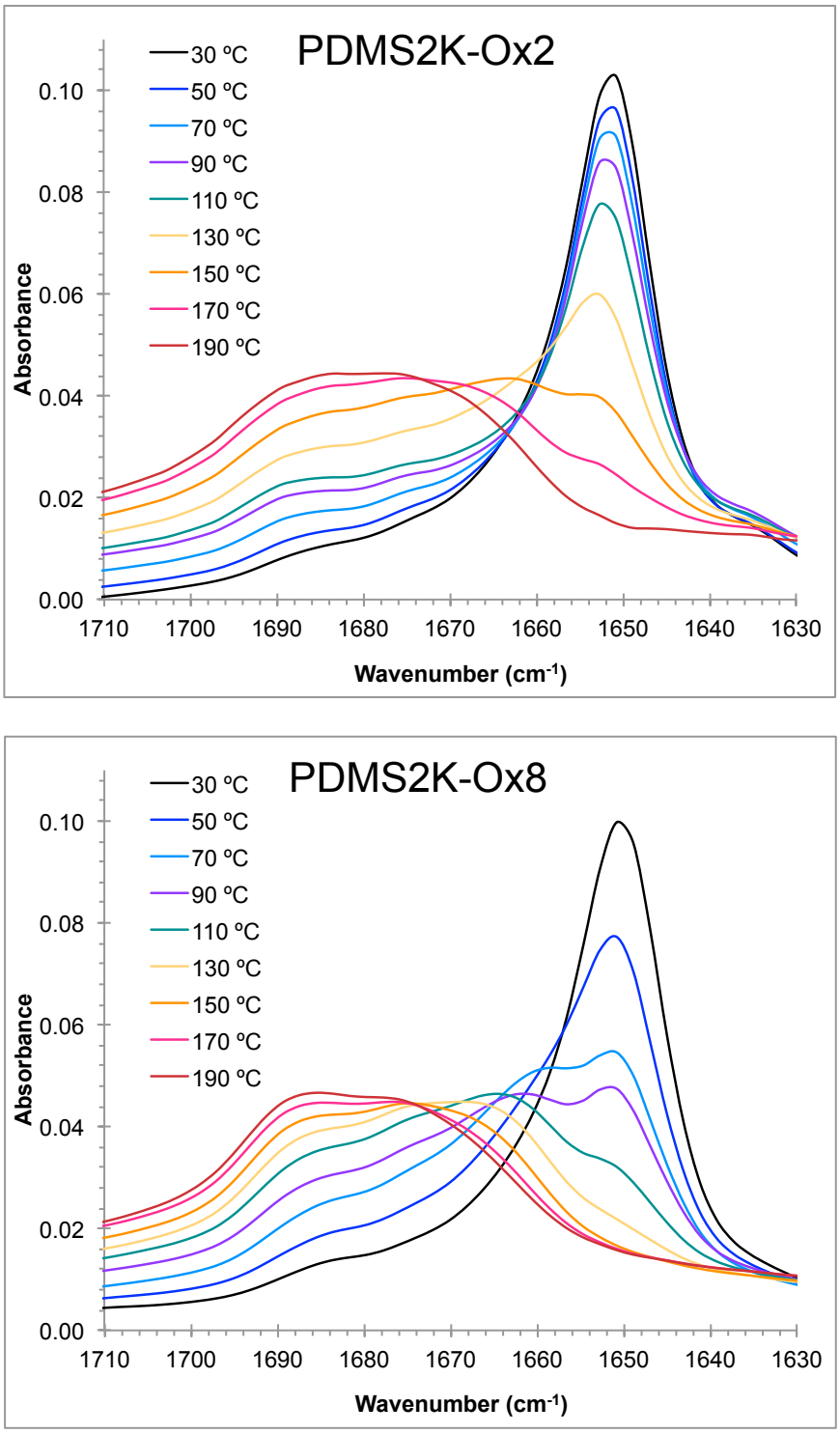

Figure 7.4 Carbonyl-stretching region of variable temperature FTIR spectra for the (top) PDMS2K-Ox2 and (bottom) PDMS2K-Ox8 samples

The significance of the oxamide spacer length in the hydrogen bonding interactions of these copolymers is also apparent in the variable temperature data. The IR spectra for PDMS2K-Ox8 show complete dissociation of the ordered hydrogen bonding around 130 ºC. Above this temperature only disordered bonding and free carbonyl groups are observed. For PDMS2K-Ox2 this dissociation is not complete until 190 ºC. This discrepancy in temperature is attributed to the enhanced packing efficiency of the copolymer chains with shorter spacer lengths between oxamide groups, allowing for more thermally stable hydrogen-bonding interactions. However, longer, more flexible methylene linkages prevent the oxamide groups from packing together as tightly and result in decreased thermal stability. This phenomenon is further emphasized in Figure 7.6, which shows the carbonyl region for each of the four PDMS2K-Ox samples at 100 ºC. At this temperature, the major contribution to the carbonyl-stretching absorption for PDMS2K-Ox2 is still from ordered hydrogen bonding. As the oxamide spacing increases to 4, 6, and 8 methylene units, a corresponding decrease in ordered hydrogen bonding is observed, while contributions from disordered hydrogen bonding (1665 cm^{-1}) and free carbonyl groups increase. This further confirms that the shortest methylene spacer provided the most ordered and thermally stable hard segment hydrogen bonding interactions.[6]

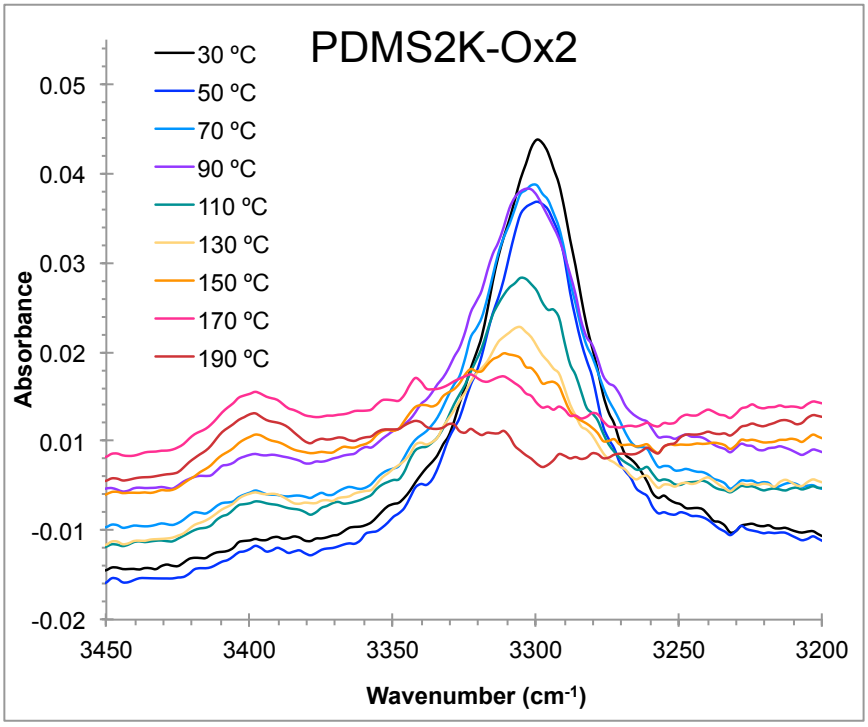

Figure 7.5 NH-stretching region of variable temperature FTIR spectra for PDMS2K-Ox2

In conclusion, variable temperature FTIR analysis was able to provide valuable information regarding the effects of oxamide spacing to hard segment hydrogen bonding interactions in these PDMS-Ox copolymers. This analysis was used in combination with several other analytical techniques to complete a thorough study into the structure-property relationship of these copolymers. In general, FTIR results indicated that the smallest methylene spacer provided the most thermally stable hydrogen bonding interactions. This was in good agreement with DSC results, which showed an increase in the hard segment melting temperature with decreasing spacer length. In addition, the polymer with the smallest oxamide spacing was also shown to exhibit the best mechanical properties out of all the samples tested.[6]

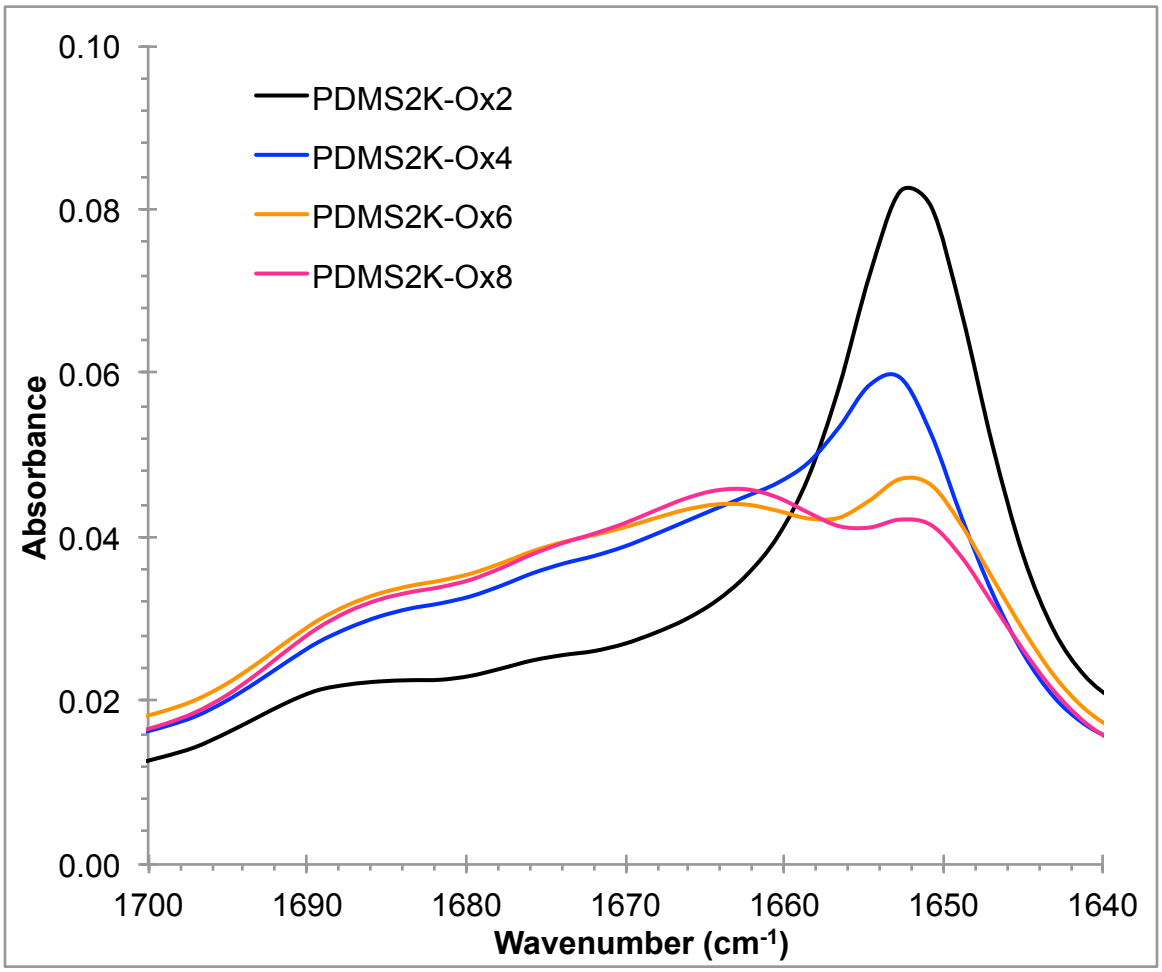

Figure 7.6 Carbonyl-stretching region of FTIR spectra for PDMS2K-Ox samples at 100 ºC

7.4 Variable Temperature FTIR Analysis of Hydrogen Bonding in Poly(propylene glycol) Poly(trioxamide) and Poly(urea oxamide) Segmented Copolymers

7.4.1 Background & Experimental Details

In 2014, Buckwalter *et al*. conducted a similar study to the one in Section 8.3 involving the synthesis of segmented copolymers with tunable hydrogen bonding architectures.[9] In this investigation two novel poly(propylene glycol) (PPG) based copolymers were synthesized with

strong hydrogen bonding hard segments. PPG polytrioxamide (PPG-TriOx) and PPG poly(urea oxamide) (PPG-UOx) both contain multiple hydrogen bond donors and acceptors per hard segment. PPG polyoxamide (PPG-Ox) and PPG polyuria (PPG-U) were also synthesized as structurally similar analogs with fewer hydrogen bonding sites. This study looked at the synthesis and characterization of the four copolymers, with specific emphasis on the increased hydrogen-bonding interactions observed in PPG-TriOx and PPG-UOx and their effect on the thermal and mechanical properties.[9]

Variable temperature FTIR experiments were performed on each of the four copolymers to assess the hydrogen bonding interactions and to investigate hydrogen bond dissociation at elevated temperatures. The instrument used in these experiments was a Varian 670-IR equipped with a PIKE GladiATR^{TM} heated diamond stage attachment. Spectra were collected from 4000 to 400 cm^{-1} at a resolution of 4 cm^{-1}, and each spectrum was an average of 32 scans. Initial spectra were collected at 30 ºC, and then in 5 ºC increments as the temperature increased to 195 ºC at a ramping rate of 1 ºC/min. (Figures are plotted in 20 ºC increments for ease of viewing.) Each sample was dried prior to FTIR analysis. For some of the experiments, the sample was cooled at ambient conditions after the first heating cycle and then heated again to look at thermal reversibility.[9]

7.4.2 Results & Discussion

Similar to the first study, Buckwalter *et al*. focused on the carbonyl and NH-stretching regions to monitor hydrogen bonding in the FTIR spectra for these copolymers.[6,9] Figure 7.7

shows the variable temperature FTIR spectra for PPG-Ox and PPG-TriOx in the carbonyl-stretching region. At 30 ºC, PPG-Ox displays an ordered hydrogen-bonding peak at 1649 cm^{-1} and PPG-TriOx shows a similar peak at 1618 cm^{-1}. The large downshift in wavenumbers for the PPG-TriOx peak is indicative of more ordered, efficient packing between the trioxamide hard segments than what is present in the PPG-Ox hard segments. Both samples also display a small peak around 1684 cm^{-1}, corresponding to free carbonyl groups. This peak appears as a shoulder in the PPG-TriOx sample, due to the additional small peak at 1673 cm^{-1} that is due to unreacted oxamic hydrazide end-groups. The absorption in the NH-stretching region, shown in Figure 7.8, shows the same trend in wavenumber shift. The NH band for PPG-Ox is centered at 3295 cm^{-1}, while the more ordered hydrogen bonding in PPG-TriOx appears at much lower wavenumbers, around 3210 cm^{-1}.[9]

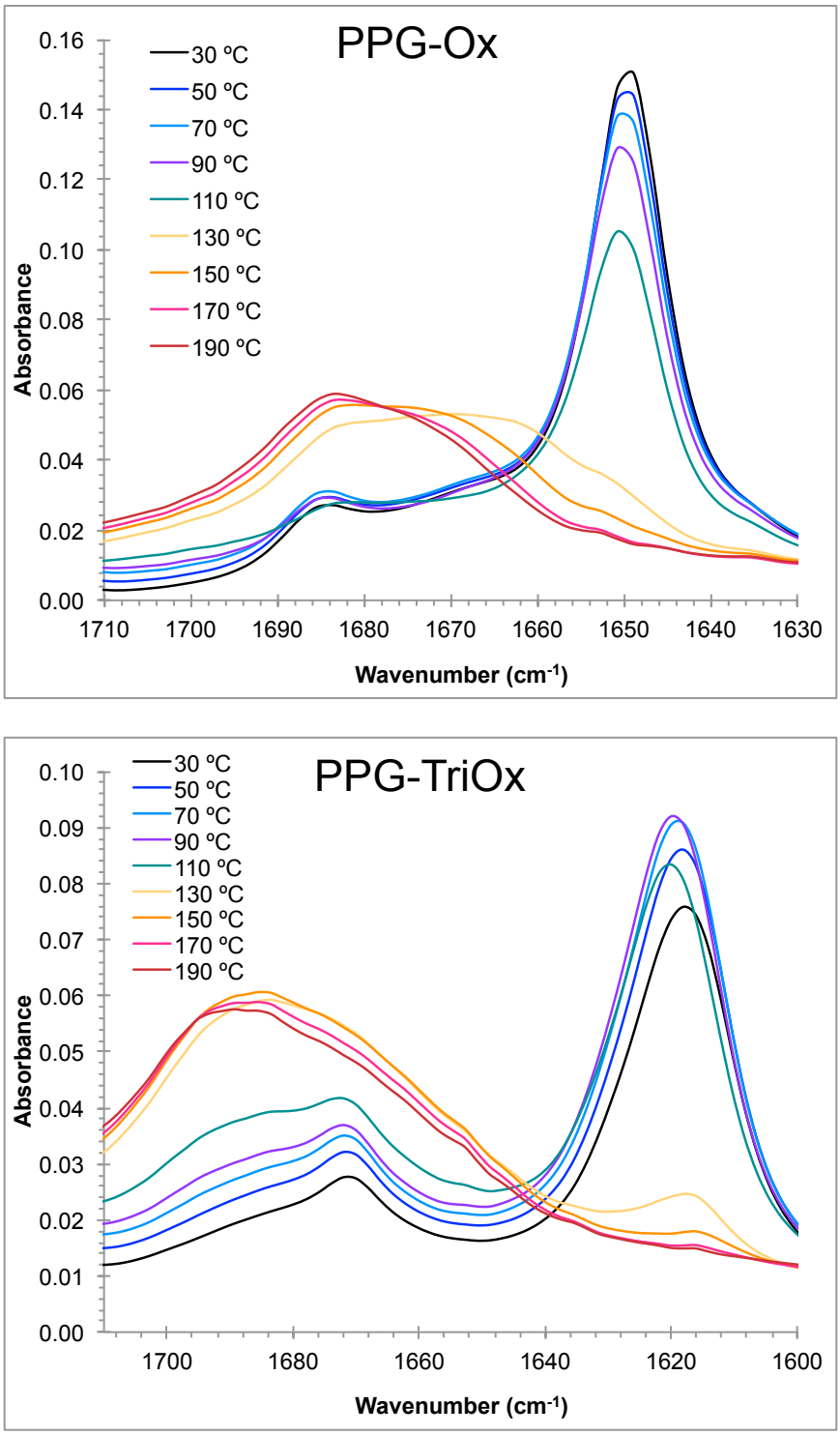

Figure 7.7 Carbonyl-stretching region of variable temperature FTIR spectra for the (top) PPG-Ox and (bottom) PPG-TriOx samples

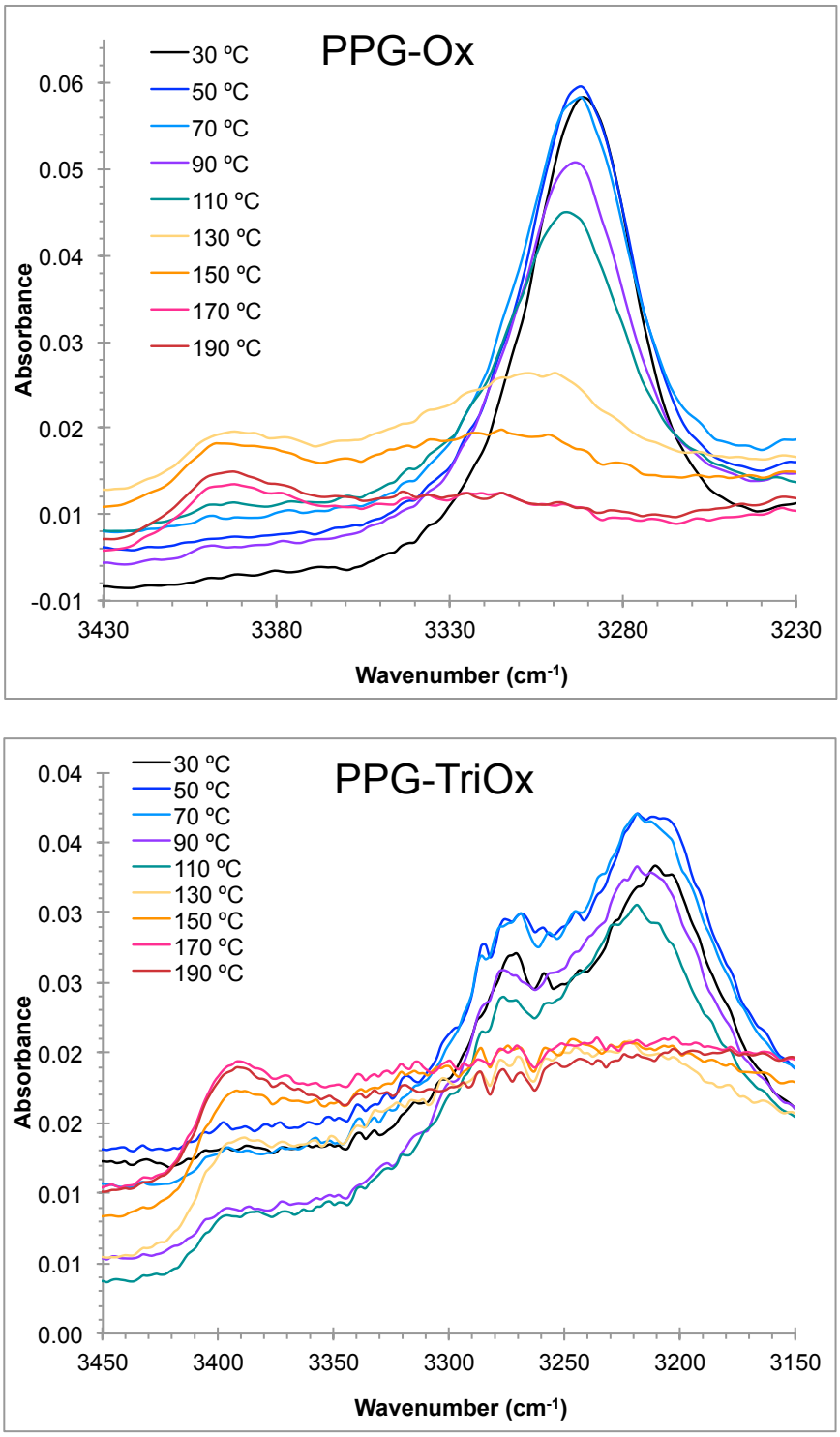

Figure 7.8 NH-stretching region of variable temperature FTIR spectra for the (top) PPG-Ox and (bottom) PPG-TriOx samples

PPG-Ox and PPG-TriOx display very similar hydrogen bond dissociation profiles at elevated temperatures in Figure 7.7. Between 110 ºC and 130 ºC we observe a dramatic reduction in the contribution from ordered hydrogen bonding and a corresponding increase in the disordered hydrogen bonding and free carbonyl bands. Figure 7.8 shows similar dissociation behavior in the NH-stretching bands. Both spectra exhibit a dramatic loss in the hydrogen-bonding peak at 130 ºC, as the free NH peak starts to grow in around 3390 cm^{-1}. Furthermore, Figure 7.9 shows the thermoreversible nature of the hydrogen bonding interactions for PPG-TriOx. After the sample was initially heated to 195 ºC, it was cooled back down to room temperature at ambient conditions and then reheated to 195 ºC under the same conditions as the first heating cycle. As shown, the two spectra are almost identical and the carbonyl-stretching bands return to their original wavenumbers after cooling. The only differences that were observed are a slight decrease in intensity and complete dissociation of the ordered hydrogen bonds occurs at 110 ºC, instead of 130 ºC, during the second heating cycle. In general, however, elevated temperatures do not appear to damage the copolymer or permanently alter the hydrogen bonding interactions.[9]

The variable temperature FTIR profiles for PPG-U and PPG-UOx, as shown in Figure 7.10, are very different from the PPG-Ox and PPG-TriOx. The individual contributions to the carbonyl-stretching region are less apparent in these spectra because of the very broad and convoluted nature of the peaks. At 30 ºC, the center of the carbonyl peak is at 1630 cm^{-1} for PPG-U. A small shoulder is also present around 1685 cm^{-1}. This is attributed to free carbonyl groups. The carbonyl-stretching band for PPG-UOx is centered at 1665 cm^{-1}. This higher wavenumber for the oxamide-containing hard segment may be related to the fact that the peak

contains contributions from both the oxamide and urea carbonyl groups.[9] However, it is also higher than the hydrogen-bonded carbonyl bands observed for all three of the other copolymers in this study, which is indicative of weaker hydrogen-bonding interactions.[4] Across the temperature range, we see a gradual shift and broadening of the peaks, from 1630 to 1652 cm^{-1} in the PPG-U and from 1665 to 1683 cm^{-1} in the PPG-UOx. As the temperature increased, the PPG-U spectra also showed an increase in the free carbonyl peak intensity at 1685 cm^{-1}, due to the disruption of hydrogen-bonding interactions. It is probable that the free carbonyl band is also convoluted within the single, broad peak observed for PPG-UOx, which would play a role in the shift to higher wavenumbers at elevated temperatures.[9]

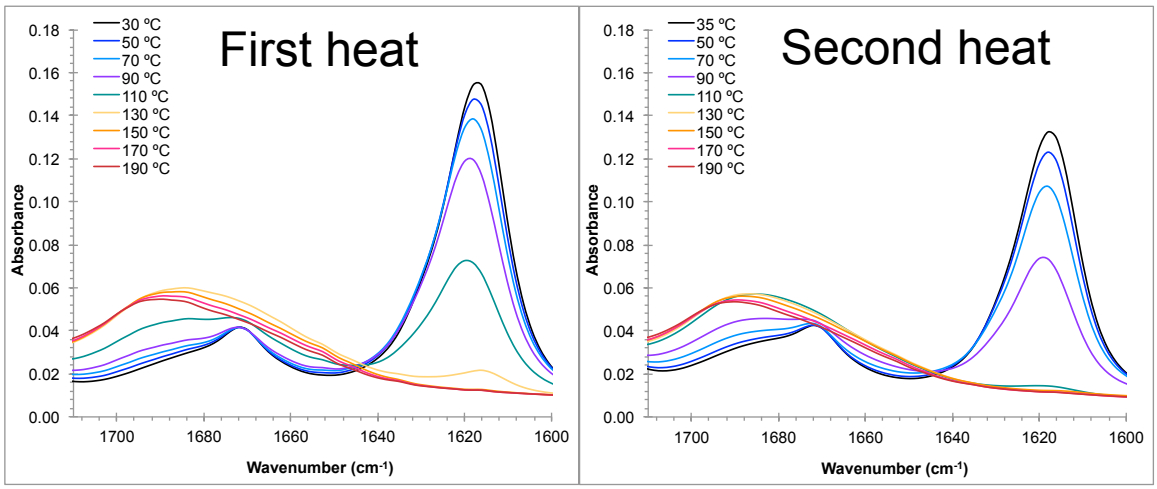

Figure 7.9 Carbonyl-stretching region of variable temperature FTIR spectra of the PPG-TriOx polyurethane for the first and second heat cycles

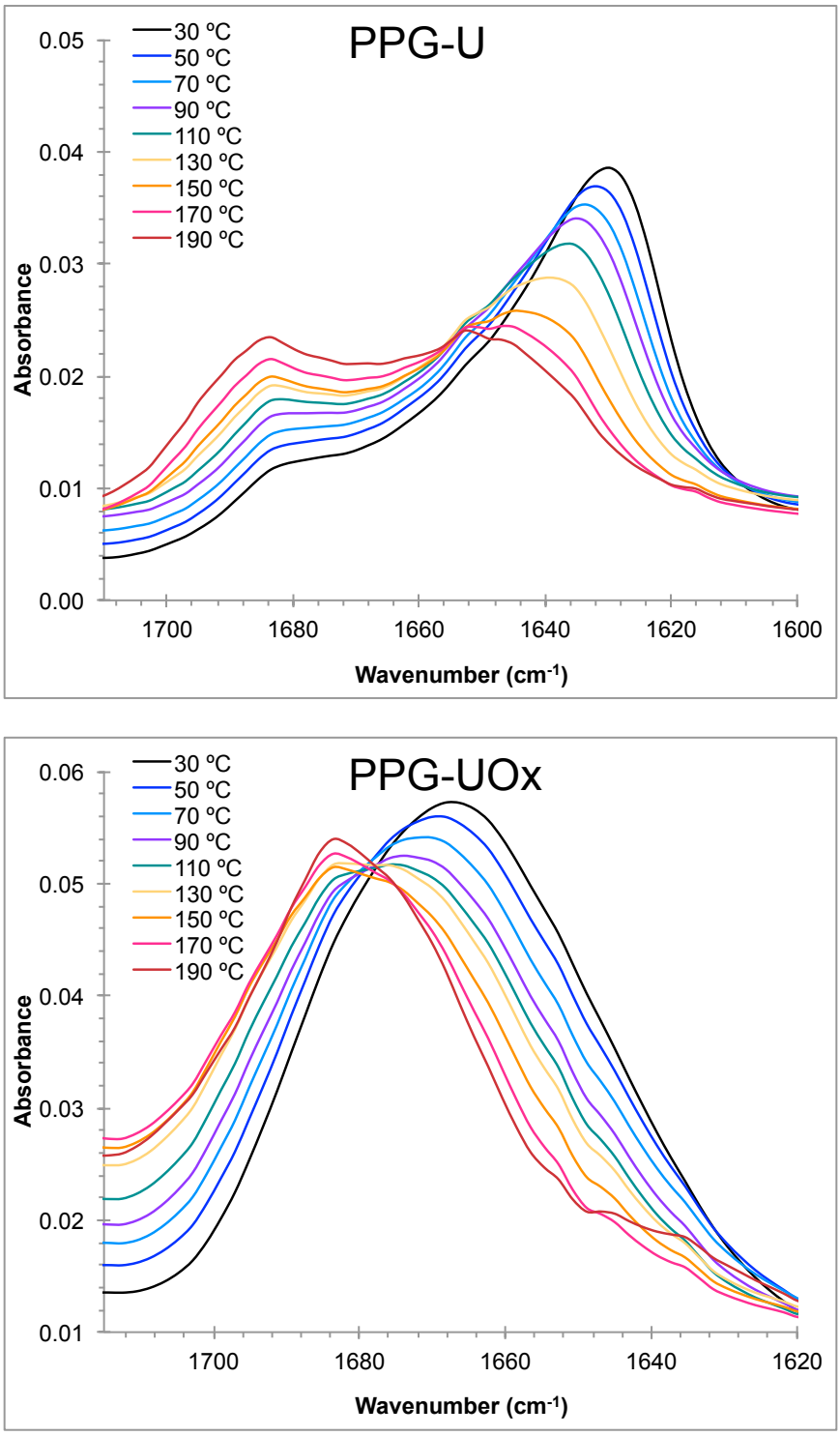

Figure 7.10 Carbonyl-stretching region of variable temperature FTIR spectra for the (top) PPG-U and (bottom) PPG-UOx samples

In summary, variable temperature FTIR analysis was successfully utilized to gain a better understanding into the hydrogen-bonding interactions present in these segmented copolymers. The PPG-TriOx copolymer showed highly ordered and thermally reversible hydrogen-bonding interactions, with dissociation temperatures similar to that of the PPG-Ox. These temperatures were in good agreement with the melting temperatures observed with DSC. The PPG-UOx spectra revealed weaker hydrogen bonds, which was consistent with the poor physical properties observed in additional experiments.[9]

7.5 Variable Temperature FTIR Analysis of Hydrogen Bonding in Nucleobase-Containing Triblock Copolymers and Supramolecular Blends

7.5.1 Background & Experimental Details

Zhang *et al*. reported on the novel synthesis of ABA triblock copolymers that contain nucleobases in 2015.[10] Poly(*n*-butyl acrylate) (P*n*BA) was used as the soft, central block between either adenine acrylic (AdA) or thymine acrylic (ThA) hard, external blocks. A supramolecular blend of poly(AdA-*b*-*n*BA-*b*-AdA) and poly(ThA-*b*-*n*BA-*b*-ThA) at a 1:1 ratio was also formed to look at the effects of complementary hydrogen bonding between adenine and thymine. In addition to other analytical techniques, variable temperature FTIR was used to probe the hydrogen bonding interactions of these triblock copolymers, with specific emphasis on thermoreversibility.[10]

Variable temperature FTIR experiments were performed on a Varian 670-IR equipped with a PIKE GladiATR^{TM} heated diamond stage attachment. Spectra were collected from 4000 to 400 cm^{-1} at a resolution of 4 cm^{-1}, and each spectrum was an average of 32 scans.

Starting at 30 ºC, spectra were collected every 10 ºC as the temperature increased to 190 ºC at a ramping rate of 1 ºC/min. (Figures are plotted in 20 ºC increments for ease of viewing.) After the heating cycle was complete, each sample was cooled at ambient conditions to room temperature and an additional spectrum was collected to examine the thermal reversibility of the hydrogen bonding interactions.[10]

7.5.2 Results & Discussion

Figure 7.11 shows the FTIR spectra, from 1750 to 1560 cm^{-1}, for each of the triblock copolymers at 30 ºC. The dominant peak observed for each of these samples at 1730 cm^{-1} is attributed to the carbonyl groups in the P*n*BA central block. The thymine-containing copolymer displays a broad peak at 1670 cm^{-1}, which corresponds to hydrogen-bonded carbonyls on the thymine units. The free, nonbonding carbonyl groups on thymine are reflected in the shoulder at 1690 cm^{-1}. Both of these peaks are also present in the blend spectrum. The adenine-containing polymer does not display any additional carbonyl groups in its spectrum, but there are three small N-H bending peaks. The two peaks at 1645 cm^{-1} and 1600 cm^{-1} are associated with hydrogen bonded N-H groups while the smaller peak at 1575 cm^{-1} is attributed to free N-H groups. These peaks are also visible in the blend.[10]

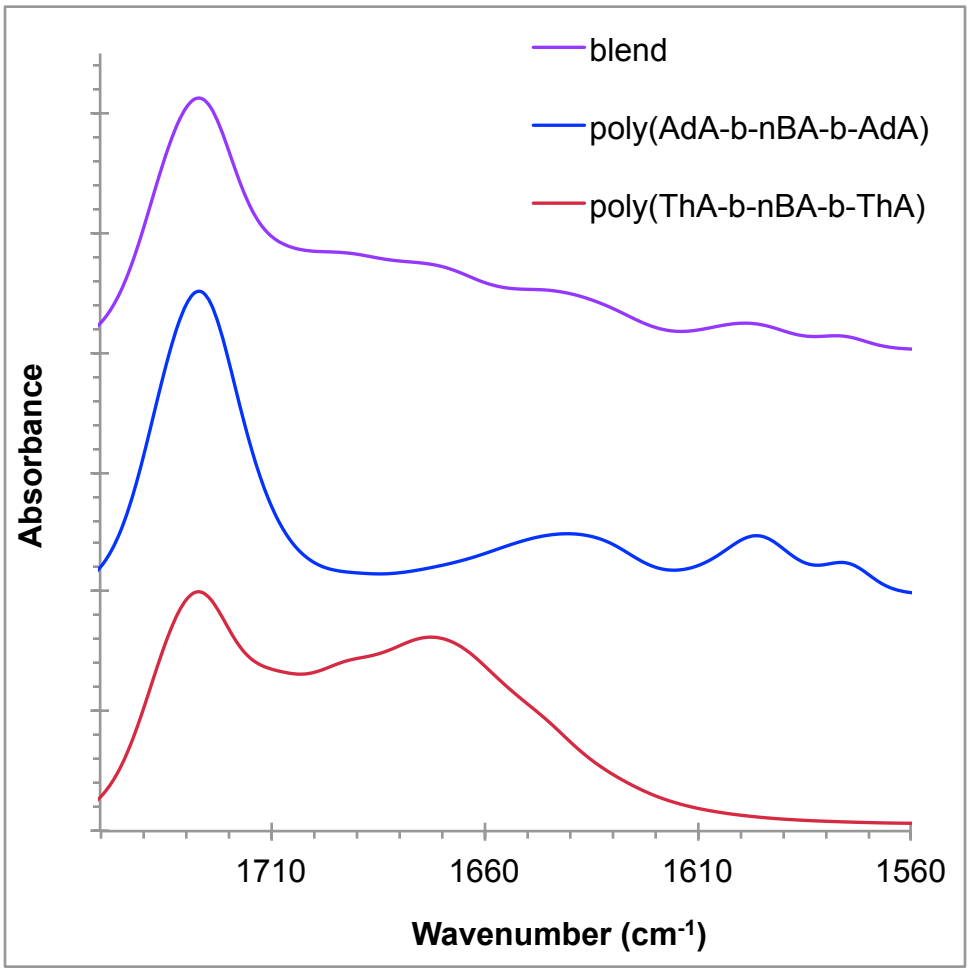

Figure 7.11 FTIR spectra in the 1750-1560 cm^{-1} region for ABA nucleobase-containing triblock copolymers and the supramolecular blend at 30 ºC (absorption values omitted because the data is vertically offset)

Figure 7.12 shows the variable temperature infrared spectra for the thymine-containing copolymer. As the temperature increases, the hydrogen-bonding carbonyl peak shifts to higher wavenumbers as the bonds dissociate and more free carbonyl groups are generated. A very minimal shift to higher wavenumbers is seen for the P*n*BA carbonyl peak as well. However, after the sample was cooled back down to ambient conditions, all of the peaks shifted back to their original wavenumbers, confirming the presence of thermoreversible hydrogen bonding

interactions in the thymine-containing copolymers. In Figure 7.13 we also observe a shift in wavenumbers at elevated temperatures for the adenine-containing copolymer. However, in this sample the N-H bending peaks shift to lower wavenumbers with increasing temperature. This is attributed to a less restricted bending motion as the hydrogen bonds dissociate. The adenine-containing copolymer also exhibited thermoreversible behavior, as all of the N-H bending peaks shifted to their original wavenumbers after cooling. Figure 7.14 confirms that the same hydrogen bond dissociation and thermoreversibility from the complementary nucleobases are also reflected in the supramolecular blend.[10]

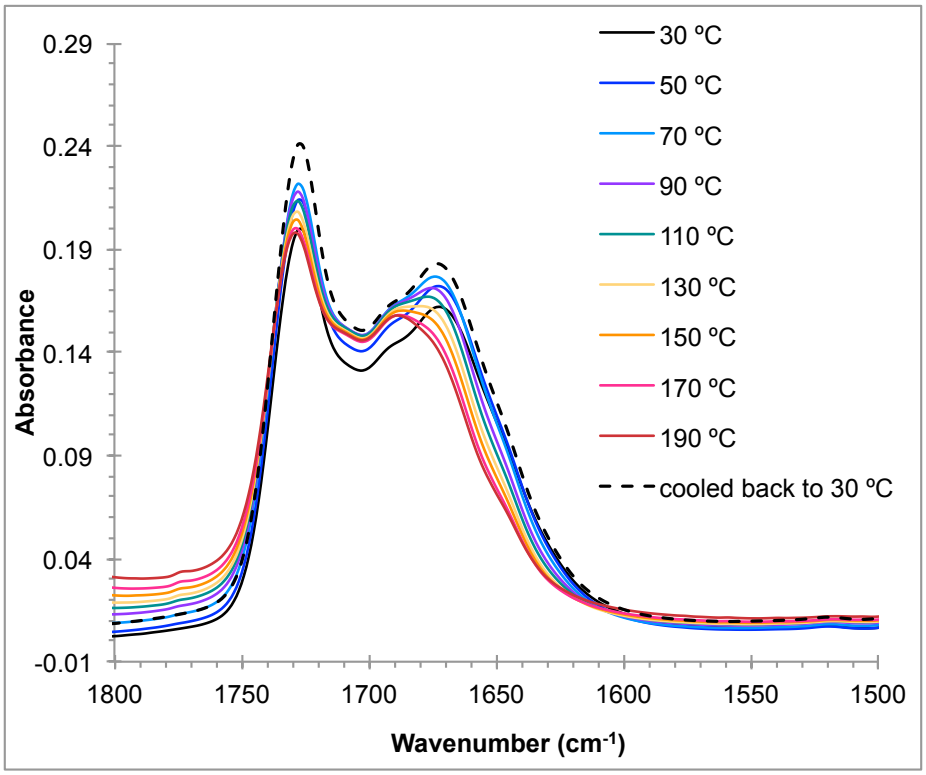

Figure 7.12 Variable temperature FTIR spectra for the poly(ThA-*b*-*n*BA-*b*-ThA) triblock copolymer in the 1750-1550 cm^{-1} region

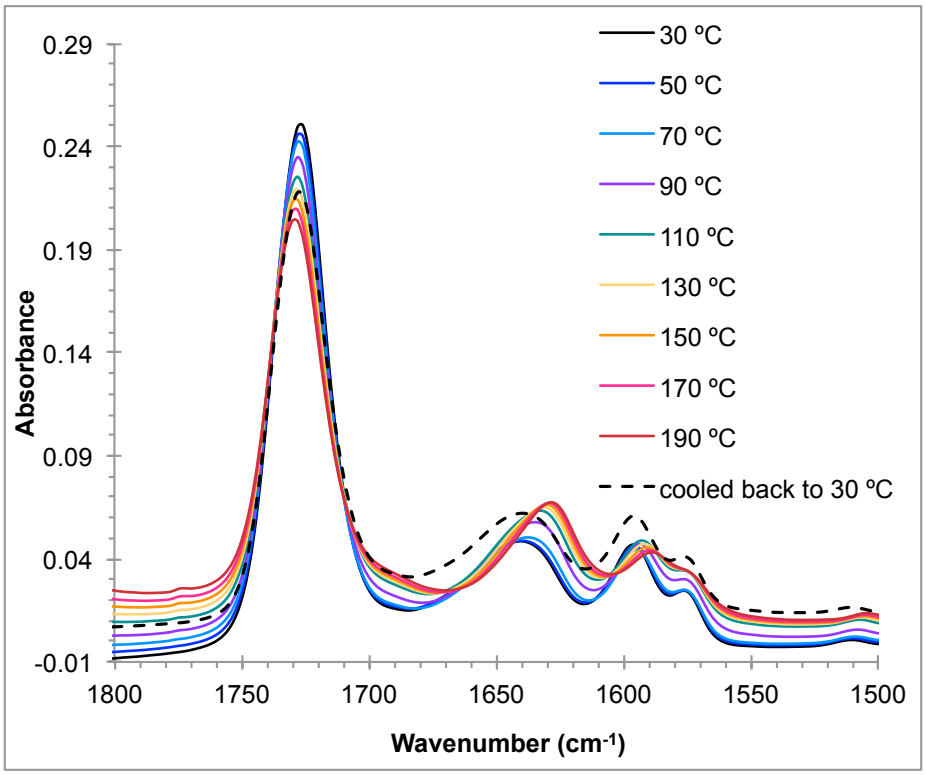

Figure 7.13 Variable temperature FTIR spectra for the poly(Ada-*b*-*n*BA-*b*-Ada) triblock copolymer in the 1750-1550 cm^{-1} region

In conclusion, variable temperature FTIR analysis confirmed that the poly(AdA-*b*-*n*BA-*b*-AdA) and poly(ThA-*b*-*n*BA-*b*-ThA) triblock copolymers, as well as the supramolecular blend of the two, all contained thermoreversible hydrogen bonding interactions. In addition, the supramolecular blend spectra exhibited contributions from multiple forms of hydrogen bonds, due to the complementarity of thymine and adenine while they were mixed in the same sample. These results also provided additional support for other morphological and mechanical analyses, including SAXS, DMA, and AFM.[10]

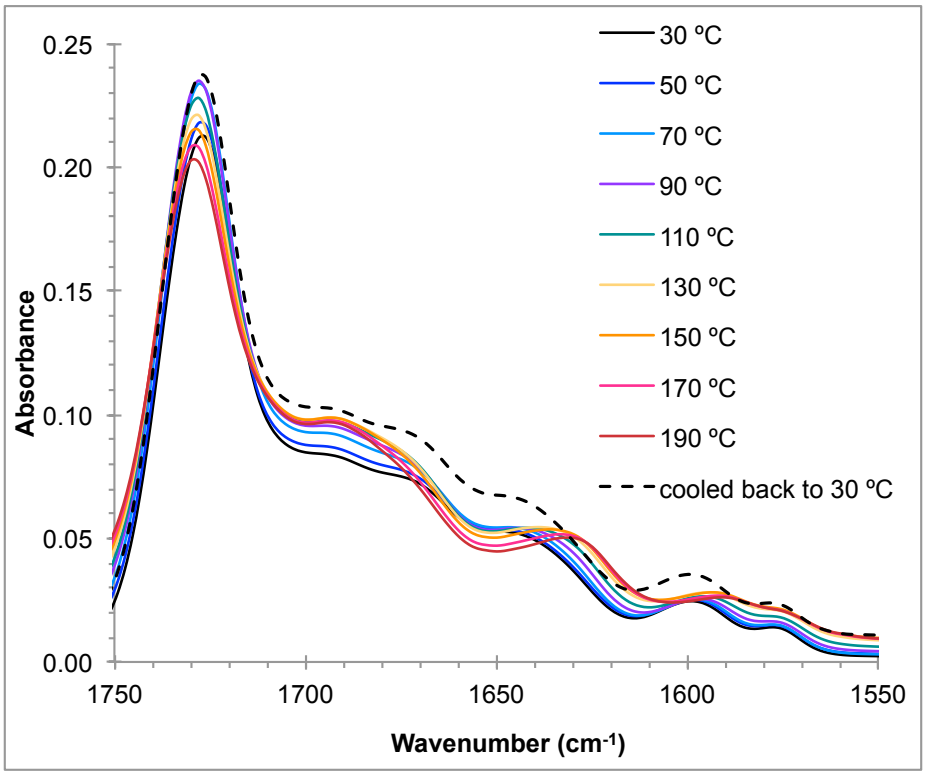

Figure 7.14 Variable temperature FTIR spectra for the supramolecular blend sample in the 1750-1550 cm^{-1} region

7.6 Conclusions

In summary, variable temperature FTIR has been proven itself to be an invaluable asset when investigating hydrogen-bonding interactions, and can be applied to a variety of different polymer structures. Some of the samples in these publications included polyurethanes that contain triptycene, PPG and PDMS based segmented copolymers, and nucleobase-containing triblock copolymers. The data collected in these studies were used not only to determine the strength of hydrogen-bonding interactions, based on the relative wavenumber locations of carbonyl and N-H group vibration frequencies, but also to investigate the dissociation of these interactions at elevated temperatures to probe thermal stability. In addition, several experiments

also explored the thermoreversible nature of these unique, hydrogen-bonding systems. In general, a great deal of information can be gleaned from these FTIR experiments alone; however, they also served as an excellent source of corroboration with other analytical techniques, such as DSC, DMA, and SAXS.

Appendix A References

1. Chang, Z.; Zhang, M.; Hudson, A. G.; Orler, E. B.; Moore, R. B.; Wilkes, G. L.; Turner, S. R. *Polymer* **2013,** *54* (26), 6910-6917.
2. Senich, G. A.; MacKnight, W. J. *Macromolecules* **1980,** *13* (1), 106-110.
3. Coleman, M. M.; Lee, K. H.; Skrovanek, D. J.; Painter, P. C. *Macromolecules* **1986,** *19* (8), 2149-2157.
4. Yilgor, I.; Yilgor, E.; Guler, I. G.; Ward, T. C.; Wilkes, G. L. *Polymer* **2006,** *47* (11), 4105-4114.
5. Williams, S. R.; Wang, W.; Winey, K. I.; Long, T. E. *Macromolecules* **2008,** *41* (23), 9072-9079.
6. Buckwalter, D. J.; Inglefield, D. L., Jr.; Enokida, J. S.; Hudson, A. G.; Moore, R. B.; Long, T. E. *Macromol. Chem. Phys.* **2013,** *214* (18), 2073-2082.
7. Skrovanek, D. J.; Howe, S. E.; Painter, P. C.; Coleman, M. M. *Macromolecules* **1985,** *18* (9), 1676-1683.
8. Skrovanek, D. J.; Painter, P. C.; Coleman, M. M. *Macromolecules* **1986,** *19* (3), 699-705.
9. Buckwalter, D. J.; Hudson, A. G.; Moore, R. B.; Long, T. E. *Polym. Int.* **2014,** *63* (7), 1184-1191.
10. Zhang, K. R.; Aiba, M.; Fahs, G. B.; Hudson, A. G.; Chiang, W. D.; Moore, R. B.; Ueda, M.; Long, T. E. *Polymer Chemistry* **2015,** *6* (13), 2434-2444.

Chapter 8 : Appendix B – Additional FTIR Data (from Chapter 4)

The following tables contain all of the data obtained in the peak fitting procedures, as outlined in Chapter 5. The top portion of each table shows the height, center, and width for each of the three Gaussian peaks (ordered hydrogen bonding, disordered hydrogen bonding, and free carbonyl) that were fit at each temperature. These values were determined by nonlinear least squares regression in Microsoft® Excel and were then used in Wolfram Mathematica® to calculate the area of each peak. The bottom section of each table contains the absolute area values obtained in Mathematica®, as well as the calculated relative areas, R_{index}, and % H-bonded values at each temperature, where $R_{index} = \frac{\text{relative area of H-bonded}}{\text{relative area of free carbonyl}}$ and $\%\text{H-bonded} = \frac{\text{relative area of H-bonded}}{\text{total relative area of carbonyl region}} \times 100\%$. The data in these tables were used to create Figure 5.9-Figure 5.18.

Table 8.1 Peak fitting data for the neat polyurethane sample

	Ordered Hydrogen Bonding			Disordered Hydrogen Bonding			Free Carbonyl		
Temp. (ºC)	**Height**	**Center (cm^{-1})**	**Width (cm^{-1})**	**Height**	**Center (cm^{-1})**	**Width (cm^{-1})**	**Height**	**Center (cm^{-1})**	**Width (cm^{-1})**
35	0.0167	1670.94	28.67	0.0620	1690.24	15.95	0.0483	1715.87	15.71
45	0.0154	1671.00	28.73	0.0627	1691.11	16.41	0.0486	1716.84	15.38
55	0.0153	1671.25	28.21	0.0647	1691.30	15.88	0.0547	1716.71	15.88
65	0.0150	1671.38	28.04	0.0707	1692.07	15.95	0.0621	1717.29	15.84
75	0.0148	1671.75	27.38	0.0747	1692.91	16.00	0.0678	1717.91	15.72
85	0.0135	1671.73	27.73	0.0743	1693.70	16.28	0.0696	1718.55	15.58
95	0.0132	1672.69	27.05	0.0719	1694.57	16.20	0.0717	1719.11	15.57
105	0.0126	1672.95	26.61	0.0697	1695.47	16.20	0.0735	1719.63	15.53
115	0.0124	1674.00	26.08	0.0675	1696.93	16.20	0.0750	1720.33	15.35
125	0.0124	1674.96	25.52	0.0663	1698.33	16.20	0.0761	1720.98	15.12
135	0.0127	1677.57	25.54	0.0647	1700.19	16.20	0.0765	1721.85	14.79
145	0.0118	1677.98	25.10	0.0633	1701.58	16.20	0.0773	1722.51	14.57
155	0.0105	1678.33	24.83	0.0586	1702.60	16.40	0.0740	1723.09	14.36
165	0.0072	1679.02	24.53	0.0436	1704.34	16.74	0.0622	1724.03	13.87
175	0.0037	1679.04	24.92	0.0251	1705.18	15.50	0.0554	1724.52	13.46
185	0.0041	1687.95	24.35	0.0153	1704.69	12.36	0.0551	1724.28	13.65

Temp. (ºC)	**Ordered Area**	**Disordered Area**	**Free Area**	**Relative H-bonded Area**	**Relative Free Area**	**R_{index}**	**% H-bonded**
35	1.19	2.48	1.90	0.66	0.58	1.13	53.0
45	1.10	2.58	1.87	0.66	0.58	1.15	53.4
55	1.08	2.58	2.18	0.63	0.64	0.98	49.5
65	1.04	2.83	2.46	0.61	0.66	0.92	47.9
75	1.01	3.00	2.67	0.60	0.68	0.88	46.8
85	0.93	3.03	2.72	0.59	0.70	0.85	46.0
95	0.89	2.92	2.8	0.58	0.72	0.80	44.3
105	0.84	2.79	2.86	0.56	0.75	0.74	42.6
115	0.81	2.72	2.89	0.55	0.77	0.71	41.7
125	0.79	2.68	2.88	0.55	0.78	0.70	41.3
135	0.83	2.64	2.85	0.55	0.77	0.71	41.6
145	0.75	2.56	2.81	0.54	0.79	0.69	40.8
155	0.65	2.41	2.66	0.53	0.80	0.67	40.2
165	0.44	1.83	2.16	0.51	0.83	0.61	38.1
175	0.23	0.97	1.87	0.39	1.04	0.38	27.3
185	0.25	0.47	1.89	0.28	1.24	0.22	18.2

Table 8.2 Peak fitting data for the composite containing purified MWCNTs at 0.18 wt.% loading

	Ordered Hydrogen Bonding			Disordered Hydrogen Bonding			Free Carbonyl		
Temp. (ºC)	**Height**	**Center (cm^{-1})**	**Width (cm^{-1})**	**Height**	**Center (cm^{-1})**	**Width (cm^{-1})**	**Height**	**Center (cm^{-1})**	**Width (cm^{-1})**
35	0.0189	1664.90	24.88	0.0879	1689.94	16.38	0.0593	1715.72	15.30
45	0.0201	1665.34	24.44	0.1009	1690.50	16.20	0.0708	1716.12	15.31
55	0.0192	1665.69	24.06	0.1030	1691.16	16.09	0.0768	1716.57	15.41
65	0.0176	1665.87	23.84	0.1015	1691.73	16.08	0.0796	1717.02	15.49
75	0.0159	1666.14	23.47	0.0984	1692.47	16.21	0.0803	1717.69	15.39
85	0.0144	1666.36	23.10	0.0949	1693.17	16.33	0.0809	1718.26	15.32
95	0.0132	1666.61	22.64	0.0915	1693.97	16.50	0.0813	1718.89	15.21
105	0.0120	1666.97	22.03	0.0881	1695.03	16.81	0.0808	1719.66	14.98
115	0.0109	1667.46	21.29	0.0850	1696.56	17.31	0.0789	1720.61	14.64
125	0.0100	1668.22	20.41	0.0825	1698.75	17.91	0.0751	1721.74	14.20
135	0.0090	1669.17	19.80	0.0802	1701.39	18.62	0.0687	1723.01	13.64
145	0.0082	1670.20	18.95	0.0762	1703.08	18.87	0.0641	1723.73	13.35
155	0.0069	1671.82	18.17	0.0635	1704.00	18.46	0.0614	1724.05	13.32
165	0.0046	1674.98	16.65	0.0425	1705.53	17.87	0.0534	1724.64	13.02
175	0.0022	1676.61	15.24	0.0280	1707.87	17.62	0.0476	1725.28	12.64
185	0.0012	1676.69	15.10	0.0216	1708.49	17.00	0.0468	1725.47	12.66

Temp. (ºC)	**Ordered Area**	**Disordered Area**	**Free Area**	**Relative H-bonded Area**	**Relative Free Area**	**R_{index}**	**% H-bonded**
35	1.18	3.61	2.23	0.68	0.54	1.26	55.7
45	1.22	4.06	2.69	0.66	0.58	1.15	53.4
55	1.15	4.03	2.93	0.64	0.62	1.03	50.8
65	1.08	4.07	3.05	0.63	0.64	0.99	49.7
75	0.94	3.98	3.03	0.62	0.65	0.95	48.7
85	0.81	3.89	3.05	0.61	0.67	0.90	47.4
95	0.74	3.76	3.03	0.60	0.69	0.87	46.5
105	0.66	3.71	2.98	0.59	0.69	0.86	46.2
115	0.59	3.68	2.83	0.60	0.68	0.88	46.9
125	0.51	3.67	2.61	0.62	0.66	0.94	48.4
135	0.45	3.72	2.30	0.64	0.61	1.06	51.5
145	0.38	3.57	2.09	0.65	0.59	1.11	52.5
155	0.31	2.92	2.00	0.62	0.65	0.94	48.6
165	0.19	1.87	1.69	0.55	0.77	0.71	41.6
175	0.08	1.23	1.48	0.47	0.91	0.52	34.2
185	0.05	0.93	1.45	0.40	1.02	0.39	28.2

Table 8.3 Peak fitting data for the composite containing purified MWCNTs at 1.8 wt.% loading

	Ordered Hydrogen Bonding			Disordered Hydrogen Bonding			Free Carbonyl		
Temp. (ºC)	Height	Center (cm^{-1})	Width (cm^{-1})	Height	Center (cm^{-1})	Width (cm^{-1})	Height	Center (cm^{-1})	Width (cm^{-1})
35	0.0159	1661.89	29.21	0.0614	1690.00	17.93	0.0379	1716.56	14.27
45	0.0171	1661.88	29.21	0.0719	1690.30	17.70	0.0469	1716.79	14.57
55	0.0198	1664.67	28.71	0.0789	1690.82	16.81	0.0575	1716.76	14.99
65	0.0202	1666.45	29.45	0.0830	1691.51	16.63	0.0646	1717.20	15.05
75	0.0204	1668.58	30.47	0.0849	1692.20	16.48	0.0706	1717.64	15.12
85	0.0194	1668.88	30.25	0.0856	1692.97	16.64	0.0740	1718.24	15.06
95	0.0181	1669.24	29.97	0.0844	1693.97	16.95	0.0755	1718.99	14.90
105	0.0172	1669.62	29.61	0.0842	1695.09	17.29	0.0772	1719.72	14.72
115	0.0157	1669.91	29.70	0.0838	1697.07	18.17	0.0746	1720.90	14.25
125	0.0147	1670.97	28.92	0.0833	1700.06	19.11	0.0679	1722.32	13.63
135	0.0137	1671.28	28.61	0.0803	1701.30	18.95	0.0677	1722.74	13.63
145	0.0125	1672.52	27.65	0.0786	1703.79	19.72	0.0596	1723.83	13.10
155	0.0111	1673.42	26.97	0.0722	1705.40	20.00	0.0541	1724.45	12.79
165	0.0078	1675.01	25.42	0.0545	1706.34	19.50	0.0526	1724.72	13.07
175	0.0056	1677.26	22.91	0.0422	1708.14	18.90	0.0489	1725.38	12.79
185	0.0029	1677.92	22.03	0.0307	1708.94	18.50	0.0486	1725.53	12.98

Temp. (ºC)	Ordered Area	Disordered Area	Free Area	Relative H-bonded Area	Relative Free Area	R_{index}	% H-bonded
35	1.17	2.74	1.35	0.74	0.44	1.69	62.9
45	1.24	3.19	1.70	0.72	0.47	1.52	60.4
55	1.44	3.33	2.15	0.69	0.53	1.30	56.5
65	1.47	3.46	2.42	0.67	0.56	1.19	54.4
75	1.52	3.51	2.65	0.65	0.59	1.11	52.6
85	1.43	3.59	2.74	0.65	0.60	1.07	51.7
95	1.35	3.57	2.75	0.64	0.61	1.05	51.1
105	1.26	3.64	2.78	0.64	0.62	1.03	50.8
115	1.19	3.82	2.61	0.66	0.59	1.12	52.9
125	1.08	3.96	2.27	0.69	0.53	1.30	56.5
135	1.00	3.78	2.27	0.68	0.55	1.23	55.2
145	0.83	3.87	1.93	0.71	0.50	1.42	58.7
155	0.74	3.56	1.69	0.72	0.48	1.49	59.8
165	0.50	2.61	1.69	0.65	0.60	1.08	51.8
175	0.32	1.96	1.53	0.60	0.69	0.87	46.6
185	0.16	1.42	1.55	0.50	0.85	0.60	37.3

Table 8.4 Peak fitting data for the composite containing purified MWCNTs at 2.4 wt.% loading

	Ordered Hydrogen Bonding			Disordered Hydrogen Bonding			Free Carbonyl		
Temp. (ºC)	**Height**	**Center (cm^{-1})**	**Width (cm^{-1})**	**Height**	**Center (cm^{-1})**	**Width (cm^{-1})**	**Height**	**Center (cm^{-1})**	**Width (cm^{-1})**
35	0.0091	1657.40	30.09	0.0402	1691.77	20.95	0.0200	1718.46	12.85
45	0.0089	1657.36	30.11	0.0417	1692.20	20.69	0.0224	1718.74	13.21
55	0.0089	1657.34	30.09	0.0449	1692.72	20.42	0.0262	1719.04	13.62
65	0.0090	1658.21	29.49	0.0480	1693.80	20.58	0.0285	1719.79	13.46
75	0.0090	1658.20	29.46	0.0502	1694.27	20.34	0.0321	1720.01	13.83
85	0.0092	1659.69	28.39	0.0528	1695.84	20.79	0.0332	1721.03	13.35
95	0.0092	1660.65	27.81	0.0542	1696.85	20.76	0.0355	1721.52	13.40
105	0.0091	1661.47	27.34	0.0550	1697.87	20.83	0.0370	1721.96	13.39
115	0.0090	1662.30	26.88	0.0556	1699.06	20.95	0.0379	1722.45	13.33
125	0.0088	1663.29	26.39	0.0570	1700.76	21.26	0.0380	1723.10	13.12
135	0.0087	1664.60	25.76	0.0600	1703.06	21.78	0.0368	1723.85	12.61
145	0.0089	1666.03	25.75	0.0621	1704.27	21.50	0.0394	1724.19	12.57
155	0.0083	1666.01	25.75	0.0584	1704.67	21.34	0.0425	1724.20	12.98
165	0.0071	1668.05	24.72	0.0529	1706.29	21.00	0.0442	1724.75	12.80
175	0.0051	1672.94	21.72	0.0427	1708.77	20.40	0.0446	1725.40	12.62
185	0.0036	1676.47	19.02	0.0358	1711.04	19.90	0.0420	1725.91	12.40

Temp. (ºC)	**Ordered Area**	**Disordered Area**	**Free Area**	**Relative H-bonded Area**	**Relative Free Area**	**R_{index}**	**% H-bonded**
35	0.68	2.09	0.64	0.81	0.32	2.53	71.7
45	0.67	2.17	0.72	0.80	0.35	2.31	69.8
55	0.46	2.30	0.88	0.76	0.41	1.83	64.7
65	0.66	2.47	0.95	0.77	0.40	1.93	65.8
75	0.66	2.54	1.09	0.75	0.43	1.72	63.2
85	0.65	2.75	1.09	0.76	0.42	1.82	64.6
95	0.64	2.80	1.19	0.74	0.44	1.69	62.8
105	0.62	2.85	1.22	0.74	0.44	1.66	62.5
115	0.61	2.92	1.25	0.74	0.45	1.65	62.3
125	0.58	3.01	1.22	0.75	0.43	1.72	63.2
135	0.56	3.22	1.14	0.77	0.40	1.94	66.0
145	0.57	3.29	1.20	0.76	0.41	1.88	65.3
155	0.53	3.05	1.37	0.72	0.47	1.53	60.4
165	0.44	2.74	1.38	0.70	0.52	1.35	57.4
175	0.28	2.15	1.39	0.64	0.62	1.02	50.6
185	0.17	1.75	1.27	0.60	0.68	0.88	46.9

Table 8.5 Peak fitting data for the composite containing purified MWCNTs at 5 wt.% loading

	Ordered Hydrogen Bonding			Disordered Hydrogen Bonding			Free Carbonyl		
Temp. (ºC)	Height	Center (cm^{-1})	Width (cm^{-1})	Height	Center (cm^{-1})	Width (cm^{-1})	Height	Center (cm^{-1})	Width (cm^{-1})
35	0.0154	1661.59	29.85	0.0626	1689.64	18.02	0.0373	1716.19	14.70
45	0.0169	1662.46	29.19	0.0743	1690.26	17.85	0.0460	1716.70	14.71
55	0.0182	1664.36	28.62	0.0800	1690.76	17.21	0.0546	1716.78	15.06
65	0.0180	1664.92	28.32	0.0843	1691.38	17.08	0.0609	1717.17	15.17
75	0.0178	1665.45	27.89	0.0890	1692.16	17.08	0.0669	1717.72	15.14
85	0.0169	1665.80	27.58	0.0891	1692.86	17.07	0.0708	1718.17	15.21
95	0.0161	1666.44	26.95	0.0880	1693.93	17.36	0.0718	1718.96	14.98
105	0.0152	1666.95	26.43	0.0869	1695.07	17.67	0.0726	1719.72	14.78
115	0.0141	1667.34	26.20	0.0865	1696.73	18.29	0.0715	1720.75	14.43
125	0.0137	1668.25	25.30	0.0866	1698.81	18.73	0.0696	1721.75	14.05
135	0.0129	1669.29	24.99	0.0875	1701.60	19.42	0.0635	1723.07	13.40
145	0.0122	1670.18	24.78	0.0859	1703.38	19.70	0.0595	1723.81	13.04
155	0.0111	1670.54	25.70	0.0813	1705.10	20.26	0.0529	1724.36	12.62
165	0.0098	1671.09	25.47	0.0693	1706.48	20.12	0.0484	1724.76	12.38
175	0.0054	1671.02	25.39	0.0432	1707.54	18.99	0.0464	1725.04	12.54
185	0.0014	1671.01	25.31	0.0258	1709.23	16.65	0.0463	1725.55	12.48

Temp. (ºC)	Ordered Area	Disordered Area	Free Area	Relative H-bonded Area	Relative Free Area	R_{index}	% H-bonded
35	1.12	2.84	1.35	0.75	0.43	1.72	63.2
45	1.24	3.31	1.68	0.73	0.46	1.58	61.3
55	1.29	3.45	2.05	0.70	0.52	1.35	57.5
65	1.28	3.60	2.28	0.68	0.54	1.25	55.6
75	1.26	3.81	2.50	0.67	0.56	1.19	54.3
85	1.17	3.81	2.66	0.65	0.60	1.09	52.3
95	1.08	3.83	2.65	0.65	0.60	1.08	52.0
105	0.99	3.85	2.65	0.65	0.61	1.07	51.6
115	0.92	3.94	2.55	0.66	0.59	1.11	52.7
125	0.89	4.07	2.41	0.67	0.56	1.20	54.6
135	0.81	4.26	2.07	0.71	0.50	1.43	58.9
145	0.74	4.21	1.89	0.72	0.47	1.53	60.5
155	0.71	4.06	1.64	0.74	0.44	1.70	63.0
165	0.63	3.43	1.46	0.74	0.45	1.63	61.9
175	0.34	2.02	1.41	0.63	0.64	0.98	49.5
185	0.09	1.08	1.40	0.46	0.93	0.49	32.8

Table 8.6 Peak fitting data for the composite containing purified MWCNTs at 10 wt.% loading

	Ordered Hydrogen Bonding			Disordered Hydrogen Bonding			Free Carbonyl		
Temp. (ºC)	Height	Center (cm^{-1})	Width (cm^{-1})	Height	Center (cm^{-1})	Width (cm^{-1})	Height	Center (cm^{-1})	Width (cm^{-1})
35	0.0215	1662.81	41.11	0.0558	1690.61	19.79	0.0298	1717.10	12.12
45	0.0220	1663.10	40.81	0.0601	1691.27	19.88	0.0338	1717.64	12.24
55	0.0226	1663.48	40.45	0.0656	1692.16	20.00	0.0385	1718.22	12.34
65	0.0231	1663.84	40.15	0.0712	1693.13	20.09	0.0431	1718.77	12.39
75	0.0231	1664.09	39.98	0.0756	1693.99	20.21	0.0467	1719.26	12.41
85	0.0227	1664.35	39.80	0.0781	1695.02	20.46	0.0489	1719.80	12.35
95	0.0218	1664.61	39.62	0.0785	1696.09	20.80	0.0495	1720.33	12.25
105	0.0206	1664.89	39.47	0.0775	1697.38	21.23	0.0484	1720.89	12.07
115	0.0196	1665.31	39.14	0.0769	1698.94	21.60	0.0467	1721.44	11.80
125	0.0186	1665.33	39.11	0.0754	1699.93	21.13	0.0485	1721.66	11.97
135	0.0186	1668.07	37.60	0.0740	1701.96	21.01	0.0463	1722.31	11.61
145	0.0182	1670.81	38.09	0.0714	1703.43	20.72	0.0450	1722.79	11.36
155	0.0184	1671.27	37.93	0.0714	1704.17	20.65	0.0453	1722.99	11.28
165	0.0160	1674.63	35.48	0.0634	1705.35	19.57	0.0480	1723.35	11.52
175	0.0129	1678.65	31.83	0.0548	1707.16	18.82	0.0462	1723.98	11.43
185	0.0100	1681.45	28.75	0.0426	1708.55	17.86	0.0446	1724.45	11.44

Temp. (ºC)	Ordered Area	Disordered Area	Free Area	Relative H-bonded Area	Relative Free Area	R_{index}	% H-bonded
35	2.20	2.77	0.91	0.85	0.26	3.19	76.2
45	2.19	2.99	1.04	0.83	0.29	2.91	74.4
55	2.27	3.30	1.20	0.82	0.30	2.71	73.1
65	2.26	3.57	1.33	0.81	0.32	2.56	71.9
75	2.20	3.84	1.45	0.81	0.33	2.44	70.9
85	2.24	3.99	1.51	0.80	0.33	2.41	70.7
95	2.13	4.07	1.49	0.81	0.33	2.43	70.9
105	2.03	4.12	1.44	0.81	0.32	2.50	71.4
115	1.92	4.13	1.38	0.81	0.32	2.56	71.9
125	1.82	3.94	1.43	0.80	0.34	2.36	70.2
135	1.76	3.85	1.33	0.81	0.33	2.47	71.2
145	1.68	3.64	1.27	0.81	0.33	2.45	71.0
155	1.67	3.63	1.26	0.81	0.33	2.46	71.1
165	1.40	3.06	1.37	0.77	0.40	1.90	65.6
175	1.02	2.57	1.30	0.73	0.45	1.61	61.8
185	0.71	1.91	1.27	0.67	0.56	1.21	54.7

Table 8.7 Peak fitting data for the composite containing AO-MWCNTs at 0.18 wt.% loading

	Ordered Hydrogen Bonding			Disordered Hydrogen Bonding			Free Carbonyl		
Temp. (ºC)	**Height**	**Center (cm^{-1})**	**Width (cm^{-1})**	**Height**	**Center (cm^{-1})**	**Width (cm^{-1})**	**Height**	**Center (cm^{-1})**	**Width (cm^{-1})**
35	0.0151	1657.56	20.31	0.0913	1690.32	18.35	0.0516	1717.20	14.34
45	0.0169	1662.60	23.92	0.0877	1690.43	16.66	0.0605	1716.21	15.44
55	0.0160	1663.80	24.04	0.0853	1691.24	16.59	0.0626	1716.81	15.44
65	0.0150	1663.77	24.04	0.0869	1691.61	16.37	0.0689	1716.98	15.78
75	0.0143	1664.53	23.35	0.0892	1692.74	16.67	0.0720	1717.98	15.40
85	0.0133	1664.99	22.85	0.0878	1693.64	16.85	0.0738	1718.68	15.25
95	0.0123	1665.37	22.38	0.0854	1694.53	17.05	0.0747	1719.34	15.11
105	0.0113	1665.88	21.74	0.0831	1695.73	17.40	0.0749	1720.17	14.85
115	0.0104	1666.40	21.13	0.0808	1697.12	17.79	0.0740	1721.00	14.60
125	0.0096	1667.24	20.40	0.0795	1699.28	18.39	0.0709	1722.12	14.16
135	0.0089	1668.17	19.67	0.0784	1701.53	18.87	0.0667	1723.13	13.74
145	0.0079	1669.31	19.70	0.0748	1703.38	19.20	0.0628	1723.88	13.45
155	0.0071	1670.82	19.00	0.0664	1704.30	18.86	0.0611	1724.22	13.39
165	0.0047	1672.52	17.94	0.0476	1706.32	18.84	0.0521	1724.89	13.07
175	0.0022	1675.78	15.66	0.0303	1709.45	18.48	0.0448	1725.66	12.57
185	0.0011	1675.80	15.55	0.0223	1710.14	17.59	0.0448	1725.78	12.68

Temp. (ºC)	**Ordered Area**	**Disordered Area**	**Free Area**	**Relative H-bonded Area**	**Relative Free Area**	**R_{index}**	**% H-bonded**
35	0.76	4.18	1.85	0.73	0.47	1.56	61.0
45	1.01	3.67	2.34	0.67	0.57	1.17	53.9
55	0.96	3.53	2.42	0.65	0.60	1.09	52.0
65	0.90	3.57	2.72	0.62	0.65	0.96	49.0
75	0.82	3.72	2.77	0.62	0.65	0.96	48.9
85	0.74	3.72	2.82	0.61	0.66	0.92	48.0
95	0.67	3.63	2.83	0.60	0.68	0.89	47.0
105	0.60	3.62	2.78	0.60	0.68	0.89	47.0
115	0.53	3.61	2.70	0.61	0.68	0.90	47.3
125	0.49	3.64	2.51	0.62	0.65	0.96	49.0
135	0.44	3.69	2.30	0.64	0.61	1.05	51.2
145	0.39	3.60	2.12	0.65	0.59	1.10	52.4
155	0.34	3.12	2.04	0.63	0.63	0.99	49.8
165	0.21	2.26	1.70	0.59	0.70	0.85	45.9
175	0.09	1.39	1.41	0.51	0.84	0.61	38.0
185	0.04	0.97	1.43	0.41	1.00	0.41	29.3

Table 8.8 Peak fitting data for the composite containing AO-MWCNTs at 1.8 wt.% loading

	Ordered Hydrogen Bonding			Disordered Hydrogen Bonding			Free Carbonyl		
Temp. (ºC)	**Height**	**Center (cm^{-1})**	**Width (cm^{-1})**	**Height**	**Center (cm^{-1})**	**Width (cm^{-1})**	**Height**	**Center (cm^{-1})**	**Width (cm^{-1})**
35	0.0127	1660.09	30.47	0.0474	1690.52	19.07	0.0281	1717.14	13.62
45	0.0125	1660.56	30.40	0.0493	1691.26	19.29	0.0298	1717.81	13.63
55	0.0130	1661.05	30.34	0.0548	1692.09	19.28	0.0348	1718.39	13.69
65	0.0135	1661.58	30.21	0.0608	1692.88	19.28	0.0402	1718.92	13.75
75	0.0137	1662.04	29.97	0.0652	1693.68	19.30	0.0450	1719.43	13.81
85	0.0135	1662.50	29.71	0.0672	1694.48	19.40	0.0481	1719.90	13.83
95	0.0131	1663.02	29.36	0.0680	1695.46	19.62	0.0501	1720.48	13.80
105	0.0125	1663.52	29.05	0.0683	1696.62	19.92	0.0516	1721.10	13.74
115	0.0124	1664.20	28.58	0.0715	1698.31	20.46	0.0527	1721.88	13.45
125	0.0123	1665.45	29.22	0.0773	1701.04	21.36	0.0513	1722.85	12.89
135	0.0126	1667.14	28.24	0.0778	1702.66	21.00	0.0519	1723.38	12.73
145	0.0121	1668.81	28.09	0.0778	1704.28	21.00	0.0513	1723.91	12.58
155	0.0114	1670.40	27.32	0.0744	1705.36	20.60	0.0516	1724.31	12.56
165	0.0105	1672.34	27.37	0.0682	1706.48	20.30	0.0500	1724.69	12.53
175	0.0091	1673.45	27.00	0.0591	1707.65	20.20	0.0463	1725.10	12.38
185	0.0073	1673.44	26.99	0.0460	1708.13	19.99	0.0459	1725.19	12.64

Temp. (ºC)	**Ordered Area**	**Disordered Area**	**Free Area**	**Relative H-bonded Area**	**Relative Free Area**	**R_{index}**	**% H-bonded**
35	0.96	2.25	0.96	0.77	0.39	1.96	66.2
45	0.94	2.37	1.02	0.76	0.40	1.90	65.5
55	0.98	2.66	1.20	0.75	0.42	1.77	63.9
65	1.01	2.95	1.38	0.74	0.44	1.68	62.7
75	1.04	3.14	1.56	0.73	0.46	1.57	61.0
85	0.96	3.26	1.66	0.72	0.48	1.49	59.8
95	0.95	3.34	1.73	0.71	0.49	1.45	59.2
105	0.94	3.39	1.79	0.71	0.50	1.41	58.6
115	0.86	3.66	1.78	0.72	0.48	1.48	59.7
125	0.87	4.12	1.65	0.75	0.42	1.77	63.9
135	0.92	4.10	1.66	0.75	0.42	1.77	63.9
145	0.84	4.10	1.61	0.75	0.42	1.79	64.2
155	0.75	3.81	1.64	0.74	0.45	1.63	61.9
165	0.72	3.45	1.57	0.73	0.47	1.55	60.8
175	0.61	2.98	1.43	0.72	0.49	1.47	59.5
185	0.49	2.30	1.46	0.66	0.59	1.12	52.8

Table 8.9 Peak fitting data for the composite containing AO-MWCNTs at 2.4 wt.% loading

	Ordered Hydrogen Bonding			Disordered Hydrogen Bonding			Free Carbonyl		
Temp. (ºC)	**Height**	**Center (cm^{-1})**	**Width (cm^{-1})**	**Height**	**Center (cm^{-1})**	**Width (cm^{-1})**	**Height**	**Center (cm^{-1})**	**Width (cm^{-1})**
35	0.0191	1668.51	33.15	0.0588	1689.67	16.97	0.0408	1715.98	15.09
45	0.0212	1669.07	32.68	0.0686	1690.04	16.68	0.0495	1716.16	15.28
55	0.0229	1669.38	32.33	0.0805	1690.65	16.53	0.0603	1716.55	15.39
65	0.0230	1669.63	32.04	0.0858	1691.18	16.46	0.0668	1716.90	15.49
75	0.0226	1670.03	31.58	0.0888	1691.87	16.48	0.0716	1717.40	15.48
85	0.0221	1670.41	31.13	0.0908	1692.62	16.53	0.0761	1717.92	15.43
95	0.0215	1670.82	30.63	0.0928	1693.51	16.66	0.0806	1718.49	15.34
105	0.0205	1671.35	30.00	0.0916	1694.72	16.94	0.0817	1719.27	15.13
115	0.0193	1671.78	29.76	0.0915	1696.32	17.49	0.0810	1720.26	14.78
125	0.0183	1672.44	29.36	0.0924	1698.42	18.12	0.0789	1721.41	14.33
135	0.0175	1673.43	28.99	0.0934	1700.88	18.87	0.0727	1722.65	13.75
145	0.0165	1674.16	29.12	0.0920	1702.61	19.25	0.0680	1723.38	13.44
155	0.0156	1674.62	28.75	0.0878	1703.64	19.16	0.0664	1723.73	13.38
165	0.0133	1674.62	28.71	0.0769	1704.17	18.72	0.0664	1723.85	13.49
175	0.0095	1676.83	26.35	0.0608	1707.32	19.54	0.0507	1725.08	12.69
185	0.0045	1680.31	22.10	0.0363	1710.10	18.76	0.0445	1725.77	12.44

Temp. (ºC)	**Ordered Area**	**Disordered Area**	**Free Area**	**Relative H-bonded Area**	**Relative Free Area**	**R_{index}**	**% H-bonded**
35	1.54	2.51	1.55	0.72	0.47	1.53	60.4
45	1.69	2.88	1.91	0.71	0.50	1.40	58.3
55	1.83	3.31	2.31	0.69	0.53	1.30	56.5
65	1.82	3.55	2.59	0.67	0.56	1.21	54.8
75	1.79	3.68	2.79	0.66	0.58	1.15	53.4
85	1.69	3.77	2.93	0.65	0.60	1.09	52.1
95	1.67	3.88	3.10	0.64	0.61	1.05	51.1
105	1.56	3.91	3.10	0.64	0.62	1.03	50.8
115	1.40	4.03	2.99	0.64	0.61	1.06	51.5
125	1.31	4.18	2.83	0.66	0.58	1.13	53.1
135	1.23	4.40	2.51	0.69	0.53	1.31	56.7
145	1.23	4.43	2.28	0.71	0.49	1.45	59.2
155	1.15	4.22	2.21	0.71	0.50	1.42	58.7
165	0.93	3.61	2.22	0.67	0.56	1.20	54.5
175	0.63	2.98	1.62	0.69	0.53	1.30	56.6
185	0.25	1.69	1.37	0.59	0.71	0.83	45.3

Table 8.10 Peak fitting data for the composite containing AO-MWCNTs at 5 wt.% loading

	Ordered Hydrogen Bonding			Disordered Hydrogen Bonding			Free Carbonyl		
Temp. (ºC)	**Height**	**Center (cm^{-1})**	**Width (cm^{-1})**	**Height**	**Center (cm^{-1})**	**Width (cm^{-1})**	**Height**	**Center (cm^{-1})**	**Width (cm^{-1})**
35	0.0203	1654.58	30.36	0.0869	1690.34	20.37	0.0402	1717.54	12.70
45	0.0248	1664.94	36.27	0.0815	1690.79	18.28	0.0495	1717.02	13.54
55	0.0256	1665.60	35.72	0.0895	1691.68	18.34	0.0566	1717.64	13.49
65	0.0257	1666.70	35.73	0.0926	1692.49	18.26	0.0620	1718.09	13.59
75	0.0248	1667.10	35.42	0.0927	1693.38	18.45	0.0640	1718.66	13.59
85	0.0234	1667.62	35.01	0.0908	1694.62	18.88	0.0638	1719.45	13.41
95	0.0218	1667.99	34.87	0.0887	1695.88	19.38	0.0622	1720.20	13.23
105	0.0199	1668.24	35.27	0.0869	1697.41	20.13	0.0590	1721.03	12.93
115	0.0186	1668.98	35.02	0.0855	1699.38	20.82	0.0545	1721.89	12.50
125	0.0176	1669.87	34.11	0.0846	1701.48	21.15	0.0505	1722.65	12.06
135	0.0172	1672.34	34.04	0.0823	1703.43	20.88	0.0483	1723.28	11.77
145	0.0161	1673.50	32.82	0.0809	1705.11	20.71	0.0460	1723.88	11.44
155	0.0155	1675.19	31.89	0.0759	1705.76	19.80	0.0487	1724.16	11.71
165	0.0145	1677.07	31.19	0.0700	1707.05	19.35	0.0468	1724.62	11.53
175	0.0108	1678.66	29.46	0.0584	1708.67	18.81	0.0437	1725.23	11.40
185	0.0042	1682.65	23.98	0.0415	1711.65	17.65	0.0388	1726.24	11.05

Temp. (ºC)	**Ordered Area**	**Disordered Area**	**Free Area**	**Relative H-bonded Area**	**Relative Free Area**	**R_{index}**	**% H-bonded**
35	1.51	4.43	1.27	0.82	0.30	2.74	73.2
45	2.23	3.71	1.68	0.78	0.38	2.07	67.4
55	2.29	4.09	1.91	0.77	0.39	1.95	66.1
65	2.29	4.25	2.09	0.76	0.41	1.83	64.7
75	2.18	4.30	2.16	0.75	0.43	1.75	63.7
85	1.99	4.30	2.13	0.75	0.43	1.73	63.3
95	1.89	4.31	2.03	0.75	0.42	1.79	64.1
105	1.74	4.37	1.89	0.76	0.40	1.89	65.4
115	1.64	4.40	1.69	0.78	0.37	2.09	67.6
125	1.52	4.46	1.51	0.80	0.34	2.32	69.8
135	1.43	4.24	1.40	0.80	0.34	2.37	70.3
145	1.30	4.14	1.30	0.81	0.33	2.45	71.0
155	1.19	3.72	1.42	0.78	0.38	2.02	66.9
165	1.08	3.35	1.34	0.77	0.40	1.93	65.9
175	0.81	2.70	1.24	0.74	0.45	1.66	62.3
185	0.26	1.83	1.06	0.66	0.58	1.15	53.6

Table 8.11 Peak fitting data for the composite containing AO-MWCNTs at 10 wt.% loading

	Ordered Hydrogen Bonding			Disordered Hydrogen Bonding			Free Carbonyl		
Temp. (ºC)	Height	Center (cm^{-1})	Width (cm^{-1})	Height	Center (cm^{-1})	Width (cm^{-1})	Height	Center (cm^{-1})	Width (cm^{-1})
35	0.0130	1657.57	39.86	0.0366	1690.87	21.48	0.0171	1717.28	11.65
45	0.0149	1658.14	39.60	0.0444	1691.66	21.48	0.0214	1717.90	11.77
55	0.0172	1658.93	39.26	0.0550	1692.58	21.46	0.0274	1718.55	11.90
65	0.0189	1660.12	39.33	0.0630	1693.43	21.34	0.0326	1719.05	11.99
75	0.0199	1661.01	39.16	0.0685	1694.39	21.42	0.0363	1719.59	12.01
85	0.0201	1662.90	40.20	0.0686	1695.14	21.22	0.0389	1719.89	12.18
95	0.0198	1663.36	39.83	0.0696	1696.11	21.43	0.0400	1720.37	12.19
105	0.0196	1664.02	39.29	0.0716	1697.47	21.80	0.0407	1721.00	12.01
115	0.0209	1666.43	40.09	0.0763	1698.74	21.71	0.0442	1721.40	11.93
125	0.0215	1667.37	39.33	0.0789	1700.03	21.50	0.0466	1721.82	11.95
135	0.0221	1670.05	39.74	0.0800	1702.08	21.59	0.0450	1722.43	11.52
145	0.0219	1671.06	39.09	0.0800	1703.17	21.28	0.0463	1722.80	11.52
155	0.0216	1671.99	38.69	0.0789	1704.23	21.06	0.0465	1723.12	11.51
165	0.0204	1672.70	38.23	0.0754	1705.33	20.88	0.0455	1723.46	11.40
175	0.0171	1673.44	36.05	0.0659	1706.45	20.49	0.0446	1723.94	11.50
185	0.0117	1678.62	32.66	0.0481	1708.59	19.42	0.0423	1724.87	11.48

Temp. (ºC)	Ordered Area	Disordered Area	Free Area	Relative H-bonded Area	Relative Free Area	R_{index}	% H-bonded
35	1.29	1.99	0.50	0.87	0.22	3.87	79.5
45	1.47	2.34	0.62	0.86	0.24	3.59	78.2
55	1.68	2.96	0.81	0.85	0.25	3.37	77.1
65	1.86	3.37	0.99	0.84	0.27	3.09	75.5
75	1.94	3.65	1.08	0.84	0.28	3.03	75.2
85	2.00	3.67	1.19	0.83	0.30	2.79	73.6
95	1.97	3.74	1.22	0.82	0.30	2.74	73.2
105	1.92	3.91	1.23	0.83	0.30	2.77	73.5
115	2.10	4.14	1.32	0.83	0.30	2.76	73.4
125	2.06	4.26	1.41	0.82	0.31	2.62	72.4
135	2.18	4.33	1.30	0.83	0.28	2.93	74.5
145	2.15	4.27	1.33	0.83	0.29	2.82	73.8
155	2.13	4.17	1.34	0.82	0.30	2.75	73.3
165	1.91	3.93	1.29	0.82	0.31	2.65	72.6
175	1.53	3.39	1.29	0.79	0.36	2.23	69.0
185	0.96	2.34	1.21	0.73	0.46	1.59	61.5

Table 8.12 Peak fitting data for the composite containing AA-MWCNTs at 0.18 wt.% loading

	Ordered Hydrogen Bonding			Disordered Hydrogen Bonding			Free Carbonyl		
Temp. (ºC)	Height	Center (cm^{-1})	Width (cm^{-1})	Height	Center (cm^{-1})	Width (cm^{-1})	Height	Center (cm^{-1})	Width (cm^{-1})
35	0.0170	1667.12	26.77	0.0600	1690.23	16.33	0.0440	1715.92	15.39
45	0.0177	1667.40	26.43	0.0655	1690.54	16.12	0.0499	1716.10	15.54
55	0.0183	1667.81	25.87	0.0726	1691.11	15.89	0.0581	1716.46	15.64
65	0.0180	1668.11	25.44	0.0775	1691.75	15.83	0.0648	1716.90	15.67
75	0.0165	1668.08	25.44	0.0773	1692.06	15.65	0.0693	1717.07	15.98
85	0.0154	1668.65	24.57	0.0786	1693.37	16.09	0.0707	1718.24	15.45
95	0.0142	1668.64	24.09	0.0784	1694.29	16.37	0.0723	1718.96	15.25
105	0.0134	1669.02	23.39	0.0777	1695.43	16.62	0.0735	1719.73	14.99
115	0.0125	1669.51	22.55	0.0771	1697.03	17.01	0.0738	1720.69	14.63
125	0.0112	1669.52	22.08	0.0776	1698.99	17.73	0.0718	1721.79	14.16
135	0.0105	1670.49	20.94	0.0771	1701.01	18.02	0.0696	1722.74	13.77
145	0.0095	1671.35	20.08	0.0749	1702.69	18.23	0.0670	1723.48	13.47
155	0.0083	1672.13	19.43	0.0698	1703.99	18.44	0.0632	1724.05	13.25
165	0.0065	1673.00	18.78	0.0580	1705.36	18.57	0.0572	1724.58	13.08
175	0.0042	1675.83	16.47	0.0434	1708.61	19.38	0.0449	1725.52	12.35
185	0.0019	1675.83	16.32	0.0282	1709.52	18.34	0.0451	1725.66	12.49

Temp. (ºC)	Ordered Area	Disordered Area	Free Area	Relative H-bonded Area	Relative Free Area	R_{index}	% H-bonded
35	1.14	2.46	1.69	0.68	0.55	1.25	55.5
45	1.19	2.63	1.94	0.66	0.58	1.15	53.5
55	1.17	2.91	2.26	0.64	0.61	1.06	51.4
65	1.15	3.06	2.53	0.62	0.64	0.97	49.3
75	1.08	3.02	2.74	0.60	0.69	0.88	46.7
85	0.92	3.19	2.73	0.60	0.68	0.88	46.8
95	0.85	3.20	2.73	0.60	0.69	0.87	46.5
105	0.76	3.25	2.75	0.59	0.70	0.85	46.0
115	0.68	3.28	2.69	0.60	0.69	0.86	46.3
125	0.61	3.46	2.53	0.62	0.66	0.94	48.5
135	0.58	3.47	2.39	0.63	0.63	0.99	49.8
145	0.48	3.42	2.24	0.64	0.62	1.02	50.5
155	0.40	3.23	2.07	0.64	0.62	1.03	50.6
165	0.31	2.69	1.85	0.62	0.65	0.95	48.7
175	0.17	2.07	1.38	0.62	0.65	0.95	48.7
185	0.08	1.28	1.40	0.49	0.87	0.57	36.2

Table 8.13 Peak fitting data for the composite containing AA-MWCNTs at 1.8 wt.% loading

	Ordered Hydrogen Bonding			Disordered Hydrogen Bonding			Free Carbonyl		
Temp. (ºC)	**Height**	**Center (cm^{-1})**	**Width (cm^{-1})**	**Height**	**Center (cm^{-1})**	**Width (cm^{-1})**	**Height**	**Center (cm^{-1})**	**Width (cm^{-1})**
35	0.0196	1663.99	32.21	0.0662	1690.79	18.29	0.0404	1717.09	13.58
45	0.0214	1665.48	31.25	0.0701	1690.79	17.19	0.0485	1716.66	14.34
55	0.0213	1666.14	31.24	0.0738	1691.32	17.00	0.0542	1717.00	14.57
65	0.0208	1667.44	31.70	0.0762	1692.04	16.91	0.0597	1717.50	14.67
75	0.0197	1667.94	31.34	0.0791	1692.89	17.03	0.0641	1718.14	14.62
85	0.0182	1668.34	31.03	0.0787	1693.77	17.23	0.0661	1718.82	14.54
95	0.0168	1668.78	30.67	0.0775	1694.82	17.59	0.0669	1719.57	14.36
105	0.0157	1669.23	30.18	0.0770	1695.95	17.98	0.0675	1720.31	14.15
115	0.0144	1669.68	29.67	0.0763	1697.73	18.64	0.0659	1721.32	13.76
125	0.0132	1670.36	29.03	0.0772	1700.45	19.71	0.0601	1722.57	13.14
135	0.0125	1671.55	27.66	0.0777	1703.15	19.98	0.0557	1723.55	12.64
145	0.0116	1672.56	26.45	0.0773	1704.91	20.16	0.0528	1724.16	12.32
155	0.0109	1673.06	25.93	0.0738	1705.92	20.17	0.0511	1724.47	12.21
165	0.0097	1674.00	24.96	0.0676	1707.30	20.25	0.0470	1724.90	11.94
175	0.0066	1675.93	22.65	0.0524	1709.45	20.21	0.0410	1725.43	11.65
185	0.0034	1681.34	16.45	0.0356	1712.07	18.75	0.0389	1726.15	11.57

Temp. (ºC)	**Ordered Area**	**Disordered Area**	**Free Area**	**Relative H-bonded Area**	**Relative Free Area**	**R_{index}**	**% H-bonded**
35	1.60	3.03	1.36	0.77	0.39	1.99	66.6
45	1.64	3.02	1.75	0.73	0.47	1.56	60.9
55	1.64	3.15	1.96	0.71	0.50	1.43	58.8
65	1.66	3.22	2.19	0.69	0.53	1.30	56.6
75	1.56	3.37	2.33	0.68	0.55	1.24	55.3
85	1.39	3.41	2.39	0.67	0.57	1.17	54.0
95	1.30	3.39	2.40	0.66	0.58	1.14	53.3
105	1.21	3.47	2.36	0.66	0.57	1.16	53.7
115	1.04	3.55	2.26	0.67	0.56	1.19	54.3
125	0.94	3.79	1.96	0.71	0.50	1.41	58.5
135	0.83	3.89	1.76	0.73	0.46	1.57	61.1
145	0.79	3.87	1.63	0.74	0.44	1.67	62.6
155	0.71	3.71	1.55	0.74	0.44	1.67	62.5
165	0.61	3.42	1.40	0.74	0.44	1.68	62.7
175	0.37	2.60	1.19	0.71	0.49	1.46	59.3
185	0.14	1.67	1.12	0.62	0.65	0.95	48.6

Table 8.14 Peak fitting data for the composite containing AA-MWCNTs at 2.4 wt.% loading

	Ordered Hydrogen Bonding			Disordered Hydrogen Bonding			Free Carbonyl		
Temp. (ºC)	Height	Center (cm^{-1})	Width (cm^{-1})	Height	Center (cm^{-1})	Width (cm^{-1})	Height	Center (cm^{-1})	Width (cm^{-1})
35	0.0170	1661.40	27.41	0.0637	1690.05	17.68	0.0408	1716.36	14.51
45	0.0201	1665.90	29.00	0.0670	1690.59	16.78	0.0485	1716.36	14.80
55	0.0207	1666.39	28.90	0.0740	1691.14	16.63	0.0564	1716.71	14.98
65	0.0207	1666.73	28.68	0.0801	1691.77	16.52	0.0647	1717.09	15.16
75	0.0193	1667.27	28.28	0.0799	1692.65	16.68	0.0671	1717.79	15.10
85	0.0181	1667.77	27.99	0.0798	1693.56	16.95	0.0685	1718.51	14.92
95	0.0170	1668.29	27.48	0.0791	1694.61	17.20	0.0702	1719.23	14.78
105	0.0159	1668.76	27.10	0.0791	1696.03	17.68	0.0707	1720.14	14.49
115	0.0149	1669.35	26.56	0.0807	1698.11	18.47	0.0693	1721.31	14.00
125	0.0138	1669.87	26.16	0.0818	1700.17	19.16	0.0662	1722.31	13.58
135	0.0127	1670.72	25.29	0.0814	1702.34	19.76	0.0611	1723.25	13.13
145	0.0117	1671.55	24.31	0.0800	1704.00	20.00	0.0572	1723.92	12.76
155	0.0110	1672.09	23.91	0.0751	1704.70	19.70	0.0573	1724.12	12.83
165	0.0102	1673.44	22.91	0.0666	1705.73	19.30	0.0550	1724.49	12.73
175	0.0071	1675.43	21.00	0.0507	1707.38	19.00	0.0493	1725.09	12.52
185	0.0032	1680.85	15.10	0.0333	1710.47	18.10	0.0438	1725.95	12.19

Temp. (ºC)	Ordered Area	Disordered Area	Free Area	Relative H-bonded Area	Relative Free Area	R_{index}	% H-bonded
35	1.17	2.84	1.49	0.73	0.46	1.57	61.1
45	1.45	2.82	1.77	0.71	0.50	1.41	58.5
55	1.52	3.08	2.09	0.69	0.53	1.29	56.3
65	1.51	3.31	2.45	0.66	0.58	1.15	53.5
75	1.34	3.34	2.52	0.65	0.60	1.09	52.1
85	1.26	3.40	2.56	0.65	0.61	1.06	51.6
95	1.17	3.41	2.57	0.64	0.61	1.04	51.0
105	1.09	3.50	2.56	0.64	0.61	1.05	51.2
115	1.00	3.75	2.40	0.66	0.57	1.16	53.6
125	0.92	3.93	2.23	0.69	0.54	1.27	56.0
135	0.82	4.00	1.99	0.71	0.50	1.42	58.6
145	0.73	3.99	1.81	0.72	0.47	1.52	60.4
155	0.66	3.68	1.82	0.70	0.51	1.39	58.2
165	0.57	3.22	1.74	0.69	0.54	1.27	56.0
175	0.37	2.41	1.52	0.65	0.60	1.07	51.7
185	0.12	1.49	1.33	0.55	0.77	0.71	41.4

Table 8.15 Peak fitting data for the composite containing AA-MWCNTs at 5 wt.% loading

	Ordered Hydrogen Bonding			Disordered Hydrogen Bonding			Free Carbonyl		
Temp. (ºC)	**Height**	**Center (cm^{-1})**	**Width (cm^{-1})**	**Height**	**Center (cm^{-1})**	**Width (cm^{-1})**	**Height**	**Center (cm^{-1})**	**Width (cm^{-1})**
35	0.0238	1662.79	38.10	0.0648	1691.11	19.45	0.0350	1717.07	12.28
45	0.0244	1663.03	37.94	0.0716	1691.71	19.50	0.0396	1717.57	12.49
55	0.0245	1663.88	38.26	0.0765	1692.57	19.61	0.0438	1718.16	12.60
65	0.0236	1664.81	38.84	0.0787	1693.62	19.92	0.0456	1718.88	12.57
75	0.0223	1665.20	38.55	0.0800	1694.46	20.02	0.0480	1719.42	12.69
85	0.0209	1665.64	38.23	0.0806	1695.37	20.19	0.0496	1719.97	12.77
95	0.0197	1666.58	37.68	0.0806	1696.65	20.61	0.0499	1720.71	12.63
105	0.0186	1667.33	37.18	0.0799	1697.81	20.92	0.0498	1721.27	12.57
115	0.0177	1668.28	36.45	0.0791	1699.36	21.34	0.0482	1721.91	12.33
125	0.0179	1671.35	36.09	0.0773	1701.04	21.27	0.0472	1722.50	12.13
135	0.0176	1672.97	34.79	0.0767	1702.58	21.09	0.0471	1722.96	12.09
145	0.0175	1674.78	33.15	0.0757	1703.78	20.70	0.0484	1723.31	12.13
155	0.0169	1676.21	31.58	0.0761	1705.81	20.92	0.0444	1724.01	11.53
165	0.0164	1677.66	29.90	0.0727	1706.93	20.56	0.0438	1724.40	11.49
175	0.0152	1678.95	28.17	0.0660	1707.88	20.13	0.0430	1724.75	11.55
185	0.0124	1680.44	25.65	0.0564	1709.22	19.76	0.0411	1725.22	11.55

Temp. (ºC)	**Ordered Area**	**Disordered Area**	**Free Area**	**Relative H-bonded Area**	**Relative Free Area**	**R_{index}**	**% H-bonded**
35	2.24	3.17	1.08	0.83	0.28	2.93	74.6
45	2.23	3.52	1.25	0.82	0.31	2.69	72.9
55	2.34	3.73	1.39	0.81	0.32	2.55	71.9
65	2.28	3.94	1.45	0.81	0.32	2.51	71.5
75	2.08	4.01	1.52	0.80	0.34	2.34	70.1
85	1.97	4.09	1.60	0.79	0.36	2.21	68.9
95	1.85	4.17	1.58	0.79	0.36	2.23	69.0
105	1.74	4.18	1.57	0.79	0.36	2.21	68.8
115	1.62	4.21	1.48	0.80	0.35	2.30	69.7
125	1.60	4.08	1.42	0.80	0.34	2.34	70.1
135	1.55	4.04	1.42	0.80	0.35	2.30	69.7
145	1.40	3.92	1.45	0.79	0.37	2.15	68.2
155	1.34	3.95	1.27	0.81	0.33	2.44	70.9
165	1.19	3.73	1.27	0.79	0.35	2.27	69.4
175	1.06	3.30	1.24	0.78	0.38	2.06	67.3
185	0.77	2.75	1.18	0.75	0.43	1.74	63.6

Table 8.16 Peak fitting data for the composite containing AA-MWCNTs at 10 wt.% loading

	Ordered Hydrogen Bonding			Disordered Hydrogen Bonding			Free Carbonyl		
Temp. (ºC)	Height	Center (cm^{-1})	Width (cm^{-1})	Height	Center (cm^{-1})	Width (cm^{-1})	Height	Center (cm^{-1})	Width (cm^{-1})
35	0.0244	1659.04	40.86	0.0591	1690.47	20.95	0.0271	1716.58	11.04
45	0.0244	1659.29	40.86	0.0618	1691.14	21.19	0.0288	1717.12	11.19
55	0.0246	1659.78	40.87	0.0648	1692.14	21.45	0.0309	1717.77	11.22
65	0.0254	1660.21	40.62	0.0713	1693.29	21.59	0.0348	1718.41	11.40
75	0.0264	1660.83	40.46	0.0786	1694.35	21.71	0.0388	1719.02	11.42
85	0.0261	1661.32	40.17	0.0836	1695.44	21.78	0.0423	1719.64	11.53
95	0.0253	1662.23	39.85	0.0850	1696.58	21.92	0.0438	1720.21	11.58
105	0.0249	1664.55	40.44	0.0835	1697.79	21.83	0.0450	1720.71	11.54
115	0.0238	1665.24	39.93	0.0827	1699.20	22.03	0.0444	1721.24	11.44
125	0.0235	1667.37	40.36	0.0800	1700.76	21.94	0.0433	1721.69	11.23
135	0.0233	1668.30	40.08	0.0776	1702.23	21.58	0.0427	1722.09	11.13
145	0.0235	1670.79	41.40	0.0736	1703.49	20.99	0.0420	1722.50	10.94
155	0.0224	1671.21	41.11	0.0713	1704.62	20.80	0.0409	1722.90	10.85
165	0.0215	1673.04	41.00	0.0673	1705.44	20.11	0.0418	1723.27	10.95
175	0.0203	1673.55	41.06	0.0645	1706.39	19.94	0.0403	1723.61	10.84
185	0.0190	1674.66	41.49	0.0586	1707.23	19.46	0.0392	1723.88	10.80

Temp. (ºC)	Ordered Area	Disordered Area	Free Area	Relative H-bonded Area	Relative Free Area	R_{index}	% H-bonded
35	2.37	3.10	0.75	0.88	0.21	4.27	81.0
45	2.37	3.29	0.81	0.87	0.21	4.09	80.3
55	2.47	3.49	0.87	0.87	0.22	4.01	80.0
65	2.46	3.83	1.00	0.86	0.23	3.68	78.6
75	2.55	4.29	1.12	0.86	0.24	3.57	78.1
85	2.54	4.57	1.21	0.85	0.25	3.44	77.5
95	2.42	4.65	1.28	0.85	0.26	3.23	76.4
105	2.46	4.58	1.30	0.84	0.27	3.17	76.0
115	2.33	4.56	1.26	0.85	0.26	3.20	76.2
125	2.35	4.37	1.21	0.85	0.26	3.25	76.5
135	2.24	4.19	1.20	0.84	0.27	3.13	75.8
145	2.30	3.87	1.15	0.84	0.27	3.14	75.8
155	2.19	3.67	1.11	0.84	0.27	3.09	75.5
165	2.18	3.35	1.15	0.83	0.29	2.81	73.8
175	1.99	3.18	1.08	0.83	0.30	2.80	73.7
185	1.90	2.86	1.05	0.82	0.31	2.65	72.6

Table 8.17 Peak fitting data for the composite containing AU-MWCNTs at 0.18 wt.% loading

	Ordered Hydrogen Bonding			Disordered Hydrogen Bonding			Free Carbonyl		
Temp. (ºC)	Height	Center (cm^{-1})	Width (cm^{-1})	Height	Center (cm^{-1})	Width (cm^{-1})	Height	Center (cm^{-1})	Width (cm^{-1})
35	0.0101	1667.18	26.72	0.0367	1690.11	16.57	0.0270	1715.81	15.30
45	0.0104	1668.05	25.39	0.0408	1691.10	16.78	0.0301	1716.79	15.00
55	0.0104	1668.31	24.83	0.0452	1691.63	16.58	0.0350	1717.21	15.00
65	0.0113	1668.92	23.60	0.0551	1692.57	16.66	0.0436	1717.92	14.82
75	0.0121	1669.13	22.80	0.0688	1693.28	16.62	0.0558	1718.38	14.73
85	0.0129	1668.47	21.35	0.0871	1694.03	16.63	0.0723	1718.84	14.61
95	0.0115	1668.70	20.57	0.0860	1695.01	16.91	0.0728	1719.54	14.39
105	0.0090	1666.20	19.28	0.0857	1696.33	17.82	0.0703	1720.60	13.91
115	0.0067	1661.38	12.16	0.0852	1698.74	20.18	0.0607	1722.18	13.08
125	0.0056	1663.03	12.03	0.0835	1700.98	20.75	0.0564	1723.03	12.59
135	0.0046	1664.86	11.87	0.0825	1703.47	21.23	0.0508	1723.79	11.97
145	0.0040	1667.39	11.20	0.0782	1705.16	21.06	0.0484	1724.24	11.73
155	0.0029	1669.09	10.96	0.0710	1706.93	21.34	0.0429	1724.63	11.30
165	0.0016	1670.64	10.50	0.0547	1708.68	20.94	0.0397	1725.00	11.24
175	-0.0002	1670.59	10.60	0.0368	1709.87	19.37	0.0409	1725.35	11.59
185	-0.0027	1639.06	26.74	0.0276	1711.49	17.30	0.0412	1725.88	11.52

Temp. (ºC)	Ordered Area	Disordered Area	Free Area	Relative H-bonded Area	Relative Free Area	R_{index}	% H-bonded
35	0.67	1.54	1.02	0.68	0.54	1.27	55.9
45	0.64	1.72	1.11	0.68	0.55	1.24	55.4
55	0.62	1.87	1.29	0.66	0.58	1.13	53.0
65	0.65	2.30	1.60	0.65	0.60	1.08	51.9
75	0.69	2.87	2.02	0.64	0.62	1.03	50.8
85	0.70	3.62	2.58	0.63	0.64	0.98	49.5
95	0.62	3.64	2.57	0.62	0.64	0.97	49.2
105	0.43	3.83	2.38	0.64	0.61	1.05	51.1
115	0.20	4.27	1.95	0.70	0.52	1.34	57.3
125	0.17	4.27	1.73	0.72	0.48	1.50	60.0
135	0.14	4.34	1.50	0.75	0.43	1.75	63.6
145	0.11	4.03	1.38	0.75	0.43	1.75	63.7
155	0.08	3.69	1.19	0.76	0.41	1.85	64.9
165	0.04	2.80	1.10	0.72	0.48	1.51	60.2
175	-0.01	1.75	1.16	0.60	0.68	0.88	46.8
185	-0.18	1.19	1.15	0.47	0.91	0.51	33.9

Table 8.18 Peak fitting data for the composite containing AU-MWCNTs at 1.8 wt.% loading

	Ordered Hydrogen Bonding			Disordered Hydrogen Bonding			Free Carbonyl		
Temp. (ºC)	**Height**	**Center (cm^{-1})**	**Width (cm^{-1})**	**Height**	**Center (cm^{-1})**	**Width (cm^{-1})**	**Height**	**Center (cm^{-1})**	**Width (cm^{-1})**
35	0.0314	1669.92	31.68	0.1017	1689.56	15.22	0.0760	1714.96	15.24
45	0.0294	1669.94	31.67	0.0987	1689.79	15.19	0.0770	1715.13	15.49
55	0.0275	1670.35	31.51	0.0966	1690.54	15.49	0.0767	1715.93	15.23
65	0.0256	1670.70	31.10	0.0936	1691.17	15.61	0.0775	1716.47	15.20
75	0.0236	1671.04	30.66	0.0907	1691.91	15.80	0.0782	1717.10	15.12
85	0.0214	1671.33	30.24	0.0882	1692.70	16.03	0.0787	1717.74	14.99
95	0.0191	1671.65	29.71	0.0858	1693.69	16.39	0.0788	1718.53	14.79
105	0.0169	1672.06	28.98	0.0830	1694.97	16.92	0.0770	1719.45	14.45
115	0.0152	1672.45	28.22	0.0807	1696.51	17.56	0.0742	1720.39	14.05
125	0.0133	1672.85	27.31	0.0810	1699.46	18.79	0.0673	1721.91	13.27
135	0.0125	1673.73	25.92	0.0812	1702.24	19.38	0.0606	1723.04	12.62
145	0.0112	1674.43	24.80	0.0792	1704.10	19.68	0.0557	1723.75	12.21
155	0.0102	1674.94	23.97	0.0757	1705.29	19.76	0.0528	1724.18	12.01
165	0.0093	1675.55	23.10	0.0698	1706.55	19.77	0.0492	1724.57	11.81
175	0.0064	1676.11	22.32	0.0554	1707.50	19.77	0.0460	1724.75	11.93
185	0.0039	1681.95	14.53	0.0405	1710.73	18.82	0.0395	1725.77	11.29

Temp. (ºC)	**Ordered Area**	**Disordered Area**	**Free Area**	**Relative H-bonded Area**	**Relative Free Area**	**R_{index}**	**% H-bonded**
35	2.44	3.81	2.86	0.69	0.54	1.28	56.1
45	2.29	3.81	2.94	0.67	0.56	1.21	54.8
55	2.20	3.88	2.89	0.68	0.55	1.23	55.2
65	2.01	3.68	2.88	0.66	0.57	1.16	53.6
75	1.83	3.60	2.90	0.65	0.60	1.09	52.3
85	1.58	3.53	2.90	0.64	0.62	1.03	50.7
95	1.41	3.53	2.86	0.63	0.63	1.01	50.3
105	1.23	3.52	2.72	0.64	0.62	1.02	50.5
115	1.06	3.56	2.54	0.65	0.61	1.06	51.5
125	0.89	3.80	2.17	0.68	0.54	1.26	55.8
135	0.79	3.90	1.88	0.71	0.49	1.46	59.3
145	0.68	3.86	1.67	0.73	0.46	1.59	61.4
155	0.60	3.71	1.56	0.73	0.45	1.62	61.8
165	0.54	3.41	1.42	0.74	0.45	1.63	61.9
175	0.36	2.67	1.34	0.69	0.52	1.32	56.9
185	0.14	1.84	1.10	0.64	0.61	1.05	51.3

Table 8.19 Peak fitting data for the composite containing AU-MWCNTs at 2.4 wt.% loading

	Ordered Hydrogen Bonding			Disordered Hydrogen Bonding			Free Carbonyl		
Temp. (ºC)	**Height**	**Center (cm^{-1})**	**Width (cm^{-1})**	**Height**	**Center (cm^{-1})**	**Width (cm^{-1})**	**Height**	**Center (cm^{-1})**	**Width (cm^{-1})**
35	0.0260	1668.41	37.31	0.0683	1690.48	17.71	0.0436	1716.52	13.72
45	0.0271	1669.38	36.88	0.0754	1691.15	17.64	0.0508	1717.06	13.74
55	0.0268	1669.89	36.28	0.0795	1692.01	17.62	0.0568	1717.68	13.75
65	0.0262	1670.28	35.85	0.0828	1692.81	17.71	0.0618	1718.17	13.87
75	0.0247	1670.69	35.54	0.0840	1693.81	17.97	0.0641	1718.87	13.77
85	0.0233	1670.71	35.53	0.0837	1694.32	17.76	0.0679	1719.07	13.96
95	0.0216	1671.19	35.33	0.0840	1696.02	18.77	0.0650	1720.25	13.46
105	0.0198	1671.57	35.10	0.0833	1697.59	19.34	0.0630	1721.07	13.15
115	0.0186	1672.24	34.31	0.0826	1699.44	19.81	0.0602	1721.90	12.82
125	0.0169	1672.72	34.14	0.0830	1701.46	20.50	0.0556	1722.71	12.33
135	0.0156	1673.56	33.14	0.0819	1703.47	20.87	0.0507	1723.39	11.89
145	0.0138	1674.30	32.29	0.0791	1705.06	20.88	0.0479	1723.87	11.65
155	0.0121	1675.47	30.86	0.0753	1706.75	21.05	0.0435	1724.33	11.25
165	0.0092	1677.70	28.09	0.0608	1708.28	20.46	0.0410	1724.84	11.28
175	0.0053	1681.49	22.65	0.0435	1710.99	19.73	0.0363	1725.53	10.96
185	0.0003	1681.49	22.66	0.0305	1711.62	19.16	0.0383	1725.64	11.42

Temp. (ºC)	**Ordered Area**	**Disordered Area**	**Free Area**	**Relative H-bonded Area**	**Relative Free Area**	**R_{index}**	**% H-bonded**
35	2.38	3.02	1.50	0.78	0.37	2.11	67.8
45	2.45	3.31	1.74	0.77	0.40	1.94	65.9
55	2.41	3.49	1.94	0.75	0.42	1.78	64.0
65	2.30	3.68	2.12	0.74	0.45	1.65	62.3
75	2.19	3.78	2.17	0.73	0.46	1.61	61.7
85	2.02	3.73	2.33	0.71	0.49	1.44	59.1
95	1.92	3.94	2.15	0.73	0.46	1.59	61.4
105	1.73	4.01	2.03	0.74	0.45	1.65	62.3
115	1.61	4.09	1.89	0.75	0.43	1.76	63.8
125	1.43	4.22	1.70	0.77	0.40	1.94	66.0
135	1.31	4.22	1.49	0.79	0.36	2.17	68.5
145	1.12	4.05	1.37	0.79	0.36	2.21	68.8
155	0.92	3.86	1.22	0.80	0.35	2.29	69.6
165	0.64	3.05	1.14	0.76	0.40	1.89	65.4
175	0.30	2.06	0.97	0.71	0.50	1.42	58.7
185	0.02	1.40	1.06	0.57	0.73	0.78	43.9

Table 8.20 Peak fitting data for the composite containing AU-MWCNTs at 5 wt.% loading

	Ordered Hydrogen Bonding			Disordered Hydrogen Bonding			Free Carbonyl		
Temp. (ºC)	Height	Center (cm^{-1})	Width (cm^{-1})	Height	Center (cm^{-1})	Width (cm^{-1})	Height	Center (cm^{-1})	Width (cm^{-1})
35	0.0118	1665.62	41.72	0.0235	1690.42	18.89	0.0145	1716.24	12.77
45	0.0122	1665.76	41.39	0.0264	1692.02	19.94	0.0158	1717.72	12.21
55	0.0128	1665.63	41.60	0.0309	1693.28	20.74	0.0180	1718.72	12.02
65	0.0137	1665.56	41.74	0.0353	1693.86	20.53	0.0220	1719.02	12.52
75	0.0135	1665.51	42.39	0.0387	1695.73	21.86	0.0217	1720.24	11.75
85	0.0137	1665.51	42.45	0.0422	1696.52	21.67	0.0252	1720.63	12.01
95	0.0138	1666.04	42.08	0.0446	1698.00	22.25	0.0256	1721.29	11.78
105	0.0136	1666.11	42.04	0.0462	1698.88	21.98	0.0280	1721.65	12.00
115	0.0136	1667.19	41.27	0.0484	1700.91	22.66	0.0268	1722.36	11.42
125	0.0133	1667.96	40.81	0.0501	1702.44	22.69	0.0268	1722.85	11.19
135	0.0128	1669.01	40.03	0.0516	1704.20	22.55	0.0264	1723.41	10.87
145	0.0114	1668.98	40.04	0.0506	1704.88	22.22	0.0279	1723.61	11.35
155	0.0103	1669.24	39.73	0.0498	1705.80	21.54	0.0297	1724.12	11.27
165	0.0089	1671.10	37.80	0.0482	1707.74	21.70	0.0287	1724.49	10.96
175	0.0065	1678.06	30.34	0.0403	1710.82	20.19	0.0293	1725.58	10.64
185	-0.0007	1677.89	30.67	0.0279	1712.02	18.90	0.0342	1725.95	11.29

Temp. (ºC)	Ordered Area	Disordered Area	Free Area	Relative H-bonded Area	Relative Free Area	R_{index}	% H-bonded
35	1.21	1.09	0.45	0.84	0.28	2.99	74.9
45	1.21	1.30	0.49	0.84	0.28	3.00	75.0
55	1.31	1.60	0.54	0.84	0.27	3.15	75.9
65	1.42	1.79	0.68	0.83	0.30	2.76	73.4
75	1.33	2.12	0.64	0.84	0.27	3.15	75.9
85	1.44	2.26	0.74	0.83	0.29	2.92	74.5
95	1.43	2.48	0.76	0.84	0.28	3.01	75.1
105	1.43	2.50	0.83	0.83	0.30	2.77	73.5
115	1.40	2.68	0.76	0.84	0.27	3.14	75.8
125	1.29	2.78	0.75	0.84	0.27	3.17	76.0
135	1.27	2.86	0.70	0.86	0.25	3.45	77.5
145	1.07	2.77	0.78	0.83	0.29	2.88	74.2
155	0.97	2.63	0.83	0.81	0.32	2.54	71.7
165	0.82	2.53	0.78	0.81	0.32	2.51	71.5
175	0.49	1.96	0.76	0.76	0.40	1.89	65.3
185	-0.06	1.29	0.94	0.57	0.74	0.77	43.4

Table 8.21 Peak fitting data for the composite containing AU-MWCNTs at 10 wt.% loading

	Ordered Hydrogen Bonding			Disordered Hydrogen Bonding			Free Carbonyl		
Temp. (ºC)	Height	Center (cm^{-1})	Width (cm^{-1})	Height	Center (cm^{-1})	Width (cm^{-1})	Height	Center (cm^{-1})	Width (cm^{-1})
35	0.0236	1654.41	43.39	0.0492	1690.10	22.63	0.0190	1716.26	10.12
45	0.0247	1654.40	43.44	0.0536	1690.61	22.60	0.0219	1716.66	10.57
55	0.0263	1656.57	44.63	0.0568	1691.95	22.81	0.0237	1717.45	10.34
65	0.0271	1656.82	44.53	0.0609	1692.77	22.82	0.0264	1717.94	10.60
75	0.0288	1658.32	45.18	0.0658	1693.80	22.76	0.0297	1718.45	10.73
85	0.0305	1658.69	45.01	0.0726	1694.74	22.87	0.0335	1718.93	10.78
95	0.0322	1660.18	45.52	0.0774	1695.89	22.93	0.0366	1719.39	10.75
105	0.0328	1661.32	45.60	0.0796	1696.99	22.85	0.0389	1719.75	10.83
115	0.0320	1662.51	45.46	0.0786	1698.37	22.86	0.0390	1720.20	10.77
125	0.0313	1663.95	45.59	0.0770	1699.59	22.64	0.0394	1720.58	10.78
135	0.0310	1666.58	46.10	0.0740	1700.93	22.09	0.0396	1720.98	10.73
145	0.0293	1667.39	45.49	0.0731	1702.23	21.96	0.0394	1721.44	10.67
155	0.0271	1668.65	44.69	0.0703	1703.43	21.64	0.0396	1721.91	10.68
165	0.0239	1669.34	44.18	0.0653	1704.28	21.43	0.0398	1722.25	10.91
175	0.0191	1672.48	41.77	0.0550	1706.06	20.67	0.0385	1723.11	10.84
185	0.0106	1680.69	30.97	0.0396	1709.30	18.52	0.0380	1724.72	10.82

Temp. (ºC)	Ordered Area	Disordered Area	Free Area	Relative H-bonded Area	Relative Free Area	R_{index}	% H-bonded
35	2.52	2.76	0.48	0.92	0.14	6.43	86.5
45	2.63	3.04	0.58	0.91	0.16	5.72	85.1
55	2.79	3.24	0.62	0.91	0.16	5.69	85.0
65	2.89	3.46	0.69	0.90	0.17	5.38	84.3
75	3.14	3.73	0.80	0.90	0.18	5.02	83.4
85	3.24	4.14	0.89	0.89	0.18	4.85	82.9
95	3.49	4.37	0.99	0.89	0.19	4.64	82.3
105	3.60	4.52	1.05	0.89	0.20	4.52	81.9
115	3.48	4.46	1.05	0.88	0.20	4.42	81.6
125	3.37	4.30	1.05	0.88	0.21	4.27	81.0
135	3.39	4.03	1.07	0.87	0.22	4.06	80.2
145	3.14	4.10	1.04	0.87	0.21	4.07	80.3
155	2.88	3.72	1.06	0.86	0.24	3.64	78.5
165	2.53	3.42	1.08	0.85	0.26	3.22	76.3
175	1.91	2.79	1.05	0.82	0.31	2.62	72.4
185	0.84	1.82	1.01	0.72	0.47	1.54	60.6